# New Building Blocks for Dual-Property Molecule-Based Magnets

Shari Venneri

A thesis submitted to the Department of Chemistry in partial fulfillment of the requirements for the Degree of Master of Science

Supervised By

**Professor Melanie Pilkington**

**Brock University**

**St. Catharines Ontario, Canada**

**September 2011**

## Abstract

Two classes of compounds have been prepared and characterized as building blocks for chiral magnets and ferromagnetic conductors. In the first project, the organic framework of a pentadentate, ($N_3O_2$) macrocycle has been synthetically modified to introduce phenyl substituents into its organic framework and the synthesis of four new [Fe(II)($N_3O_2$)($CN)_2$] complexes **(I)** – **(IV)** is presented.

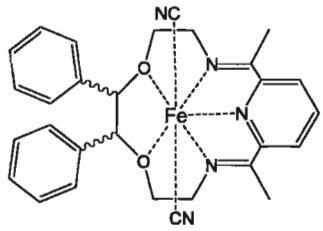


**R,R (I), S,S (II), racemic (III), meso (IV)**

This work represents the first structural and magnetic studies of a family of spin crossover macrocycles that comprise of both structural and stereo-isomers. Magnetic susceptibility and Mössbauer data for the *R,R*-complex **(I)** is consistent with both a thermal and a light induced spin crossover transition. The X-ray data supports a change in geometry accompanying the thermal spin transition, from a high spin (HS) 7-coordinate complex at room temperature to a low spin (LS) 5-coordinate complex at 100 K. The crystal structure of the *racemic* complex **(III)** reveals a HS, 7-coordinate complex at 200 K that undergoes no significant structural changes on cooling. In contrast, the magnetic susceptibility and Mössbauer data collected on a powder sample of the *racemic* complex are consistent with a LS complex. Finally, the *meso* complex **(IV)** was prepared and its structure and magnetic properties are consistent with a 5-coordinate LS complex that remains low spin, but undergoes conformational changes on cooling in solution. The

chiral $[Fe(II)(N_3O_2)(CN)_2]$ macrocycle **(I)**, together with its Mn(II) and Fe(II) derivatives have also been exploited as building blocks for the self-assembly of chiral magnets.

In the second project, a synthetic route for the preparation of tetrathiafulvalene (TTF) donors covalently attached to a diisopropyl verdazyl radical via a cross conjugated pyridyl linker is presented. Following this strategy, four new TTF-py-(diisopropyl)verdazyl radicals have been prepared and characterized **(V)** – **(VIII)**.

$R_1$ = TTF
$R_2$ = verdazyl radical

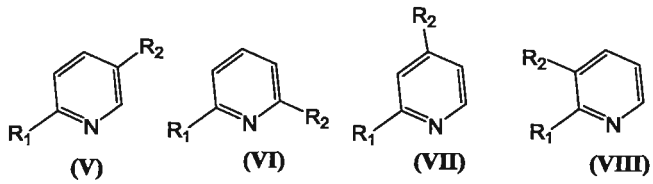


The first (2:1) charge transfer complex of a TTF-py-(diisopropyl)verdazyl radical donor and a TCNQ acceptor has been prepared and structurally characterized. The crystal packing shows that the donor and acceptor molecules are organized in a mixed stacking arrangement consistent with its insulating behaviour. EPR and magnetic susceptibility data support intramolecular ferromagnetic interactions between the TTF and the verdazyl radicals and antiferromagnetic interactions between TTF donors within a stack. In an attempt to increase the intramolecular exchange interaction between the two radicals, a TTF-π-(diisopropyl)verdazyl radical **(IX)** was prepared, where the two radicals are connected via a conjugated divinylene linker. The neutral radical donors stack in a more favourable head-to-head arrangement but the bulky isopropyl groups prevent the donor radicals from stacking close enough together to facilitate good orbital overlap.

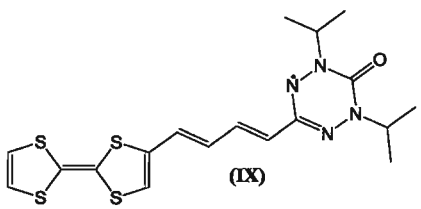

## Acknowledgments

Firstly and foremost, I would like to thank Prof M. Pilkington for her guidance and patience throughout the completion of my thesis. This thesis would not have been possible without her editing and proof-reading. I would also like to thank the entire Pilkington group for their help and suggestions and for making the past couple of years successful through their support and friendship. I am especially grateful to Emma Gavey and Nick Hurley for their help with the proof-reading of my thesis and Roland Acha and Roger Gumbau-Brisa for being my mentors in the development of my lab techniques. I would also like to acknowledge Dr. Q. Wang for his collaboration and support on this project. Being able to work with Dr. Q. Wang helped to further develop my synthetic skills and advance my lab techniques.

I am also appreciative to my advisory committee, Prof. M. Lemaire and Prof. T. Dudding for their helpful suggestions. I would especially like to acknowledge Prof. M. Lemaire for his assistance with my magnetic susceptibility and UV-Vis measurements.

I would like to thank Dr. P. Poddutoori and Sam Mula for taking the time to help me with my EPR experiments and simulations.

I owe my deepest gratitude to Tim Jones for the numerous mass spectroscopy experiments and Razvan Simionescu for his assistance with the NMR experiments and analysis.

I wish to also thank my collaborators for their crucial contributions to this thesis. Dr. Cédric Desplanches and Dr. Hongfeng Wang (CNRS, Bordeaux, France), for my magnetic measurements. Dr. Victor Polo (University of Zaragoza, Spain), for his

computational studies and Dr. Scott Turner (University of Surrey, UK), for the resistivity measurements.

Finally I would like to thank my family and friends for their ongoing patience and support throughout the completion of my degree.

# Table of Contents

# List of Figures

# List of Tables

# List of Schemes

# Abbreviations

| | |
|---|---|
| 0-D | zero-dimensional |
| 1-D | one-dimensional |
| 2-D | two-dimensional |
| 3-D | three-dimensional |
| Å | Ångstrom |
| BEDT- TTF | *bis*(ethylenedithio) tetrathiafulvalene |
| B.M. | Bohr magneton |
| br | Broad (NMR and IR peak descriptor) |
| Bu | butyl |
| cald | calculated |
| °C | degree celsius |
| CD | circular dichroism |
| CN | cyanide |
| COSY | correlation spectroscopy |
| CV | cyclic voltammetry |
| d | Doublet |
| dd | doublet of doublets |
| DCM | dichloromethane |
| DFT | density functional theory |
| DMF | dimethyl formamide |
| DMSO | dimethyl sulfoxide |
| e | electron charge |
| EI | electron impact ionization |
| EPR | electron paramagnetic resonance |
| Et | Ethyl |

| | |
|---|---|
| FAB | fast-atom bombardment |
| g | Grams |
| *g* | g-factor, proportionality constant |
| GCE | glassy carbon electrode |
| h | hour(s) |
| HMBC | heteronuclear multiple bond correlation |
| HOMO | highest occupied molecular orbital |
| HRMS | high resolution mass spectroscopy |
| HSQC | heteronuclear single quantum correlation |
| HS | high spin |
| Hz | Hertz |
| *i*-Pr | Isopropyl |
| IR | infrared |
| ICT | intramolecular charge transfer |
| *J* | coupling constant (NMR), magnetic exchange parameter |
| K | Kelvin |
| LDA | lithium diisopropyl amide |
| LIESST | light-induced excited state spin trapping |
| LS | low spin |
| LUMO | lowest unoccupied molecular orbital |
| *m* | Multiplet |
| M | Molar |
| min | Minutes |
| mL | Milliliters |
| MLCT | metal-ligand charge transfer |
| mmol | Millimole |
| M.p. | melting point |

| | |
|---|---|
| $M_r$ | remnant magnetization |
| ms | millisecond |
| $m_s$ | quantum number for the z-component of the electron spin |
| $M_{sat}$ | saturated magnetization |
| MS | mass spectroscopy |
| *m/z* | mass/charge ratio |
| NMR | nuclear magnetic resonance |
| nm | nanometer |
| NN | nitronyl nitroxide |
| NOESY | nuclear overhauser enhancement spectroscopy |
| ORTEP | oak ridge thermal ellipsoid plot |
| OAc | acetate |
| ppm | parts per million |
| py | pyridine |
| R | agreement factor |
| rt | room temperature |
| s | singlet |
| *S* | spin quantum number |
| SCO | spin crossover |
| SCM | single chain magnet |
| SMM | single molecule magnet |
| SOMO | singly occupied molecular orbital |
| SQUID | superconducting quantum interference device |
| str | stretch |
| t | triplet |
| T | temperature |
| $T_c$ | critical temperature |

| | |
|---|---|
| $T_N$ | neel temperature |
| TCNQ | tetracyano-*p*-quinodimethane |
| THF | tetrahydrofuran |
| TLC | thin layer chromatography |
| TTF | tetrathiafulvalene |
| $TTF^{+\cdot}$ | tetrathiafulvalene radical cation |
| $TTF^{2+}$ | tetrathiafulvalene dication |
| TMTSF | tetramethyltetraselenafulvalene |
| UV-Vis | ultra violet-visible |
| ver | verdazyl radical |
| $\mu_B$ | Bohr magneton |
| $\mu_{eff}$ | magnetic moment |
| $\lambda$ | wavelength |
| $\chi$ | magnetic susceptibility |
| $\chi_M$ | molar magnetic susceptibility |

# List of Compounds

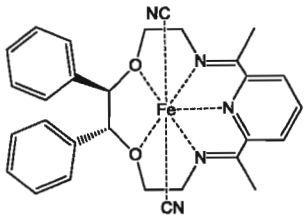


**R,R (2.9)**

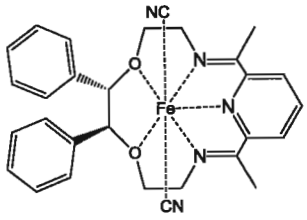


**S,S (2.10)**

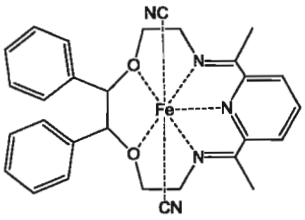


**racemic (2.11)**

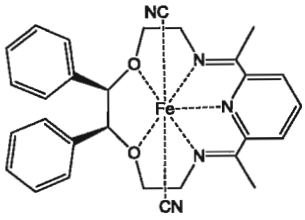


**meso (2.12)**

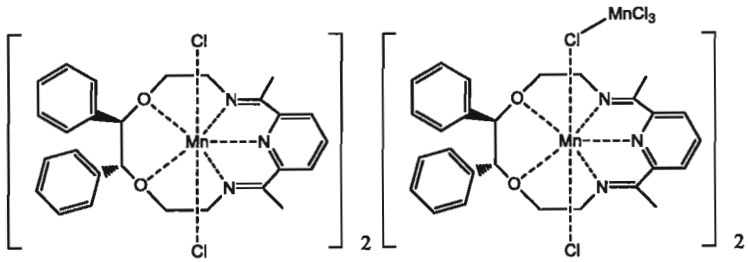


**(2.16)**

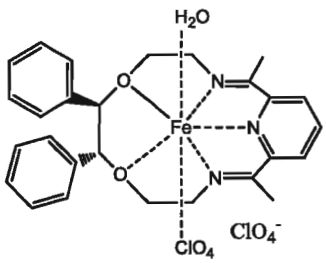


**(2.15)**

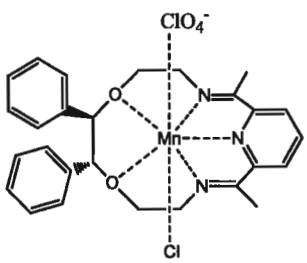


**(2.17)**

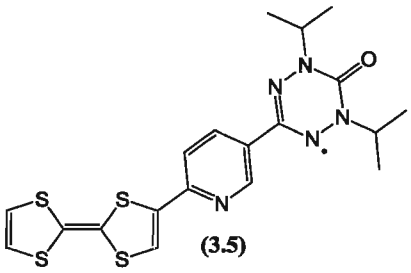

(3.5)

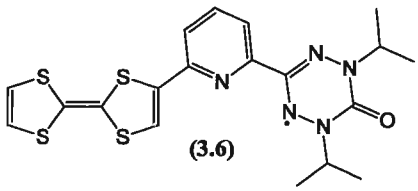

(3.6)

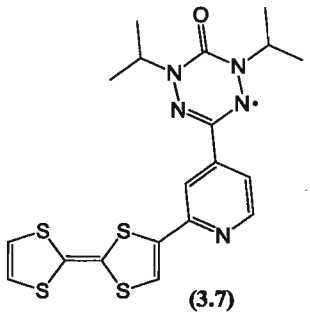

(3.7)

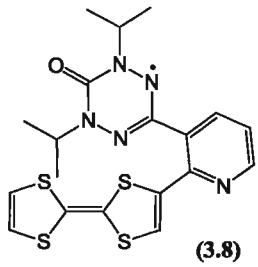

(3.8)

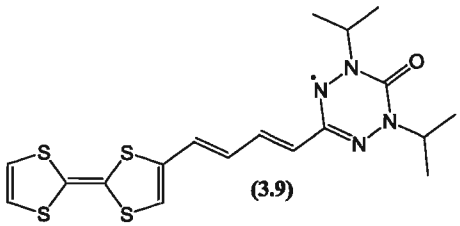

(3.9)

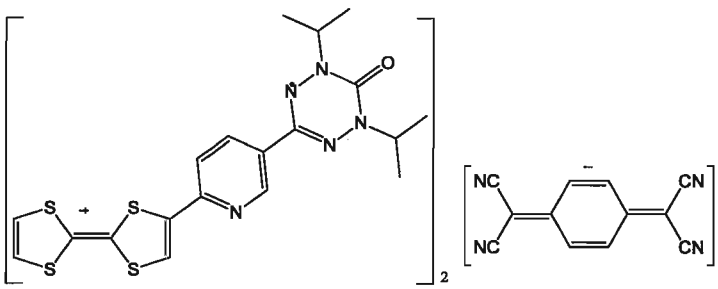

(3.28)

# CHAPTER 1- Introduction to Dual Property Materials

Multifunctional materials have been receiving a considerable amount of attention in recent years, with the primary focus centered around the combination of ferromagnetism, together with conductivity and/or chirality.[1] The driving force for the design and preparation of multifunctional materials stems from the combination of at least two of the aforementioned physical properties and examining if the role each plays is independent of the other or, if there is an interplay between them.[1] A survey of the chemical literature reveals these properties have been combined to form three main classes of dual-property materials namely: ferromagnetic conductors, chiral conductors and chiral magnets. The incorporation of these properties in a material or compound is ultimately dependent on the design and organization of its molecular components or building blocks. The manner in which these building blocks are connected and interact forms the basis for the type of properties the compounds exhibit. These building blocks can consist of solely organic-based materials or can include coordination compounds. The focus of my research is the preparation and characterization of chiral magnets and ferromagnetic conductors, from organic molecule-based building blocks and/or coordination compounds.

## 1.1 Magnetism

### 1.1.1 Traditional *vs.* Molecule Based Magnets

Traditionally, magnets are atom-based materials where the magnetic ordering arises as a consequence of co-operative spin-spin interactions between unpaired electrons located in either the *d* or *f*-orbitals.[2] Synthetically, conventional magnets are prepared via solid state chemistry which typically involves high temperature metallurgical routes.[2]

Molecule-based magnets have been a focus of research in the past few decades due to the advantages offered that include synthetic versatility and size.[2] The appeal stems from the ideal for miniaturization of electronics and optical memory storage in a limited space.[2] The ultimate difference in atom versus molecule is the location of the active spin sites. As previously mentioned, atom-based materials have spins located in the *d* or *f* orbitals, while molecule-based magnets may contain their active spin site in σ or π molecular orbitals made up of *s* or *p* atomic orbitals, not just the *d* or *f* orbitals.[2] Since it has been previously realized that the properties of molecule-based magnets are a consequence of the crystalline architecture of the molecules, the manipulation and fine-tuning of the orientation and interacting distances between the active spin sites is achievable.[2] This is carried out by choosing molecular precursors which contain an unpaired spin and arranging them in such a way that the spin-spin interactions are optimal.[2] Since magnetism is a co-operative effect, it is important that the spin-spin interactions extend to all three dimensions, either through space or through bond(s).

### 1.1.2 Magnetism: An Overview

Bulk magnetic properties of a molecule are predicted in response to the movement of electrons in a particular molecule. The types of electron motion are orbital and spin motion.[3] Orbital motion is due to the movement of an electron around the nucleus, while spin motion is the motion of an electron spinning about its own axis with a magnetic moment and angular moment being associated with this movement.[3] The resultant behaviour of these electrons spinning about an individual axis and moving in their own orbits dictate the type of magnetic behaviour of a particular molecule.[3] Since molecules have multiple electrons, the magnetic moment is the vector sum of all its electronic

moments.[3] Therefore, the spin of the electron and how they interact determines the type of magnetic properties exhibited by the molecule.[4] If moving electron pairs are placed in a magnetic field, this external magnetic field results in an additional internal magnetic field which opposes the direction of the external field.[3] The internal field will be weaker than the applied external field causing the sample to be repelled by the applied field, resulting in diamagnetic behaviour, Figure 1.1.[3] Therefore, diamagnetism is present in every sample. If the cancellation of the electronic moments is only partial, there is a net magnetic moment, resulting in paramagnetism.[3] This partial cancellation is due to a singly occupied orbital with an unpaired electron. In the presence of an external magnetic field, the magnetic moment aligns itself with the external field and increases the internal field of the sample.[3] For paramagnetism, the sample is drawn into the magnetic field, causing an attraction between the magnetic field and the paramagnet, Figure 1.1.[3] The contribution of a paramagnetic electron is two orders of magnitude greater than diamagnetic contributions, therefore a single unpaired electron overshadows diamagnetism.[3]

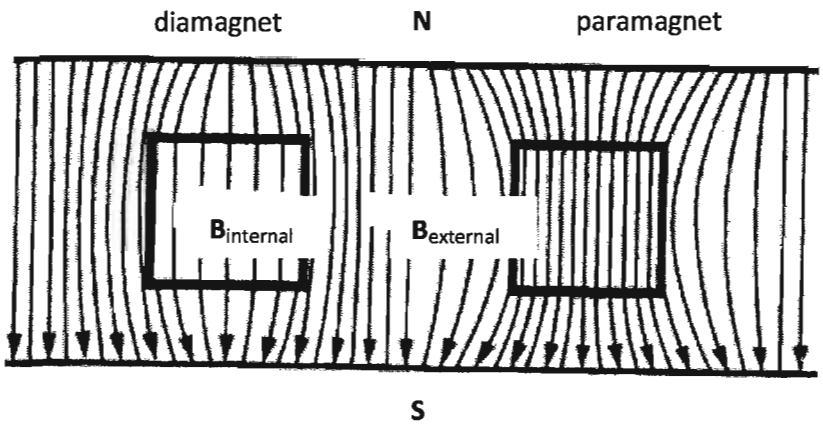


**Figure 1.1:** Cartoon representation of a diamagnet (left) and a paramagnet (right), in the presence of internal magnetic field $B_{internal}$ and external magnetic field $B_{external}$.[5] "Adapted from figure 2.7 reference 5."

Paramagnets can be further characterized by a series of different magnetic behaviours depending on the type of interaction between the unpaired electrons, or spin contributions. The most common classes are: ferromagnetism, the parallel alignment of the magnetic moments; antiferromagnetism, the alignment of two equivalently but oppositely oriented magnetic moments; and ferrimagnetism, the alignment of two inequivalent oppositely oriented magnetic moments, Figure 1.2.[5] The individual ordering behaviours occur below a magnetic ordering, or critical temperature, $T_c$.[4] Other types of magnetic behaviour are present but are usually subtle variations of the aforementioned classes.

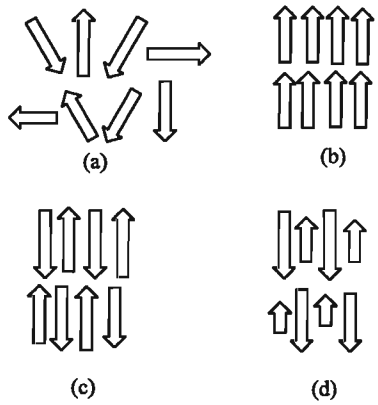


**Figure 1.2:** Schematic drawing of most common spin coupling behaviours (a) paramagnetic; (b) ferromagnetic; (c) anti-ferromagnetic; and (d) ferrimagnetic.[6] "Adapted from figure 3 reference 6."

A spin-only formula is used as an initial approximation of the magnetic moment of a paramagnetic substance, i.e. the number of unpaired electrons.[4] By ignoring the orbital angular momentum of the electron, the magnetic moment, μ, can be determined from the number of unpaired electrons, *n*.[4] The number of unpaired electrons is related to the spin quantum number *S*, where $S = \Sigma M_s$ and $M_s = \pm ½$ per unpaired electron, therefore the spin-only formula is represented by equation (1).[4]

$$\mu = 2\sqrt{S(S+1)} \qquad (1)$$

The different types of magnetic behaviour are predicted via cooperative interactions between the magnetic moments.[7] Spin interactions are typically necessary in all directions, that is three-dimensional (3D), in order to achieve long-range magnetic order and bulk ferromagnetic behaviour.[6] However, it is possible that two-dimensional (2D) spin interactions may suffice. For one-dimensional (1D) spin interactions, long-range ordering occurs at 0 K.[6] But if there is an anisotropic interaction for a 1D chain, hysteretic effects mimicking 3D order may occur.[6] The exchange coupling interaction between different spin environments is represented by *J,* where *J* is dependent on intermolecular, intramolecular and interchain interactions.[6] The sign and magnitude of *J* for two interacting spins ultimately predicts the type of magnetic behaviour demonstrated.[6] If *J* results in a negative value, antiferromagnetic coupling between spins is present and if *J* results in a positive value, ferromagnetic coupling between spins is present.[6]

Magnetic behavior of a molecule-based magnet can be measured using a superconducting quantum interference device (SQUID).[8] The behaviour is frequently measured through response or susceptibility $\chi$ of the material to a magnetic field, and is defined by the ratio of magnetization of the material *M*, and the applied field *H*.[4] The magnitude of the interaction between the unpaired electrons is dependent on the distance between themy.[4] Susceptibility can be measured quantitatively through molar susceptibility which indicates the magnetization ability of a material per unit molecular weight.[9] Determination of molar magnetic susceptibility $\chi_M$ and the effective Bohr magneton number, $\mu_{eff}$, are two important magnetic measurements specific to this

research. The effective magnetic moment can be obtained from $\chi_M$, using the expression demonstrated in equation (2).[9]

$$\mu_{eff} = 0.7977\sqrt{\chi_M T} \quad (2)$$

When the spins are not interacting, they are said to obey the Curie Law, equation (3), where T is temperature in Kelvin and C is the Curie constant.[4] If the spins are independent, i.e. paramagnetic, the molecule obeys the Curie Law with the susceptibility $\chi$ being proportional to 1/T.[4] Obeying the Curie Law means if the compound has more than one magnetic moment they are magnetically isolated and there are no cooperative interactions.

$$\chi = \frac{C}{T} \quad (3)$$

However, the Curie Law is rarely obeyed, this may be due to one or more of several factors. Firstly, the presence of orbital angular momentum may contribute to the magnetic moment. The coupling of the spin and orbital components to the magnetism via spin-orbit coupling not only leads to deviation from Curie law but also leads to a large anisotrpy.[10] Deivation from Curie behaviour can also occur if the spins interact, coupling ferro- or antiferromagnetically.[4] The susceptibility can be modeled as a function of temperature by the Curie-Weiss expression, equation (4), where θ is the Weiss constant.[4] To accommodate non-Curie behaviour, the additional θ parameter is used to fit the data. The magnitude of θ is proportional to the strength of the coupling between the adjacent spins.[4] For a ferromagnetic interaction, $\chi$ is enhanced, and $\theta > 0$. The ordering changes from paramagnetic, below $T_c$, to ferromagnetic above $T_c$, when the thermal energy is sufficient to overcome the ferromagnetic alignment and paramagnetic behaviour

prevails.[4] For antiferromagnetic behavior $\chi$ is suppressed, $\theta < 0$, and antiferromagnetic alignment is expected to occur below $T_N$, as the temperature decreases there is less thermal energy available and paramagnetic behaviour reduces rapidly. [4]

$$\chi = \frac{C}{T - \theta} \quad (4)$$

An output from a SQUID can be presented in several different forms, including a plot of susceptibility *vs.* temperature which is not very useful for determining the type of magnetic interactions occurring. The only visible deviation is for an antiferromagnetic sample which exhibits a maximum at low temperature.[4] The strength of the interaction can be extrapolated from the graph since stronger interactions are reflected in $\chi_{max}$ at higher temperatures. For the temperature-dependent paramagnetic behaviour of a sample, $\chi_M T$ *vs.* T plots are useful, Figure 1.3, since they present information about the type of magnetic interaction exhibited.[4] Paramagnetic behaviour is demonstrated by a linear response since there is no variation in $\chi_M T$ with temperature. At higher temperatures, all classes of magnetism exhibit the same paramagnetic behaviour above their critical temperatures. There is an upward deviation from paramagnetic behaviour for a ferromagnet, and conversely a downward deviation for an antiferromagnet with magnetic behaviour with decreasing temperature.[4] There is a slight downward curvature observed for a ferrimagnet due to antiferromagnetic interactions between adjacent magnetic moments, followed by an upward curvature due to an increasing correlation in the material.[4] An inverse susceptibility *vs.* temperature plot shows a linear response for an ideal paramagnet, crossing through zero obeying the Curie Law. Deviations from a linear

behaviour occur when cooperative effects are present. A ferromagnet exhibits a downward curvature, while an antiferromagnet exhibits an upward curvature.[4]

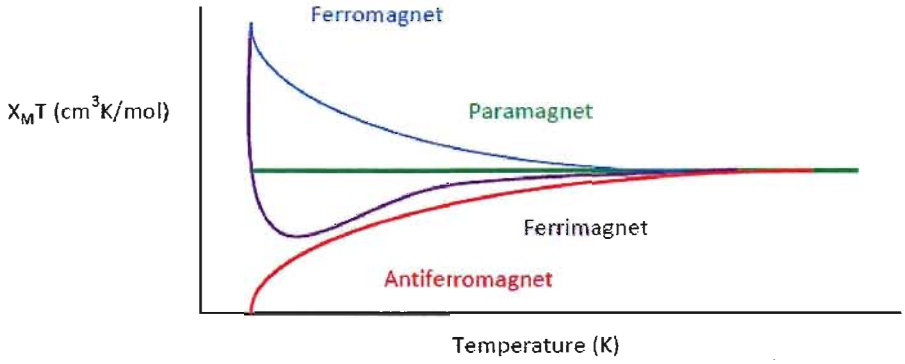


**Figure 1.3a:** A plot of $\chi_M T$ vs. T for paramagnetic, ferromagnetic, ferrimagnetic and antiferromagnetic response.[4] "Adapted from figure 2 reference 4."

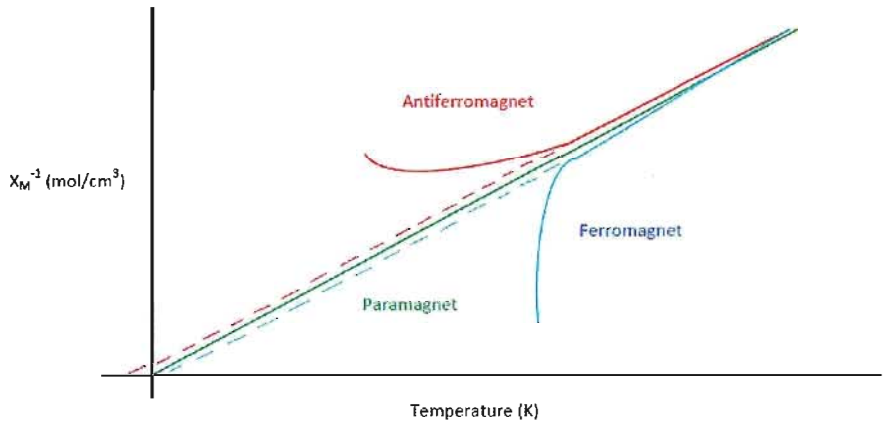


**Figure 1.3b:** A plot of $\chi_M^{-1}$ *vs.* T for a paramagnetic, antiferromagnetic and ferromagnetic response.[4] "Adapted from figure 2 reference 4."

In the presence of a magnetic field, each of the classes of magnetism demonstrates a different response. For a paramagnet, the magnetic moments orient randomly in the absence of a magnetic field, while in the presence of a magnetic field the spins tend to align parallel to the field resulting in magnetization that is proportional to the applied field.[4] At sufficiently lower temperatures, the thermal energy is insufficient and cannot

overcome the tendency for the magnetic moments to align in a long-range fashion and therefore, the material will exhibit bulk magnetic ordering. Ferro-, ferri- and antiferromagnetism arise from cooperative interactions of spins at various centres. In an antiferromagnetic material the magnetic moments align anti-parallel to each other, and result in no overall magnetic moment due to the cancellation of spins since the opposing magnetic moments are of equal magnitude.[4] Ferrimagnetic materials contain magnetic moments of different magnitudes, i.e. there is more than one type of magnetic ion, resulting in an overall magnetic moment in the presence of an applied field; however, not all of the magnetic moments contribute positively to the overall magnetization.[4] Ferromagnetism is a special case because in the presence of a magnetic field the spins are aligned parallel to the field contributing to an overall magnetic moment; however, the magnetic moment remains in the absence of the magnetic field.[4]

### 1.1.3 Bulk Ferromagnetism

As previously mentioned, diamagnetism and paramagnetism are properties of individual molecules; however, ferromagnetism is a cooperative property of a group of molecules.[11] When individual magnetic moments of molecules interact and align in a parallel fashion, they produce regions or domains that are permanently and spontaneously magnetized.[11] Each individual domain exhibits its own degree of magnetization.[11] The theory of domains is important when recognizing that the initial magnetization of a ferromagnet is zero.[11] Weiss was the first to hypothesize about ferromagnetic domains. He postulated that there is a molecular field in a ferromagnet that is strong enough to magnetize the molecule even in the absence of an applied external field.[11] He concluded that a ferromagnet is a paramagnet with a large internal molecular field. When a

ferromagnet is in a demagnetized state, magnetic spins in different domains have different orientations, resulting in magnetization that averages to zero.[11] When a magnetic field is applied the spins all orient in the same direction resulting in a net magnetic moment. Ferromagnetic domains are formed due to three different types of energy; magnetostatic, magnetocrystalline and magnetostrictive energy.[11]

In the presence of a demagnetizing field i.e. a field applied in the opposite direction to the magnetization, there is a resulting magnetostatic energy which is dependent on the shape of the sample, Figure 1.4(a).[11] The magnitude of the magnetostatic energy can be reduced by reducing the external demagnetizing field, which can be carried out by dividing the sample into domains, Figure 1.4(b). [11] In order to result in no magnetostatic energy a domain pattern which leaves no magnetic poles is essential, Figure 1.4(c).[11]

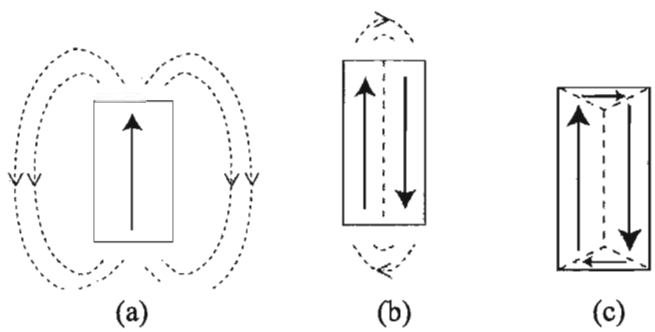


**Figure 1.4:** (a) a ferromagnet in the presence of an external demagnetizing field; (b) a ferromagnet with two domains with a reduced external demagnetizing field; (c) a ferromagnet with domains.[11] "Adapted from figure 7.3 reference 11."

Magnetocrystalline energy is the next type of energy that helps to determine the arrangement of domains in a ferromagnetic sample. This is the phenomenon that allows magnetization to align along preferred crystallographic directions. It has been determined that it is "easier" to align the magnetization in specific directions, resulting in lower energy than other directions, deemed "harder". For example, it is easier to align the

magnetization along the edge of a cube lattice rather than diagonally across the faces or body of the cell.[11] Therefore, domains will form along directions where magnetization can align "easily".[11] It is also preferable to have the largest amount of domains with the fewest boundaries.

Magnetostrictive energy occurs due to the change in length a sample undergoes when it is magnetized. Some samples may elongate or constrict in the direction of the magnetization.[11] The vertical and horizontal domains attempt to elongate in each direction, but since this is not possible it introduces an elastic restrain energy.[11] The elastic strain energy is proportional to the volume of the domain closure and can be lowered by making these domains smaller; however, this results in an increase of the primary domains.[11] Therefore, domain structure is a compromise between the different domain energies, Figure 1.5.[11]

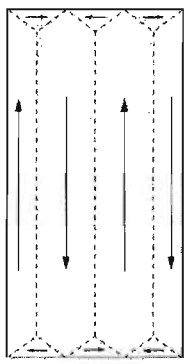

**Figure 1.5:** Arrangement of domain walls minimizing magnetostatic, magnetocrystalline and magnetostrictive energies.[11] "Adapted from figure 7.7 reference 11."

When a ferromagnet is subjected to a strong enough magnetic field, the domains will become aligned in the same direction and remain aligned once the field is removed.[11] This is demonstrated in Figure 1.6, which depicts the domain alignments at each stage of magnetization. The magnetic moments will remain aligned in this manner unless placed

in some sort of reversal field. The tendency for a ferromagnet to 'remember' its magnetic history in this fashion introduces hysteresis.[11] Hysteresis can be observed for a ferro- or ferrimagnet below their critical temperature and occurs because of a rearrangement of the domain walls.[11] For cases when hysteresis is present a coercive field and remnant magnetization are exhibited. The remnant magnetization is obtained by applying and removing a large magnetic field and represents the extent of the spontaneous magnetic behaviour observed.[11] When a sample exhibits hysteresis, a coercive field is present and is applied in the reverse direction to reduce the magnetization back to zero.[11] The sample initially shows zero magnetization because of an overall cancellation of magnetic moment in each domain. In the presence of a magnetic field, all of the domains are aligned creating an overall magnetic moment, finally the applied field is sufficient to overcome all the domain walls leaving a single domain.[11]

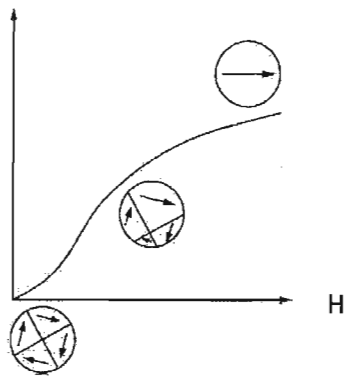


**Figure 1.6:** A plot of the change in domain structure through the different stages of magnetization.[11] "Reprinted with permission from reference 11. Copyright {2003} Cambridge University Press."

It is noted that the type of magnetization is dependent on the interactions of the magnetic moment as well as the purity of a sample. This will determine if the sample is a "hard" or permanent magnet, which requires a large field to magnetize it but will retain a large portion of magnetization once the field is removed, and has a high coercive field; or

a "soft" magnet which is easily magnetized and demagnetized and exhibits a low coercive field.[11]

## 1.2 Synthetic Strategies for the Preparation of Molecule-based Magnets

Molecule-based magnets were given significant attention after the first two molecule-based compounds exhibiting spontaneous magnetization below a critical temperature, $T_c$, were reported in 1986 by Miller and Kahn.[12, 13] Subsequently, many different methods have been employed for the design and preparation of molecule-based magnets. Most molecule-based magnets are designed with a well-defined organic component, which does not exhibit a significant change in geometry in the solid state assembly because of the strong covalent or ionic interactions.[14] These interactions exhibit a higher energy than non-covalent interactions such as hydrogen bonding, *van der Waals*, and donor-acceptor charge transfer.[14] Therefore, this provides the opportunity of modifying the molecule by attaching different functionalities to the molecular skeleton. Two main categories of design are using purely organic building blocks utilizing a radical as the spin component and coordination chemistry involving organic ligands coordinated to a paramagnetic metal ion, Figure 1.7.

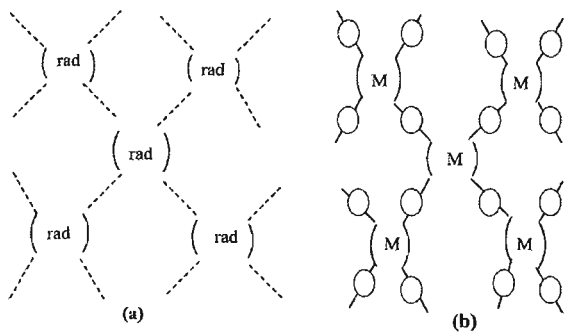


**Figure 1.7:** Schematic representation of (a) organic and (b) inorganic magnetic building blocks (white circles represent ligands).[14] "Adapted from figure 2 reference 14."

### 1.2.1 Single Molecule Magnets

The synthesis of paramagnetic clusters is one of the dominant fields of molecule-based magnets. In this respect, Mn clusters have been particularly well studied and many of them are known as single molecule magnets (SMM). The first compound to exhibit SMM behaviour was structurally characterized in 1980.[15] However it wasn't until 1991 that Gatteschi *et al.* discovered this compound demonstrated a large ground spin state ($S$) of $S = 10$, and retained magnetization for extended periods of time at helium temperatures, therefore behaving like a magnet.[16] SMMs are unique due to the fact that their magnetic properties are not a consequence of cooperative effects within magnetic domains, but are due to the individual molecules themselves.[17] In 1993, a $Mn_{12}$ SMM was reported with an $S = 10$ ground state, Figure 1.8 (a).[18] The large ground state spin arises from antiferromagnetic interactions between the $S = 3/2$ spins of $Mn^{IV}$ and the $S = 2$ spins of $Mn^{III}$ ions, which do not cancel each other out.[17] The fact that the spins do not compensate leads to an $S = 10$ ground state. The presence of zero field splitting results in splitting of the $S = 10$ state into 21 $M_s$ levels.[17] The zero-field splitting parameter is represented by D. If D is negative, there is a potential energy barrier between the "spin-up" where spin quantum number $M_s = -10$ and "spin-down" $M_s = 10$ orientations of the magnetic moment of an individual $Mn_{12}$ molecule, Figure 1.8 (b).[17] Figure 1.8 (b) demonstrates that some energy is needed in order to switch from the spin-up to the spin-down state, and if the energy barrier is appreciable ($\Delta E = DS^2$) the spin of a SMM can be magnetized in one direction. In order for magnetism to be observed in a SMM several criteria have to be met: (i) high-spin ground state; (ii) a high zero-splitting, and (iii) a negligible interaction between molecules.[17] Therefore, SMMs are designed with desirable

properties such as large *S* values, and with appreciable negative D values. This field of molecule-based magnets is continuously expanding via increasing the ground spin state values, using mixed metals, and the design of a variety of clusters. Although many manganese oxalate/acetate clusters have been reported, iron and more recently nickel ions have also been successfully incorporated.[17] However, the downfall of these types of molecule-based magnets is the realization of a long relaxation time at room temperature for potential applications in information storage, since this phenomenon currently only occurs at liquid helium temperatures.[17]

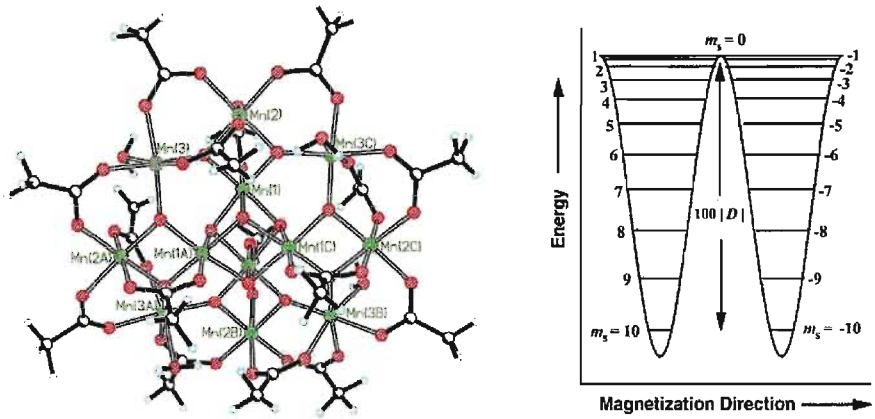


(a) (b)

**Figure 1.8:** (a) SMM $[Mn_{12}O_{12}CCH_2tBu)_{16}(MeOH)_4]$[15] (b) Plot of the potential energy *vs.* the magnetization direction for a SMM with an $S = 10$ ground state experiencing axial zero-field splitting.[17] "Reprinted with permission from reference 17. Copyright {2000} MRS Bulletin."

### 1.2.2 Single Chain Magnets

Following the groundwork of SMMs was an idea to produce a material composed of magnetically isolated chains which can be individually magnetized, termed single chain magnets (SCM), Figure 1.9.[19] SCMs, like SMMs, can exhibit finite magnetization that can be frozen in the absence of an applied magnetic field. This is important in the realization of permanent magnets.[20] The synthetic strategy here involves the ability to

connect one-dimensionally, to magnetically couple without complete cancellation of chain magnetization. In this case, intermolecular interactions must be much weaker than intramolecular interactions.[20] Progress in this field was initialized in 2001 by Gatteschi *et al.* with reports of a cobalt (II) ligand radical polymer, the first SCM.[21] It was determined to have an antiferromagnetic interaction between the Co(II) ion and bridging ligand radicals.[21] Following this work was mixed metal 1D chains and the inclusion of rare earth metals.[20] Challenges presented by this class of molecule-based magnets are similar to SMMs, since the operating temperatures are extremely low ($\Delta E = 8J + |D|S^2$) though now depends on |J| and |D|.

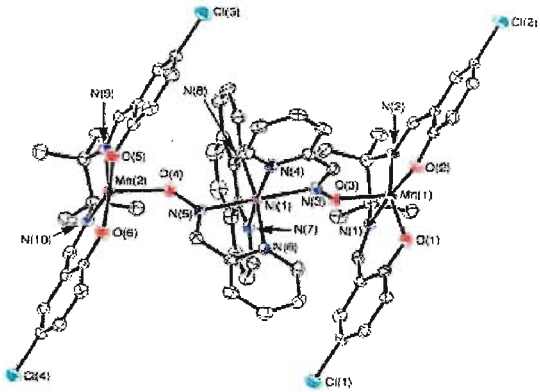


**Figure 1.9:** SCM of cation [Mn–Ni–Mn] trinuclear unit.[19] "Reprinted with permission from reference 19. Copyright {2006} American Chemical Society."

### 1.2.3 Polycyanometallates

Another class of molecule-based magnets is the polycyanometallates or Prussian Blue analogues. Prussian Blue is a well-known compound, the structure of which was elucidated by Ludi and Gudel in 1973, from a powder diffraction sample.[22] It was determined to be a highly disordered cubic cell consisting of alternating ferrocyanide and ferric ions with Fe(II)-N-C-Fe(III) bridges, Figure 1.10.[22] Prussian Blue analogues have remained at the forefront of molecule-based magnetic research for several reasons: they

can be prepared at room temperature from chemically stable building blocks, their metal ions are covalently linked into a 3D network, and a series of different metals can be exchanged while maintaining the 3D face centered cubic structural topology.[23] The long history of research surrounding Prussian Blue has demonstrated the important properties of cyanide bridging ligands, which make them optimal candidates as part of the design of molecular magnets. It has been proven that cyanide can complex with virtually all metals usually in different oxidation states. It has the ability to act as both a monodentate ligand with carbon as the donor atom, as well as a bidentate ligand, as demonstrated by Prussian Blue, allowing it to also form linear systems.[24] Another important feature of cyanide as a bridging ligand are studies observing its pathway for magnetic exchange.[24] Utilization of Prussian Blue analogues have proved successful for the preparation of molecule-based magnets with high critical temperatures, $T_c$, for example, $V[Cr(CN)_6]\cdot 2.8H_2O$ and $[Cr_{2.12}(CN)_6]\cdot 2.8H_2O$ with $T_c$ = 315 K and 270 K, respectively.[25, 26] A new series of Prussian Blue analogues has been examined exhibiting a new phenomenon involving structural changes mediated by different external stimuli, such as pressure, temperature and light.[27] The photomagnetic effect was first exhibited by a Co-Fe Prussian Blue analogue, the $Co^{III}$ low spin—NC-$Fe^{II}$ ground state is reversibly converted into a $Co^{II}$ high spin—NC-$Fe^{III}$ magnetic state.[28] This effect was observed by irradiating the Prussian Blue analogue with red light at low temperature followed by irradiation with blue light at high temperature to return the compound back to its original state.[28] Progress in the field of Prussian Blue analogues is now focused around the preparation of photomagnetic materials with a switching ability between two stable oxidation states.

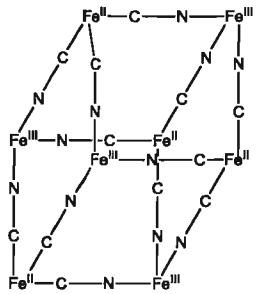

**Figure 1.10:** Repeating unit of Prussian Blue, formula $Fe_4^{III}[Fe^{II}(CN)_6]_3 \cdot 14H_2O$.[22] Adapted from reference 22.

### 1.2.4 Spin Crossover Compounds

A class of molecule-based magnets that is specifically important to this research is spin crossover compounds, (SCO).[29] Contemporary chemists have focused a significant amount of research effort around the use of molecular materials as building blocks for a series of technological applications. An example of this is the ability of a molecule to switch between two stable states. The capability of these two states to exhibit different chemical and physical properties is an important part of this research. A compound that exhibits a spin crossover, or a spin transition is one whose spin state is changed due to an external perturbation.[30] Different types of perturbations include pressure, light irradiation, application of an external magnetic field and most commonly temperature changes.[31] The "crossover" of the energy *vs.* field strength curves, of the ground state terms of ion $d^n$ configurations demonstrated in Tanabe-Sugano and other related diagrams, termed the phenomenon spin crossover.[31] The term spin-transition refers to the actual physical event of the high spin/low spin change.[31] For example, when temperature is used as the external perturbation, the spin transition temperature is the temperature at which 50% of the SCO active complex molecules have changed their spin state.[31] SCO can occur for first transition series ions with the d configurations of $d^4$, $d^5$, $d^6$ and $d^7$.[31] There are a few

reported examples of second series transition metals with SCO,[32] however, due to lower spin pairing energy and high ligand fields these examples are limited. The field of spin crossover complexes has been centered around $d^6$ ions due to this phenomenon being demonstrated most commonly in Fe(II) complexes.[33] The ligand field tends to be weaker for Fe(II) in comparison to other $d^6$ ions and therefore spin-pairing is not strongly favoured and it is possible to prepare stable high or low spin complexes using a wide range of ligands, Figure 1.11.[31] However, for Fe(III), a $d^5$ ion, the low spin (LS) state is more favoured, and high spin (HS) Fe(III) can be readily hydrolyzed, Figure 1.11.[31] The spin state *S*, represents the number of unpaired electrons in these systems and ultimately reflects the type of magnetic behaviour presented. An important consequence of spin crossover is the change in metal to ligand bond distances, which is a consequence of changes in relative occupancies of the $t_{2g}$ and $e_g$ orbitals as well as changes in the magnetic properties.[31] This change in magnetic properties occurs due to a change from LS to HS increasing the paramagnetic magnitude of the system.[31]

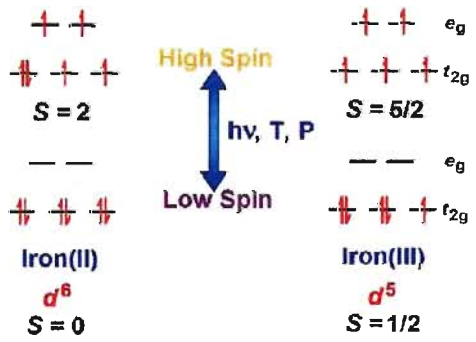


**Figure 1.11:** Schematic representation of the two possible spin states for iron(II) and iron(III) coordination compounds in an octahedral environment.[33] "Reprinted with permission from reference 33. Copyright {2009} Royal Society of Chemistry."

Since switching between states has been demonstrated to be more facile for Fe(II) compounds, many accomplishments in the field of spin crossover have revolved around

this metal ion. The energy gap between the LS, diamagnetic state and the HS, excited paramagnetic state is close to thermal energy, therefore, it is easier for an external perturbation to switch these states.[30] Conversion between states occurs due to a transfer of two electrons between the $t_{2g}$ and $e_g$ orbitals, which has an influence on the magnetic and optical properties.[30]

The first example of a SCO complex was reported in the 1960s by Busch and co-workers, who focused on Fe(II) and Co(II) studies and eventually identified the crossover region for Co(II).[34] In 1966, the first example of a Fe(II) spin crossover system was demonstrated for a $[Fe(phen)_2(NCS)_2]$ complex, Figure 1.12.[35]

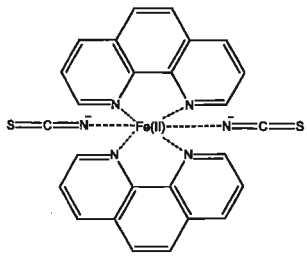


**Figure 1.12:** First Fe(II) spin crossover complex $[Fe(phen)_2(NCS)_2]$.[35]

Sorai and co-workers demonstrated through thermodynamic studies that a LS to HS transition is an entropy driven transition, due to the metal-to-ligand bond lengths being shorter in the LS state compared to the HS state.[36] This work led towards the conclusion that the high spin is favoured at high temperatures for thermal transitions.[36] In 1984, Decurtins and co-workers observed a light-induced LS to HS conversion, where molecules can be trapped in the excited high spin state at lower temperatures, this feature is known as light-induced excited-spin-state trapping (LIESST).[37] A complex was cooled until it was primarily in the low spin state, which was followed by light illumination to induce the high spin state.[37] Irradiation of compound $[Fe(ptz)_6]$-$(BF_4)_2$ (ptz=1-propyltetrazole) Figure 1.13, by green light at low temperature when it is in the

stable low spin state, resulted in its conversion to the metastable high spin state.[37] This LIESST property was confirmed for several Fe(II) SCO compounds with optical, Mössbauer and magnetic susceptibility measurements.[37] Hauser expanded on this research and proved that LIESST is a reversible process.[38] It was determined that changing the wavelength of the light returns the complex from HS back to LS.[38] This finding enlightened the idea of SCO compounds being utilized for photo-switching applications.

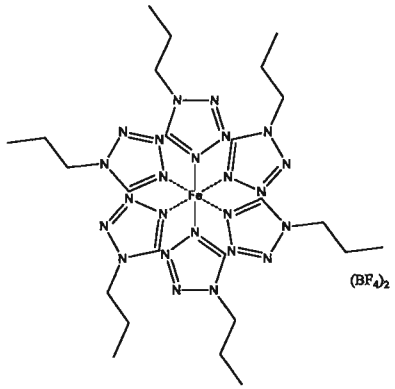


**Figure 1.13:** $[Fe(ptz)_6]$-$(BF_4)_2$ (ptz=1-propyltetrazole).[37]

In order to measure the relative concentrations of HS and LS states as a function of temperature, a curve can be constructed based on HS molar fraction $\gamma_{HS}$ *vs.* T, Figure 1.14.[39] A sample in solution will demonstrate behaviour similar to the curve in Figure 1.14 (a), since the sample is not in the solid state, the transition occurs at the molecular level due to the lack of constraints of lattice interactions.[39] Solid state samples can demonstrate this behaviour as illustrated in Figure 1.14 (a)-(e). [39] The transition may be gradual as in Figure 1.14 (a), it can also be abrupt and occur within a narrow temperature range, Figure 1.14 (b).[39] The transition may be a two-step process, Figure 1.14 (d), or the transition may be incomplete, Figure 1.14 (e).[39] Figure 1.14 (c) demonstrates the progression of the phenomenon of SCO through the discovery by Kahn and Launay, who

found that the course of the spin transition follows an abrupt change with associated hysteresis.[40] Hysteresis is demonstrated by complexes which display a high degree of cooperativity, and the hysteresis effect reflects the presence of the samples' history.[40] As the cooperativity increases, the transition becomes more abrupt and may occur within a narrow temperature range, where the transition temperature $T_{1/2}$ is defined as the temperature at which the fractions of HS and LS are equal.[40] Kahn and Launay defined molecular bistability as "the property of a molecule to evolve from one stable state to another in a reversible and detectable fashion in response to a controlled perturbation."[40] They then coined three conditions with this definition: (i) the molecule has to have two states that are close in energy, (ii) some external perturbation has to be identified that can reversibly change the relative energy of the two states, and (iii) there has to be some measurable response function, e.g. magnetic susceptibility.[40] Resulting in the possibility of a memory characteristic for SCO systems and their potential use as memory or display devices.

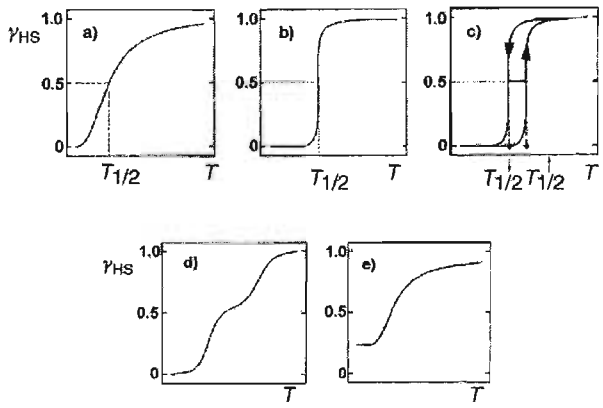


**Figure 1.14:** Spin transition curves of temperature (T) vs. high spin fraction ($\gamma_{HS}$) (a) gradual; (b) abrupt; (c) with hysteresis; (d) with steps; (e) incomplete.[39] "Reprinted with permission from reference 39. Copyright {2000} Royal Society of Chemistry."

Several different synthetic strategies are utilized for the preparation of SCO systems. An important strategy which has been employed for decades is the use of organic macrocycles as the building blocks for these coordination complexes. Macrocycles can be prepared in a predictable manner using template synthesis. Preparation of these macrocycles is usually based around an equatorial design with two free axial positions which are utilized for the coordination of bridging ligands. An important ligand utilized for the preparation of a spin crossover compounds is the ($N_3O_2$), (L), ligand. In 1977, Drew *et al.* reported the preparation of a ($N_3O_2$) macrocycle via a Schiff-base condensation of equimolar quantities of 2,6-diacetylpyridine and 3,6-dioxaoctane-1,8-diamine in methanol in the presence of a divalent metal cation, Figure 1.15.[41] The structure was elucidated for the manganese (II) macrocycle with coordinated axial thiocyanate ligands, and the complex was determined to be seven-coordinate with the two axial thiocyanate ligands coordinating through the nitrogen atoms.[41] Evidence for the formation of a series of other complexes was elucidated by comparing data with that of the original Mn(II) complex, and the presence of a C=N stretch at 1650 $cm^{-1}$ in the IR spectra.[41] Through preliminary susceptibility measurements and Mössbauer experiments it was determined that the Fe(II) and Mn(II) are high spin complexes.[41]

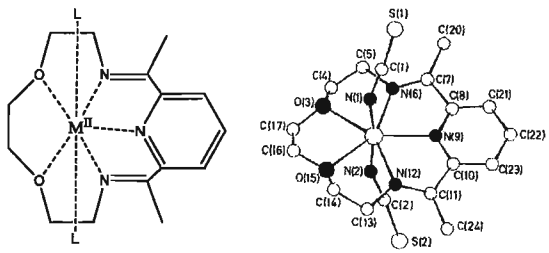


**Figure 1.15:** Parent ligand, [$N_3O_2$] (L) macrocycle $M^{II}$= Mg, Cr, Mn, Fe, Co, Zn, Cd; L= Cl, SCN, CN; and crystal structure of [$M^{II}(SCN)_2$].[41] "Reprinted with permission from reference 41. Copyright {1977} Royal Society of Chemistry."

The ($N_3O_2$) macrocycle was initially determined to exhibit SCO properties upon complexation to a Fe (II) ion, it was reported that there is a thermal transition from the HS state ($S$ = 2) to the reversible LS state ($S$ = 0).[42] However, no single crystals were obtained in the 1970s in order to fully understand the coordination geometry of this complex inn both spin states. It was later determined that the $[Fe(N_3O_2)(CN)_2]$ macrocycle undergoes a two-step SCO transition, the first one from LS to a 1:1 ratio of LS to HS at 150 K and then to HS at 270 K.[42] At 270 K the Fe(II) ion was determined to be in a pentagonal bipyramidal environment, with the macrocycle occupying the pentagonal girdle and the cyanide carbon atoms coordinating axially, Figure 1.16.[43] The macrocycle was determined to be nearly planar as expected due to the presence of the two imine bonds.[43] Although the HS structure was completely elucidated, the crystals were too brittle at low temperatures to measure the structure of the LS state at that time. Studies of this macrocycle progressed even further when the Fe(II) complex $[Fe^{II}(L)(CN)_2]\cdot H_2O$ was shown to exhibit SCO behaviour, as well as a LIESST effect.[43] LIESST results determined by Sato *et al.* demonstrated that the relaxation temperature from the metatstable HS to the LS state is above 130 K, which was the highest temperature reported for a molecule-based magnet at that time.[43] These temperature dependent susceptibility measurements were taken on a SQUID magnetometer, and the results observed for the single crystal were found to correspond with the results determined for the powder sample.[43] Another important observation made by Sato and co-workers was that upon rapid cooling (i.e. the sample is cooled in only a few seconds) the HS state is "frozen-in," and the LS state transition will not be observed.[43] Having a

"frozen-in" state for a spin crossover system is not observed frequently and exists in the temperature range below 130 K.

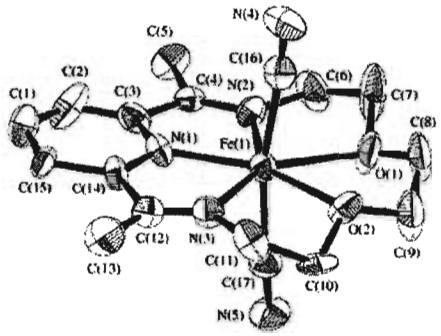


**Figure 1.16:** ORTEP view for complex $[Fe(L)(CN)_2]\cdot H_2O$ at high spin (270 K) state.[43] "Reprinted with permission from reference 43. Copyright {2001} American Chemical Society."

The results in 2001, describing the room temperature molecular structure of the Fe(II) macrocycle paved the way for exploiting further the coordination geometry of this macrocycle. It was initially thought that the macrocycle may only coordinate with one of the oxygen atoms bonded within the distance of the *van der Waals* radius and the other one off. However, it is shown that in the HS state the macrocycle is a seven coordinated complex with pentagonal bipyramidal crystal splitting geometry, Figure 1.17.[43] The iron atom as expected is coordinated to the pentagonal macrocycle with two cyanide carbon atoms occupying the axial positions.[43] The structure in the LS state was undetermined since there was destruction of the single crystals as the temperature was lowered.[43]

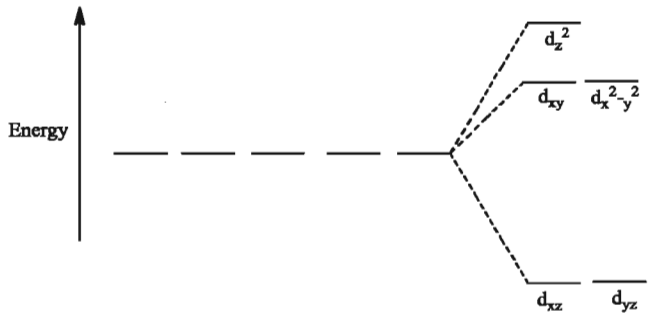


**Figure 1.17:** Pentagonal bipyramidal crystal splitting diagram.[44] "Adapted from figure 21.11 reference 44."

Following their result in 2001, Sato *et al.* examined the LIESST properties of the Fe(II) macrocycle. It was determined that not only was it possible to use light to induce a transition for LS to HS but this could also be reversed by changing the wavelength of the light to convert the complex from HS to LS.[45] Being able to have a switchable process from HS to LS and from LS to HS through irradiation of light is important for the realization of the ($N_3O_2$) macrocycle being utilized as a memory storage device.[45]

In 2007, Letard *et al.* took a further look into the crystal structure of the $[Fe(N_3O_2)(CN)_2]\cdot H_2O$ macrocycle, since they were able to measure the structure of the complex at low temperature in the LS state.[46] It was determined that at room temperature the crystal structure adopted a C2/c space group, with a hepta-coordinate iron and metal-to-ligand bond distances characteristic of the HS state, Figure 1.18.[46] In this case the Fe(II) sits on a two-fold axis and the two Fe-O bonds are crystallographically equivalent. In the LS state however, there is a loss of the two-fold axis and the structure adopts a $P2_1/c$ space group.[46] The loss of symmetry is due to one of the metal to oxygen bonds being broken at lower temperatures, resulting in a hexa-coordinate Fe(II), Figure 1.18.[46] These results were found to correspond with previous predictions by Nelson *et al.* and helped to give a further understanding of the conformational changes accompanying the spin transition in the solid state.

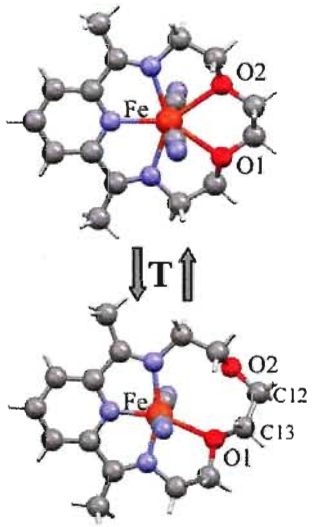


**Figure 1.18:** View of the molecular structure of $[FeL(CN)_2]$ in HS (top) and LS (bottom) showing the reversible transition from a hepta-coordinate high spin state (HS-7, $FeN_3C_2O_2$) to a hexa-coordinate low spin state (LS-6, $FeN_3C_2O$) for $[Fe(L)(CN)_2]\cdot H_2O$ in the solid state.[46] "Reprinted with permission from reference 46. Copyright {2007} Royal Society of Chemistry."

Pilkington *et al.* reported the synthesis, structure and magnetic properties of a bimetallic compound containing two covalently tethered ($N_3O_2$) (L) macrocycles, $[Mn(N_3O_2)]Cl\cdot H_2O\}_2 2Cl\cdot 10.5H_2O$, Figure 1.19.[47] They examined the bimetallic compound as a prospect for a novel molecule-based magnet. Structure examination determined the bimetallic Mn(II) ion environment was similar to the Fe(II) macrocycle. It was shown that both metal centres contained pentagonal bipyramidal environments on an equatorial plane and with a $Cl^-$ ion and water molecule bound axially.[47]

**Figure 1.19:** ORTEP representation of the molecular structure $[Mn(N_3O_2)]Cl{\cdot}H_2O\}_2 2Cl{\cdot}10.5H_2O$ (ellipsoids at 50% probability). The Cl counterions are omitted for clarity.[47] "Reprinted with permission from reference 47. Copyright {2007} American Chemical Society."

Following the preliminary studies on the solid state structure and LIESST properties of the $(N_3O_2)$ macrocycle, came an interest in chain networks utilizing the axial ligands as a bridge between components. The $(N_3O_2)$ macrocycle was promising for this approach since it usually entailed using transition metal complexes that have terminal ligands which allow for bridging, while the other can be used for coordination. Decurtins and co-workers followed this approach using $[M(CN)_n]^{m-}$((M) Cr(III), Mn(III), Fe(III),Fe(II)) complexes as building blocks.[48] These chains were promising since they characteristically afford multidimensional architectures that may lead to these molecular assemblies exhibiting paramagnetism, ferromagnetism, ferrimagnetism or metamagnetism.[48] Decurtins *et al.* reported eight different materials, all of which are assembled from the $[Mn(II)(N_3O_2)]$ macrocycle, and a cyanometallate.[48] Out of the eight structures, the one shown in Figure 1.20 was the only compound found to exhibit a weak ferromagnetic exchange interaction between the Mn(II) and the cyano-bridged Fe(II) ions.[48] In contrast a second compound containing a Cr(III) cyano-bridged ion demonstrated antiferromagnetic exchange interactions.[48]

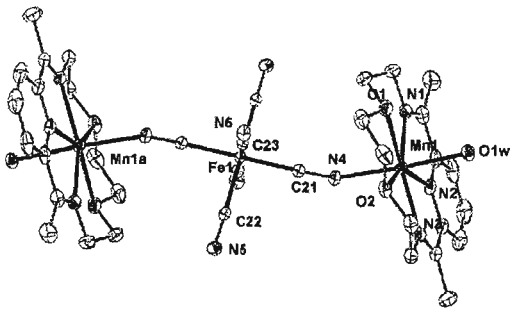


**Figure 1.20:** ORTEP representation (ellipsoids at 50% probability) of $[(Mn^{II}LH_2O)_2(Fe^{II}(\mu\text{-}CN)_2(CN)_4)]\cdot MeOH\cdot 10H_2O$. H atoms and solvent molecules are omitted for clarity.[48] "Reprinted with permission from reference 48. Copyright {2005} American Chemical Society."

The first publication of these coordination polymers sparked further work by other groups in this field of research. Sato *et al.*, published a 1-D coordination polymer, $[Fe(L)(CN)_2][Mn(hfac)_2]$.[49] It followed the same heterometallic bridged structure as shown by Decurtins *et al.*, -CN-Fe-CN-Mn-, as shown in Figure 1.21, it also showed exciting magnetic results.[49] This coordination polymer exhibits LIESST effects, following illumination with antiferromagnetic coupling present between the Fe(II) and Mn(II) ions.[49]

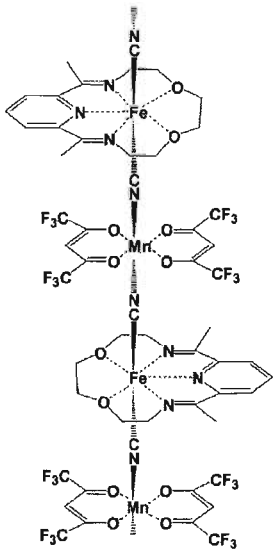


**Figure 1.21:** Schematic representation of 1-D $[Fe(L)(CN)_2][Mn(hfac)_2]$.[49] "Reprinted with permission from reference 49. Copyright {2005} American Chemical Society."

In 2006, Paraschiv *et al.* also focused on the preparation of novel coordination polymers. They were able to prepare three different trinuclear networks, using Mn(II) macrocycles with M(III) hexacyanometallates.[50] They were able to achieve a ferromagnetic coupling exchange between a [Mn(II)($N_3O_2$)] macrocycle bridged to a Fe(III) ion, Figure 1.22.[50]

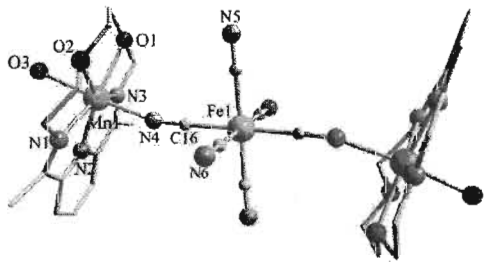


**Figure 1.22:** Perspective view of [($H_2O$)(L)Mn–NC–Fe($CN)_4$–CN–Mn(L)($H_2O$)](NCS)·1.5$H_2O$.[50] "Reprinted with permission from reference 50. Copyright {2006} Royal Society of Chemistry."

In 2009, Zhang *et al.* prepared these chain networks with the same ($N_3O_2$) macrocyclic building blocks and with the same intentions to use a cyanide bridging building block. However, they examined the use of another macrocycle with trans complexed cyanide ligands. In this respect, 1-D magnetic chains were prepared from [Mn(L)$(CN)_2$] together with[Fe(bpb)$(CN)_2$], bpb=N,N-bis(2-pyridinecarboxamide)-1,2-benzene. This strategy afforded single chains, as seen in Figure 1.23.[51] The magnetic properties of these 1-D chains reveal an antiferromagnetic coupling interaction between neighbouring Mn(II)-Fe(III) metal centres.[51]

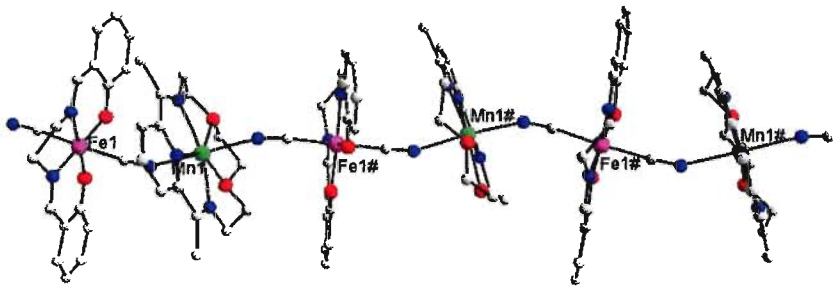


**Figure 1.23:** $[Mn^{II}(L)(CN)_2]$ together with$[Fe^{III}(bpb)(CN)_2]$, bpb=N,N-bis(2-pyridinecarboxamide)-1,2-benzene, 1-D assembled chains.[51] "Reprinted with permission from reference 51. Copyright {2010} American Chemical Society."

Most recently Zhang *et al.* reported the preparation of a single molecule magnet, utilizing the $(N_3O_2)$ macrocycle complexed to an Fe(II) ion and bridged to a Cr(III) hexacyanometallate unit, Figure 1.24.[52] Magnetic studies revealed ferromagnetic coupling between the cyano-bridged Cr(III) and the HS-Fe(II) ion.[52]

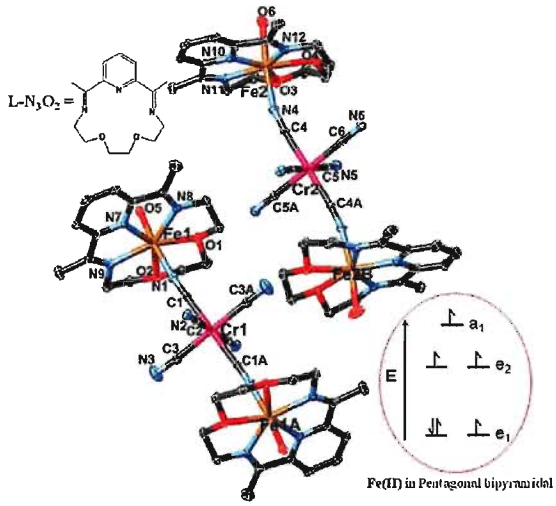


**Figure 1.24:** 1-D chain of trinuclear Fe(II)$(N_3O_2)$-CN-Cr(III)-CN-Fe(II)$(N_3O_2)$.[52] "Reprinted with permission from reference 52. Copyright {2010} Royal Society of Chemistry."

A significant amount of progress has been made in the field of SCO materials, however there are still several challenges that need to be overcome.[20] Operating temperatures closer to room temperature need to be observed and the ability to read or write to individual molecules needs to be realized.[20] The main goal is to understand

which features lead to cooperativity in solid systems, and to gain a full understanding of LIESST properties.[20] Progress is also moving towards the adhesion of individual molecules to surfaces in arrays or films for device applications. SCO systems have also been examined for host-guest nanoporous frameworks, for applications in molecular sensing. Recently, Fe(III) SCO systems have been prepared and examined for liquid crystal properties.[31] SCO systems have a promising future with many areas of progression and potential applications, stemming from their already rich background.

### 1.2.5 Organic Radicals

The magnetic or spin component can be incorporated using a radical due to the presence of an unpaired electron instead of the more frequently used metals. The advantage of using a radical in comparison to a metal is the ability to have control over the design of the radical by appending different substituents to increase the stability, solubility or planarity of the molecule. In contrast, there is not as much control over the coordination of a metal beyond prediction of the coordination geometry.[53] Radicals are considered to be subvalent compounds since they have one less bond than expected.[53] The ultimate requirements for utilization of a radical are that it must be stable enough for preparation, characterization and isolation.[53] A stable radical can be defined as one that can be isolated and handled as a pure compound.[54] The addition of bulky substituents is the method most commonly exploited in order to increase stability of these reactive compounds.[54] However, if the ultimate goal is to utilize these radicals as building blocks for molecular magnets, the spin must still be able to interact with its environment, so the selection of appropriate substituents is vital.[54] The majority of stable radicals are based on the inclusion of heteroatoms, such as nitrogen, oxygen and sulfur since they are effective

carriers of spin-density.[54] Stable radicals can be split into different categories such as, hydrocarbon based, nitrogen and/or oxygen based, and sulfur-nitrogen based. Specific stable radicals that can be prepared using straightforward laboratory procedures include nitronyl nitroxide, verdazyl, thiazyl and phenoxy.[54]

Hydrocarbon based radicals were the first organic free radicals to be exploited.[54] The landmark discovery by Gomberg and the synthetic preparation of the triphenylmethyl radical jump started the interest in the field.[55] Since the discovery of hydrocarbon based free radicals different classes have been examined for their interesting magnetic properties. A few substituted triphenylmethyl radicals have been examined as paramagnetic ligands, Figure 1.25 (a).[56] Chlorinated triphenylmethyl radicals have been studied by Veciana *et al.* for the possibility of linking these radicals via coordinate bonds or non-covalent interactions, Figure 1.25 (b).[56, 57] These particular radicals have been determined to exhibit interesting magnetic and nanoporous properties. The galvinoxyl radicals are another interesting family of hydrocarbon based radicals which are exceptionally stable, and have been determined to have unusual solid state magnetic properties, Figure 1.25 (c).[58]

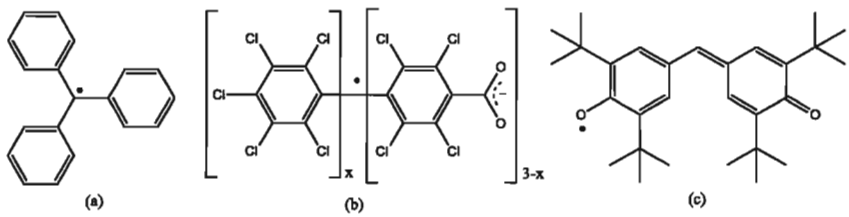


**Figure 1.25:** (a) triphenylmethyl radical;[56] (b) perchlorinated triphenylmethyl radical;[57] (c) galvinoxyl radical.[58]

The idea for nitrogen-sulfur based radicals was prompted by knowledge that a larger element such as sulfur (which is a versatile stable odd-electron compound) could substitute for a bulky substituent.[54] These thiazyl compounds, Figure 1.26(a), have been

examined extensively for different physical properties, most importantly magnetic.[59] Oakly *et al.* have examined these sulfur-nitrogen based radicals and have elucidated some interesting results. Dithiazolyl radicals, Figure 1.26 (b) have been determined to be hysteretic in nature from the transition of monomeric to dimeric structures, exhibiting a solid-state bistability.[60] Other dithiazolyl radicals have been determined to possess analogous temperature dependent and cooperative properties.[61, 62 63, 64] Another advancement in this class of sulfur-nitrogen radicals was reported in 1996 for a dithiadiazolyl radical which exhibits a significantly high canted antiferromagnetic ordering at 36 K, Figure 1.26 (c).[65] Many research groups worldwide as well as Canadian based groups have contributed significantly to the advancements for sulfur-nitrogen based radicals.[65, 66]

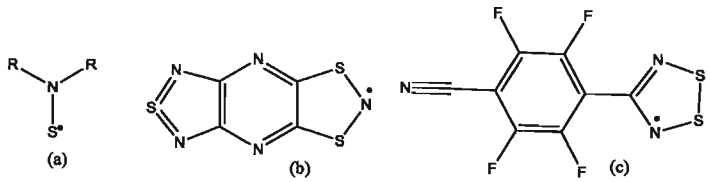


**Figure 1.26:** (a) A simple example of a sulfur-nitrogen based radical;[59] (b) a tricyclic fused 1,3,2-dithiazolyl radical;[64] (c) dithiadiazolyl radical.[65]

The final group of stable radicals discussed here are the nitrogen and/or oxygen based radicals and several of these different classes of this grouping of radicals have been exploited for their magnetic properties. The nitronyl nitroxide (NN) radicals have been extensively examined and have a very rich magnetic background. An important early advancement in purely organic based magnets involves the utilization of a nitronyl nitroxide radical.[67] A *p*-nitrophenyl nitronyl nitoxide was found to transition to a ferromagnetic long-range ordering state at 0.6 K, Figure 1.27.[67] Aminyl and verdazyl

radicals have also been exploited for their magnetic behaviour individually, as well as complexed to metal ions.[54]

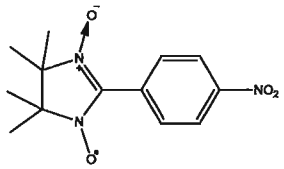

**Figure 1.27:** A *p*-nitrophenyl nitronyl nitoxide radical.[67]

The verdazyl family of radicals are of particular interest in this research, since they are the only air and moisture stable radicals.[68] The preparation of this radical was first discovered in the 1960's by Kuhn and Trishmann, Figure 1.28.[69] However, it was not until the 1980's that Neugebauer and Fischer prepared the 6-oxo and 6-thiooxoverdazyl radicals in a straightforward manner, Figure 1.28.[70]

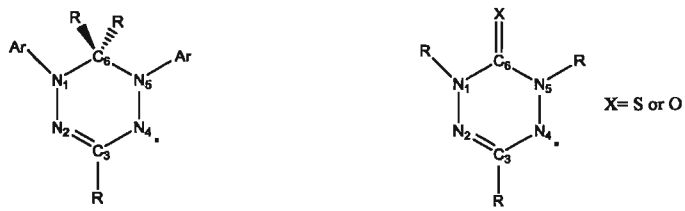


**Figure 1.28:** Two families of verdazyl radicals. Left discovered by Kuhn and Trishmann, right Neugebauer and Fischer.[69, 70]

The presence of the carbonyl group at $C_6$ is the most significant difference between the two classes of verdazyl radicals. The class of verdazyl radicals that do not have a carbonyl present at the $C_6$ position but instead a $sp^3$ carbon, exhibit a half-chair conformation.[68] The presence of the carbonyl group at $C_6$ makes the verdazyl radical planar in comparison to a methyl substituent.[68] The stability and lifetime of the verdazyl radical family is dependent highly on the substituted R groups.[68] It has been

demonstrated recently that verdazyl radicals substituted with an isopropyl group in the R position have been proven to be more robust when compared to methyl substituents.[68]

The type of spin distribution is identical for both classes of verdazyl radicals, and is dominated by the four nitrogen atoms.[68] Several different calculations have been performed using Hückel and density functional theory in order to visualize the electronic structure of the verdazyl radicals.[68] Both classes contain seven electrons on the internal part of the ring excluding $C_6$, and the odd electron is in a $\pi^*$ singly occupied molecular orbital (SOMO) distributed across the four nitrogen atoms, Figure 1.29.[68] There is a lack of spin distribution on $C_3$ due to the presence of the node.[68]

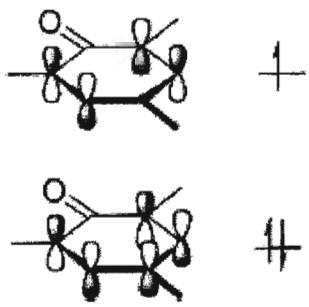

**Figure 1.29:** Highest occupied orbital's of the verdazyl radical.[71] "Reprinted with permission from reference 71. Copyright {2009} American Chemical Society."

The magnetic characterization of verdazyl radicals can be divided into three general classes depending on the type of magnetic interaction they display. The first class is a through-bond interaction between di- and polyradicals.[68] The radicals are attached through covalent bonds which is common practise for the evaluation of magnetic properties of organic radicals. This area was first examined for di- and tri-verdazyl radicals by Kuhn and co-workers, Figure 1.30 (a).[72] It was determined that there was no significant magnetic interactions in these types of systems.[72] A series of other attempts

were made to prepare bi- and polyradicals linked through different spacers, connected through different atoms on the radical. However, there has not been much success when examining the magnetic properties of these systems. An attempt to prepare biradicals connected to a spacer via the nitrogen atom was made, Figure 1.30 (b).[73] It was determined that some of these systems exhibited antiferromagnetic interactions, with the magnitude of the interaction being dependent on the type of linker. [73] Systems a, b, g and h were determined to be the most strongly coupled.

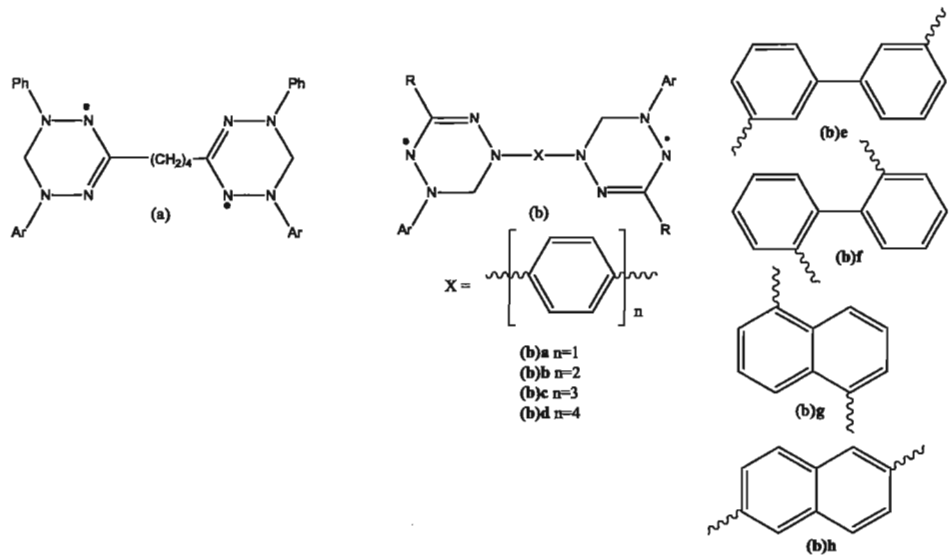


**Figure 1.30:** (a) biradical connected through *n*-butyl spacer;[69] (b) biradical connected through a series of spacers.[73]

The second general class are those which demonstrate through-space magnetic interactions. The 1,3,5-triphenylverdazyl radical was among the first verdazyl radicals to be characterized magnetically and structurally, Figure 1.31 (a).[74] It was determined to exhibit antiferromagnetic coupling in the solid state.[74] These results are utilized as a good reference point when examining the behaviour of other verdazyl radical systems since understanding the complexity of intermolecular radical interactions has proven to be

challenging. By examining the solid state packing of the 1,3,5-triphenylverdazyl radical, a derivative was prepared to alter the packing arrangement.[75] The addition of a nitro-group on the phenyl ring at the C3 position and an additional phenyl group at C6 leads to significant changes in the solid state structures, Figure 1.26 (b).[75] Ferromagnetic behaviour was observed for the first time for verdazyl radical based materials.[75] Following this landmark for the magnetochemistry of verdazyl radical based materials was the preparation of the 1,3,5-triphenyl-6-oxoverdazyl and 1,5-dimethyl-3-(2-pyridyl)-6-oxoverdazyl radicals, Figure 1.31 (c) and (d) respectively.[76] Through examination of the magnetic properties of these two systems it was determined that the less bulky methyl substituents allowed for a stronger intrachain antiferromagnetic exchange in comparison to the phenyl substituents. The phenyl derivative was determined to posses canted antiferromagnetic ordering giving rise to weak ferromagnetic ordering below 5 K, which is one of the highest ordering temperatures for a purely organic system.[76, 77]

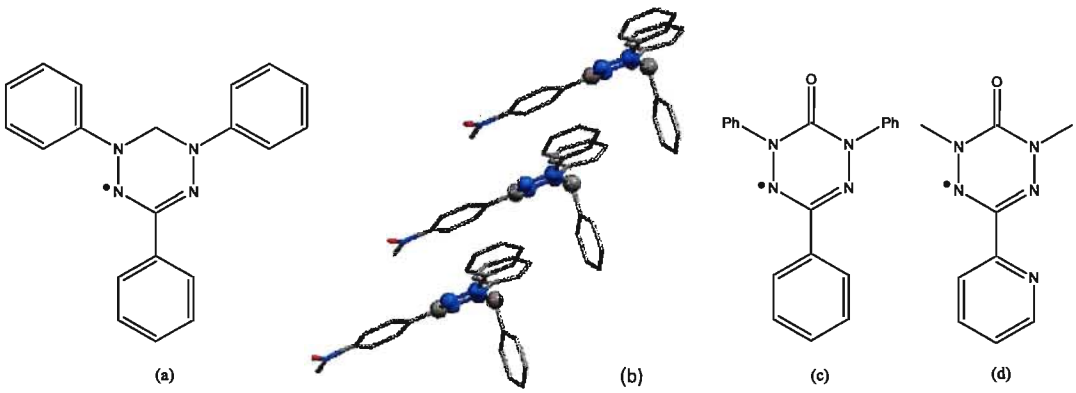


**Figure 1.31:** (a) 1,3,5-triphenylverdazyl radical;[74] (b) packing diagram of 1,3,5-triphenylverdazyl radical derivative;[75] (c) 1,3,5-triphenyl-6-oxoverdazyl radical;[76] (d) 1,5-dimethyl-3-(2-pyridyl)-6-oxoverdazyl.[77]

The final class are the metal complexed verdazyl radicals. The first reports of a complexed verdazyl radical were by Brook *et al.* who coordinated the radical to a Cu(I) ion, Figure 1.32 (a).[78] Magnetic susceptibility revealed an antiferromagnetic exchange for

all three complexes.[78] Although this class of radicals does not have an extended rich background, a verdazyl radical complexed to a Ni(II) ion was determined to have a large ferromagnetic exchange interaction for a metal-radical complex, Figure 1.32 (b).[79]

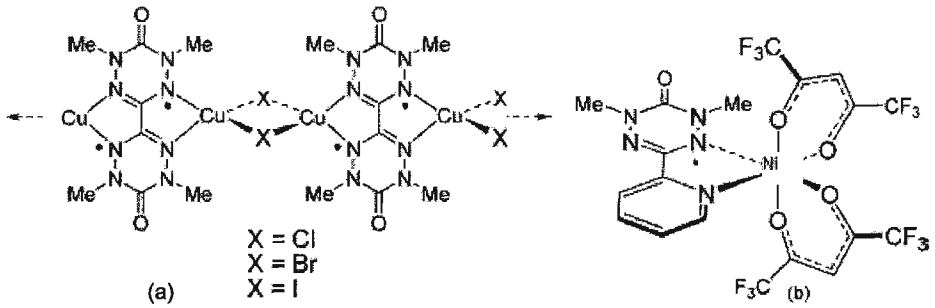


**Figure 1.32:** (a) verdazyl radical coordinated to Cu(I) ion;[78] "Reprinted with permission from reference 78. Copyright {2001} American Chemical Society." (b) Verdazyl radical coordinated to a Ni(II) ion.[79] "Reprinted with permission from reference 79. Copyright {1997} Royal American Chemical Society."

As noted above, the verdazyl radical has an extended magnetic background focused around three different general classes of compounds. Consequently, the verdazyl radical is a good candidate for the preparation of molecule-based magnetic materials and will be utilized for this work.

As demonstrated above there are several different strategies employed for the realization of molecule-based magnets. The ultimate goal in this field of magnetochemistry is the realization of a molecule-based magnet that exhibits permanent magnetization in the absence of a magnetic field as close to room temperature as possible.

### 1.3 Dual-Property Materials

Following the rich background in molecule-based magnets, the desire emerged to increase the magnetic complexities of these systems in order to control individual physical properties to achieve a collective phenomenon.[2] More recently, chemists have

attempted to add to the complexity of magnetic properties in order to combine them with other physical characteristics. As previously mentioned, three important physical properties are magnetism, conductivity and chirality. The following will examine the combination of these three physical properties through; magnetic conductors, and chiral magnets.

### 1.3.1 Magnetic Conductors

Traditionally, conductivity is metal based; however, the utilization of metals as conductive materials limits the control of size and the ability to fine-tune the components in order to introduce the possibility of a second physical property. Exploiting molecule-based materials presents the ability to have more control over size and production of conductive systems. A suitable approach for the design of dual-property molecule-based materials is a two-network system, for example host-guest solids or cation-anion salts.[80] The main prerequisite for this design is that each network contributes to the physical properties.[80] The following presents two concepts for constructing dual-property hybrid systems developed via the two-network approach; the first is an organic π-electron donor network that furnishes the pathway for electronic conductivity, together with a complexed inorganic metal that acts as the magnetic component, while the second utilizes the same organic type π-electron donor with the difference lying in the magnetic component which is an organic radical.

### 1.3.2 TTF-Based Magnetic Conductors

Most of the studies focused on magnetic conductors incorporating tetrathiafulvalene (TTF) and its derivatives as the donor molecular building blocks, Figure 1.33.[81] These derivatives are chosen because of the presence of sulfur and

selenium atoms which allow for the presence of a conductive pathway through S···S, Se···Se or S···Se intermolecular contacts.[81]

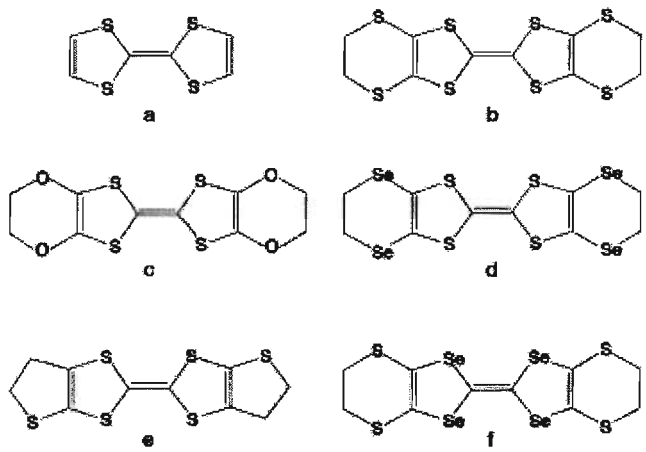


**Figure 1.33:** TTF derivatives: (a) TTF; (b) bis(ethylenedithio)-TTF or ET; (c) bis(ethylenedioxo-TTF or BEDO; (d) bis(ethylenediseleno)-TTF or BEST; (e) bis(ethylenthio)-TTF or BET; and (f) bis(ethylenedithio)tetraselenafulvalene or BETS.[81]

The appropriate design and composition of the donors is important for the realization of molecule-based conductors. The first important step is choosing a suitable π-electron donor atom.[81] A number of requirements must be satisfied when choosing an appropriate donor: it must be partially oxidized, it should have an array of S···S, Se···Se or S···Se intermolecular contacts which are shorter than the *van der Waals* radii, and a planar molecule is optimal.[81] Depending on the packing arrangement, different dimensional layers can be formed, Figure 1.34 demonstrates the typical packing motifs of a TTF donor molecule.[81] The packing ultimately depicts the type of electronic properties present, for example, β and κ exhibit metallic or even superconductive behaviour, while α exhibits semi-conducting behaviour.[81]

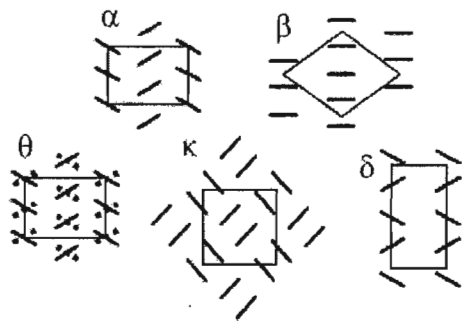


**Figure 1.34:** Some common packing motifs observed in radical salts of the TTF family. Each line represents the donor molecule viewed along its long molecular axis.[81] "Reprinted with permission from reference 81. Copyright {2005} Royal Society of Chemistry."

The synthesis of TTF was discovered in 1970 by Wudl.[82] Following the preparation of TTF was an examination of its redox potential, TTF was determined to have three stable redox states, Figure 1.35.[83] Since TTF and its derivatives are strong π-donors their redox ability is strongly influenced by the surrounding environment, sensors and switches can be designed to include TTF.[83] TTF is a non-aromatic molecule and can be easily oxidized to form $TTF^{\cdot+}$ and $TTF^{2+}$ resulting in aromatic molecules, with $TTF^{\cdot+}$ having one 6π-electron, 1,3-dithiolium ring and $TTF^{2+}$ having two 6π-electron, 1,3-dithiolium rings.[83] Another important feature of TTF is its ability to link to an electron acceptor, to form a donor-acceptor system where there is an intramolecular charge transfer, and this electron transfer can be switched on or off.[83]

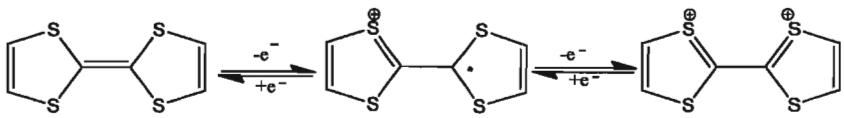


**Figure 1.35:** Three readily accessible and stable redox states of TTF.[83] "Adapted from scheme 1 reference 83."

### 1.3.3 Hybrid Organic-Inorganic Magnetic Conductors

The first example of the two-network design strategy is the utilization of an organic π-electron donor together with a magnetic component. For organic-inorganic hybrid materials the oxalate dianion (ox = $C_2O_4^{2-}$) has been exploited due to its versatility as a coordinating ligand.[81] The magnetic properties of this ligand can be tuned as a consequence of its *bis*-bidentate chelate form.[81] Oxalate ligands incorporating a metal centre have been determined to afford molecular magnets demonstrating ferri-, and ferromagnetic ordering with a critical temperature of 45 K.[81] Utilizing the magnetic properties of a metal oxalate network, together with the electron donor properties of TTF derivatives is a promising design for this type of dual-property material.

In 2000, Coronado *et al.* reported promising results utilizing the aforementioned design strategy for the preparation of a multifunctional material.[84] They utilized the BEDT-TTF donor derivative together with a bimetallic oxalate complex, $MnCr(C_2O_4)_3$, that yielded crystals via an electrocrystallization strategy, Figure 1.36.[84] The structure contained organic layers consisting of the BEDT-TTF organic cation, with alternating honeycomb layers of a bimetallic oxalate anionic network.[84] This hybrid material was determined to be a magnet below a critical temperature of 5.5 K, exhibiting ferromagnetic behaviour.[84] The conductivity measurements concluded that this compound was conductive at room temperature down to 2 K.[84] These results are a significant step towards the realization of dual-property magnetic/conductive materials and are seen as an important advancement in the field. However, there was no interplay observed between the ferromagnetic and conductive lattices for this dual-property material.[84]

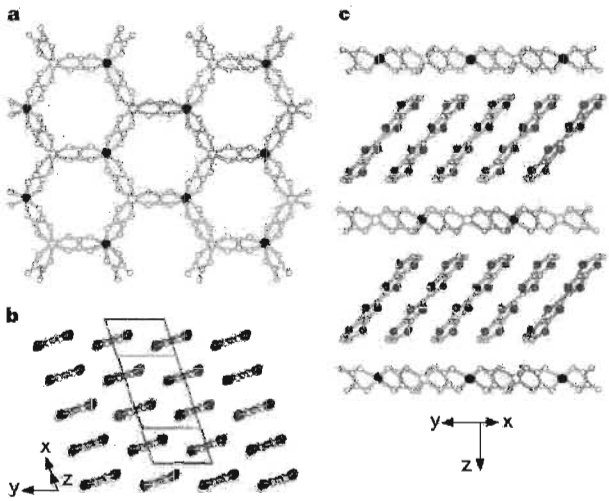


**Figure 1.36:** Two sublattices of the hybrid materials. a) View of the $[M^{II}M^{III}(C_2O_4)_3]^-$ bimetallic layers. Filled and open circles represents two types of metals. b) Structure of the organic layer, showing the β packing of the BEDT-TTF molecules. c) Representation of the hybrid structure along the *c*-axis showing alternating organic/inorganic layers.[84]"Reprinted with permission from reference 84. Copyright {2000} Nature."

### 1.3.4 Organic Magnetic Conductors

Ferromagnetic conductors are traditionally thought to incorporate a metal coordinated to a ligand; however, recently focus has been centered around "organic ferromagnetic conductors." This type of dual property material integrates physical properties which are normally thought to be metal based into a completely organic system. The idea that organic molecules are only insulators was changed in the 1970s when the completely organic charge transfer salt, tetrathiafulvalene-tetracyanoquinonedimethane (TTF-TCNQ) was discovered.[85] The TTF-TCNQ charge transfer system was of interest since it behaved like a metal over a large temperature range and was reported to possess the largest maximum electrical conductivity of any organic compound ( $\sigma_{max}$ (obsd) = 1.47 X $10^{-4}$ $ohm^{-1}$ $cm^{-1}$ at 66 K).[85] Ferromagnetic

conductors incorporating organic materials sparked interest because these novel materials could be designed and tuned to alter their physical properties and assemblies in the solid state. Given that it has been demonstrated with previous ground breaking results that organic materials can exhibit both conductive and magnetic properties separately. Research has now been directed towards the hybridization of these two physical properties; organic ferromagnetic conductors. This research was initiated by findings in 1991 by Tamura and co-workers, where a *p*-nitrophenyl nitronyl nitroxide system exhibited a ferromagnetic phase transition. Although the Curie temperature was found to be quite low, this was still groundbreaking.[67] To date, there are more than 20 organic ferromagnets, although the realization of these ferromagnets for inexpensive spin devices is not yet realistic due to the phase transitions being observed at very low temperatures.[81] Therefore, work in this field is aimed towards designing organic ferromagnets that exhibit phase transitions at more ambient temperatures. The main obstacle faced is the ability to design and prepare molecule-based materials which self-assemble in the solid state, with appropriate inter- and intramolecular interactions, in order to obtain an interplay of the two physical properties, i.e. magnetism and conductivity. An important method contributing to the design of organic based systems follows the spin-polarized donor model.

A spin-polarized donor is a building block that consists of a donor unit connected to a spin unit or radical, through a (cross) conjugated linker, Figure 1.37.[86] As shown in Figure 1.37, TTF or its derivatives can be used as the donor unit in a spin-polarized system, once TTF is oxidized the unpaired electron is delocalized over the entire molecule, and the ultimate goal is for ferromagnetic coupling with the radical site.[87]

Another prerequisite for the realization of a spin-polarized donor resulting in an organic ferromagnetic conductor is columnar stacking, where the partially oxidized TTF molecules are aligned forming a conduction pathway for an itinerante electron.[87] If columnar stacking is achieved, movement of the itinerante electron is then expected to align the spin on the radical unit in a parallel fashion, Figure 1.37.[87]

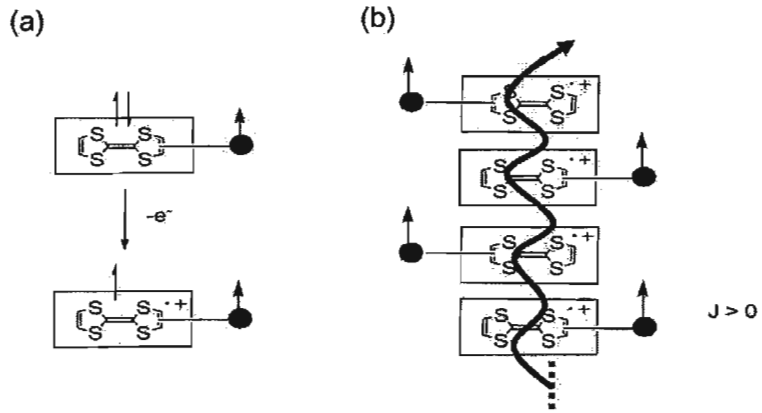


**Figure 1.37:** Schematic drawing of: (**a**) Spin polarized TTF donor; (**b**) organic π-π diradical system prepared *via* the self-assembly of a doped TTF derivative that possesses a covalently appended stable organic radical.[87] "Reprinted with permission from reference 87. Copyright {2009} Benthamscience."

In 1990, Yamaguchi and co-workers examined the idea of organic ferromagnetic conductors through computational studies, and determined that introducing a radical into a donor-acceptor charge transfer salt could ultimately lead to an organic ferromagnetic conductor.[86] It was also determined through these studies that the magnetic interaction between the unpaired electron on the radical and the itinerate electrons were dependent of the stacking arrangement, as previously mentioned, Figure 1.33.[86] When designing dual-property materials that contain donor, acceptor and radical units, there are three important factors that need to be considered; (i) intramolecular interactions, which are interactions between the donor and the radical, $J_{ab}$; (ii) intermolecular interactions, which occur between the donor and acceptor molecule, $J_{ac}$; and (iii) interchain interactions,

which are interactions between chains, $J_{ad}$, Figure 1.38.[86] Controlling the arrangement of individual chains is important, however the transition temperature $T_c$ and whether or not the system is ferromagnetic is also highly dependent on interchain interactions.[86] When a radical is appended to a donor or acceptor molecule as in Figures 1.38 (a) and (b), an intermolecular ferromagnetic exchange interaction is possible. For a 3-dimensional organic ferromagnet, $J_{ad}$ could also exhibit a ferromagnetic exchange.[86] This model highlights the importance of assembly in the solid state for these systems.

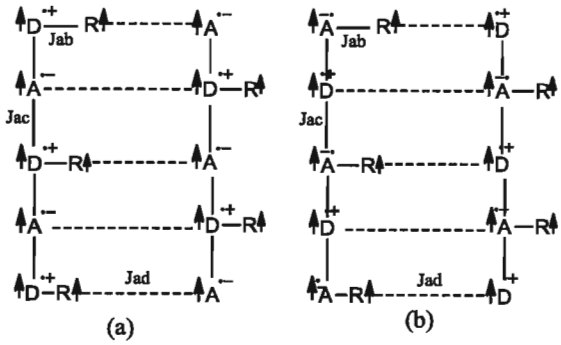


**Figure 1.38:** Organic ferromagnets which consist of the high-spin (HS) DA-type charge transfer (CT) complexes with radical groups (R). $J_{ab}$, $J_{ac}$ and $J_{ad}$ denote, respectively, the intramolecular, intermolecular and interchain effective exchange integrals; these are assumed to be positive.[86] "Adapted from figure 1 reference 86."

In 1994 Sugawara and co-workers, followed the theoretical results for the successful preparation of a TTF donor radical system.[88] They appended a TTF and a *p*-benzoquinone to a nitronyl nitroxide, NN, radical derivative, Figure 1.39.[88] The magnetic behaviour of these compounds were characterized by EPR. After oxidizing the TTF moiety of compound **(a)**, Figure 1.39 it was determined that the spins interact antiferromagnetically, and it was demonstrated that the multiplicity of the ground state was proportional to the dihedral angle between the NN radical and TTF.[88] After reducing

the *p*-benzoquinone, acceptor **(b)**, Figure 1.38 a ferromagnetic interaction was observed between the two radical spins.[88]

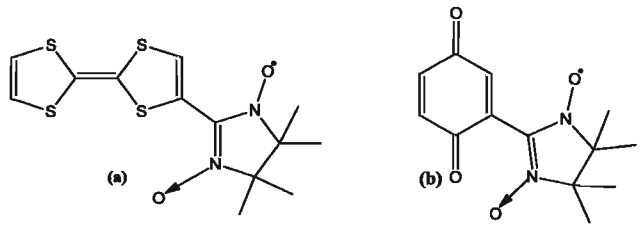


**Figure 1.39:** A TTF and *p*-benzoquinone attached to the nodal carbon of a nitronyl nitroxide radical, **1** and **2** respectively.[88]

The next step in this research was to increase the interaction between the TTF donor and the radical moiety. This was achieved via the addition of a cross-conjugated linker between the donor and radical moieties. In 1999, the preparation of TTF appended to a NN radical through a phenyl linker was demonstrated by Sugawara and co-workers, Figure 1.40.[89] They extended the idea of a spin-polarized donor successfully when the system was found to afford ground state triplet cation diradicals after one electron oxidation.[89] This research highlighted that a TTF as a spin-polarized donor is a useful building block for the preparation of organic ferromagnetic conductors.

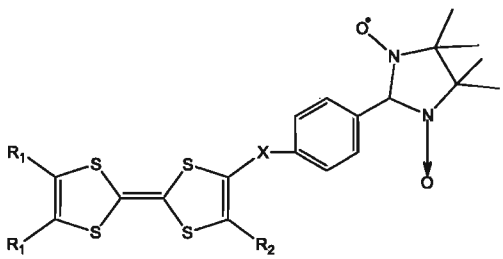


**Figure 1.40:** Molecular structure of a TTF-linker-NN.[89]

Recently, Komatsu *et al.* utilized the idea of a spin-polarized system and prepared a donor radical consisting of a dibrominated benzo-TTF containing a nitronyl nitroxide

group, 2-[2-(4,5-dibromo-[1,3]dithiol-2-ylidene)-1,3-benzodithiol-5-yl]-4,4,5,5-tetra-methyl imidazoline-3-oxide-1-oxyl (BTBN), Figure 1.41.[90] Their results showed that the conductance of the crystal can be controlled via the application of an external magnetic field, even at low temperatures.[90] The spin-polarized system also exhibited a weak intramolecular ferromagnetic interaction and a weak antiferromagnetic interaction between chains.[90] These findings are seen as a step forward in the design of molecule-based spintronics.

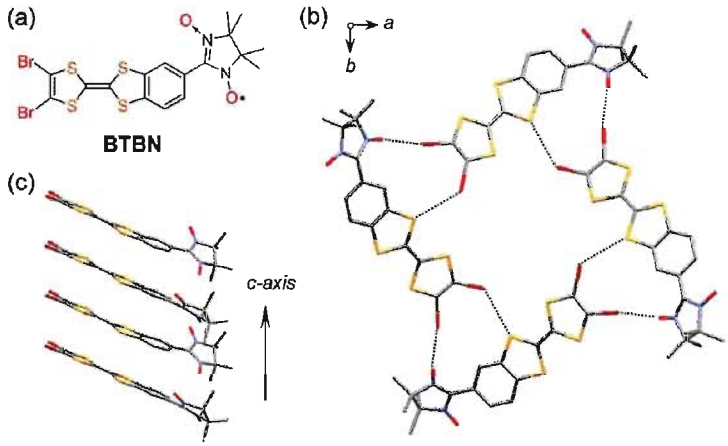


**Figure 1.41:** Crystal structure of BTBN. (a) Structural formula of BTBN. (b) Molecular arrangement viewed along the *c* axis. (c) Columnar stack along the *c* axis.[90]"Reprinted with permission from reference 90. Copyright {2010} American Chemical Society."

Although most of the research in this field is focused around the use of nitronyl nitroxides as the radical unit, this particular research has focused on the verdazyl radical due to the features previously mentioned.[54] In 2006, Pilkington *et al.* prepared the first TTF donor appended to a verdazyl radical as the spin unit, through a pyridine ring, Figure 1.42 (a).[91] Soon after, Pilkington *et al.* prepared the same system with a π-ethylene linker to attempt to change the interaction between the donor and radical moieties, Figure 1.42 (b).[92] It was determined that compound (b) Figure 1.42, demonstrated a negative Curie

Weiss constant which is characteristically an antiferromagnetic interaction, unfortunately single crystals have not yet been obtained for this system.[92]

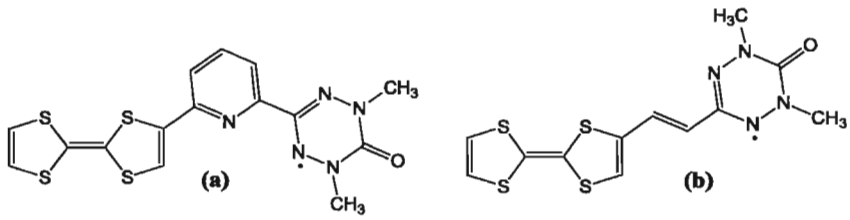


**Figure 1.42:** Molecular structure of (a) TTF-pyridine-verdazyl radical; (b) TTF-ethylene-verdazyl radical.[91, 92]

Following, the synthetic strategies developed for the preparation of these TTF donors appended through a linker to a verdazyl radical, theoretical studies were undertaken to find suitable linkers which would optimize the interaction between donor and radical moieties. The intramolecular magnetic exchange coupling constant *J*, was calculated for a series of conjugated linkers to investigate the type and magnitude of interaction that occurs between donor and radical promoted by different linkers. It was determined that the π-conjugated linkers optimized the interaction in the diradical system, demonstrating strong ferromagnetic interactions expected with magnitudes of 152, 192, and 234 K, for Figures 1.43 (a), (b), and (c), respectively.[93]

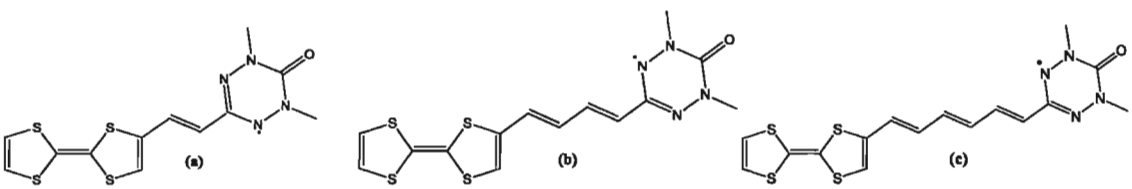


**Figure 1.43:** Molecular structure of (a) TTF-ethylene-verdazyl radical; (b) TTF-divinylene-verdazyl radical; (c) TTF-trivinylene-verdazyl radical.[93]

It was determined that the magnitude of the ferromagnetic exchange interaction was probably due to their planar structure which allows for (i) a more efficient orbital

overlap between the π-systems; (ii) the lack of heteroatom's interrupting the spin polarization pathway and (iii) the unique spin polarization path present instead of alternative competitive routes.[93] However, these theoretical results are in contrast with the results previously determined for compound (a) Figure 1.43. These findings were explained through torsion angle, θ effects; Packing in the solid state has been previously determined to modify the intramolecular magnetic exchange values, by adding geometrical constraints.[91] It was determined that the solid state packing strongly influences the torsion angles between the planes of the spin carriers and the linker. Also, as angles $\theta_{SC1}$ (torsion angle between TTF and linker) and $\theta_{SC2}$ (torsion angle between verdazyl radical and linker) increase this reduces the *J* values for the ferromagnetic interactions. A distortion angle of 60° of one of the spin carriers can reduce the *J* value by a half or quarter depending on the diradical.[93] As for a distortion angle of 90°, this results in antiferromagnetic coupling because of the polarization of the sigma orbital's of the linker by the π-orbital that contains the unpaired electron.[93] Therefore, it was theoretically determined that different linkers can increase and contribute to a ferromagnetic *J* value at equilibrium geometry, however, as torsion angles, $\theta_{SC1}$ and $\theta_{SC2}$ increase this decreases the magnitude of the interaction.[93]

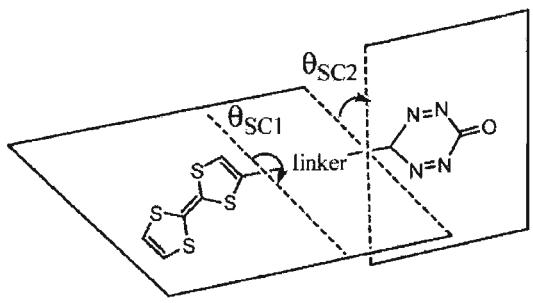


**Figure 1.44:** Schematic representation of torsion angles $\theta_{SC1}$ and $\theta_{SC2}$.[93] "Reprinted with permission from reference 93. Copyright {2008} Wiley."

These theoretical studies show that the pairing of a TTF donor molecule with a verdazyl radical shows promise for the realization of dual property materials. Since the magnetic interactions are highly dependent on the packing of these molecules in the solid state, the next step in this research is the synthetic realization of the different linker systems, making progress towards the realization of crystalline materials. The ultimate goal of this research is to achieve a packing arrangement in the solid state that is organized with an alignment of donor stacks where the appended radicals alternate. If this goal is achieved it would hopefully afford to a higher $T_c$ organic based ferromagnet.

**1.4 Chiral Magnets**

Understanding chirality and its contribution to multifunctional materials is important for the design and preparation of molecule-based systems. A molecule that exists as two non-superimposable mirror-images is said to be chiral, with the presence of two enantiomers. A mixture of equal amounts of the enantiomers is known as a racemate.[94] Chirality can be expressed in coordination compounds at the molecular and supramolecular level, and may be achieved in several different ways.[94] Chirality can be realized through the spatial arrangement of chelating ligands around a metal ion, from the formation of double or triple helices, from the helical twist of a macrocyclic ligand or from a chiral organic enantiopure building block.[94] When a molecule is chiral it exhibits optical activity, which is an important property observed for an enantiopure material, due to the rotation of the plane of polarized light, Figure 1.45.[94] Enantiomers will rotate the light in equal quantities, but in opposite directions. The extent and sign of the rotation are dependent on the wavelength of the incident light.[94]

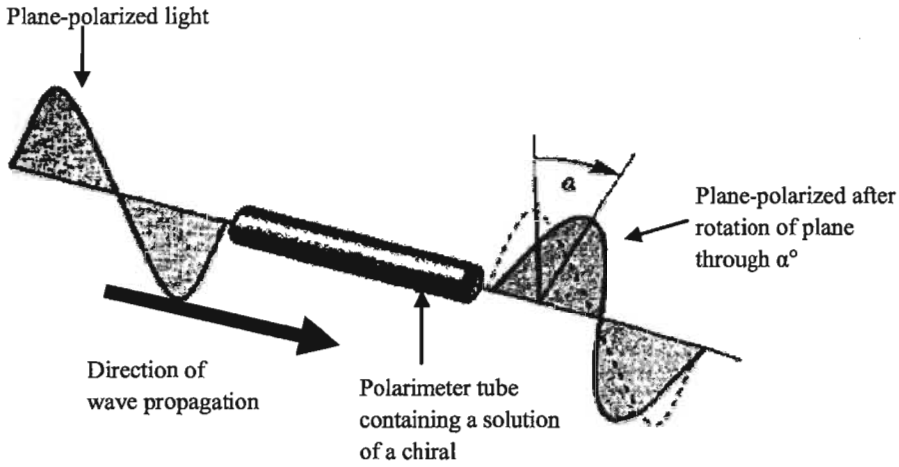


**Figure 1.45:** One of the enantiomers of a chiral compound rotates the plane of linearly polarized light through a characteristic angle, α°; the direction indicated (clockwise) is designated as +α°. The other enantiomer of the same compound rotates the plane of polarized light through an angle -α°.[44] "Adapted from figure 20.14 references 44."

Chirality has become important in the preparation of dual-property materials, since the realization of magneto-chiral effects.[95] Over 20 years ago it was predicted that light is absorbed slightly differently in a chiral molecule depending if the beam was travelling parallel or antiparallel with respect to an applied magnetic field.[96] It was determined that this effect is independent of the polarization state of the light and has opposite signs for the two enantiomers.[97] This effect was coined as magneto-chiral dichroism (MChD) in absorption or emission.[97] Magneto-chiral dichroism was first observed by Rikken and Raupach in 1997, through the discovery of a small MChD in a chiral paramagnet.[97] They started their efforts by examining the relationship between natural optical activity, which has been previously described occurring in chiral molecules, and magnetic optical activity.[97] Magnetic optical activity also represents the difference in absorption and refraction between left and right circularly polarized light, but in the presence of a magnetic field parallel to the wavevector of the light.[97]

Combining these two activities results in MChD. Magneto-chiral dichroism effects can be increased when the magnetic ordering is arranged in a ferromagnetic fashion, Figure 1.46.

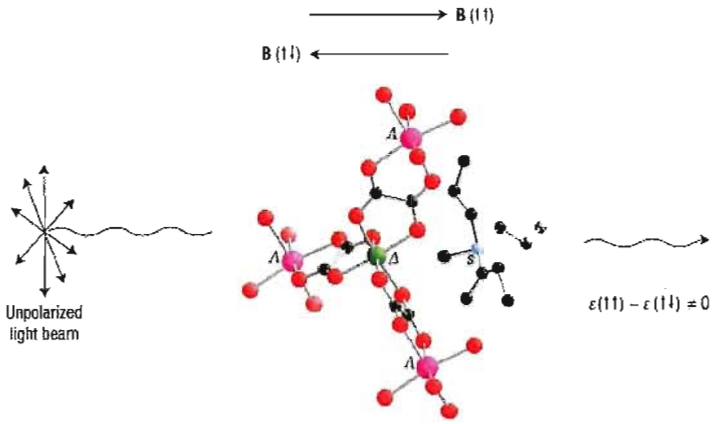


**Figure 1.46:** Magneto-chiral dichroism in a chiral ferromagnet. The absorption coefficient (ε) in a medium composed of chiral molecules of one handedness is slightly different for an unpolarized light beam when a static magnetic field (**B**) is applied parallel (↑↑) and antiparallel (↑↓) to the propagation direction.[98] "Reprinted with permission from reference 98. Copyright {1997} Nature."

Chirality in a spin-crossover system is important because the extent of chirality is strongly dependent on temperature; also chirality and magnetic moment are correlated in these systems, both increasing and decreasing (i.e. magnetic moment increases with chirality).[94] Another significant trend which utilizes chirality is ferroelectrics. Ferroelectrics are materials that exhibit a spontaneous electric polarization which can be switched by an applied electric field. Ferroelectrics can also exhibit ferroelasticity, which is a change in electric polarization showing an interplay to a change in shape.[99] These materials which can exhibit two or more "ferroic" properties are known as multiferroics.[99] Chirality comes into play because a requirement for ferroelectric material is that the compound must crystallize in a non-centrosymmetric space group.[99] Crystallization with a non-centrosymmetric arrangement of spin carriers may affect the

bulk magnetic properties of the material. Multiferroic compounds have been of great interest in the advancement of technology due to their great potential in applications as new high-density memory devices which can be electrically written and magnetically read.

Several different strategies have been utilized for the preparation of multifunctional chiral magnets. These strategies can be split into two major categories, enantioselective synthesis or resolution of chiral ligands, transferring the chirality to a metal ion through control of its configuration by coordination bonds and the chiral inductive effect of resolved building blocks to yield supramolecular structures.[100] The following will describe chiral bimetallic oxalate based polymers leading to chiral magnets with 2- and 3-dimensionality, chiral SMM's, chiral SCO compounds, and chiral magnets incorporating the ($N_3O_2$) ligand.

### 1.4.1 Chiral Oxalates

The oxalate ligand has been exploited for multifunctional, chiral magnets. The 3-D chiral oxalates have a general formula of $[M^{II}(bpy)_3][M^{II}M^{III}(ox)_3]$ and $[M^{II}(bpy)_3][M^{II}{}_2(ox)_3]$. The propeller like mononuclear subunits assemble in a homochiral manner, Figure 1.47.[94] Figure 1.47 depicts the anionic network, and cations $[M^{II}(bpy)_3]$ fill the vacancies. These anionic networks in homochiral structures, correspond to three sets of interconnected homochiral helices, defining cavities where the counter-cations can be incorporated into a helicoidal fashion.[94]

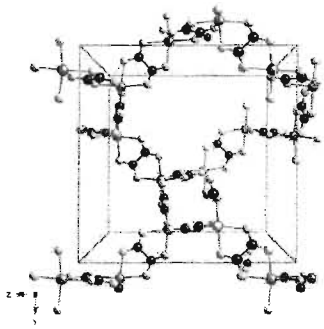

**Figure 1.47:** Anion $[M^{II}M^{III}(ox)_3]$ 3-D network.[100] "Reprinted with permission from reference 100. Copyright {2006} Elsevier."

For bimetallic 2-D optically active oxalate networks the general formula is $[M^{II}M^{III}(ox)_3][C]$ where C is a counter-cation.[94] The structure for these networks consists of honeycomb like layers with alternating $M^{II}$ and $M^{III}$ metal centres, however, control of chirality in 2-D networks is less predictable and more difficult to obtain.[94] Train *et al.* has recently, had a successful breakthrough with the preparation of a 2D bimetallic oxalate bridged network in both enantiomeric forms.[101] This was accomplished by using a chiral template tetraalkylammonium counter-cation with a chiral carbon on the alkyl chain, Figure 1.48.[101] The magnetic properties were especially interesting with an abrupt paramagnetic-to-ferromagnetic phase transition at 7 K, exhibiting strong magnetochiral effects.[101] Train and co-workers demonstrated this effect through the co-existence of ferromagnetism and chirality, and determined that MChD increased substantially in the presence of ferromagnetic ordering.[101] This was achieved by exploiting the interaction between Mn(II) and Cr(III) ions bridged by a diamagnetic oxalate ligand, resulting in the crystallization of a chiral ferromagnet, Figure 1.48.[101]

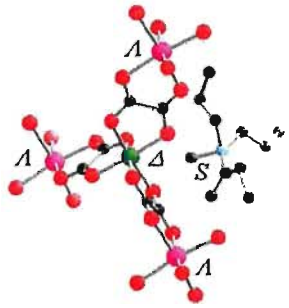


**Figure 1.48:** Magneto-chiral effect in chiral ferromagnet $S_N$-$L_{Mn}$-$D_{Cr}$ (Cr in green and Mn in pink).[101] "Reprinted with permission from reference 101. Copyright {2000} Nature."

### 1.4.2 Chiral SMMs

When utilizing SMMs for chiral magnets, the strategy for achieving a homochiral framework with large chiral voids, is to exploit large, robust, enantiopure chiral metal-organic cluster building blocks.[102] This can be achieved by using building blocks such as oxo-bridged trinuclear metal carboxylates (often known as `basic' carboxylates) $[M_3(\mu\text{-}O)(O_2CR)_6(H_2O)_3]^{n+}$ (M = divalent or trivalent transition metal ions, $O_2CR$ = organic carboxylate anions), Figure 1.49.[102] Chirality for this system stems from an enantiopure ligand which allows for enantioselective complexation of metals into its pores.[102]

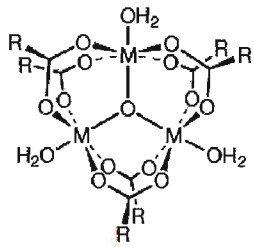


**Figure 1.49:** Oxo-bridged trinuclear metal carboxylates $[M_3(\mu\text{-}O)(O_2CR)_6(H_2O)_3]^{n+}$ (M = divalent or trivalent transition metal ions, $O_2CR$ = organic carboxylate anions).[102] "Reprinted with permission from reference 102. Copyright {2000} Nature."

### 1.4.3 Chiral SCO Compounds

Coordination chemists have observed that the cooperativity between chirality and magnetism affords magnetooptical properties and this is thought to be especially interesting for the introduction of chirality into a SCO compound.[103] The first homochiral SCO compound was reported in 2003, for a 2-D material comprised of chiral building blocks $[Fe^{II}H_3L]^{2+}$ and $[Fe^{III}L]$, where $H_3L$ = tris([2-((imidazole-4-yl)methylidene)amino]ethyl)amine), Figure 1.50.[104] The goal of this research is to use optical activity to observe the switching of spin states for a reading process.[104] The $\chi_M T$ value was reported at 200 K to be 3.6 $cm^3Kmol^{-1}$ which is in the expected range for HS Fe(II) (S = 2) and LS Fe(III) (S = ½).[104]

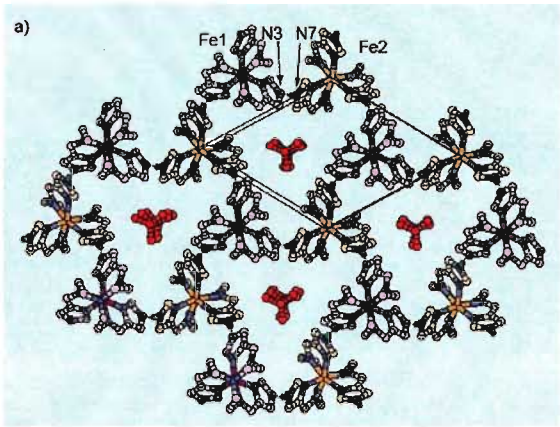


**Figure 1.50:** A view showing the homochiral 2D sheets of $[Fe^{II}H_3L]^{2+}$ and $[Fe^{III}L]$, with trigonal voids.[104] "Reprinted with permission from reference 104. Copyright {2003} Wiley."

Sato *et al.* reported a family of SCO complexes using imidazole containing ligands to complex Fe(II), Figure 1.51.[105] Chirality was realized upon complexation of this compound, forming a 1-D rod-like structure, stabilized via hydrogen bonding interactions.[105] The compound exhibits SCO properties in the solid state, but no thermal hyseresis was observed.[105]

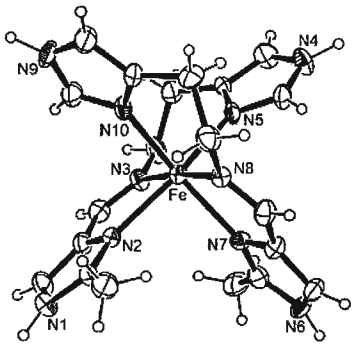


**Figure 1.51:** ORTEP drawing of $[Fe(H_2L_2\text{-}Me)_2]^{2+}$. The $Fe^{II}$ complex is a chiral molecule due to octahedral coordination of two tridentate ligands.[105] "Reprinted with permission from reference 105. Copyright {2009} Chemistry Letters."

### 1.4.4 Chiral ($N_3O_2$)

Zhang and Sato recently prepared for the first time a 3D cyano-bridged Cr(III) Co(II) compound[51] that self-assembles into an interesting homochiral interlocking structure composed of left-handed single helices and right-handed double helicle strands, Figure 1.52.[51] The magnetic properties revealed ferromagnetic behaviour below 12 K.[51]

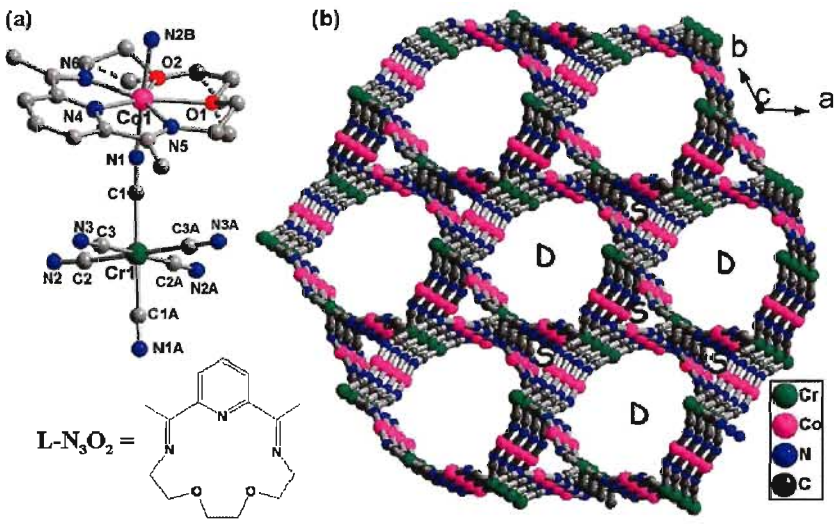


**Figure 1.52:** (a) View of the ball-and-stick structure of an asymmetric unit, where $[Cr^{III}(L^2)(CN)_2]$ and $[Co^{II}(CN)_6]$. (b) Chiral 3D tubular network down the c axis interlocked by single or double helices. (Only bridging cyanide and corresponding metallic ions are reserved for clarity.[51] "Reprinted with permission from reference 51. Copyright {2010} American Chemical Society."

All the recent investigations revolving around the ($N_3O_2$) macrocycle, keep it at the forefront of SCO research. The next step is to modify the organic framework of the macrocycle to prepare new derivatives such as the diphenyl derivative shown in Figure 1.53 which can be assembled from a chiral hydrobenzoin derivative.

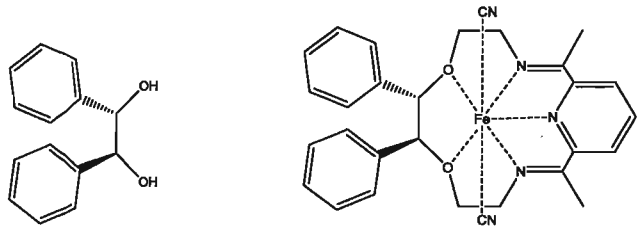


**Figure 1.53:** Molecular structure of (left) chiral hydrobenzoin precursor, (right) chiral Fe(II) macrocycle.

# CHAPTER 2- Synthesis and Study of a Novel Family of $[Fe(N_3O_2)(CN)_2]$ Macrocycles

## 2.1 Introduction

As previously mentioned, the parent $[Fe(N_3O_2)(CN)_2]$ macrocycle **(2.1)** was first prepared by Nelson *et al.* in the 1970s.[41]

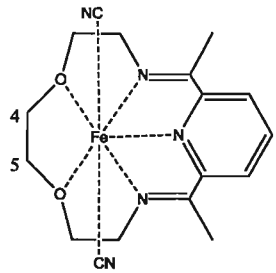


**(2.1)**

**Figure 2.1:** Molecular drawing of the parent $[Fe(N_3O_2)(CN)_2]$ macrocycle **(2.1)**; positions 4 and 5 are highlighted to identify where chirality will be introduced.[41]

Since Nelson *et al.*'s work, there have been a series of studies reported in the chemical literature concerning this macrocycle that include the structure determination of the Fe(II) complex in both its HS and LS states, as well as the characterization of its SCO properties including LIESST studies.[37, 43, 45] Although the parent $[Fe(N_3O_2)(CN)_2]$ macrocycle **(2.1)** has a rich background, a major drawback is its poor solubility in common organic solvents. Rather surprisingly, a search of the chemical literature reveals that no synthetic derivatives of this macrocycle have been reported to date. The goal of my research is therefore to prepare a new family of $(N_3O_2)$ macrocycles that are more soluble in organic solvents, facilitating their structural and magnetic characterization, and subsequent coordination chemistry experiments. Through the careful selection of substituents, it should also be synthetically possible to introduce chiral centers into the

organic framework of the macrocyclic ring, thereby not only improving the solubility of the complex, but also affording macrocycles with ligand centered chirality. In this respect, there are very few examples of chiral SCO compounds in the literature and SCO complexes prepared from chiral ligands are particularly rare.[106, 107] The short term goals of this project are therefore to prepare a more soluble class of macrocycle and examine the magnetic and structural changes that occur when chirality is introduced into the 4 and 5 positions of the organic framework of the parent $[Fe(N_3O_2)(CN)_2]$ complex, Figure 2.1. The longer term goals are to exploit these macrocycles as building blocks for the preparation and characterization of new chiral 0-, 1-, 2- and 3-D magnetic materials.[48] Utilizing macrocycles with axial ligands such as $CN^-$ that can chelate transition metal ions in a bidentate manner provides us with a versatile methodology for assembling new chiral magnetic molecule-based materials.[48] As previously discussed, the parent macrocycle **(2.1)** is assembled via a metal templated, Schiff-base condensation of 2,6-diacetyl pyridine together with an appropriate diamine, Scheme 2.1.

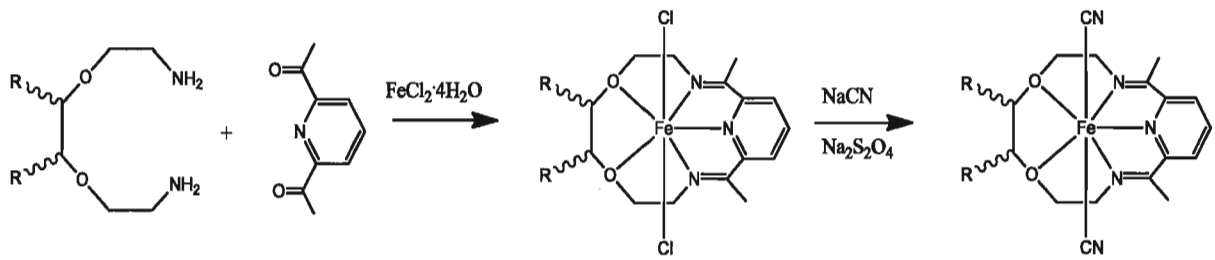


**Scheme 2.1:** Preparation of the $Fe(N_3O_2)(CN)_2$ macrocycle; R = H or Ph.[41]

As previously mentioned, our objectives are to introduce functional groups into the 4 and 5 positions of the macrocycle. Since this functionality comes from the diamine precursor, the first step is the preparation and characterization of the appropriate diamine precursors. With these objectives in mind, a synthetic pathway for the preparation of a

novel chiral 4*R*,5*R*-primary diamine **(2.6)**, was developed.[108] The *R,R* diamine was prepared in 5 steps from commercially available *R,R*-hydrobenzoin, Scheme 2.2.[108] The hydrobenzoin starting material was reacted with allyl bromide to afford the diene **(2.3)**. Oxidation with $OsO_4$ and $NaIO_4$, and reduction with $NaBH_4$ afforded **(2.4)** that was reacted with triphenylphosphine, phthalimide and diisopropyl azodicarboxylate to afford the diphthalimide derivative **(2.5)**. Finally, reaction of **(2.5)** with hydrazine monohydrate gave the final primary diamine **(2.6)** in 78% yield.

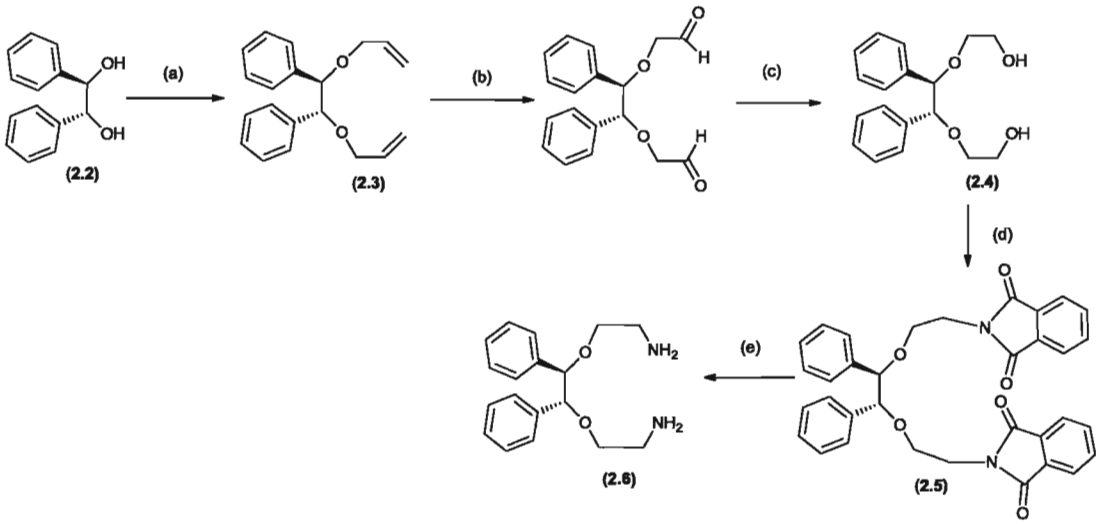


(a) NaH, THF, allyl bromide, reflux; (b) $OsO_4$, $NaIO_4$, $THF/H_2O$; (c) $NaBH_4$, DCM/NaOH; (d) phthalimide, triphenylphosphine, diisopropyl azodicarboxylate, THF, 4 days; (e) hydrazine monohydrate, ethanol, reflux

**Scheme 2.2:** Synthetic route for the preparation of (4*R*,5*R*)-4,5-diphenyl-3,6-dioxa-1,8-octanediamine **(2.6)**.

Following the synthetic strategy shown above, three new primary diamines **(2.6)**, **(2.7)**, and **(2.8)** were prepared and characterized. All of the synthetic intermediates to these compounds have been characterized and the data is summarized in Table 2.1.

**Table 2.1:** Characterization of the intermediates to primary diamines (**2.7**) and (**2.6**).

| Compound | HRMS (FAB) | $^1$H NMR ($CDCl_3$, 300 MHz) δ (ppm) | IR (KBr, $cm^{-1}$) | CHN |
|---|---|---|---|---|
| 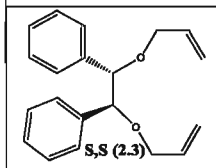 S,S (2.3) | Found *m/z* = 294.16215 $[M]^+$; Calcd. 294.16198 $C_{20}H_{22}O_2$. | 7.21 (s, 6H), 7.12 (s, 4H), 5.91 (m, 2H), 5.33 (d, *J* = 14.32 Hz, 2H), 5.21 (d, *J* = 10.55 Hz, 2H), 4.62 (s, 2H), 4.12 (dd, *J* = 13.19 Hz, 1H), 3.97 (dd, *J* = 13.56 Hz, 1H). | 3084 ($sp^2$ C-H); 1647 (C=C); 1087 (C-O). | ----- |
| 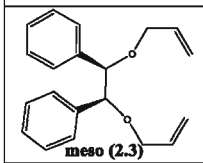 meso (2.3) | Found *m/z* = 294.16039 $[M]^+$; Calcd. 294.16198 for $C_{20}H_{22}O_2$ | 7.39 (s, 10H), 5.82 (s, 4H), 5.09 (m, 4H), 4.55 (s, 2H), 4.12 (m, 2H), 3.80 (m, 2H). | 3083 ($sp^2$ C-H); 1647 (C=C); 1453; 1099 (C-O). | ----- |
| 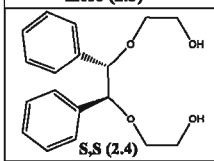 S,S (2.4) | Found *m/z* = 303.15372 $[M]^+$; Calcd. 303.15963 for $C_{18}H_{23}O_4$ | 7.21 (s, 6H), 7.06 (s, 4H), 4.50 (s, 2H), 3.78 (m, 4H), 3.66 (m, 2H), 3.51 (m, 2H), 3.18 (s, 2H). | 3350 broad (O-H); 1077 (C-O). | ----- |
| 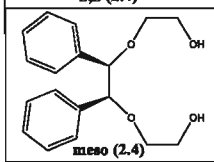 meso (2.4) | Found *m/z* = 303.15544 $[M]^+$; Calcd. 303.15963 for $C_{18}H_{23}O_4$ | 7.31 (s, 10H), 4.41 (s, 2H), 3.58 (m, 6H), 3.26 (m, 2H), 1.85 (s, 2H). | 3418 broad (O-H); 1077 (C-O). | ----- |
| 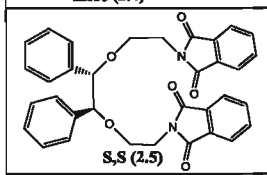 S,S (2.5) | ----- | 7.83 (s, 4H), 7.73 (s, 4H), 6.94 (m, 6H), 6.82 (d, *J* = 6.78 Hz, 4H), 4.41 (s, 2H), 3.79 (dt, *J* = 15, 4.95 Hz, 4H), 3.62 (t, *J* = 5.65 Hz, 4H). | 1720 (C=O); 1397 (C-N); 1106 (C-O). | Found C: 71.84, H: 5.22, N: 4.81%; Calcd. For $(C_{34}H_{28}N_2O_6)\cdot 0.35H_2O$ C: 72.03; H: 5.10; N: 4.94%. |
| 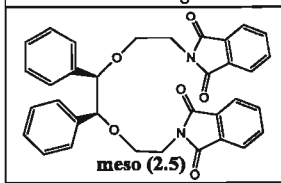 meso (2.5) | ----- | 7.80 (m, 4H), 7.74 (m, 4H), 7.16 (d, *J* = 7.91 Hz, 6H), 6.95 (m, 4H), 4.20 (s, 2H), 3.70 (m, 4H), 3.60 (m, 4H) 3.32 (m, 2H). | 1714 (C=O); 1396 (C-N); 1115 (C-O). | Found C: 71.84, H: 5.22, N: 4.81%; Calcd. for $(C_{34}H_{28}N_2O_6)$ C: 72.03; H: 5.10; N: 4.94%. |

From these, a new series of diphenyl $[Fe(N_3O_2)(CN)_2]$ macrocycles were synthesized. Macrocycles **(2.9)**, **(2.10)**, **(2.11)**, and **(2.12)** were prepared and characterized from the appropriate diamines following the general procedure outlined in Scheme 2.1.[109]

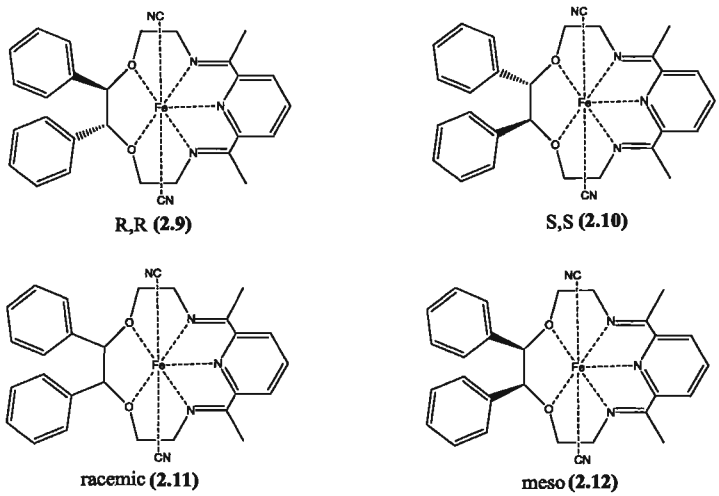


Two of the macrocycles, *S,S* $[Fe(N_3O_2)(CN)_2]$ **(2.10)** and *R,R* $[Fe(N_3O_2)(CN)_2]$ **(2.9)**, are enantiomers; complexes **(2.11)** and **(2.12)** are the *racemic* and *meso* derivatives, respectively. The structural and magnetic properties of all four macrocycles were compared in order to investigate if changing the spatial symmetry of the substituents on the macrocyclic ring alters in any way their SCO properties. In this respect, we hope to understand in more detail the factors that contribute to both the thermal and light-induced spin crossover for this family of macrocycles and assess the suitability of the complexes for future applications as molecular switches. In addition, we are interested to study whether or not the chirality of the molecules will open up any new avenues of investigation. In this respect, in the solid state, a chiral space group will essentially break the symmetry of the parent macrocycle by forcing the chiral macrocycles to crystallize in non-centrosymmetric space groups. Since structure often

dictates magnetic properties, it is reasonable to expect that the chiral macrocycles should display different SCO properties from their non-chiral counterparts. Furthermore, chiral molecule-based ferromagnets have recently been shown to possess magneto-chiral dichroism. [101]

### 2.2 Molecular structure of *R,R* $[Fe(N_3O_2)(CN)_2]\cdot 2H_2O\cdot Et_2O$ (2.9)

Following the synthetic route shown in Scheme 2.1, the *R,R* $[Fe(N_3O_2)(CN)_2]$ macrocycle **(2.9)** was isolated as a dark blue solid in 54% yield. This complex was first prepared and crystallized by Dr. Qiang Wang, a postdoc in the Pilkington group. Single crystals were grown in the refridgerator via the liquid diffusion of diethyl ether into an acetonitrile solution of the *R,R* $[Fe(N_3O_2)(CN)_2]$ macrocycle **(2.9)**. X-ray diffraction measurements on dark purple, single crystals were carried out at both 250 and 100 K. Unfortunately, above 250 K the crystals split and the diffraction intensity was lost, so no single crystal measurements at or above room temperature were possible. The single crystal was suspended in paraffin oil and mounted quickly onto a nylon loop on a copper pin and flash cooled to 250 K in the stream of liquid nitrogen on the diffractometer. Once the dataset was collected, the crystal was slowly cooled to 100 K and a second low temperature dataset was collected. Diffraction experiments were carried out at two temperatures in order to determine whether or not there were any structural changes in the Fe(II) macrocycle consistent with a SCO transition in the solid state, as was previously reported for the parent macrocycle **(2.1)**.[46]

At 250 K, the chiral *R,R* $[Fe(N_3O_2)(CN)_2]$ macrocycle **(2.9)** crystallizes in the chiral monoclinic space group $P2_1$, with two independent macrocycles in the unit cell

(molecules **A** and **B**). The molecular structure of **(2.9)** is shown in Figure 2.2. The crystal structure of the chiral macrocycle **(2.9)** reveals that for both molecules, the macrocycle coordinates the Fe(II) centres in the equatorial plane with two axial cyanide ligands completing their coordination geometries. Rather surprisingly, the Fe(II) centers in **A** and **B** adopt different coordination geometries. In molecule **A**, the Fe(II) is closer to a six-coordinate octahedral geometry, whereas in molecule **B** the Fe(II) adopts a seven-coordinate, pentagonal bipyramidal geometry. Selected bond lengths and angles for molecules **A** and **B** are shown in Tables 2.2 and 2.3. Molecule **A** has one long and one short Fe-O bond (Fe(1)···O(1) = 3.097(5) Å) and Fe(1)-O(2) = 2.263(2) Å). Since the Fe(1)-O(1) bond length is larger than the sum of the *van der Waals* radii, the geometry for the Fe(II) centre is interpreted as being closer to six coordinate. For molecule **B**, the Fe-O bond distances are much closer in length, 2.418(2) Å and 2.475(8) Å respectively, which together with the axial $CN^-$ ligands, confers a slightly distorted pentagonal bipyramidal geometry around the Fe(II) centre. Close examination of the bond lengths of the coordinated atoms reveals that Fe-N and Fe-CN bond lengths are significantly different for the two complexes. It can be noted that when the macrocycle is seven-coordinate, the Fe-N and Fe-CN bond lengths are longer in comparison with those coordinated to the Fe(II) centre that is closer to an octahedral geometry. The N-C-Fe bond angles for the two macrocycles show a deviation from 180°. For molecule **A**, the bond angles are 178.41° and 175.63° and for molecule **B** the angles are bent to a greater degree being 175.39° and 174.80°. The deviation of the Fe(II) ion from the plane of the macrocyclic ring was also examined; the plane was defined by Fe(1), O(1), O(2), N(1-3) C(9), C(10), C(25) and C(26) for molecule **A** and Fe(2), O(3), O(4), N(6-8) C(38), C(39),

C(54) and C(55) for molecule **B**. It was determined that molecule **A** deviates by 0.026 Å and molecule **B** deviates by 0.017 Å. From this analysis it is apparent that when the Fe(II) is in the more symmetrical, 7-coordinate environment, it lies closer to the plane of the pentagonal girdle. Another difference between the two macrocycles is the deviation of the ethylene bridge, O-CH(Ph)-CH(Ph)-O, from the plane defined by the two oxygen atoms and the Fe ion. For molecule **A**, the C(11) and C(18) atoms deviate from the $FeO_2$ plane by +0.914 and +0.125 Å, respectively. For molecule **B**, C(40) and C(47) are located on opposite sides of this plane, deviating by +0.493 and -0.305 Å respectively. This indicates that the macrocycle in molecule **B** is closer to being planar than the six coordinate macrocycle in molecule **A**.

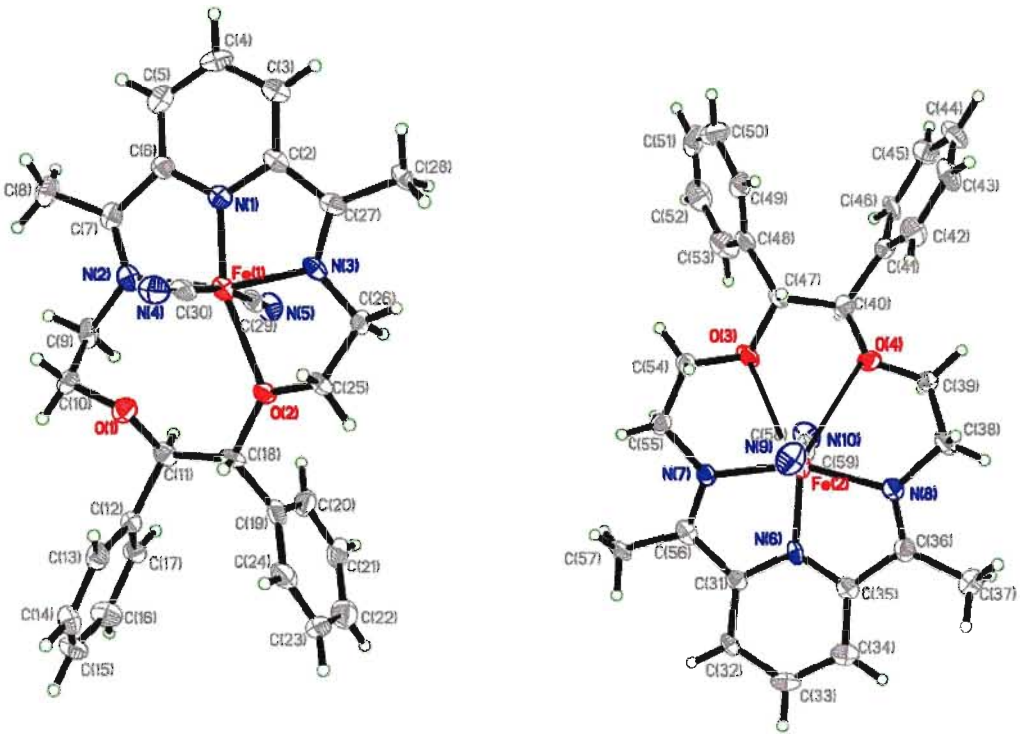


**Figure 2.2:** ORTEP[110] representation of the molecular structure of **(2.9)** at 250 K. Thermal ellipsoids are plotted at 50% probability.

**Table 2.2:** Selected bond lengths (Å) for **(2.9)** at 250 K.

| Molecule A | Bond Length (Å) | Molecule B | Bond Length (Å) |
|---|---|---|---|
| Fe(1)-O(1) | 3.097(5) | Fe(2)-O(3) | 2.418(2) |
| Fe(1)-O(2) | 2.263(2) | Fe(2)-O(4) | 2.475(8) |
| Fe(1)-N(1) | 1.872(4) | Fe(2)-N(6) | 2.040(5) |
| Fe(1)-N(2) | 2.036(6) | Fe(2)-N(7) | 2.140(5) |
| Fe(1)-N(3) | 1.956(5) | Fe(2)-N(8) | 2.123(5) |
| Fe(1)-C(29) | 1.986(7) | Fe(2)-C(58) | 2.107(8) |
| Fe(1)-C(30) | 1.989(7) | Fe(2)-C(59) | 2.093(8) |

**Table 2.3:** Selected bond angles (°) for **(2.9)** at 250 K.

| Molecule A | Bond Angle (°) | Molecule B | Bond Angle (°) |
|---|---|---|---|
| N(1)-Fe(1)-N(2) | 79.6(2) | N(6)-Fe(2)-N(7) | 74.8(2) |
| N(1)-Fe(1)-N(3) | 79.7(2) | N(6)-Fe(2)-N(8) | 74.5(2) |
| N(1)-Fe(1)-O(2) | 157.1(2) | N(6)-Fe(2)-O(3) | 146.8(2) |
| N(1)-Fe(1)-C(29) | 94.5(2) | N(6)-Fe(2)-C(58) | 92.5(3) |
| N(1)-Fe(1)-C(30) | 94.4(2) | N(6)-Fe(2)-C(59) | 97.8(3) |
| N(2)-Fe(1)-N(3) | 159.2(2) | N(7)-Fe(2)-N(8) | 149.2(2) |
| N(2)-Fe(1)-O(2) | 123.2(2) | N(7)-Fe(2)-O(3) | 72.1(2) |
| N(2)-Fe(1)-C(29) | 89.0(3) | N(7)-Fe(2)-C(58) | 90.4(3) |
| N(2)-Fe(1)-C(30) | 88.4(3) | N(7)-Fe(2)-C(59) | 91.5(3) |
| N(3)-Fe(1)-O(2) | 77.4(2) | N(8)-Fe(2)-O(3) | 138.6(2) |
| N(3)-Fe(1)-C(29) | 90.3(3) | N(8)-Fe(2)-C(58) | 90.3(3) |
| N(3)-Fe(1)-C(30) | 95.5(2) | N(8)-Fe(2)-C(59) | 93.2(3) |
| O(2)-Fe(1)-C(29) | 85.6(2) | O(3)-Fe(2)-C(58) | 89.6(2) |
| O(2)-Fe(1)-C(30) | 87.9(2) | O(3)-Fe(2)-C(59) | 81.3(2) |
| C(29)-Fe(1)-C(30) | 170.2(3) | C(58)-Fe(2)-C(59) | 169.7(3) |

Figure 2.3 shows the crystal packing of macrocycle **(2.9)** at 250 K, which crystallizes along with two independent $CH_3CN$ molecules and one independent $Et_2O$

molecule. Examination of the packing reveals that the closest intermolecular distance between Fe(II) centres is 10.542 Å. A view down the *b*-axis of the unit cell reveals that the macrocycles pack in a slightly offset head-to-head arrangement. There are no significant π-π interactions between the pyridine rings of neighboring macrocycles which could be in part due to the bulky nature of the phenyl rings, Figure 2.3.

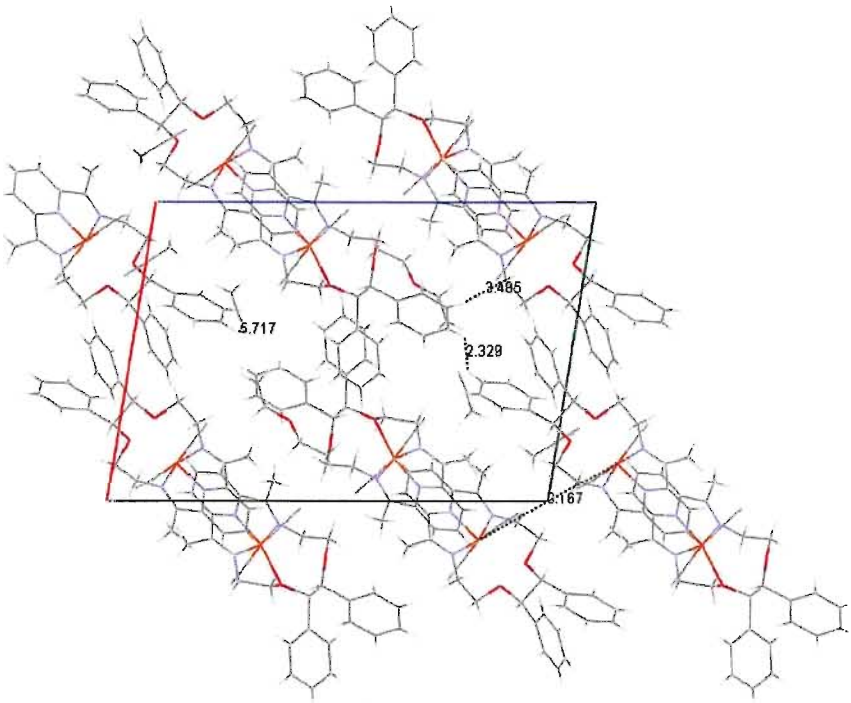


**Figure 2.3:** Packing diagram of *R,R* $[Fe(N_3O_2)(CN)_2]$ **(2.9)** at 250 K, view down the *b*-axis.[111]

The solvent molecules occupy the voids in the structure. Hydrogen bonding interactions range from 2.562-2.734 Å. The shortest H-bonds are those involving the protons of the phenyl rings that are H-bonded to the nitrogen atom of a cyanide ligand, (H···N-C = 2.562-2.626 Å) as well as to the oxygen atoms of the $Et_2O$ (H···O-C = 2.571 Å). Longer H-bonds involve the nitrogen atom of the cyanide ligand being H-bonded to

a proton from a neighboring $CH_3CN$ (N···H-C = 2.734 Å) and the ethylene proton of a neighboring macrocycle (N···H-C = 2.626 Å).

The molecular structure of **(2.9)** at 100 K is shown in Figure 2.4. At low temperature, the chiral monoclinic $P2_1$ space group and the two independent molecules in the unit cell are retained. Molecule **A** maintains its 6-coordinate geometry displaying relatively similar bond lengths and angles to those found at 250 K, Tables 2.4 and 2.5. The coordination geometry of Molecule **B** however, changes significantly upon cooling; this is most evident by the change in the Fe-O bond lengths; the Fe(2)-O(3) and Fe(2)-O(4) distances change from 2.418(2) and 2.475(8) Å at 250 K, to 2.583(2) Å and 2.638(5) Å at 100 K. This change is too large to be due to thermal contraction and can be interpreted as a subtle geometrical change. At 100 K, the Fe(II) centre is closer to a square pyramidal coordination geometry, bound to the pyridine and two imine nitrogen atoms of the macrocycle as well two axial cyanide ligands. This change in geometry is also reflected in the other metal-ligand bond lengths. The Fe-$N_{imino}$ bond lengths (Fe(2)-N(8)) for molecule **B** shorten from 2.141(5) and 2.123(5) Å at 250 K, to 2.015(6) and 2.013(6) Å 100 K. The Fe-$N_{pyridine}$ bond length, Fe(2)-N(6), also decreases from 2.040(5) Å at 250 K to 1.860(5) Å at 100 K. The Fe-CN bond lengths also change from 2.107(8) Å to 1.976(9) Å for Fe(2)-C(58) and 2.093(8) Å to 1.989(9) Å for Fe(2)-C(59). The N-C-Fe bond angles for molecule **B** move closer to 180° as the temperature is decreased. Examination of the metal-to-ligand bond lengths is important for determining the spin state of the Fe(II) ion. In the HS state the antibonding $e_g$* orbital is occupied increasing the metal-to-ligand bond length by about 0.2 Å, in comparison to the LS state which has an empty antibonding $e_g$* orbital.[39] For molecule **A**, the deviation of ethylene bridged O-

*C*HPh-*C*HPh-O carbons, C(11) and C(18) from the Fe(II)$O_2$ plane are similar namely, 0.895 and +0.113 Å. In this case, both atoms are located on the same side of the plane. For molecule **B**, the deviation of the ethylene bridged carbons from the $FeO_2$ plane is +0.503 and -0.292 Å for C(40) and C(47) respectively. For this molecule, the carbon atoms are located on opposite sides of the $FeO_2$ plane as observed for the 7-coordinate macrocycle at 250 K. Comparing the two sets of deviations for the 5-and 7-coordination geometries we conclude that due to the larger difference in the deviation of the ethylene C(40) and C(47) atoms from the $FeO_2$ plane, the 5-coordinate Fe(II) macrocycle is slightly less symmetrical.

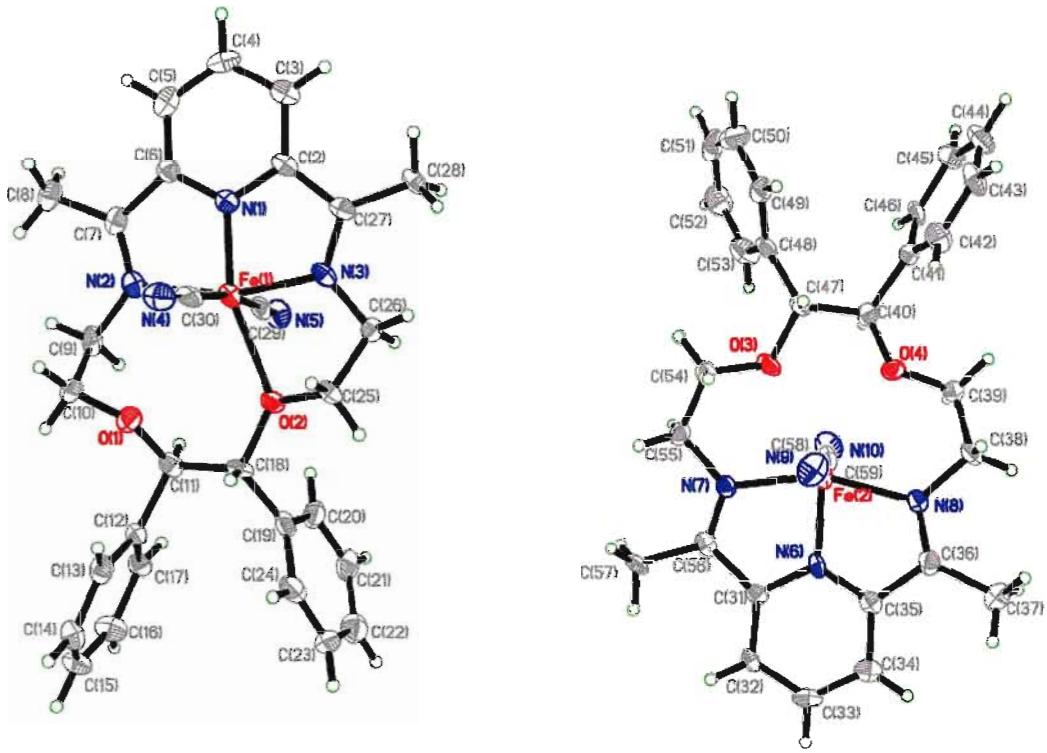


**Molecule A** **Molecule B**

**Figure 2.4:** ORTEP[110] representation of the molecular structure of **(2.9)** at 100 K. Thermal ellipsoids are plotted at 50%.

It seems reasonable to suggest that for this chiral diphenyl macrocycle, a 5-coordinate LS Fe(II) complex may be more favourable than the 6-coordinate geometry observed for the parent system. In this case, the presence of the chiral centers and the bulky nature of the phenyl rings could render the structural change from a seven- to a six-coordinate geometry very difficult for this macrocycle in the solid state and might also account for the destruction of the single crystals above 250 K.

**Table 2.4:** Selected bond lengths (Å) for **(2.9)** at 100 K.

| **Molecule A** | **Bond Length (Å)** | **Molecule B** | **Bond Length (Å)** |
|---|---|---|---|
| Fe(1)-O(1) | 3.123(3) | Fe(2)-O(3) | 2.583(2) |
| Fe(1)-O(2) | 2.251(2) | Fe(2)-O(4) | 2.638(5) |
| Fe(1)-N(1) | 1.831(5) | Fe(2)-N(6) | 1.860(5) |
| Fe(1)-N(2) | 2.042(7) | Fe(2)-N(7) | 2.015(6) |
| Fe(1)-N(3) | 1.917(6) | Fe(2)-N(8) | 2.013(6) |
| Fe(1)-C(29) | 1.939(8) | Fe(2)-C(58) | 1.976(9) |
| Fe(1)-C(30) | 1.950(9) | Fe(2)-C(59) | 1.976(9) |

**Table 2.5:** Selected bond angles (°) for **(2.9)** at 100 K.

| **Molecule A** | **Angle (°)** | **Molecule B** | **Angle(°)** |
|---|---|---|---|
| N(1)-Fe(1)-N(3) | 81.5(3) | N(6)-Fe(2)-N(8) | 78.7(3) |
| N(1)-Fe(1)-C(29) | 94.0(3) | N(6)-Fe(2)-C(59) | 99.2(3) |
| N(3)-Fe(1)-C(29) | 90.8(3) | C(58)-Fe(2)-N(8) | 89.9(3) |
| N(1)-Fe(1)-C(30) | 94.4(3) | N(6)-Fe(2)-C(58) | 93.5(3) |
| N(3)-Fe(1)-C(30) | 95.1(3) | C(59)-Fe(2)-N(8) | 92.7(3) |
| C(29)-Fe(1)-C(30) | 170.4(3) | C(59)-Fe(2)-C(58) | 167.3(3) |
| N(3)-Fe(1)-N(2) | 161.8(3) | N(8)-Fe(2)-N(7) | 158.6(2) |
| C(29)-Fe(1)-N(2) | 88.5(3) | C(58)-Fe(2)-N(7) | 90.6(3) |
| C(30)-Fe(1)-N(2) | 88.3(3) | C(59)-Fe(2)-N(7) | 91.4(3) |

At 100 K, the Fe(II) centres on neighboring molecules are closer together; the shortest intermolecular Fe···Fe distance is 9.167 Å. Hydrogen bonding interactions range from 2.482 to 2.557 Å. As observed at 250 K, the phenyl ring protons form H-bonds with the nitrogen atom of a neighbouring cyanide ligand, which decrease upon cooling from (H···N-C = 2.562-2.626 Å) at 250 K to (H···N-C = 2.540-2.557 Å) at 100 K. The phenyl protons also form H-bonds with an oxygen atom of an $Et_2O$ solvent molecule decreasing from (H···O-C = 2.571 Å) at 250 K to (H···N-C = 2.482 Å) at 100 K. The nitrogen of the cyanide ligand also forms a hydrogen bond with the proton of an ethylene group of a neighboring macrocycle which also decreases as a function of temperature from (N···H-C = 2.626 Å) to (H···N-C = 2.532 Å).

The intermolecular interactions present for the chiral macrocycle **(2.9)** do not change significantly as a function of temperature, in contrast to the parent macrocycle **(2.1)** which displays a significant modification in its hydrogen bonding interactions as the temperature is lowered.[46] The oxygen atoms of the parent macrocycle **(2.1)** are not involved in any H-bonding interactions in the HS state due to their internal positions in the coordination sphere. However, the LS 6-coordinate structure reveals H-bonding interactions between the oxygen atoms of the coordination sphere and hydrogen atoms of neighbouring water molecules.[46] Letard *et al.* found that the modification in the H-bonding interactions as a function of temperature is noteworthy since H-bonds play a paramount role in the propagation of spin crossover.[46] Although the intermolecular interactions of complex **(2.9)** do not change as significantly as the parent complex **(2.1)** as a function of temperature, there is a structural change that may be accompanied by a change in spin state that requires further investigation.

Although the complex crystallizes in a chiral space group, the Flack parameter obtained from a crystal structure measurement is not always a reliable indicator of chirality. As a consequence, circular dichroism (CD) measurements were carried out on **(2.9)** in solution in order to determine whether or not the complex is optically active. The CD spectrum for **(2.9)** is shown in Figure 2.5. If molecules are enantiomers they will absorb left and right circularly polarized light to a different degree.[112] By observing the Cotton effect for one enantiomer, we can conclude that it is chiral. The Cotton effect is evident with a change in rotation to a maximum as an absorption band is approached, which may be positive or negative, followed by a decrease to a minimum, passing through zero at the wavelength of maximum absorption.[112]

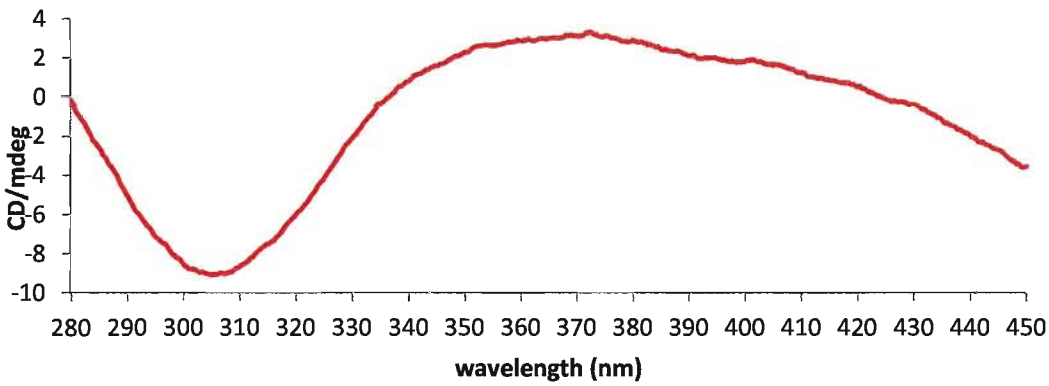


**Figure 2.5:** CD spectrum of chiral macrocycle **(2.9)** in an ethanol solution at rt.[113]

The presence of the Cotton effect at 280 nm together with a negative dichroic signal at 305 nm confirms that this complex is optically active. Although the CD measurements were carried out at room temperature, the twist and conformational changes which occur due to a temperature dependent SCO transition from HS to LS could produce a significant amount of rotation that might afford a significant quantitative variation in the molecular chirality detectable by CD spectroscopy.[114] Unfortunately, our

CD spectrometer is not equipped with a low temperature cell, but these studies could provide a future direction for this project. The rotation of linearly polarized light of a chiral molecule can be probed further by simultaneously examining its magnetic properties. This optical phenomena is known as magneto-chiral dichroism (MChD), an important property observed when chirality is introduced into a ferromagnetically ordered compound.[97]

From the structural data it is apparent that on cooling the chiral complex undergoes a subtle geometrical change in the solid state that is different compared to the parent macrocycle. It is possible that this structural change is also accompanied by a change in spin state. In order to investigate this further, magnetic studies of the complex were required. The first goal of my project was therefore to follow the synthetic methodology described previously and prepare the *R,R* $[Fe(N_3O_2)(CN)_2]$ complex for magnetic susceptibility and Mössbauer spectroscopy studies.

### 2.3 Magnetic studies of *R,R* $[Fe(N_3O_2)(CN)_2]\cdot 2H_2O$ (2.9)

Magnetic susceptibility data was collected on a powder sample of *R,R* $[Fe(N_3O_2)(CN)_2]$ **(2.9)** by the Letard group at the CNRS in Bordeaux, France. The powder was first analyzed by CHN elemental analysis and a reasonable fit was obtained for a complex of stoichiometry $[Fe(N_3O_2)(CN)_2]\cdot 2H_2O$. In this respect, it is important to note that the solvent composition of the powder is different from that of the single crystals. Attempts to measure the susceptibility of single crystals were not successful since the crystals decomposed en route to France.

Magnetic susceptibility measurements were taken from 300 to 10 K recording the susceptibility at 3 K intervals, Figure 2.6. The magnetic susceptibility was also recorded at 3 K intervals warming back up to 300 K. This was followed by another heating cycle to 370 K. At 370 K, the $\chi_M$T value is 2.78 $cm^3$ K $mol^{-1}$. As the temperature is decreased to 50 K, there is a smooth decrease in $\chi_M$T to a value of 0.64 $cm^3$ K $mol^{-1}$. Between 50 and 25 K the magnetic susceptibility is constant; however, below 25 K it begins to decrease to a value of 0.43 $cm^3$ K $mol^{-1}$ at 10 K. Through the cycle of decreasing and increasing temperature, there was no visible hysteresis. The spin transition is gradual with an incomplete conversion at both high and low temperature. The mean average for $\chi_M$T in the HS state is determined to be 3 $cm^3$ K $mol^{-1}$, with a high spin fraction of 92.6 %. At 50 K, the LS state fraction is estimated to be 21.3 %. The gradual decrease observed for $\chi_M$T below 25 K can be attributed to zero field splitting of the remaining HS fraction.

The gradual spin transition is most likely a result of poor cooperativity between molecules in the crystal lattice, which is consistent with the weak H-bonding interactions observed in the crystal structure. This is in sharp contrast to the parent macrocycle **(2.1)** which crystallizes as a 1-D chain with strong intermolecular interactions between the macrocyclic oxygen atoms and protons from neighbouring solvent water molecules, giving rise to a thermal hysteresis in the SCO data.[46]

Photomagnetic studies were also carried out on **(2.9)**. An attempt was made to photoexcite the complex with light of varying wavelengths. It was determined that the best photomagnetic conversion was seen after illumination with green light ($\lambda$ = 514 nm) at 10 K. As one can see in Figure 2.6, the open circles represent the magnetic susceptibility data for the irradiated sample. The irradiated sample shows an increase in

susceptibility from 0.43 $cm^3$ K $mol^{-1}$ to 0.86 $cm^3$ K $mol^{-1}$, at 10 K after photoexciting the sample for 10 hours with a power source of 70 mW at the entry of the glass fiber. By increasing the temperature by 0.3 K/min in the dark and recording the magnetic susceptibility at 1 K intervals, the temperature at which the photoexcited spin state relaxes can also be seen in Figure 2.6. The photoconversion is very small and incomplete up to 370 K, where the parent $[Fe(N_3O_2)(CN)_2]$ macrocycle **(2.1)** was determined to have a complete photo-induced conversion at 370 K.[26] The percentage of photo-induced conversion between 10 and 370 K, where $\chi_M T$ is 0.43 and 2.78 $cm^3$ K $mol^{-1}$, respectively, is approximately (0.86-0.43)/ (2.78-0.43) = 18.3 %. Unfortunately, to elucidate the T(LIESST) accurately is difficult for a complex with such a low conversion. This slow decrease in $\chi_M T$ may be a consequence of the presence of the bulky phenyl groups, creating a larger energy barrier to lattice reorganization for this chiral complex. Although the photo-induced conversion is small, this is the first time a LIESST effect has been observed for a chiral Fe(II) complex.

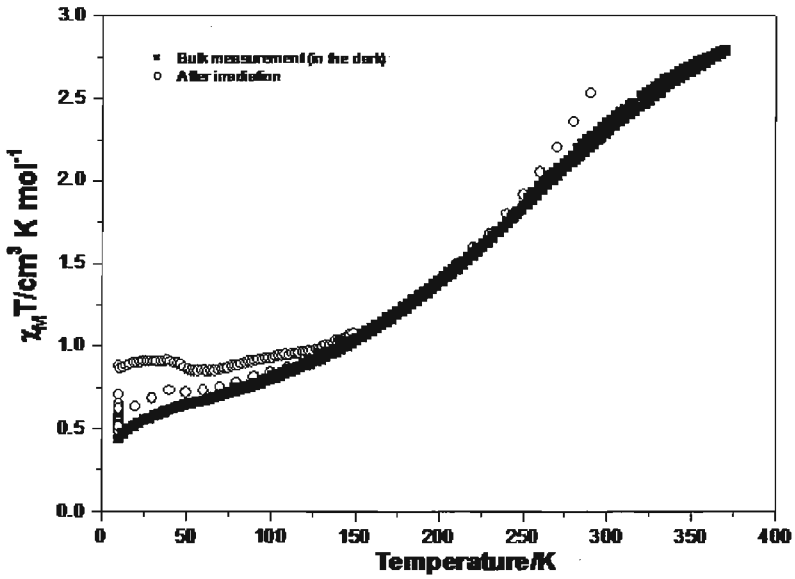


**Figure 2.6:** A plot of $\chi_M T$ *vs* T for a powder sample of *R,R* $[Fe(N_3O_2)(CN)_2]\cdot 2H_2O$ **(2.9)**.

Variable temperature Mössbauer data was also collected for complex **(2.9)**. The spectra were recorded on the powder sample from 293 to 5 K. The HS state transition is indicated by the green line and LS state transition by the blue line, Figure 2.7. Mössbauer experiments provide two parameters of information about the Fe(II) centre: (i) the isomer shift δ is determined by the displacement of the spectrum from zero and (ii) the quadropole splitting $\Delta E_Q$, is defined by the magnitude of the separation of an absorption line into a doublet.[115] The parameters in Table 2.6 show that the transition into the high spin state starts to increase at 100 K, and at the temperature maxima of 293 K the complex is in a 44:56 LS:HS ratio. It is clear that the proportion of the HS state is more significant around room temperature than at lower temperatures. The results at 293 K show a consistency with the magnitude of the isomer shift and quadropole splitting previously published for the parent macrocycle **(2.1)**.[109] Although within this temperature range, a pure HS complex is not observed. The broadening of the spectrum shows that the *R,R* $[Fe(N_3O_2)(CN)_2]$ macrocycle is transitioning into the HS state, as indicated by the green line, Figure 2.7.

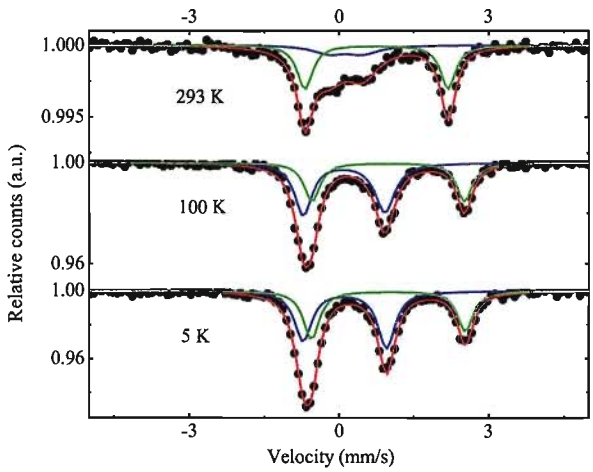


**Figure 2.7:** Mössbauer spectra for *R,R* $[Fe(N_3O_2)(CN)_2]\cdot 2H_2O$ **(2.9)** from 293 - 5 K; HS Fe(II) (green line); LS Fe(II) (blue line).

**Table 2.6:** Mössbauer parameters for *R,R* $[Fe(N_3O_2)(CN)_2]$ **(2.9)**.

| T (K) | $\delta^*$ (mm/s) | $\Delta E_Q$ (mm/s) | Fe occupancy (%) | $Fe^{2+}$ spin state |
|---|---|---|---|---|
| 5 | 0.234(4) | 1.660(5) | 62 | Low |
| | 1.113(4) | 3.058(7) | 38 | High |
| 50 | 0.220(4) | 1.650(7) | 62 | Low |
| | 1.120(5) | 3.068(8) | 38 | High |
| 100 | 0.210(5) | 1.64(6) | 60 | Low |
| | 1.005(5) | 3.047(8) | 40 | High |
| 150 | 0.18(1) | 1.62(2) | 58 | Low |
| | 1.08(1) | 2.97(2) | 42 | High |
| 230 | 0.12(1) | 1.56(2) | 53 | Low |
| | 1.08(1) | 2.74(3) | 47 | High |

DFT calculations were also performed on **(2.9)**. The atomic coordinates for the six- and seven coordinate Fe(II) macrocycles determined from the crystal structure at 250 K were used as input for the DFT calculations. Geometries were optimized at the B3LYP/SDD 6-31G(d) level. The geometry of the optimized *R,R* $[Fe(N_3O_2)(CN)_2]$ macrocycle **(2.9)** is in good agreement with the bond lengths and angles determined from the single crystal X-ray data. The calculations revealed that the 6-coordinate complex is just 3.5 $kcalmol^{-1}$ more stable than the 7-coordinate. This might account for the presence of both of these geometries in the crystal structure at 250 K. Calculations are currently in progress to probe how the molecular orbital diagram for the complex changes as the Fe(II) centres undergo a change in geometry.

Once the structural and magnetic properties of the *R,R* complex were elucidated, the next goal was to prepare and characterize the closely related *S,S*, *racemic* and *meso* macrocycles **(2.10)**, **(2.11)**, and **(2.12)**, respectively. By doing so we could: (i) prove that

the *R,R* and *S,S* complexes are chiral enantiomers; (ii) probe how changing the spatial positions of the phenyl rings affects the SCO properties of the macrocycle and (iii) directly compare the SCO properties of the chiral macrocycle together with its *racemic* and *meso* counterparts.

### 2.4 Preparation of the *S,S* primary diamine (2.7)

The second macrocycle targeted was the *S,S* enantiomer **(2.10)**. The first step was to prepare the *S,S* primary diamine **(2.7)** which is a new, previously unreported compound. Following the synthetic procedure outlined in Scheme 2.2, the *S,S* diamine **(2.7)** was prepared in 5 steps from commercially available *S,S*-(-)-hydrobenzoin **(2.13)** and isolated as a pale yellow oil in a 23% overall yield.

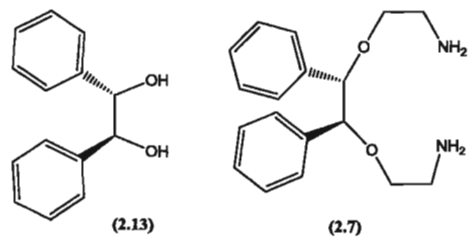


**Figure 2.8:** Molecular structures of (*S,S*)-(-)-hydrobenzoin **(2.13)** and (4S,5S)-4,5-diphenyl-3,6-dioxa-1,8-octanediamine **(2.7)**.

This chiral diamine **(2.7)** is the key intermediate in the preparation of the macrocycle since it contains the chiral centres, which will ultimately become part of the organic framework of the macrocycle. The molecular structure of **(2.7)** has been fully characterized. The FAB mass spectrum shows a parent ion $[MH]^+$ at $m/z = 301$ which is consistent with its molecular structure. The microanalysis data for **(2.7)** was the best fit for $[C_{18}H_{24}N_2O_2]\cdot H_2O$. The IR spectrum contains two NH str at 3366 and 3330 $cm^{-1}$ characteristic for the primary diamine, as well as a C-O str at 1104 $cm^{-1}$ for the ether

linkage. The 300 MHz $^1$H NMR spectrum of **(2.7)** is shown in Figure 2.9. The aromatic protons appear as two sets of multiplets centered at 7.21 and 7.13 ppm. The singlet at 4.47 ppm is assigned to the C-3 proton. The two protons at C-2 appear as two multiplets at 3.49 and 3.33 ppm. The triplet at 2.81 ppm is assigned to the $CH_2$ protons at C-1. Finally, the primary diamine protons appear as a broad peak centered at 1.45 ppm.

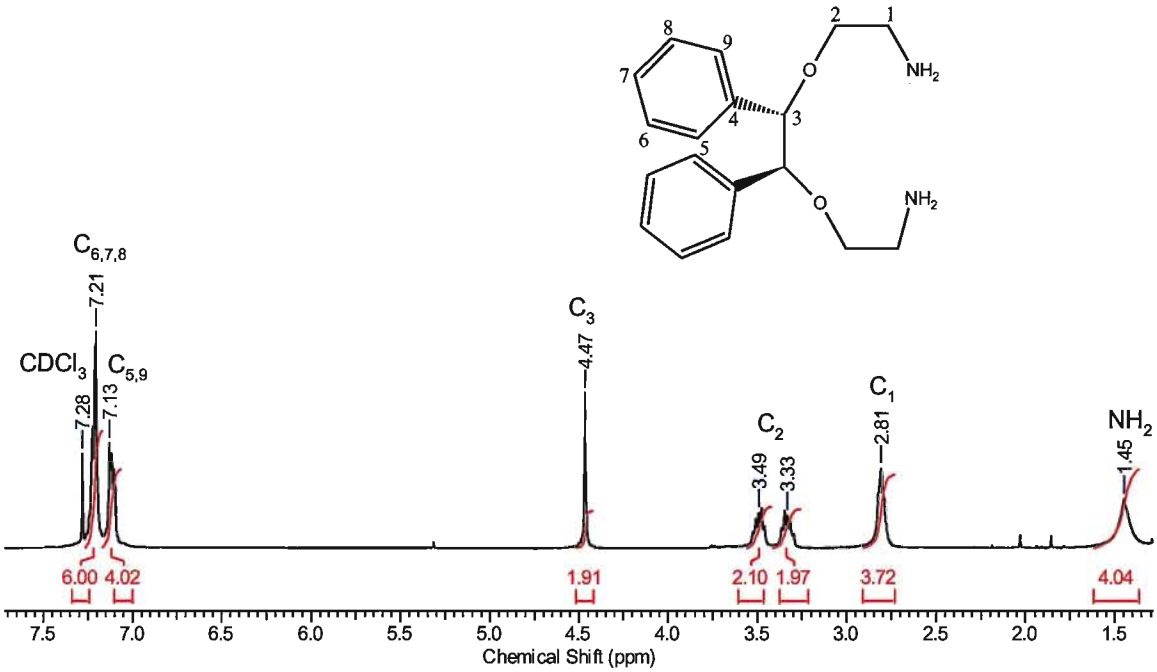


**Figure 2.9:** 300 MHz $^1$H NMR spectrum of (4S,5S)-4,5-diphenyl-3,6-dioxa-1,8-octanediamine **(2.7)** in $CDCl_3$.

The 75 MHz $^{13}$C NMR spectrum was straightforward to interpret. A peak at 138.8 ppm is assigned to the quaternary carbon at C-4. Two peaks at 128.2 and 127.5 ppm are assigned to four of the aromatic carbons. The peaks at 86.1, 72.0 and 42.0 ppm are assigned to carbon atoms appended to the ether and diamine functionalities, C-3, C-2 and C-1, respectively. It should be noted that $^1$H and $^{13}$C NMR spectra of the *S,S* diamine **(2.7)** are identical, as expected, to those recorded for the *R,R* enantiomer **(2.6)** .

## 2.5 Preparation and characterization of *S,S* $[Fe(N_3O_2)(CN)_2]$ (2.10).

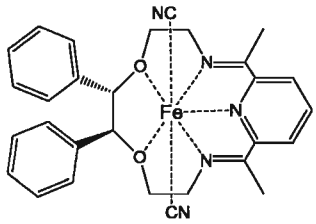


**(2.10)**

The *S,S* macrocycle **(2.10)** was prepared following the procedure outlined in Scheme 2.1. In this respect, the Schiff-base condensation of 2,6-diacetyl pyridine together with (4S,5S)-4,5-diphenyl-3,6-dioxa-1,8-octanediamine **(2.7)** in the presence of $FeCl_2 \cdot 4H_2O$, afforded the *bis* chloride intermediate that was reacted in situ with an excess of NaCN to facilitate ligand exchange, affording the *S,S*-$[Fe(N_3O_2)(CN)_2]$ macrocycle **(2.10)** as a blue solid in 74% yield. To initially test for any SCO properties, a small amount of the complex was dissolved in ethanol and cooled to 100 K, by immersing the vial in liquid nitrogen. The deep blue solution changed to a pale pink colour on cooling, indicating that in solution it is likely that the complex undergoes spin crossover. The *S,S* macrocycle **(2.10)** has been fully characterized. The FAB mass spectrum shows a fragment ion at *m/z* = 509 corresponding to the loss of one axial cyanide ligand from the parent ion $[M\text{-}CN]^+$. The IR spectrum has a band at 3419 $cm^{-1}$ consistent with the OH str of a solvent water in the crystal lattice. A CN str at 2095 $cm^{-1}$ is visible for the axially coordinated cyanide ligands. There is also a sharp C=N str at 1632 $cm^{-1}$ consistent with the formation of the *bis* imine. The CHN microanalysis data was the best fit for a complex of stoichiometry $[Fe(N_3O_2)(CN)_2] \cdot 3H_2O$. The chirality of **(2.10)** was invesigated by CD spectroscopy in ethanol at room temperature, Figure 2.10.

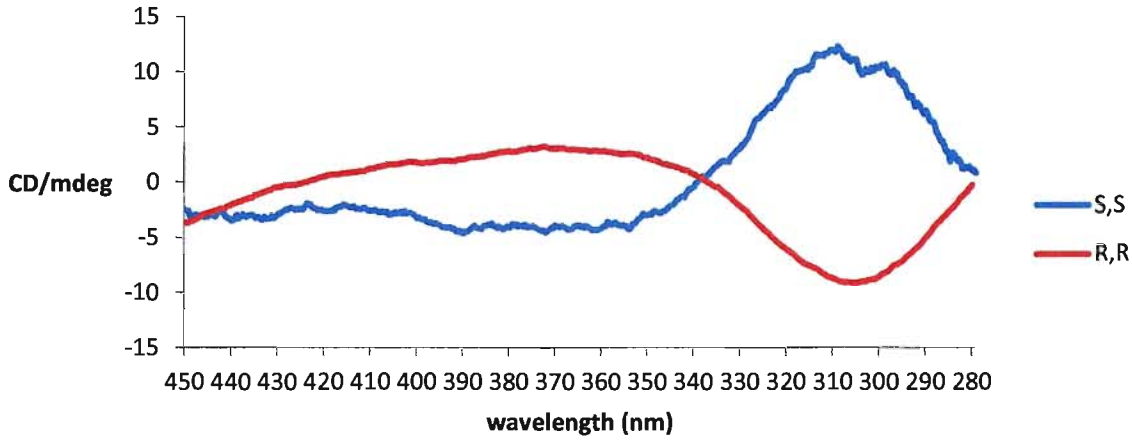


**Figure 2.10:** Circular dichroism spectra of the *R,R* and *S,S* complexes **(2.9)** (red) and **(2.10)** (blue), in ethanol at room temperature.

As expected, the CD spectrum of **(2.10)** is complementary to that recorded for the *R,R* enantiomer **(2.9)**, confirming that the two complexes are enantiomers, Figure 2.10. Each enantiomer exhibits a positive Cotton effect, where the absorption passes through zero at approximately 340 nm, followed by a continuation in the opposite direction. This behaviour is typical for optically active compounds.[101]

Variable temperature UV-Vis studies of both enantiomers, **(2.9)** and **(2.10)** also reveal identical properties in solution. UV-Vis spectroscopy is a very useful method that enables the change in spin state of SCO compounds to be characterized in solution as a function of temperature. Characteristically, six-coordinate Fe(II) HS complexes contain a band centered around $\lambda_{max}$ = 672 nm attributed to a $^5T_2 \rightarrow {}^5E$ transition whereas LS Fe(II) complexes characteristically display two bands, the first in the visible region and the second in the UV-Vis region of the spectrum.[31] The room temperature UV-Vis spectrum of the *S,S* macrocycle **(2.10)** is shown in Figure 2.11. Two bands are visible at $\lambda_{max}$ = 486 and 627 nm. The band centered around $\lambda$ = 490 nm corresponds to the LS Fe(II) $^1A \rightarrow {}^1T$ transition.[41] The band at $\lambda$ = 627 nm is assigned as a charge transfer band involving the

$d_{xy}$ and $d_{yz}$ orbitals of the Fe(II) and the low-lying $p^*_{\pi}$ antibonding orbitals of the conjugated part of the macrocycle.[41] Upon cooling to 77 K, three distinct bands are present at $\lambda_{max}$ = 486, 610, and 708 nm. The molar absorptivity of the band centered around $\lambda$ = 490 nm increases from 803 $M^{-1}cm^{-1}$ at room temperature to 1421 $M^{-1}cm^{-1}$ at 77 K, consistent with a change in spin state from HS to LS as the complex is cooled in solution. The molar absorptivity of the band at $\lambda$ = 610 nm does not change significantly as a function of temperature consistent with the CT nature of this band. The band present at $\lambda$ = 708 nm becomes more distinct at lower temperature because it decreases in molar absorptivity and no longer overlaps with the band at $\lambda$ = 610 nm. This band at $\lambda$ = 708 nm corresponds to the HS Fe (II) $^5T_2$ ➔ $^5E$ transition.[41]

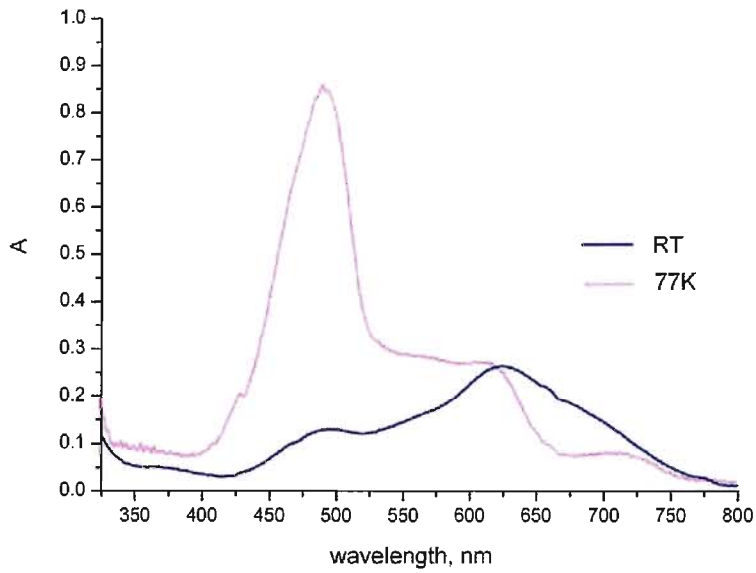


**Figure 2.11:** UV-Vis spectra of *S,S* $[Fe(N_3O_2)(CN)_2]$ **(2.10)** in ethanol at room temperature (blue line) and 77 K (pink line).

## 2.6 Characterization of *S,S* $[Fe(N_3O_2)(CN)_2]$ (2.10) by NMR spectroscopy

The growth of single crystals of the *S,S* $[Fe(N_3O_2)(CN)_2]$ macrocycle **(2.10)** has not been successful to date. At present it is unclear why the *S,S* macrocycle is difficult to crystallize. Since we could not elucidate the molecular structure of **(2.10)** in the solid state, we proposed to investigate its structure in solution by NMR spectroscopy. Although the characterization of paramagnetic complexes by NMR is far from routine, NMR studies were successfully carried out on a 6-coordinate paramagnetic Fe(II) complex that underwent conformational changes in solution and its structure was fully elucidated. [116] This study encouraged us to carry out NMR studies of our Fe(II) complex in solution. The 600 MHz $^1$H-NMR spectrum of **(2.10)** collected at 295 K in $CD_2Cl_2$ is presented in Figures 2.12 and 2.13. As expected, the spectrum displays broad, paramagnetically shifted peaks in the range of $\delta_H$ = +128 to -18 ppm which is typical for a HS Fe(II) complex.[117] Upon first examination of the spectrum it can be noted that the number and broad nature of the peaks together with their chemical shifts are consistent with a symmetrical, pentagonal bipyramidal HS Fe(II) complex. In order to make a full assignment of the spectrum, several strategies were employed: Firstly, the chemical shifts and line widths of each of the peaks were carefully determined from the NMR measurement. Assignments were made by examining the magnitude of the paramagnetic shift of the proton peaks in relation to the distances of these protons from the Fe(II) centre.[117] In this respect, the broader peaks at the highest and lowest frequency arise from those protons closest to the paramagnetic centre.[117] Secondly, relaxation times, $T_1$ were also examined, since the protons closest to the paramagnetic Fe(II) centre relax faster than those furthest away.[117] Thirdly, the integration of each peak was carefully

considered; and fourthly, $^{1}H$-$^{1}H$ COSY experiments were carried out to aid in the assignment. A summary of the correlation of the cross-peak data is given in Table 2.7.

The crystal structure of the 7-coordinate *R,R* $[Fe(N_3O_2)(CN)_2]$ macrocycle **(2.9)** was utilized as a model to estimate the distances of the protons from the Fe(II) centre, as seen in Figure 6.1 of the Appendix. As mentioned earlier, the spectrum is consistent with a HS pentagonal bipyramidal Fe(II) complex, and the 11 broad peaks are assigned symmetrically. The CH protons at C-8 and C-15 are assigned to the broad peak farthest downfield at 128.0 ppm since they are situated closest to the Fe(II) centre as indicated by their large line widths. The *para* proton of the pyridine ring at C-1 is quite far from the paramagnetic Fe(II) centre and is assigned to the peak downfield at 68.6 ppm. The broad peak at 41.1 ppm has been assigned to the protons at C-2 and C-27. The axial and equatorial protons of the ethylene groups are assigned separately, since their distances from the Fe(II) centre are not identical.[118] The equatorial protons at positions C-7 and C-22 can be assigned to the broad peak at 16.89 ppm. The axial protons are shifted further upfield at -5.45 ppm. There is a large paramagnetic shift between the axial and equatorial protons of C-7 and C-22 because the axial protons are closer to the Fe(II) centre resulting in a smaller $T_1$ and a larger line width and hence assignment to a peak more upfield. The axial and equatorial protons at C-6 and C-23 are not as paramagnetically shifted since their average distances to the Fe(II) centre are closer. The axial protons can therefore be assigned to the broad peak at -10.45 ppm, and the equatorial to the broad peak at -16.35 ppm. The peak at 5.37 ppm is representative of the $CD_2Cl_2$ solvent peak as well as the four aromatic phenyl protons at positions C-11, C-13, C-18, and C-20. The broad peak at 4.65 ppm is assigned to phenyl protons at C-12 and C-19. The remaining aromatic

protons at positions C-10, C-14, C-17, and C-21 can be assigned to the peak at -0.53 ppm. Finally, the peak upfield at -18.64 ppm is assigned to the methyl protons.

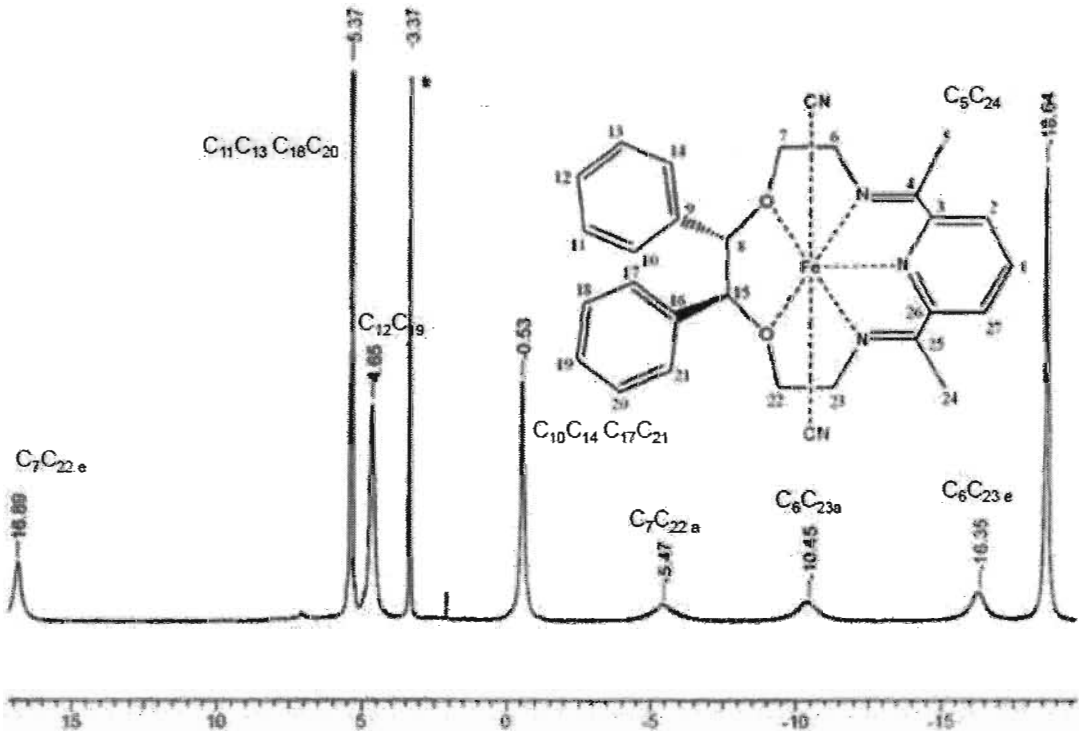


**Figure 2.12:** 600 MHz $^1$H-NMR spectrum of the *S,S* macrocycle **(2.10)** at 295 K in $CD_2Cl_2$ scanned from -20 ppm to 19 ppm; The subscripts *e* and *a* refers to equatorial and axial protons, respectively; **(*)** water.

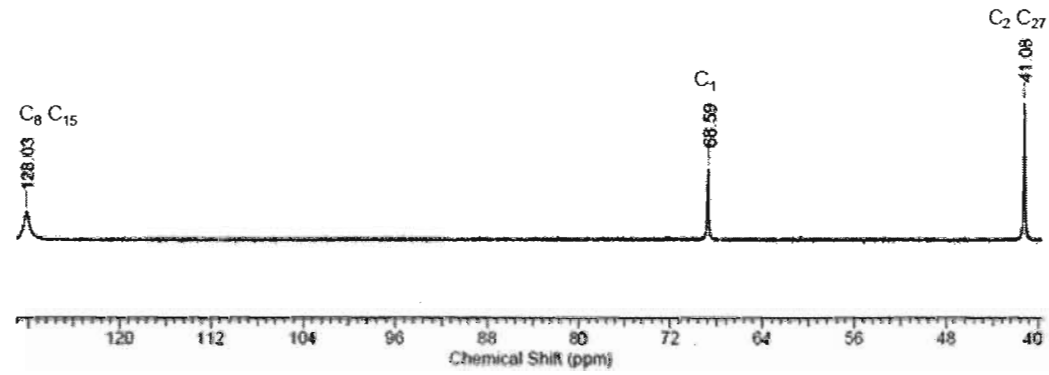


**Figure 2.13:** 600 MHz $^1$H-NMR of the *S,S* macrocycle **(2.10)** at 295 K in $CD_2Cl_2$ scanned from 40 ppm to 130 ppm.

**Table 2.7:** Proton assignment of **(2.10)** in $CD_2Cl_2$ at 295 K; The subscripts *e* and *a* refer to equatorial and axial protons, respectively.

| Assignment | Chemical shift δ (ppm) | Average Fe(II) distance (Å) | Relaxation time $T_1$ (ms) | Line width (Hz) | Integral | COSY $^1$H shift (ppm) |
|---|---|---|---|---|---|---|
| C-5,24 | -18.64 | 4.4 | 7.5 | 77 | 6.6 | --- |
| C-6,23e | -16.35 | 3.8 | 1 | 266 | 2 | --- |
| C-6,23a | -10.45 | 3.5 | 0.7 | 313 | 1.6 | --- |
| C-7,22a | -5.47 | 3.3 | 0.5 | 419 | 1.5 | --- |
| C-10,14,17,21 | -0.53 | 5.3 | 6.1 | 93 | 4.1 | 5.37 |
| C-12,19 | 4.65 | 8.3 | 111.5 | 34 | 2.3 | 5.37 |
| C-11,13,18,20 | 5.37 | 7.5 | 78.4 | 35 | 9.5 | 4.65, -0.53 |
| C-7,22e | 16.89 | 3.7 | 2.3 | 182 | 2 | --- |
| C-2,27 | 41.08 | 4.9 | 9.1 | 82 | 2 | 68.59 |
| C-1 | 68.59 | 5.7 | 25 | 82 | 1 | 41.08 |
| C-8,15 | 128.03 | 3.6 | 2.2 | 325 | 2 | --- |

$^{13}C$ NMR studies were also carried out for **(2.10)** at 295 K. Thirteen paramagnetically shifted peaks are observed in the range δ +800 to -600 ppm, Figure 2.14. Since the scan width was so broad, the measurements were carried out by measuring three spectra that were merged together to record all of the $^{13}C$ peaks, Figure 2.14. The phenyl carbons C-12, C-19, C-11, C-13, C-18, and C-20 were assigned via the cross coupling peaks present in the HSQC 2-D NMR spectrum. The carbon atoms of the axial cyanide ligands are assigned to the peaks farthest downfield at -484 ppm. A tentative assignment was attempted for the remaining carbon peaks using the average C-Fe bond distances and the recorded line widths are presented in Table 6.1 in the Appendix section. Once again we used the crystal structure of the 7-coordinate *R,R* macrocycle **(2.9)** was used to estimate the C-Fe bond distances.

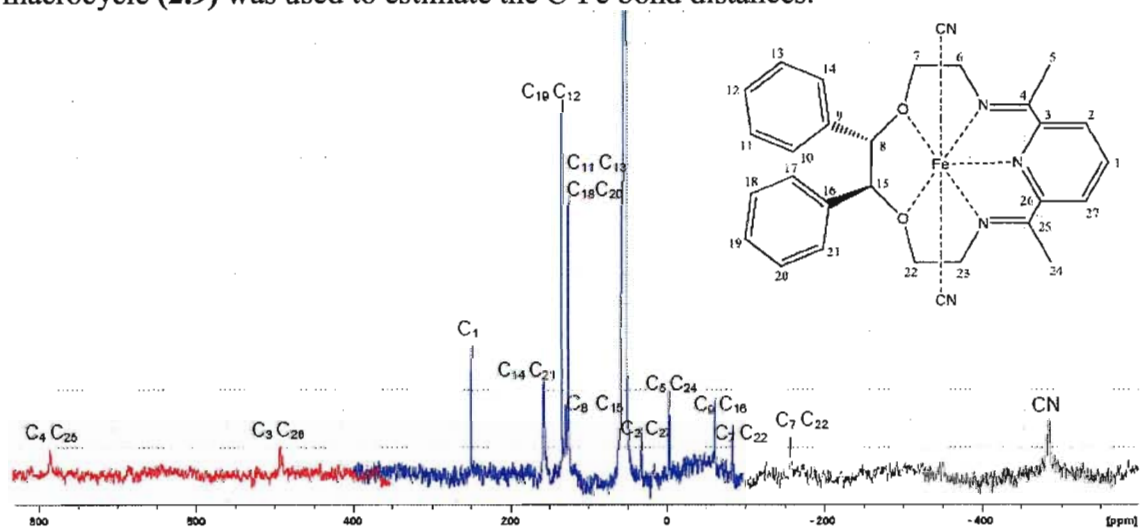


**Figure 2.14:** 150 MHz $^{13}C$ NMR spectrum of **(2.10)** in $CD_2Cl_2$ at 295 K.

For comparison, a sample of the original parent macrocycle $[Fe(N_3O_2)(CN)_2]$ **(2.1)** was prepared.[41] Although there have been detailed studies of the structural and magnetic properties of this complex in the solid state, its structural and magnetic properties have not yet been investigated in solution. The $^1H$ NMR spectrum of **(2.1)** was

recorded using a scan width of -10 ppm to 50 ppm, Figure 2.15. The six broad peaks in this spectrum are consistent with the HS, pentagonal bipyramidal Fe(II) complex reported in the solid state.[46] An assignment has been made for the six broad peaks following the rationale described previously for the *S,S* $[Fe(N_3O_2)(CN)_2]$ macrocycle **(2.10)**. In this complex, the ethylene protons (C-2 and C-3) only split into two broad peaks at 13.13 and 8.13 ppm, in sharp contrast to the four peaks seen for these protons in the chiral *S,S* $[Fe(N_3O_2)(CN)_2]$ macrocycle **(2.10)**. Assignment of the remaining peaks was more straightforward with the aromatic protons being assigned to the peaks downfield at 46.90 and 28.30 ppm for protons at C-8 and C-7, respectively. The ethylene proton at C-1 is assigned to the broad peak at 35.46 ppm. As observed in the spectrum of the *S,S* complex **(2.10)**, the $CH_3$ protons are shifted far upfield, and are visible at -8.83 ppm. Comparing the chemical shifts of the protons in both complexes, we are fairly confident in our assignments of the $^1H$ NMR of the *S,S* complex **(2.9)**. We conclude from these measurements that both the parent **(2.1)** and the chiral *S,S* $[Fe(N_3O_2)(CN)_2]$ macrocycle **(2.10)** are predominantly 7-coordinated high spin Fe(II) complexes in solution at room temperature.

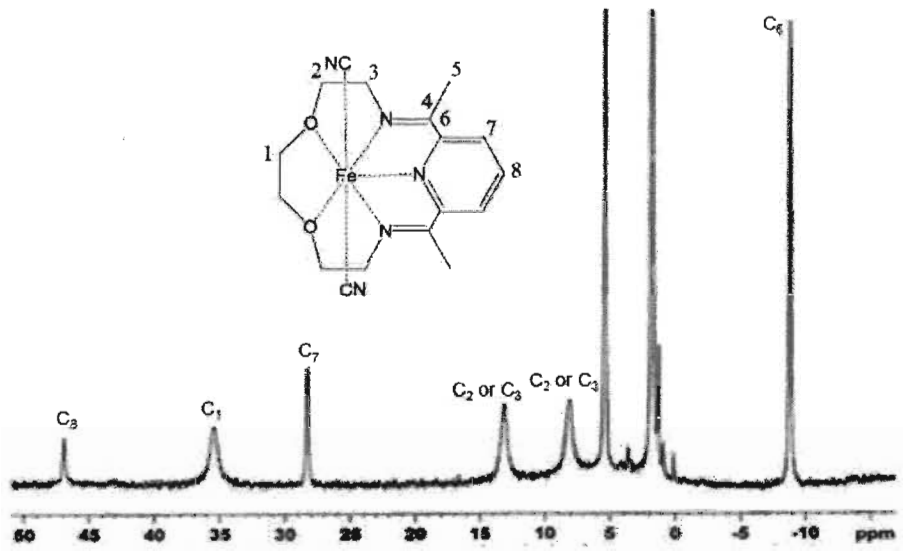


**Figure 2.15:** 600 MHz $^1$H-NMR spectrum of the parent $[Fe(N_3O_2)(CN)_2]$ macrocycle **(2.1)** in $CD_2Cl_2$ at 295 K.

In order to probe any structural rearrangements taking place in solution, a series of variable temperature $^1$H NMR spectra for the chiral macrocycle **(2.10)** were recorded from 295 to 195 K. By examining these spectra, it is apparent that in solution, a structural transition is occurring as a function of temperature, Figure 2.16. Unfortunately, due to solubility issues coupled with the temperature limits imposed on us by the solvent, we were unable to record $^1$H NMR spectra at low enough temperatures to characterize the LS complex. It can be seen that at 295 K the peaks are paramagnetically shifted due to the large fraction of HS molecules in the complex. At 195 K almost all of the peaks become too broad to observe. This could be due to the fluxionality of the molecules as they undergo a transition into the LS state. These results show that it is possible to use NMR spectroscopy as a structural tool to investigate the structural changes accompanying a SCO transition in solution. Furthermore, these are the first studies of the conformational changes that take place for this class of Fe(II) macrocycle in solution.

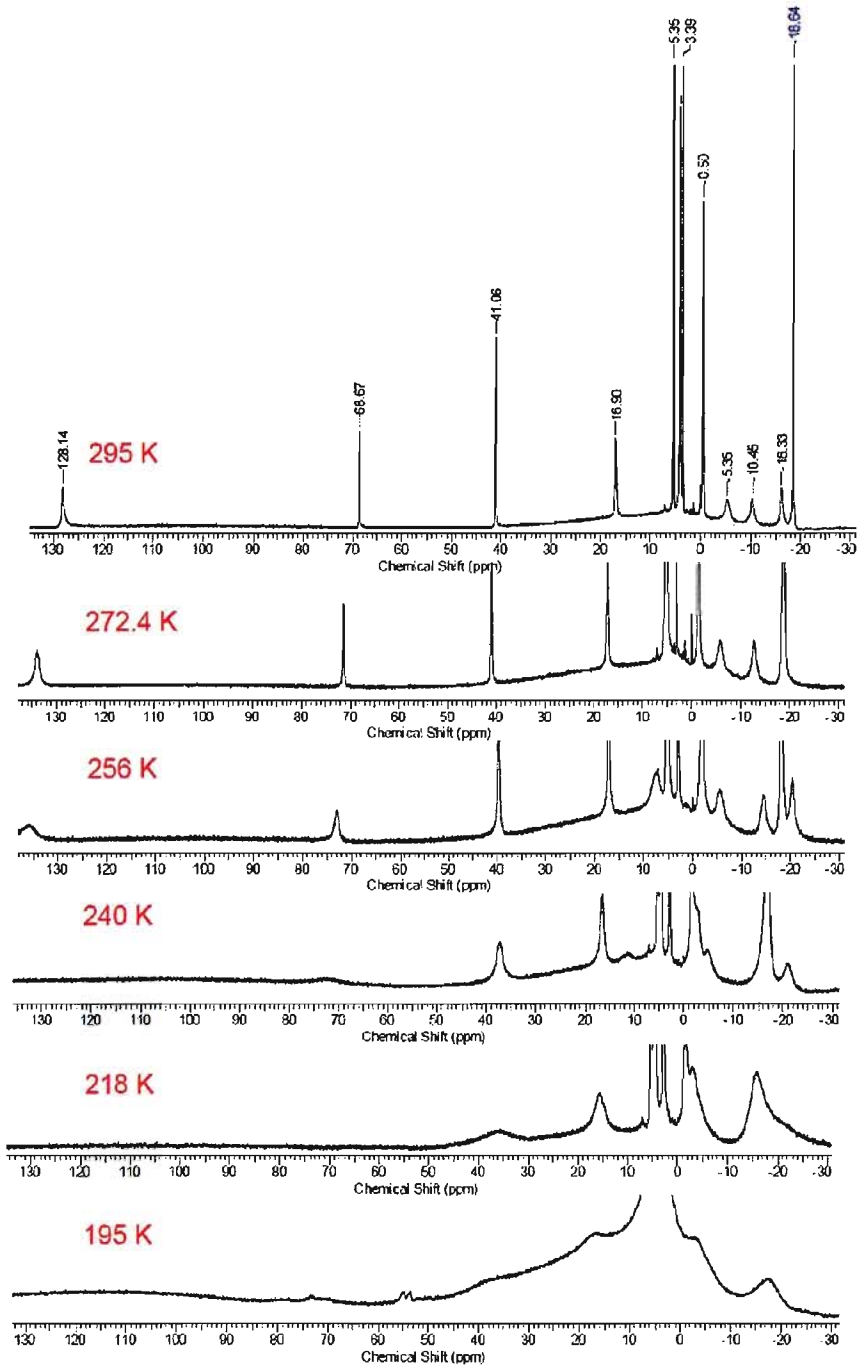


**Figure 2.16:** 600 MHz variable temperature $^{1}$H-NMR spectra of the *S,S* $[Fe(N_3O_2)(CN)_2]$ macrocycle **(2.10)** in $CD_2Cl_2$.

We could further confirm that the *R,R* and *S,S* compounds were enantiomers by comparing their $^{1}$H NMR spectra. A comparison of the $^{1}$H NMR spectra of the two

complexes is shown in Figure 2.17. The only significant difference between the two spectra is the chemical shift of the water, which is at -0.47 ppm for the *S,S* macrocycle **(2.10)**, and -0.36 ppm for *R,R* **(2.9)**. As previously discussed, it remains unclear as to why we have been unable to grow suitable single crystals of the *S,S* enantiomer for X-ray crystallography. Since we were able to fully elucidate the structure of the *R,R* complex by X-ray crystallography, the initial magnetic studies were carried on the *R,R* enantiomer.

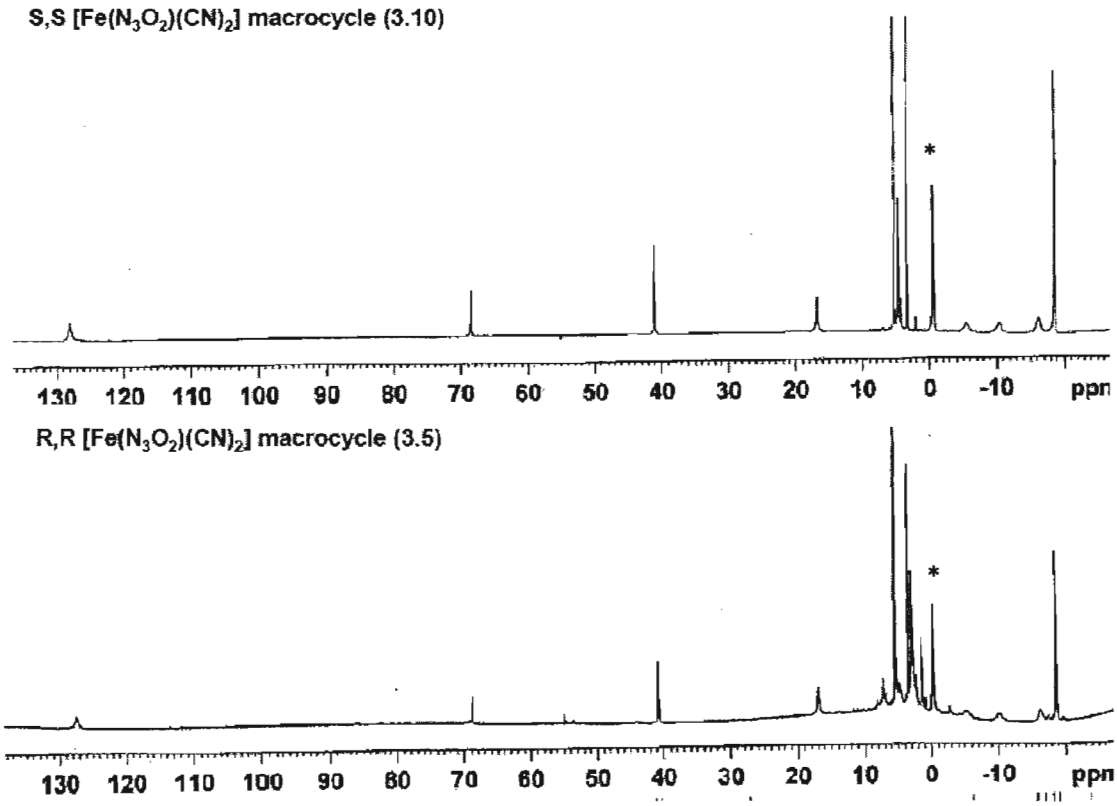


**Figure 2.17:** Comparison of the 600 MHz $^1$H-NMR spectrum of *S,S* $[Fe(N_3O_2)(CN)_2]$ **(2.10)** and *R,R* $[Fe(N_3O_2)(CN)_2]$ **(2.9)** in $CD_2Cl_2$; (*) water.

## 2.7 Preparation and characterization of *racemic* $[Fe(N_3O_2)(CN)_2]\cdot H_2O$ (2.11)

After preparation and characterization of the two enantiomers, the next objective was to prepare the *racemic* complex. The *racemic* complex **(2.11)** was obtained via the

metal templated Schiff-base condensation of a (1:1) *racemic* mixture of the primary diamine together with 2,6-diacetyl pyridine in the presence of $FeCl_2$, followed by ligand exchange as previously discussed. The *racemic* macrocycle $[Fe(N_3O_2)(CN)_2]\cdot H_2O$ **(2.11)** was isolated in 54 % yield as a blue solid, and has been fully characterized. The FAB mass spectrum of **(2.11)** shows a fragment ion at $m/z$ = 509, corresponding to the loss of one axial cyanide ligand from the parent macrocycle $[M\text{-}CN]^+$. The IR spectrum showed a band at 3436 $cm^{-1}$ attributed to the OH str of the water molecule in the crystal lattice. A CN str at 2093 $cm^{-1}$ consistent with a coordinated cyanide ligand and once again, there is also an imine C=N str at 1629 $cm^{-1}$. The CHN data for the *racemic* macrocycle **(2.11)** is within the accepted ±0.4% margin of error for a complex of stoichiometry $[Fe(N_3O_2)(CN)_2]\cdot H_2O$. CD measurements were also carried out on macrocycle **(2.11)** and there was no response, as expected for a *racemic* complex.

### 2.8 Molecular structure of *racemic* $[Fe(N_3O_2)(CN)_2]\cdot 3CH_2Cl_2$ (2.11)

Single crystals of **(2.11)** were obtained via the diffusion of hexane into a DCM solution of the macrocycle. Dark blue needles were obtained after a few days in the refrigerator. A single crystal was mounted on a nylon loop on a copper pin and the crystal was flashed cooled to 200 K. X-ray data was collected on the same crystal at both 200 and 100 K. Unfortunately, the crystals were not stable above 200 K, preventing collection of data at or above room temperature. The molecular structure of **(2.11)** is shown in Figure 2.18. The molecule crystallizes in the monoclinic space group $P2_1/c$, the same space group as the LS parent macrocycle reported by Letard *et al.*[46] In contrast to the chiral macrocycle, only one independent molecule was present in the unit cell. The macrocycle crystallizes along with three dichloromethane solvent molecules. Selected

bond lengths and angles for the *racemic* macrocycle at both 200 and 100 K are presented in Tables 2.8 and 2.9. Examination of the molecular structure of this complex reveals that at both temperatures, the Fe(II) adopts a pentagonal bipyramidal environment with three nitrogen atoms and two oxygen atoms coordinating the Fe(II) centre in the equatorial plane and two axial $CN^-$ ligands. The bond lengths and angles are similar at both temperatures, with the slight decrease in bond lengths at 100 K consistent with thermal contraction. In contrast to the structure of the parent macrocycle, the Fe(II) does not occupy a special position and the two Fe-O bond distances are not equivalent. The distance of the Fe-O bond lengths suggests that at 250 K the Fe(II) centres in the *racemic* macrocycle **(2.11)** adopt a seven-coordinate geometry. The Fe-O distances are shorter than those observed for the seven-coordinate chiral macrocycle **(2.9)**, but longer than the Fe-O distances reported for the original parent macrocycle **(2.1)** at 295 K. The Fe-CN bond lengths at 200 K are 2.175(9) Å and 2.180(10) Å which are slightly longer than the Fe-CN bond lengths determined for both the chiral and the parent macrocycles. At 200 K the $Fe\text{-}N_{imino}$ bond lengths are 2.180(7) and 2.178(7) Å and the $Fe\text{-}N_{pyridine}$ bond length is 2.103(7) Å which are very close to the comparable distances reported for the parent macrocycle. At 200 K the Fe-C-N bond angles are 177.06° and 178.29° decreasing to 176.33° and 176.80° at 100 K.

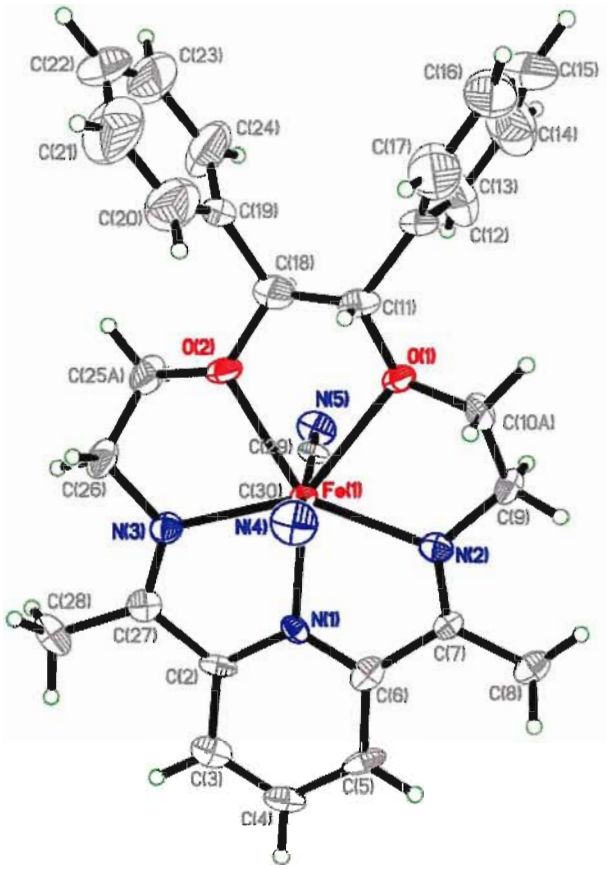


**Figure 2.18:** ORTEP[110] representation of the molecular structure of *racemic* $[Fe(N_3O_2)(CN)_2] \cdot 3CH_2Cl_2$ macrocycle **(2.11)** measured at 200 K. Thermal ellipsoids are plotted at 50%. Solvent molecules are omitted for clarity.

**Table 2.8:** Selected bond lengths (Å) of the *racemic* macrocycle **(2.11)** at 200 and 100 K.

| **Atoms** | **Bond length (Å) 200 K** | **Bond length (Å) 100 K** |
|---|---|---|
| Fe(1)-N(1) | 2.114(7) | 2.110(7) |
| Fe(1)-N(3) | 2.194(7) | 2.175(9) |
| Fe(1)-N(2) | 2.198(7) | 2.188(9) |
| Fe(1)-C(30) | 2.176(9) | 2.181(10) |
| Fe(1)-C(29) | 2.168(10) | 2.188(11) |
| Fe(1)-O(2) | 2.332(5) | 2.327(6) |
| Fe(1)-O(1) | 2.370(6) | 2.358(7) |

**Table 2.9:** Selected bond angles (°) for the *racemic* macrocycle (**2.11**) at 200 and 100 K.

| **Atoms** | **Angles (°) 200 K** | **Angles (°) 100 K** |
|---|---|---|
| N(1)-Fe(1)-N(3) | 72.5(2) | 72.7(3) |
| N(1)-Fe(1)-C(30) | 95.3(3) | 95.0(3) |
| N(3)-Fe(1)-C(30) | 92.6(3) | 92.6(3) |
| N(1)-Fe(1)-C(29) | 95.3(3) | 98.3(3) |
| N(3)-Fe(1)-C(29) | 91.7(3) | 91.9(3) |
| C(30)-Fe(1)-C(29) | 167.1(3) | 166.7(3) |
| N(1)-Fe(1)-N(2) | 72.8(2) | 73.3(3) |
| N(3)-Fe(1)-N(2) | 145.3(3) | 146.0(3) |
| C(30)-Fe(1)-N(2) | 91.5(3) | 91.2(3) |
| C(29)-Fe(1)-N(2) | 91.8(3) | 92.0(3) |
| N(1)-Fe(1)-O(2) | 144.6(2) | 145.1(3) |
| N(3)-Fe(1)-O(2) | 72.2(2) | 72.4(3) |
| C(30)-Fe(1)-O(2) | 84.6(3) | 84.5(3) |
| C(29)-Fe(1)-O(2) | 85.1(3) | 85.0(3) |
| N(2)-Fe(1)-O(2) | 142.5(2) | 141.6(3) |
| N(1)-Fe(1)-O(1) | 145.8(2) | 145.9(3) |
| N(3)-Fe(1)-O(1) | 141.7(2) | 141.4(2) |
| C(30)-Fe(1)-O(1) | 85.5(3) | 85.1(3) |
| C(29)-Fe(1)-O(1) | 83.6(3) | 83.5(3) |
| N(2)-Fe(1)-O(1) | 73.0(2) | 72.6(2) |
| O(2)-Fe(1)-O(1) | 69.59(18) | 69.0(2) |

Examination of the deviation of the ethylene bridged C(9) and C(10) carbon atoms from the $FeO_2$ plane for the two structures reveals no significant conformational changes, Figure 2.19. C(9) and C(10) are on the same side of the $FeO_2$ plane and do not show much of a variation as function of temperature. C(9) is 0.04 Å from the plane and C(10) is 0.661 Å from the plane at 200 K. A similar situation is seen for C(25) and C(26).

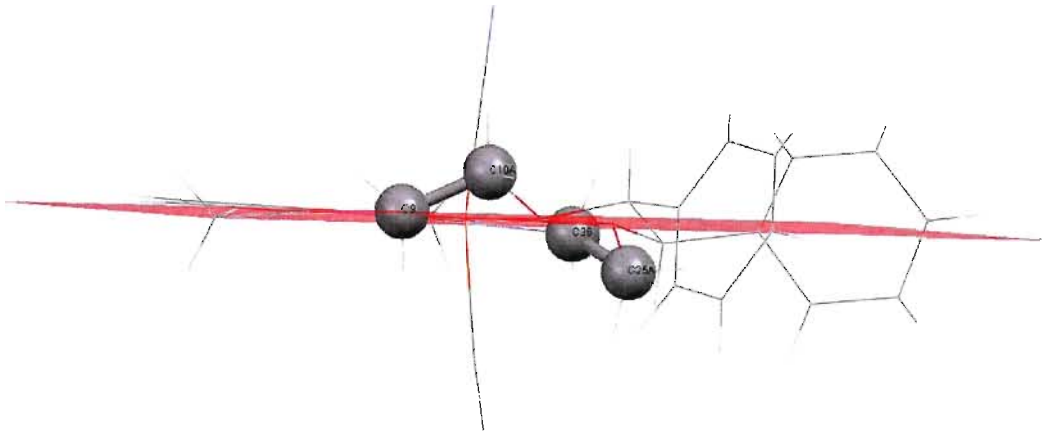

**Figure 2.19:** A view of the O-CH(Ph)-CH(Ph)-O framework of the *racemic* macrocycle **(2.11)**. The $FeO_2$ plane is shown in red.[111]

This behavior is contrary to that observed for both the parent and chiral macrocycles which show significant conformational changes in their solid state structures as the crystals are cooled.

The crystal packing of the *racemic* complex **(2.11)** is shown in Figure 2.20. A view down the *c*-axis of the unit cell reveals the macrocycles crystallize in head-to-head stacks stabilized by π-π interactions between the pyridine rings of adjacent molecules. DCM solvent molecules occupy voids within the crystal lattice and participate in hydrogen bonding interactions. Intermolecular hydrogen bonding interactions range from 2.349 to 2.763 Å. The shortest interactions are between the nitrogen atom of an axial cyanide and a hydrogen atom of a DCM solvent molecule. Also noteworthy is the H-bonding interaction between the nitrogen atom of an axial cyanide ligand and a proton from the pyridine ring. Longer interactions involve the chlorine atom of the DCM solvent molecule being H-bonded to the hydrogen atom of the pyridine ring, but at 100 K this hydrogen bonding interaction is lost. The H-bonding interactions present at both 200 and 100 K are summarized in Table 2.10.

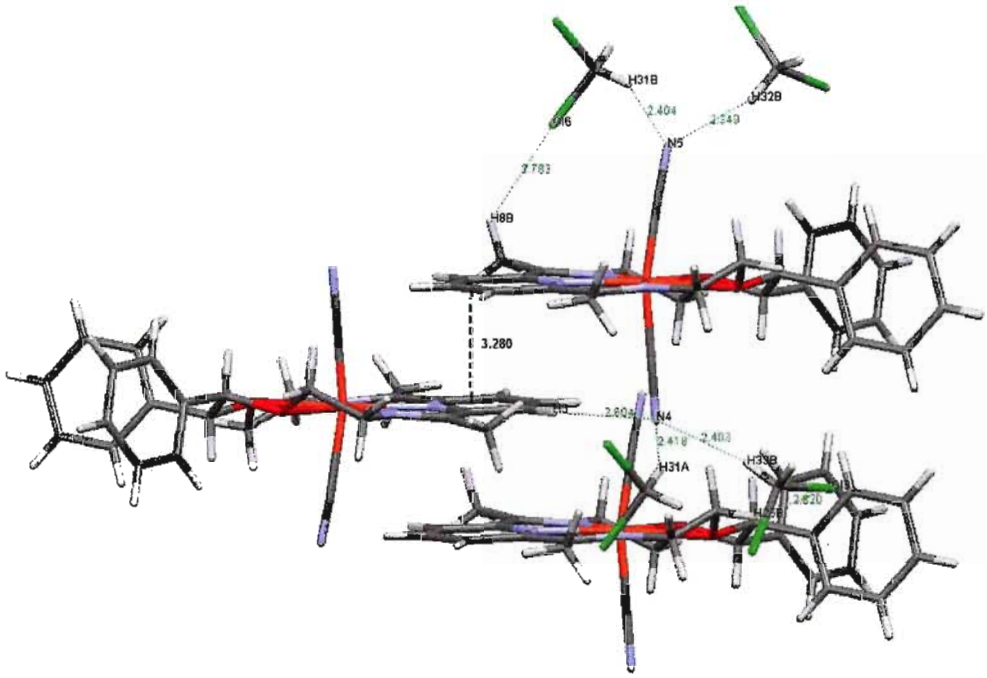


**Figure 2.20:** Significant intermolecular interactions for the *racemic* macrocycle **(2.11)** at 200 K, a view down the *c*-axis. H-bonds are shown in green and π-π interactions are shown in black. Distances are given in Å.

**Table 2.10:** Hydrogen bonding interactions (Å) present in the *racemic* macrocycle **(2.11)** at 200 and 100 K.

| H-bond | Distance at 200 K | Distance at 100 K |
|---|---|---|
| C(31)H(31A)···N(4) | 2.419 | 2.401 |
| C(33)H(33B)···N(4) | 2.403 | 2.386 |
| C(5)H(5)···N(4) | 2.604 | 2.580 |
| C(25)H(25B)···Cl(3) | 2.620 | 2.763 |
| C(8)H(8B)···Cl(6) | 2.763 | ------ |
| C(31)H(31B)···N(5) | 2.404 | 2.342 |
| C(32)H(32B)···N(5) | 2.349 | 2.311 |

At low temperature, the hydrogen bonding interactions involving the axial CN-ligands decrease, but the interactions involving the chlorine atoms of the DCM molecules increase and one is lost. In contrast to the parent macrocycle, no H-bonds or short contacts involving the macrocyclic oxygen atoms were observed; however, the offset π-π

stacking arrangement of the *racemic* macrocycles is consistent with the way in which the HS seven coordinate parent Fe(II) complex **(2.1)** packs at room temperature in the solid state, Figure 2.21.[46]

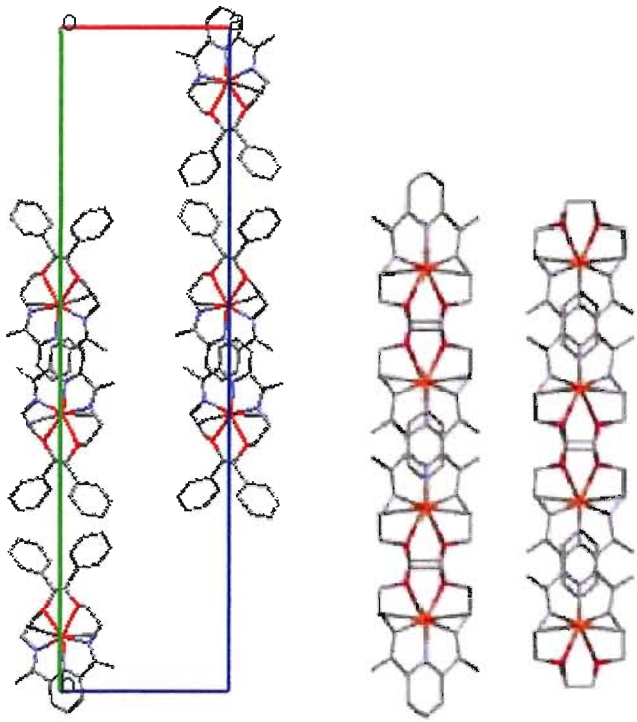

**Figure 2.21:** Packing diagram of the *racemic* $[Fe(N_3O_2)(CN)_2]\cdot 3CH_2Cl_2$ macrocycle **(2.11)** at 100 K, view down the *b*-axis (left); packing diagram of the HS $[Fe(N_3O_2)(CN)_2]$ parent macrocycle **(2.1)** at 298 K (right).[46 111]

The change in volume of both the coordination sphere of the Fe (II) ion and the unit cell on cooling the crystal has been determined from the X-ray data. As noted earlier, the change in volume of the coordination sphere is correlated to a change in volume of the unit cell. At 200 K the volume of the coordination sphere of the *racemic* complex is 17.185 $Å^3$ and at 100 K, the volume decreases slightly to 17.123 $Å^3$. This represents a volume decrease of only 0.4% in comparison to the volume of the coordination sphere of the parent macrocycle **(2.1)** which changes by 40% as a function

of temperature. The unit cell volume of the *racemic* macrocycle decreases from 3706.59 $Å^3$ at 200 K to 3584.39 $Å^3$ at 100 K. This represents a 3.3% decrease in unit cell volume that can be attributed to thermal contraction. Although the diffraction data is consistent with no significant change in the Fe(II) coordination sphere as a function of temperature, we cannot rule out that the HS Fe(II) centre was "frozen in" as a consequence of the flash cooling. Attempts were made to mount the crystals at room temperature and then slowly cool to 200 K, but the crystals were too unstable and broke apart on the diffractometer when mounted at room temperature.

## 2.9 UV-Vis and magnetic studies of *racemic* $[Fe(N_3O_2)(CN)_2]$ (2.11)

UV-Vis studies were carried out to investigate the spin state of the complex in solution. The UV-Vis spectra for **(2.11)** at 298 and 77 K are presented in Figure 2.22. The bands in the spectra very closely resemble those of the chiral complex, with the LS band centered at $\lambda_{max} = 490$ nm increasing in intensity as the complex is cooled. In this respect we conclude that the *racemic* complex most likely undergoes spin crossover in solution.

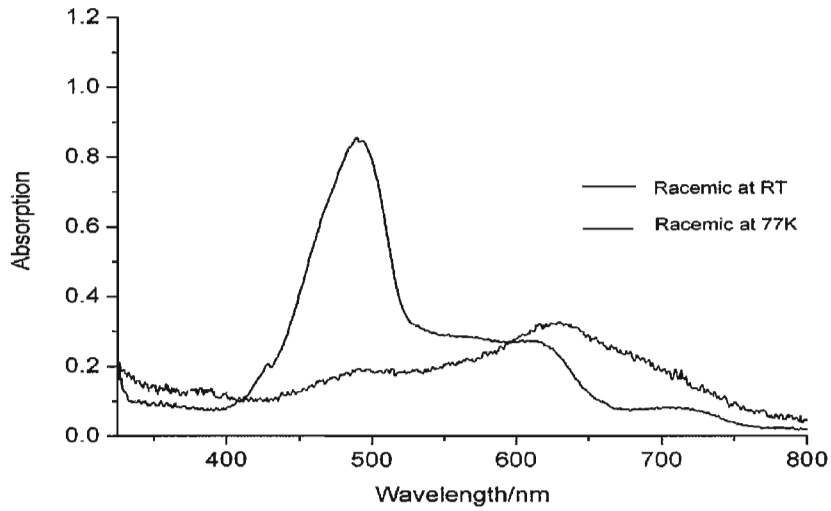


**Figure 2.22:** UV-Vis spectra of the *racemic* $[Fe(N_3O_2)(CN)_2]$ **(2.11)** in ethanol at 298 and 77 K.

To further investigate the magnetic properties of the complex in the solid state, magnetic susceptibility data was collected. Once again the powder was characterized by elemental analysis prior to the susceptibility experiments, where the best fit was obtained for a complex of stoichiometery $[Fe(N_3O_2)(CN)_2]\cdot H_2O$. This is unfortunately different from the single crystals which contain three DCM solvent molecules per formula unit instead of a single water molecule. A plot of $\chi_M T$ *vs* T for **(2.11)** is shown in Figure 2.23. To our surprise, the susceptibility data are not at all consistent with the crystal structure. Taking a mean value of 3.0 $cm^3$ K $mol^{-1}$ for the expected $\chi_M T$ value for the pure HS state, the HS fraction can be estimated to be only about 23% at low temperature which increases only very slightly to 32% at 350 K. This indicates that the majority of the complex is in the low spin S= 0 state, which contradict the findings of the structural studies that point to a HS 7-coordinate complex at both 200 and 100 K. We can only assume that in this case, the molecular structure of the powder is quite different from the single crystal, given that the crystal contains DCM solvent and the powder contains water. A powder diffraction measurement would help to further confirm this since a powder pattern simulated from the single crystal data could be directly compared with the powder diffraction data (provided the powder diffracts). Powder diffraction studies of these complexes are currently in progress as part of a collaboration with the Powell group at the University of Karlsruhe in Germany. Unfortunately, within the timeframe of this project no data has been received to-date.

Photoexcitation measurements were also performed on **(2.11)**. The sample was irradiated at 10 K with a wavelength of 514.5 nm and a power approximately 5 $mW/cm^2$. The magnetization was recorded during irradiation, however, after 30 minutes, no photo-

excitation was observed. In a second experiment, the SQUID was at 3 K and the sample was irradiated 30 minutes with a power of 16 mW/cm$^2$ and a wavelength of 514.5 nm. Despite these changes photo-excitation was not observed.

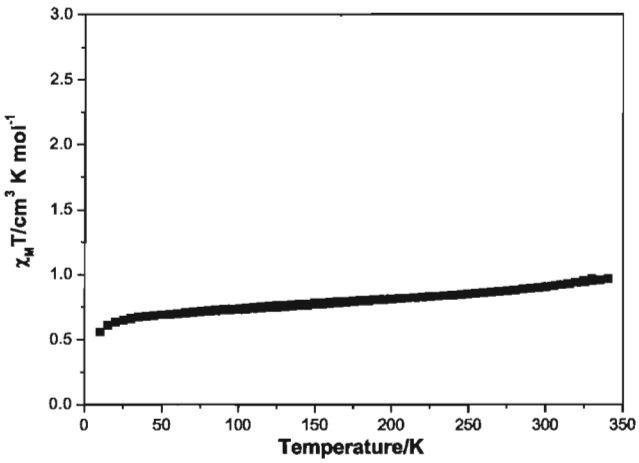


**Figure 2.23:** A plot of $\chi_M$T vs T for the *racemic* macrocycle **(2.11)**.

In order to more accurately determine the percentage occupancy of HS and LS Fe(II) sites in the material, Mössbauer spectra were recorded from 250 - 5 K on a powder sample of **(2.11),** Figure 2.24. Studying the parameters in Table 2.11, it is clear that at low temperatures, the LS complex has an occupancy of 90.4% and the HS complex an occupancy of 9.6%. Above 300 K, there is a small increase in the fraction of HS molecules reaching a maximum occupancy of 16 % HS and 84% LS. These findings are consistent with the magnetic susceptibility data and lead us to conclude that the powder comprises of a predominantly LS complex in which there is a slight increase in the HS component above 300 K. The structural changes that accompany this transition are not clear at this time.

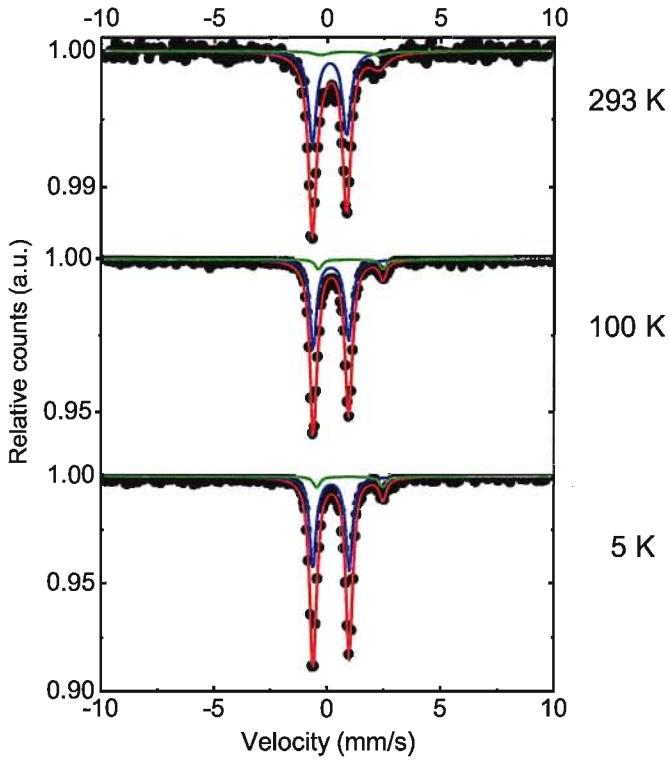


**Figure 2.24:** Mössbauer spectra of a microcrystalline sample of *racemic* $[Fe(N_3O_2)(CN)_2]\cdot H_2O$ **(2.11)** from 293- 5 K; HS Fe(II) (green line); LS Fe(II) (blue line).

**Table 2.11:** Mössbauer parameters for the *racemic* macrocycle **(2.11)**.

| T (K) | $\delta^*$ (mm/s) | $\Delta E_Q$ (mm/s) | Fe occupancy (%) | $Fe^{2+}$ spin state |
|---|---|---|---|---|
| 5 | 0.281(2) | 1.580(4) | 90.4 | Low |
| | 1.007(6) | 2.93(3) | 9.6 | High |
| 50 | 0.275(1) | 1.572(3) | 91 | Low |
| | 1.15(2) | 2.87(3) | 9 | High |
| 100 | 0.270(1) | 1.576(3) | 91 | Low |
| | 1.14(1) | 2.85(3) | 9 | High |
| 150 | 0.257(3) | 1.577(5) | 92.3 | Low |
| | 1.12(2) | 2.93(4) | 7.7 | High |
| 200 | 0.239(4) | 1.554(7) | 92 | Low |
| | 1.00(3) | 2.75(6) | 8 | High |
| 250 | 0.196(5) | 1.530(9) | 91 | Low |
| | 1.00(4) | 2.69(9) | 9 | High |
| 293 | 0.197(2) | 1.534(5) | 84 | Low |
| | 1.09(3) | 2.38(6) | 16 | High |

## 2.10 Preparation of *meso* (4,5)-4,5-diphenyl-3,6-dioxa-1,8-octanediamine (2.8)

The *meso* primary diamine **(2.8)** was prepared from commercially available *meso*-hydrobenzoin **(2.14)**, following the strategy presented in Scheme 2.2. In this case the phenyl rings are oriented in a *cis* manner, making this compound more sterically hindered than the chiral and *racemic* derivatives.

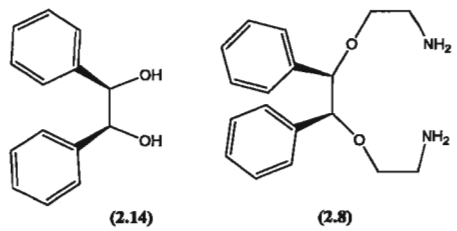


(2.14) (2.8)

**Figure 2.25:** Molecular structures of *meso*-hydrobenzoin **(2.14)** and (4,5)-4,5-diphenyl-3,6-dioxa-1,8-octanediamine **(2.8)**.

The *meso* diamine **(2.8)** was isolated as a yellow oil in a 4% overall yield and has been fully characterized. The FAB mass spectrum shows the parent peak $[MH]^+$ at $m/z$ = 301, which is consistent with its molecular structure. The microanalysis data was the best fit for $(C_{18}H_{24}N_2O_2)\cdot 1.5H_2O$. The IR spectrum contains two NH str at 3358 and 3323 $cm^{-1}$ for the primary diamine, and a C-O str at 1106 $cm^{-1}$ for the ether linkage. The $^1H$ NMR spectrum of the *meso* compound is slightly different compared to the *R,R* enantiomer **(3.4)**. Since the phenyl rings are now oriented *cis* with respect to each other, they appear as a multiplet centered at 7.38 ppm. Characterization of the rest of the ligand is straightforward. The CH protons at C-3 are assigned to the singlet at 4.30 ppm. The two multiplets at 3.37 ppm and 3.08 ppm are assigned to the $CH_2$ protons at C-2, and the multiplet at 2.62 ppm is consistent with the $CH_2$ protons at C-1. Finally the $NH_2$ protons

can be seen as a broad peak at 1.25 ppm. The $^{13}C$ NMR spectrum of the *meso* diamine **(2.8)** contains 6 peaks which have also been fully assigned.

## 2.11 Preparation and characterization of *meso* $[Fe(N_3O_2)(CN)_2]\cdot H_2O$ (2.12)

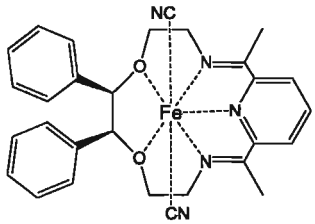


(2.12)

The *meso* macrocycle **(2.12)** was prepared following the synthetic strategy previously described for the preparation of the chiral and *racemic* complexes. The desired complex was isolated as a purple solid in 54% yield and has been fully characterized. The FAB mass spectrum shows a fragment ion at $m/z$ = 509, corresponding to the loss of one axial cyanide ligand from the parent ion $[M\text{-}CN]^+$. The IR spectrum contains an OH stretch at 3536 $cm^{-1}$ attributed to the presence of water in the complex. A CN stretch at 2094 $cm^{-1}$ is present for the axially coordinated cyanide ligands. There is a peak at 1636 $cm^{-1}$ for the C=N imine str and a band at 1129 $cm^{-1}$ corresponding the C-O str of the ether functionality. The microanalytical data was the best fit for a complex of stoichiometry $[Fe(N_3O_2)(CN)_2]\cdot H_2O$. A small amount of the complex was dissolved in ethanol and the vial was cooled in liquid nitrogen. No noticeable color change was observed and based on previous observations for the chiral and *racemic* complexes, the pink/purple color of the solution was indicative of a low spin complex.

## 2.12 NMR spectroscopic characterization of *meso* $[Fe(N_3O_2)(CN)_2]$ (2.12)

Unfortunately, growing suitable single crystals of the *meso* complex has proven to be difficult and thus we have been unable to elucidate its solid state structure. Given that the colour of the complex hinted that it was likely a low spin complex, and as such we proposed to characterize its molecular structure in solution by NMR spectroscopy. The $^1H$ NMR spectrum of the *meso* complex **(2.12)** was measured and we have attempted to assign the spectrum with the help of a series of 2-D, HSQC and COSY experiments. The $^1H$ NMR spectrum of **(2.12)** is shown in Figure 2.26. Ten peaks can be seen from $\delta_H$ 2.2 ppm to 8.6 ppm which is consistent with a LS Fe(II) complex. The number of peaks is consistent with a symmetrical complex. Since a 7-coordinate geometry is consistent with a HS Fe(II) centre, it seems reasonable to assume that a 5-coordinate geometry is more likely, since the 6-coordinate geometry would not generate a symmetrical structure as the two Fe-O distances would be inequivalent. The pyridine protons at C-1 and C-2 are assigned to the broad peaks at 8.86 and 8.68 ppm, respectively. The two broad peaks at 7.19 and 7.03 ppm are assigned to the aromatic protons on C-11, C-12, C-13, and C-10 and C-14, respectively. The CH proton on C-8 is assigned to the peak at 5.56 ppm. There is some ambiguity in the assignment of the $CH_2N$ and the $CH_2O$ protons since without X-ray data it is difficult to differentiate between their axial and equatorial protons. The axial and equatorial $CH_2N$ protons at C-6 are assigned to the peaks at 6.75 or 4.44 ppm. The axial and equatorial $CH_2O$ protons at C-7 are assigned to the peaks at 4.04 or 3.84 ppm. Looking at the chemical shifts of the ethylene protons in the $^1H$ NMR spectrum provides us with more evidence that the *meso* complex is very likely close to 5-coordinate in solution. In this respect, the $CH_2O$ protons appear in the expected range

and are both upfield and so it is very likely that these protons are not close to the Fe(II) centre. In comparison, the $CH_2N$ protons are assigned to a peak more downfield since these protons may be slightly deshielded by the Fe(II) centre. Finally, the $CH_3$ protons at C-5 are assigned to the singlet at 2.20 ppm.

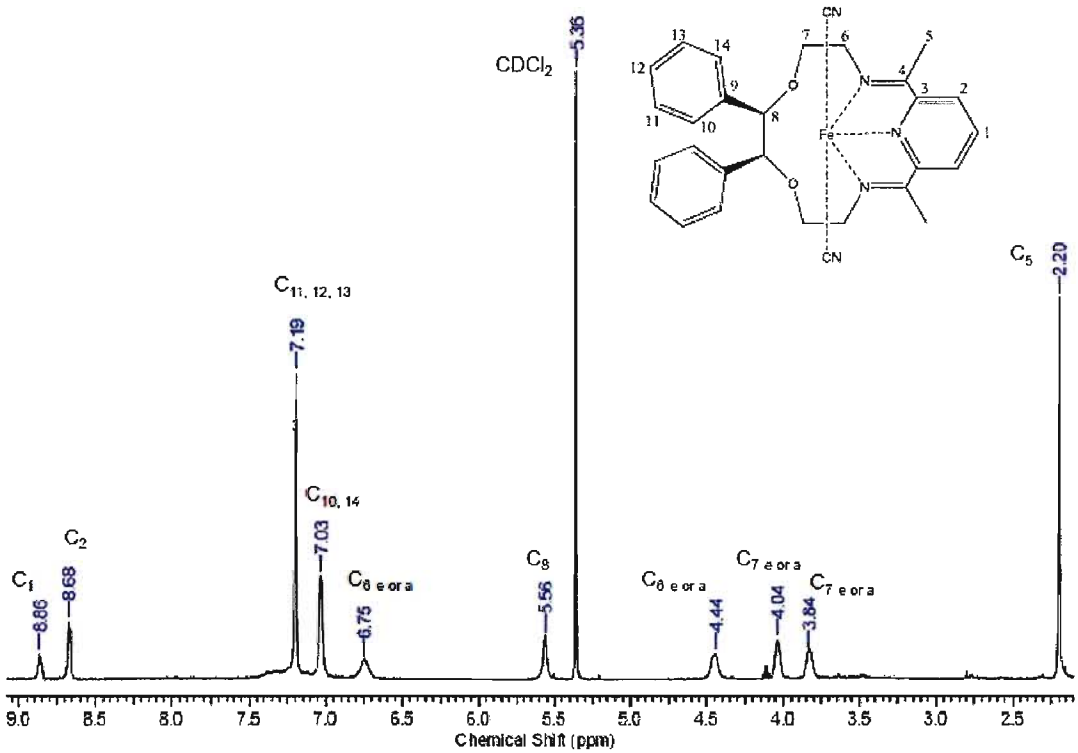


**Figure 2.26:** 600 MHz $^1$H-NMR of *meso* $[Fe(N_3O_2)(CN)_2]$ **(2.12)** in $CD_2Cl_2$ at 295 K; The subscripts *e* and *a* refer to equatorial and axial protons, respectively.

Complex **(2.12)** was also characterized by $^{13}$C NMR spectroscopy. A tentative assignment of the $^{13}$C NMR data has been made with the assistance of HSQC 2-D experiments. The spectrum contains 12 peaks consistent with a 5-coordinate Fe(II) LS complex. The peak at 160.8 ppm is assigned to the coordinated cyanides. The peak at 151.1 ppm is assigned to the imine carbon C-4. The pyridine carbons C1-C3 are present

at 135.4 and 124.3 ppm. The phenyl carbons C9-C14 are assigned to the peaks at 136.9, 129.9, 127.9, and 127.6 ppm. The carbon at C-8 is assigned to the peak 81.6 ppm. The $CH_2O$ and $CH_2N$ carbons at C-6 and C-7 are assigned to the peaks at 67.6 and 50.8 ppm, respectively. Finally the peak at 27.2 ppm is assigned to the $CH_3$ carbon at C-5. $^1$H-NMR spectra were also recorded at various intervals starting at 295 K and decreasing the temperature to 190 K, Figure 2.27. As the temperature decreases the signals become broader and the peaks corresponding to the $CH_2O$ and $CH_2N$ protons are visibly shifted. It is possible that the complex rearranges from a LS 5- to a LS 6-coordinate geometry at low temperature, thus accounting for the additional peaks present in the spectrum at 190 K. Unfortunately, sufficiently low temperature measurements were not possible, making it difficult to fully characterize or determine the thermodynamic parameters for this conformational change in solution.

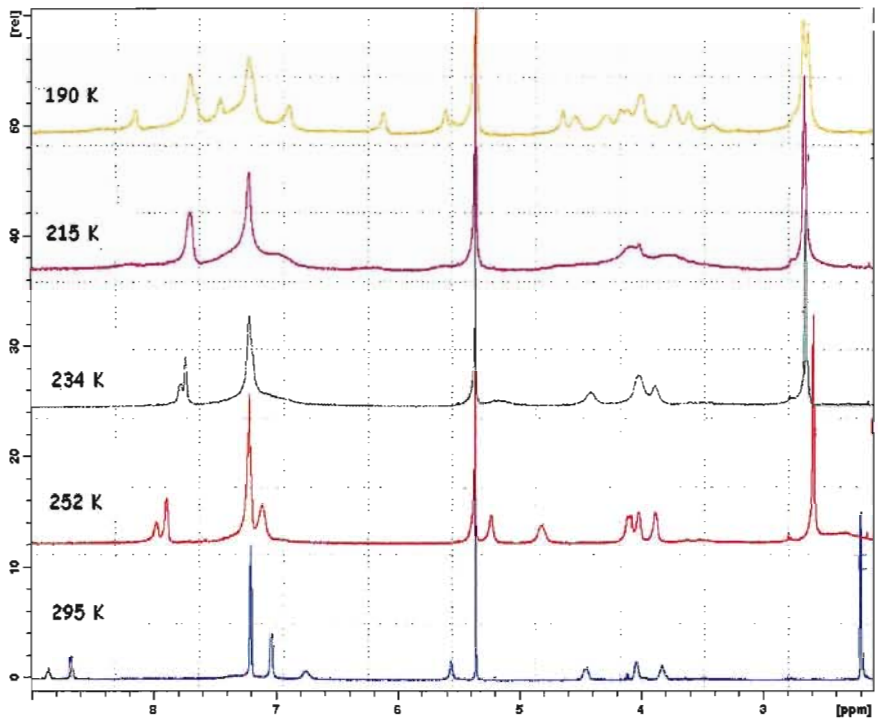


**Figure 2.27:** 600 MHz $^1$H-NMR spectra of the *meso* $[Fe(N_3O_2)(CN)_2]$ complex **(2.12)** in $CD_2Cl_2$ from 295 to 190 K.

Geometry optimization DFT calculations were carried on the *meso* complex by Dr. V. Polo at the University of Zaragoza, Spain. These calculations confirm the conclusions drawn from the assignments of the NMR spectra: that the most favorable conformation is a LS 5-coordinate Fe(II), Figure 2.28. It was determined for the seven coordinate HS state that both oxygen atoms must lie on the same plane as the Fe(II) and nitrogen atoms giving rise to a much more strained geometry. In this respect, the HS state is expected to be more unstable due to steric interactions involving the phenyl rings and the axial cyanide ligands.

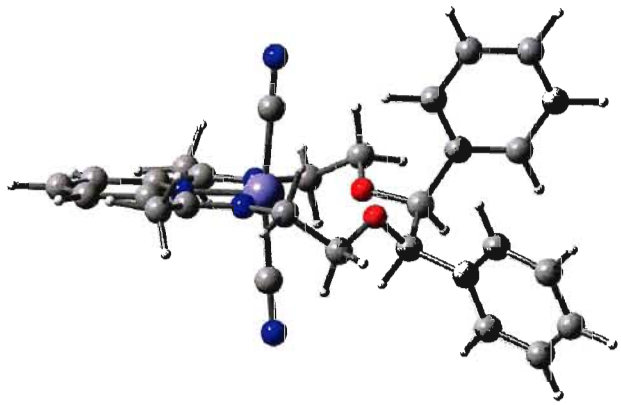

**Figure 2.28:** B3LYP/SDD 6-31G(d) optimized geometry for the *meso* macrocycle **(2.12)**.

## 2.13 UV-Vis and magnetic studies for *meso* $[Fe(N_3O_2)(CN)_2]$ (2.12)

The UV-Vis spectrum of **(2.12)** is shown in Figure 2.29. Measurements were carried out in an ethanol solution at room temperature and 77 K. In contrast to the UV-Vis data for the chiral and *racemic* complexes, the UV-Vis spectrum of the *meso* complex does not change significantly with temperature and the band at $\lambda_{max}$ = 500 nm which is present at both temperatures, is consistent with a predominantly LS complex.

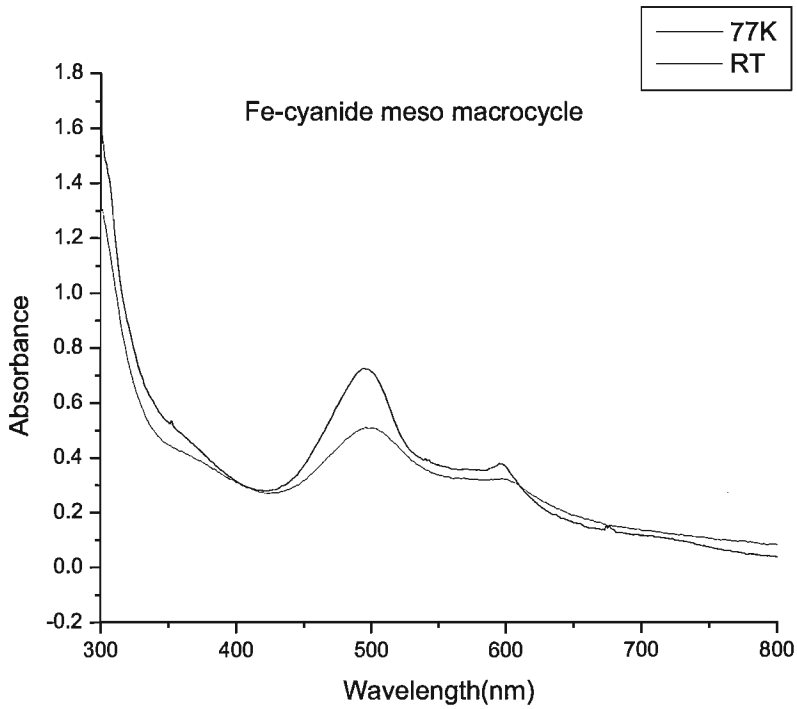


**Figure 2.29:** UV-Vis spectra of the *meso* macrocycle **(2.12)** in ethanol at room temperature (red line) and 77 K (black line).

Magnetic susceptibility experiments were carried out on a powder sample of **(2.12)**. The $\chi_M T$ *vs* T plot shows a straight flat line over a large temperature range indicating that the complex does not exhibit any SCO behavior and is therefore mostly diamagnetic from 10 – 300 K. This result is further supported by the Mössbauer data presented in Figure 2.30. As the complex is cooled from 293 to 5 K, it can be seen that the Fe(II) remains low spin. These results are consistent with the LS Fe(II) of the parent macrocycle **(2.1)**.[109] High resolution powder data for complex **(2.12)** were collected on the powder diffractometer at the University of Windsor. The data shows that the powder is microcrystalline (see Appendix), but although the powder pattern has been indexed, it has not proved possible to solve the structure to date.

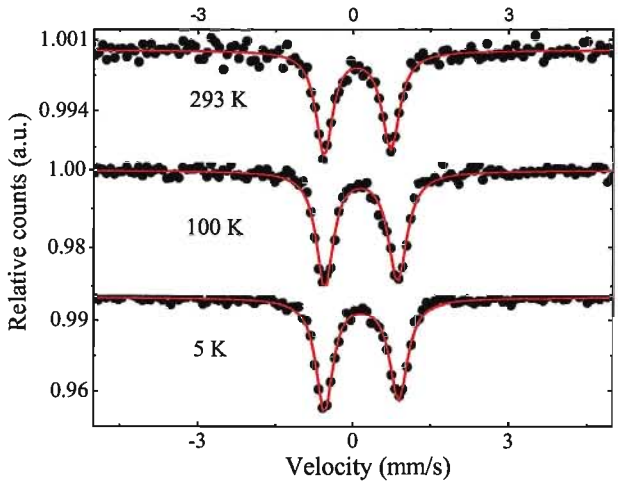


**Figure 2.30:** A series of Mössbauer spectra for the *meso* macrocycle **(2.12)** from 293 to 5 K.

## 2.14 Preparation and characterization of three novel chiral building blocks: *R,R* $[M(II)(N_3O_2)X_2]$ (where M = $Fe^{2+}$, $Mn^{2+}$; X= Cl, $ClO_4^-$).

In addition to studying the spin crossover properties of the Fe(II) complexes, the long term goals of this research are to use the macrocycles as building blocks for the self-assembly of chiral magnets. Given that a series of interesting clusters, chains, and networks have been assembled from the parent $[M(II)(N_3O_2)X_2)]$, macrocycles (where M = $Fe^2$ , $Mn^{2+}$ and X = $Cl^-$ ,$ClO_4^-$), we employed literature strategies for the preparation of new materials from our chiral building blocks. In this respect, the strategy most commonly adopted is to use the cyanide ligands of hexacyanometallate building blocks as linkers between macrocycles.[48, 51]

Following this methodology, we prepared and characterized chiral Fe(II) and Mn(II) and $[M(II)(N_3O_2)CN_2]$ building blocks and attempted to self-assemble these macrocycles together with a second building block, $K_4[Fe(CN)_6]\cdot 3H_2O$. This was achieved experimentally via liquid-liquid diffusion experiments that involved (i) the

layering of a solution of the macrocycle over the top of an aqueous solution of $K_4[Fe(CN)_6]\cdot 3H_2O$ in a test tube[48] and (ii) by placing an aqueous solution of the $K_4[Fe(CN)_6]\cdot 3H_2O$ on one side of an H-tube and a solution of the macrocycle in methanol or acetonitrile in the other side of the H-tube and then allowing them to slowly diffuse together through a frit.[51] Unfortunately, the purification and characterization of any powders obtained from in these experiments was difficult and optimal experimental conditions for the growth of single crystals of the cyanide bridged materials have not yet been found to-date. The second methodology employed was the slow diffusion of a methanol or acetonitrile solution of the macrocycle into an agar gel containing $K_4[Fe(CN)_6]\cdot 3H_2O$.[119] Initially attempts were made to assemble the *bis* $CN^-$ macrocycles **(2.9)**, **(2.10)**, **(2.11)**, and **(2.12)** together with $K_4[Fe(CN)_6]\cdot 3H_2O$, but so far this has not been successful. Instead, we prepared macrocycles with labile axial $ClO_4^-$, $H_2O$ and $Cl^-$ ligands. In this respect, perchlorate and chloride derivatives of the Fe(II) and Mn(II) macrocycles were also prepared and characterized. The Fe(II) perchlorate macrocycle was prepared following the synthetic procedure shown in Scheme 2.1, from 2,6-diacetylpyridine and (4R,5R)-4,5-diphenyl-3,6-dioxa-1,8-octanediamine ligand **(2.6)** in the presence of $FeCl_2$. Once the macrocycle was formed the axial chloride ligands were then exchanged for $ClO_4^-$ via the addition of an ethanol solution of the macrocycle into an aqueous solution containing a large excess of $NaClO_4$. Following this strategy, a complex of stoichiometry $[Fe(N_3O_2)(ClO_4)(H_2O)]ClO_4\cdot 4H_2O$ **(2.15)** was isolated as a green-blue solid. The FAB mass spectrum of **(2.15)** has a peak at $m/z = 582$ which is consistent with the fragment ion $[Fe(N_3O_2)(ClO_4^-)]^+$. The IR spectrum has an imine C=N str at 1647 $cm^{-1}$ and a C-O str at 1084 $cm^{-1}$. The spectrum also has a broad band at 3493 $cm^{-1}$ attributed

to the OH str. It has previously been established that it is possible to characterize the binding mode of a perchlorate ligand from characteristic Cl-O bands in the IR spectrum.[120] Looking at the stretching frequencies of the Cl-O str and the Cl-O-M (M = metal ion) str reveals whether or not the perchlorate is a counterion, or coordinating monodentate, or bidentate to a metal centre.[120] For the macrocyclic complex **(2.15)**, it was clear that the ClO-M str at 1052 $cm^{-1}$ is characteristic for a monodentate coordinating perchlorate ligand. The Cl-O str present at 940 $cm^{-1}$ and the $ClO_3$ bend at 627 $cm^{-1}$ are also consistent with the stretching frequencies of a mondentate coordinating perchlorate ligand.[41, 120] The microanalytic data is a good fit for $Fe(N_3O_2)(ClO_4)(H_2O)]ClO_4 \cdot 4H_2O$.

Attempts were made to prepare the *R,R* $[Mn(N_3O_2)Cl_2]$ macrocycle via templating the Schiff-base condensation of the diamine and the diketone with $MnCl_2 \cdot 4H_2O$. A red powder was isolated from the reaction mixture. The powder was dissolved in acetonitrile and single crystals were grown via the slow evaporation of solvent at room temperature.

X-ray crystallography data was collected at 100 K. It should be noted that the structure refinement was non-trivial. The structure contained electron density due to disordered solvent that was removed by applying the SQUEEZE command in PLATON.[121] The complex crystallizes in the chiral monoclinic space group $P2_1$. There are four independent macrocycles in the unit cell, two macrocycles have two monodentate axially coordinated chloride ligands and two macrocycles have one axial monodentate chloride ligand, and a second bidentate chloride ligand that bridges to a $MnCl_3$, unit, Figure 2.31. In order to rationalize the formation of this compound, we propose that during the reaction, oxidation of some of the $Mn^{2+}$ ions has taken place. This seems feasible given that the reaction was carried out in air and $Mn^{2+}$ is known to readily

oxidize to $Mn^{3+}$ in the presence of certain ligands.[122] In all four macrocycles the Mn(II) ions are 7-coordinate, chelated by the ($N_3O_2$) ligands in the equatorial plane with two axial chloride ligands completing the pentagonal bipyramidal geometry. The closest Mn···Mn distances are 4.837 Å through a bridging chloride between a Mn(2) and Mn(5). The closest through space Mn···Mn interactions are 5.371 Å between Mn(1) and Mn(5), Figure 2.31.

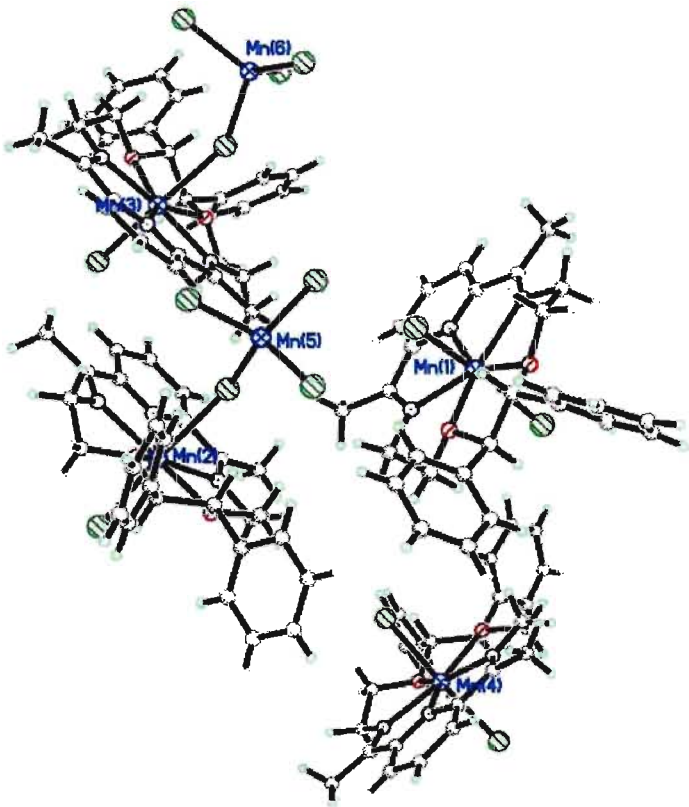


**Figure 2.31:** Plot of the molecular structure of $\{[Mn(N_3O_2)Cl_2][Mn(N_3O_2)Cl(MnCl_3)]\}_2$.

A view of the crystal packing of the complex down the *c*-axis is shown in Figure 2.32. The molecules stack in a head-to-head arrangement. Macrocycles containing *bis* chloride ligands alternate with the macrocycles that are bridged to a $MnCl_3$ unit. There are π-π stacking interactions between a set of three macrocycles within a stack, shown by

dashed lines in Figure 2.32. There are short contacts involving the chloride ligands and the protons of the phenyl and pyridine rings (Cl···H-C = 2.731-2.926 Å) and with the ethylene bridge protons (Cl···H-C = 2.663 Å).

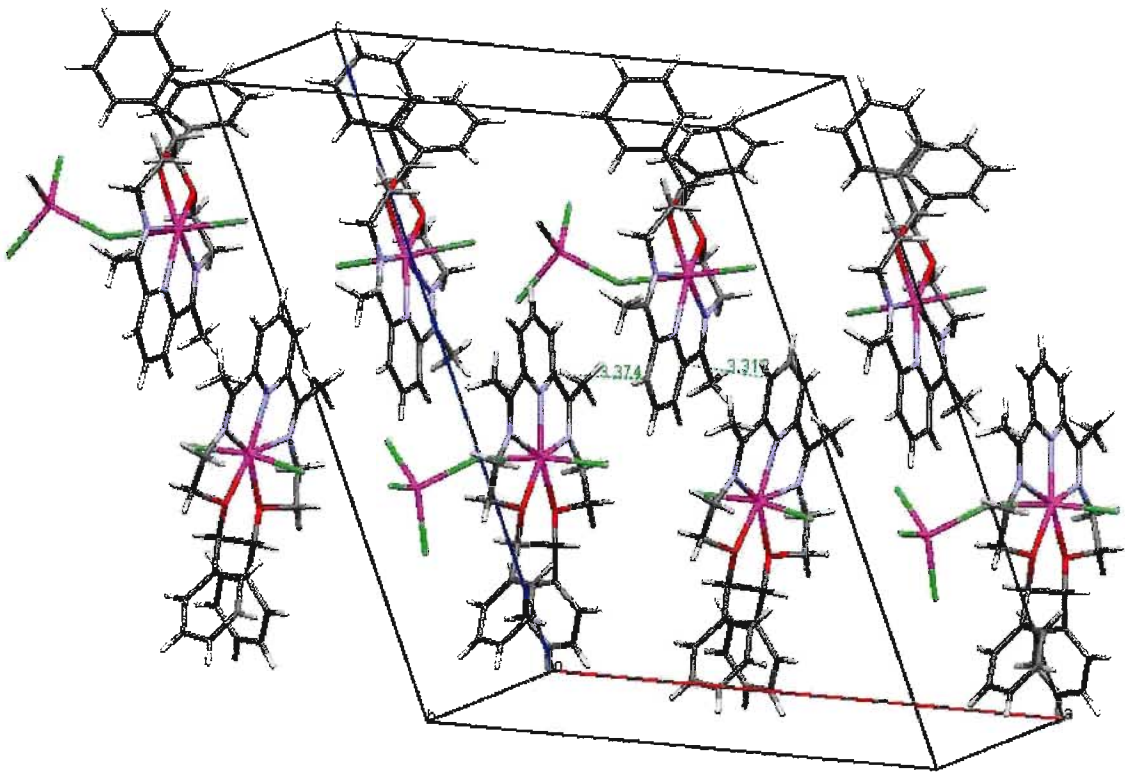

**Figure 2.32:** Packing diagram of $\{[Mn(N_3O_2)CL_2][Mn(N_3O_2)Cl(MnCl_3)]\}_2$. A view down the *c*-axis.[111]

This crystal structure demonstrates that with the appropriate choice of axial ligands the macrocycles can link to a second auxiliary paramagnetic building block. This result is encouraging for the formation of chains and networks from these building blocks. The challenge remains to obtain suitable single crystals to facilitate the characterization of these materials. Magnetic studies of complex **(2.16)** are in progress.

The Mn(II) perchlorate derivate was prepared via ligand exchange via the addition of an ethanol solution of **(2.16)** to an excess of $NaClO_4$ in ethanol. The *R,R*

complex $[Mn(N_3O_2)(ClO_4)(Cl)]$ **(2.17)** was isolated as a pale yellow solid in 64% yield and fully characterized. In this case only one of the chloride ions was exchanged for a perchlorate. The FAB mass spectrum shows a peak at *m/z* = 535 corresponding to the fragment ion $[Mn(N_3O_2)(Cl)(H_2O)]^+$ and additional peaks at *m/z* = 599 and 581 for $[Mn(N_3O_2)\ (ClO_4)(H_2O)]^+$, and $[Mn(N_3O_2)(ClO_4)]^+$, respectively. The IR spectrum contains a broad OH str at 3434 $cm^{-1}$ consistent with the presence of water molecules in the crystal lattice. An imine C=N str at 1647 $cm^{-1}$ and an ether C-O str at 1082 $cm^{-1}$ are also present. As previously discussed, the position of the ClO-M bend is indicative of the coordination mode of the ligand.[120] The ClO-M bend is observed at 1116 $cm^{-1}$ and is thus consistent with a monodentate coordinated perchlorate ligand.[120] Two additional bands observed at 921 and 628 $cm^{-1}$ are also consistent with the Cl-O and $ClO_3$ str modes of a monodentate coordinated perchlorate ligand.[120] The microanalytical data is in good agreement with the formula $[Mn(N_3O_2)(Cl)(ClO_4)]\cdot 8H_2O$. Since initially only one perchlorate ligand was chelated to the Mn centre, attempts were made to exchange the second chloride ligand. This was carried out by adding an additional excess of $NaClO_4$ in ethanol, to a solution of **(2.17)** in ethanol and heating the reaction mixture a second time to 60°C. Due to the danger of heating perchlorate salts, the temperature was not increased past 60°C and no changes were observed in the IR spectrum.

Once these complexes were prepared, a series of small scale exploratory reactions were carried out in an attempt to grow single crystals of cyanide bridged materials. Liquid–liquid and liquid-gel diffusion methodologies previously described were once again employed.[48 51] In the first set of experiments, a solution of macrocycles **(2.15)** and **(2.17)** were slowly diffused into a an aqueous solution of $K_4[Fe(CN)_6]\cdot 3H_2O$. A range of

solvents were used for the *R,R* macrocycles, but for solubility reasons, the cyanometallate salt was always dissolved in water. Liquid-liquid and liquid-gel diffusion experiments were carried out using a (2:1) ratio of the Fe(II) hexacyanometallate salt to the *R,R* macrocycle. Unfortunately, to-date no suitable single crystals have been obtained. A dark green powder was isolated from the H-tube diffusion of an acetonitrile solution of *R,R* macrocycle **(2.15)** together with an aqueous water solution of $K_4[Fe(CN)_6]\cdot 3H_2O$ . Initial characterization of the powder was carried out through FAB-MS and IR spectroscopy. The FAB mass spectrum shows a parent peak at *m/z* = 582 corresponding to the loss of an axial water ligand, $[Fe(N_3O_2)\ ClO_4]^+$. The IR spectrum has peaks at 2187, 2116 and 2046 $cm^{-1}$ consistent with the presence of $CN^-$ ligand stretches.[48] Coordinated $CN^-$ ligand stretches usually appear between 2200-2000 $cm^{-1}$, and the $K_4[Fe(CN)_6]\cdot 3H_2O$ $CN^-$ stretches usually appear at 2098, 2062 and 2044 $cm^{-1}$. [48] It has been determined that if the M-CN group forms a M-CN-M' type bridge, the $CN^-$ str shifts to a higher frequency.[123] For the most part there appears to be an increase in the $CN^-$ stretches seen here for the $Fe^{II}$-CN-$Fe^{II}$ chain in comparison to the original $K_4[Fe(CN)_6]\cdot 3H_2O$ complex. The bands at 1640 and 1082 $cm^{-1}$ are consistent with C=N and C-O str for the imine and ether functionality of the macrocycle.

## 2.15 Conclusion and outlook

To conclude, four novel $[Fe(N_3O_2)(CN)_2]$ macrocycles have been prepared and characterized. We have determined via CD measurements and $^1H$ NMR studies that the *R,R* and *S,S* macrocycles **(2.9)** and **(2.10)** are enantiomers. The structure and magnetic properties of the *R,R* macrocycle are consistent with the presence of both LS and HS molecules at room temperature, and the complex undergoes a spin crossover transition on

cooling in the solid state. Magnetic susceptibility and Mössbauer measurements support these observations. This complex is the first example of a chiral SCO complex to display a LIESST effect. DFT calculations for **(2.9)** reveal that the 6- and 7-coordinate geometries are energetically very similar. After careful analysis of the structural properties of this macrocycle we conclude that due to the phenyl substituents appended to the chiral centers, the macrocycle may not be able to undergo the 7- to 6-coordinate conformational change initially reported for the parent macrocycle **(2.1)**. This might also help to account for the small LIESST. In our case, the spin crossover might be attributed to a change in geometry from 7- to 5-coordinate. The crystal structure of the *S,S* complex **(2.9)** has not yet been determined, however, its solution structure has been elucidated by NMR spectroscopy and found to be consistent with a HS 7-coordinate complex at room temperature that undergoes conformational changes on cooling. The *racemic* macrocycle **(2.11)** has been prepared and characterized and the X-ray crystal structure of the complex reveals that it is 7-coordinate at both 200 and 100 K, with no significant changes in geometry on cooling in the solid state. Magnetic susceptibility and Mössbauer data collected on a powder sample of the complex are not consistent with the X-ray crystal data and show that the complex is predominantly in the LS state with only a slight increase in its HS fraction around 300 K. In contrast, the UV-Vis data for this complex is consistent a SCO in solution. Finally, the *meso* complex **(2.12)** has been prepared and characterized. Although we were not able to determine its molecular structure by X-ray crystallography, the NMR spectra are consistent with a five-coordinate LS Fe(II) complex that also undergoes conformational changes on cooling. The UV-Vis results indicate that in solution at room and low temperature, the complex contains a large

portion of LS molecules. This is supported by magnetic susceptibility and Mössbauer data that are also consistent with a diamagnetic LS Fe(II) complex from 300 to 10 K. It seems reasonable to suggest that the bulky *cis* phenyl groups are preventing the macrocycle from adopting the higher coordination geometry associated with the HS Fe(II) complex.

This is the first time the structural and magnetic properties have been elucidated for a family of spin crossover macrocycles comprised of both structural and stereo-isomers. It is apparent that the chiral and *racemic* complexes exhibit different structures and magnetic properties in the solid state. It seems that at least for the *racemic* complex, the structural and magnetic properties are significantly altered by the solvent molecules in the crystal lattice.[124] Powder diffraction measurements on all four complexes are currently in progress to determine the structural differences between the powder and the single crystals. Magnetic susceptibility measurements on single crystals of all four complexes are also in progress as part of collaboration with the Powell group at the University of Karlsruhe, Germany. Unfortunately, no susceptibility data for the single crystals have been received to-date. Changing the spatial position of the functional groups greatly affects their spin crossover properties. It is also apparent that the phenyl rings might be too bulky to enable the molecule to undergo any useful light-induced spin crossover. In this respect, synthetic efforts to make derivatives with smaller substituents at the chiral centers are in progress. Finally, a series of chiral macrocycles were prepared, characterized and exploited as building blocks for the preparation of chiral magnets. Work is in progress to characterize these materials and establish optimal conditions for the self-assembly of new chiral magnets.

# CHAPTER 3- Synthesis and study of TTF-π-verdazyl radicals and a CT salt

## 3.1 Introduction

As previously discussed, the first two examples of TTF donors bearing dimethyl verdazyl radicals **(3.1)** and **(3.2)** were prepared and characterized by the Pilkington group as building blocks for the preparation of ferromagnetic conductors, Figure 3.1.[91,92] For compound **(3.2)**, oxidation of the TTF donor afforded the diradical cation **[3.2]**$^{\cdot+}$ which was reported to exhibit weak, short-range antiferromagnetic interactions.[92] Unfortunately, the dimethyl series of TTF-verdazyl radicals were difficult to crystallize and attempts to obtain single crystals suitable for X-ray diffraction were unsuccessful. This hindered the progress of the project and as a consequence, attention was focused on the preparation of a second series of more crystalline TTF-verdazyl radicals.

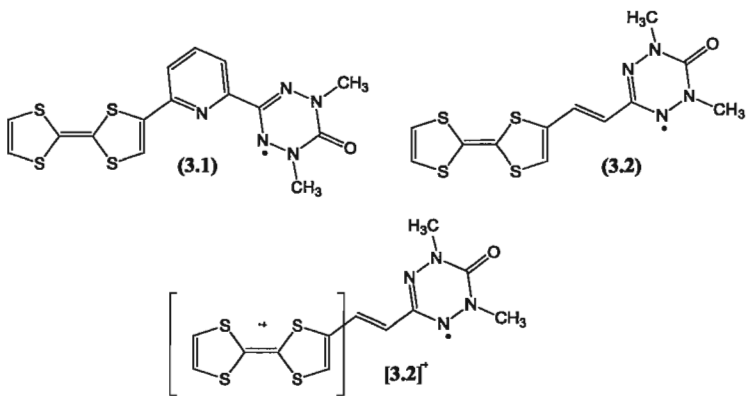


**Figure 3.1:** Molecular structures of 2,6-TTF-py-(dimethyl)verdazyl radical **(3.1)**; TTF-π-(dimethyl)verdazyl radical **(3.2)**, and TTF-π-(dimethyl)verdazyl diradical cation **[3.2]** $^{\cdot+}$.

In parallel work, theoretical studies were carried out to probe the nature of the intramolecular exchange interaction between the verdazyl and TTF radicals connected through a series of organic linkers.[93] DFT calculations were carried out to investigate the

sign and magnitude of the intramolecular exchange interaction, $J$, as well as its dependence on the torsion angle between the TTF radical cation and the linker, $\theta_{SC1}$, and the torsion angle between the verdazyl radical and the linker, $\theta_{SC2}$.[93] The first classes of organic linkers modeled were cross-conjugated phenyl groups.[93] For the diradical cations, the sign and magnitude of the $J$ value was theoretically determined for both the *para*- and *meta*-substituted compounds **(3.3)** and **(3.4)**, Figure 3.2.[93] The calculations predicted that the two radicals should couple ferromagnetically in the *para*-substituted compound **(3.5)**, whereas antiferromagnetic coupling was predicted for the *meta*-derivative **(3.6)**.[93]

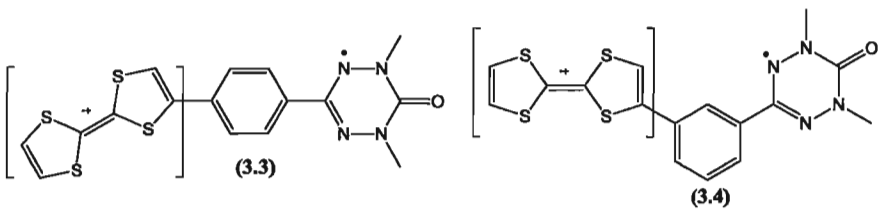


**Figure 3.2:** Molecular structures of the *para*-TTF-phenylene-(dimethyl)verdazyl diradical cation **(3.3)**; and the *meta*-TTF-phenylene-(dimethyl)verdazyl diradical cation **(3.4)**.

The second class of linkers modeled were conjugated ethylene chains. DFT calculations predicted that for these compounds, the magnitude of $J$ should increase with the number of double bonds in the conjugated linker up to a maximum of three.[93]

Given these findings, the short term objectives of my project were: (i) to prepare a new series of crystalline TTF-verdazyl diradical cations, facilitating their structural and magnetic characterization; (ii) to prepare a family of cross conjugated TTF-py-verdazyl donors and investigate how the different substitution positions of the TTF and verdazyl radical affects the sign and magnitude of the coupling between the two radicals (after oxidation of the TTF donor); and (iii) to prepare a TTF-π-verdazyl radical and examine

how increasing the length of the conjugated polyene linker affects the interaction between the two radicals, again after the oxidation of the TTF donor to generate the diradical cation species. The long term goals of the project are to use these molecules as building blocks for the self-assembly of ferromagnetic conductors. In this respect, the itinerant electrons of the conducting pathway should align the spins of the verdazyl radicals, facilitating ferromagnetic interactions via a double exchange mechanism.[93]

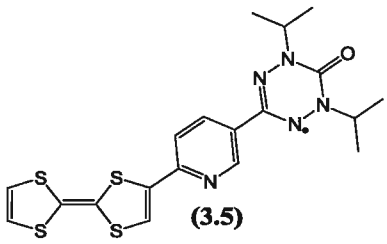
(3.5)

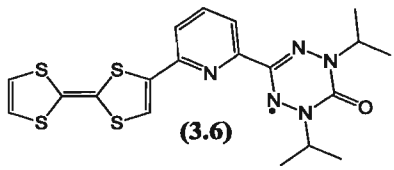
(3.6)

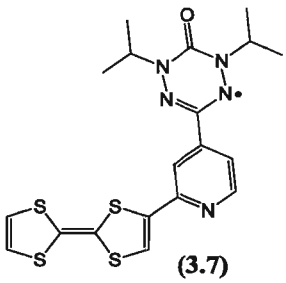
(3.7)

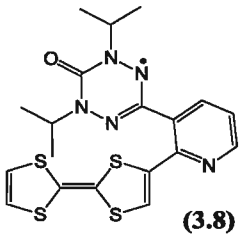
(3.8)

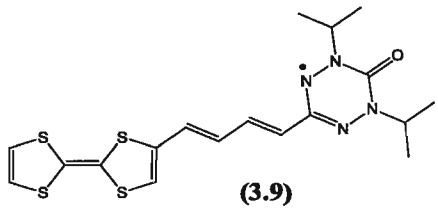
(3.9)

A search of the chemical literature revealed that a new diisopropyl verdazyl radical had been prepared and characterized and was more soluble and robust in comparison with its dimethyl derivative.[125] Based on these findings, we targeted the preparation and characterization of a new family of cross conjugated TTF-py-(diisopropyl)verdazyl radicals **(3.5)** – **(3.8)**, as well as the conjugated TTF-divinylene-(diisopropyl)verdazyl radical **(3.9)**. Pyridine was selected over phenyl as a linker since Hicks *et al.* have reported that pyridyl-verdazyl radicals can chelate transition metal ions.[68, 126] In this respect, the pyridyl linker provides us with a second strategy for

introducing unpaired electrons into the system in the form of a paramagnetic transition metal ion.

### 3.2 Systematic strategy for the preparation of TTF-py-verdazyl radical donors

The starting material for the preparation of both classes of radicals is tetrathiafulvalene (TTF). The large scale preparation of TTF was achieved following a modification of the synthetic procedure first reported by Bryce *et al.*[127] TTF **(3.10)** was isolated as orange needles in 65% yield. The melting point of the product was consistent with the range reported for TTF (119-120°C) in the chemical literature.[127] The $^{1}H$ NMR spectrum of TTF comprises a singlet corresponding to the CH protons at 6.33 ppm, and the $^{13}C$ NMR spectrum displays two peaks at 119.1 and 110.1 ppm for the outer and bridging $sp^2$ carbon atoms, respectively. This data is consistent with the $^{1}H$ and $^{13}C$ chemical shifts reported in the literature for TTF.[127]

Four TTF-py-verdazyl radicals **(3.5)** - **(3.8)** were prepared. The synthetic strategy for the preparation of the 2,5-substituted TTF-py-(diisopropyl)verdazyl radical **(3.5)** is outlined in Scheme 3.1.[91]

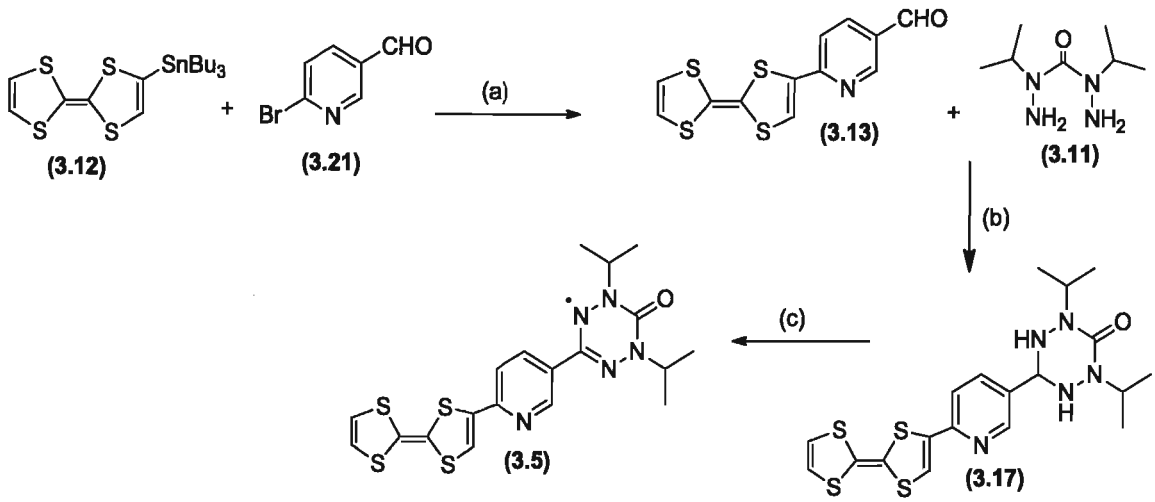


**Reagents and conditions**

(a) $Pd(PPh_3)_4$, toluene, 115°C, overnight; (b) MeOH , reflux, overnight; (c) 1,4-benzoquinone, $C_6H_6$, 60°C, 1 h.

**Scheme 3.1:** Synthetic procedure for the preparation of the 2,5-TTF-py-(diisopropyl)verdazyl radical **(3.5)**.

Lithiated TTF was treated with tributyltin chloride to afford the tributylstannyl derivative **(3.12)**.[128] Compound **(3.12)** was then converted to the aldehyde derivative **(3.13)** via cross coupling with 5-bromo-2-formylpyridine **(3.21)**. Compound **(3.13)** was isolated as a dark purple crystalline solid in 82% yield. The aldehyde **(3.13)** was then treated with 2,4-diisopropylcarbonylhydrazide *bis*-hydrochloride **(3.11)** to afford the tetrazane **(3.17)** as an orange-red solid. The tetrazane **(3.17)** was oxidized with 1,4-benzoquinone to afford the desired radical as a (1:1) mixture with hydroquinone which could be separated by flash chromatography to afford verdazyl radical **(3.5)** as a dark purple crystalline solid in 56% yield. Important intermediates in this synthetic pathway are the formyl TTF derivatives **(3.13)** – **(3.16)**, which were prepared via Stille coupling of TTF together with the appropriate bromo-formyl pyridine **(3.21)** – **(3.24)**, Figure 3.3.

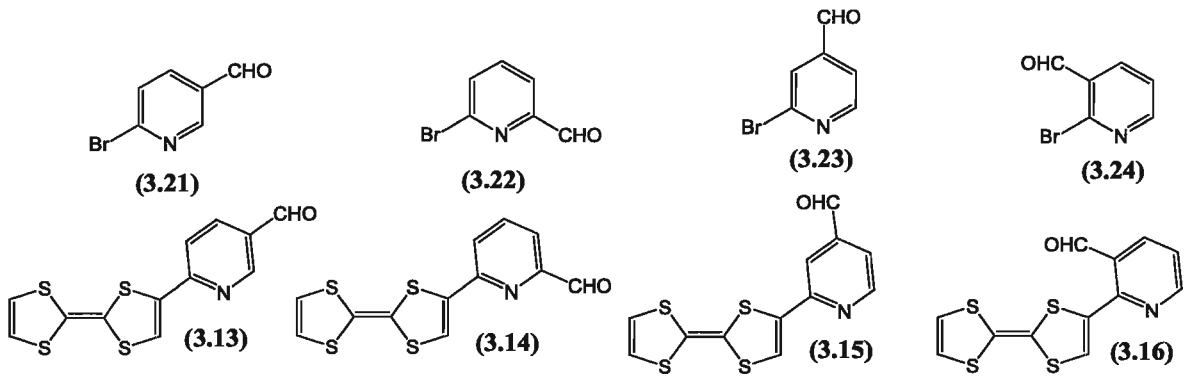


**Figure 3.3:** Molecular structures of the commercially available 2-bromo-x-formyl pyridine, where is x = 3 to 6, **(3.21)** to **(3.24)**; and their corresponding formyl TTF derivatives **(3.13)** to **(3.16)**.

Reaction of the formyl TTF derivatives with 2,4-diisopropylcarbonylhydrazide *bis*-hydrochloride **(3.11)** affords the tetrazanes. Unfortunately, the hydrazide **(3.11)** is not commercially available, but it can be prepared, following the literature procedure presented by Pare *et al.*[125] The 2,4-diisopropylcarbonylhydrazide *bis*-hydrochloride **(3.11)** was afforded as an off-white solid in 98% yield. The FAB mass spectrum of **(3.11)** shows a parent ion at $m/z$ = 175 which supports its molecular structure. The $^1$H NMR spectrum of **(3.11)** possesses a multiplet at 4.18 ppm assigned to the four $NH_2$ protons, a doublet at 1.18 ppm assigned to the four sets of methyl protons and a doublet at 1.04 ppm consistent with the presence of the two CH protons.[125]

### 3.3 Characterization of TTF-py-(diisopropyl)tetrazanes

The key precursors to the TTF-py-verdazyl radicals are the tetrazanes **(3.17)** – **(3.20)**, Figure 3.4. These compounds can be prepared on a large scale and are air stable. All four tetrazanes have been characterized and selected data for these compounds is presented in Table 3.1.

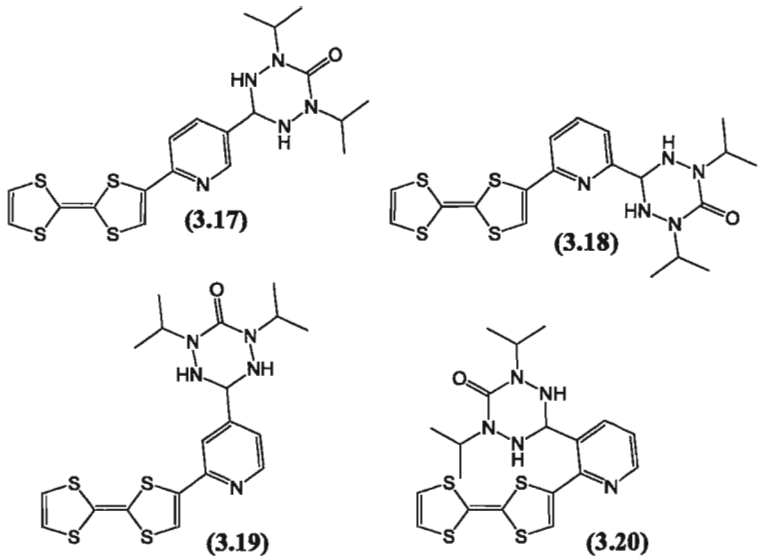


**Figure 3.4:** Molecular structures of TTF-py-(diisopropyl)tetrazanes **(3.17)** to **(3.20)**.

The first tetrazane prepared was the 2,5-derivative **(3.17)** which was isolated as an orange-red solid in 55% yield. The FAB mass spectrum of **(3.17)** shows a parent ion $[M]^+$ at $m/z = 465$, consistent with its molecular structure. The IR spectrum has an NH str at 3400 $cm^{-1}$ and a C=O stretch at 1625 $cm^{-1}$, characteristic for the tetrazane, as well as a C=C str at 1536 $cm^{-1}$ for the TTF donor. The microanalytical data for **(3.17)** is a reasonable fit for $C_{19}H_{23}N_5OS_4$. The $^1H$ and $^{13}C$ NMR data for **(3.17)** were assigned with the aid of 2-D HSQC and HMBC experiments.

**Table 3.1:** Selected data for TTF-py-(diisopropyl)tetrazanes **(3.17)** – **(3.20)**.

| Compound | MS-FAB | CHN | % Yield and appearance | IR (KBr, $cm^{-1}$) | UV-vis ($CH_3CN$) $\lambda$ (nm) | CV (V) $*E^1_{1/2/ox}$, $*E^3_{1/2/ox}$ |
|---|---|---|---|---|---|---|
| 2,5-**(3.17)** | $m/z$ = 465 $[M]^+$ (100%). | Found C: 49.95, H: 5.37, N: 14.15%; Calcd. for ($C_{19}H_{23}N_5OS_4$) C: 49.01; H: 4.98; N: 15.04%. | orange/red solid, 55% yield. | 3412 (NH), 1625 (C=O), 1536 (C=C). | 320, 430. ($\varepsilon$ = 3328 $M^{-1}cm^{-1}$; 470 $M^{-1}cm^{-1}$) | 0.50 V, 0.74 V |
| 2,6-**(3.18)** | $m/z$ = 465 $[M]^+$ (100%). | Found C: 48.69, H: 5.76, N: 14.55%; Calcd. for ($C_{19}H_{23}N_5OS_4$) C: 49.00; H: 4.98; N: 15.04%. | orange solid, 63% yield. | 3412 (NH), 1716 (C=O), 1608 (C=C). | 320, 440. ($\varepsilon$ = 1260 $M^{-1}cm^{-1}$; 233 $M^{-1}cm^{-1}$) | 0.49 V, 0.75 V |
| 2,4-**(3.19)** | $m/z$ = 465 $[M]^+$ (30%). | ----- | orange oil, 36% yield. | 3415 (NH), 1714 (C=O), 1598 (C=C). | 315, 435. ($\varepsilon$ = 1463 $M^{-1}cm^{-1}$; 233 $M^{-1}cm^{-1}$) | 0.48 V, 0.75 V |
| 2,3-**(3.20)** | $m/z$ = 465 $[M]^+$ (30.5%). | ----- | orange oil, 52% yield. | 3436 (NH), 3251, 1623 (C=O), 1585 (C=C). | 310, 415. ($\varepsilon$ = 2994 $M^{-1}cm^{-1}$; 502 $M^{-1}cm^{-1}$) | 0.47 V, 0.80 V |

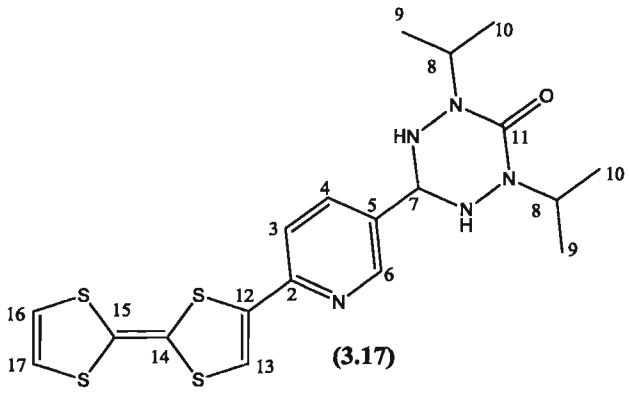


**Figure 3.5:** Molecular structure and numbering scheme for the 2,5 TTF-py-(diisopropyl)-tetrazane **(3.17)**.

The 300 MHz $^{1}$H NMR spectrum shows a singlet at 8.67 ppm for the proton at C-6, multiplets at 7.97 ppm and 7.91 ppm are assigned to the protons at C-3 and C-4, respectively. The characteristic TTF protons are observed as a singlet at 6.75 ppm for protons C-16 and C-17, as well as the singlet at 7.70 ppm assigned to the proton at C-13. The NH protons are assigned to the broad singlet at 5.76 ppm. A triplet at 5.16 ppm is assigned to the proton at C-7 and the multiplet at 4.48 ppm is assigned to the CH proton at C-18. Finally, two doublets at 1.06 and 0.97 ppm are assigned to the isopropyl protons at C-9 and C-10. The 75 MHz $^{13}$C NMR spectrum shows 14 peaks consistent with the molecular structure of **(3.17)**. The carbonyl peak appears at 153.8 ppm. Peaks 150.2 ppm, 148.1 ppm, 137.5 ppm, 135.7 ppm, 131.4 ppm, 121.2 ppm, 120.7 and 108.1 ppm are assigned to C-2, C-6, C-12, C-4, C-14, C-15, C-3 and C-5, respectively. The next peaks at 119.4 and 120.5 ppm are assigned to the TTF carbons C-16,-17 and C-13 respectively. The peak at 70.0 ppm is assigned to C-7. The peak at 47.1 ppm is assigned to C-8, the central carbon of the isopropyl group, and the final peak at 20.1 ppm is consistent with the methyl carbons of the isopropyl group C-9 and C-10. These assignments are in

agreement with data previously reported for the 2,6-TTF-py-(dimethyl)tetrazane **(3.25)**, and 2,4-diisopropyl-6-pyridin-2-yl-1,2,4,5-tetrazinan-3-one **(3.26)**, Figure 3.6.[91, 125]

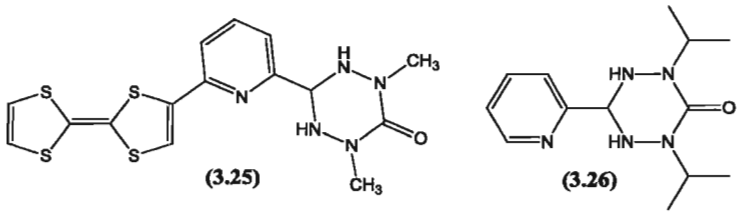


**Figure 3.6:** Molecular structures of 2,6-TTF-py-(dimethyl)tetrazane (**3.25**); and 2,4-diisopropyl-6-pyridin-2-yl-1,2,4,5-tetrazinan-3-one (**3.26**).[91, 125]

The UV-Vis spectrum of the 2,5-tetrazane **(3.17)** is shown in Figure 3.7. The first absorption band at $\lambda$ = 320 nm can be assigned to the lowest $\pi$-$\pi^*$ intramolecular transitions involving the highly conjugated $\pi$-system of the TTF.[129] The second band at $\lambda$ = 430 nm is attributed to the overlap of absorption bands from the pyridine and tetrazane moieties.[91]

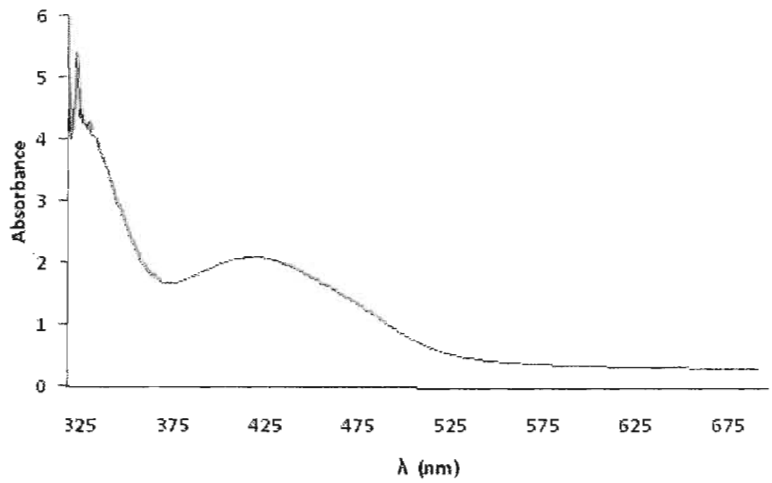


**Figure 3.7:** UV-Vis spectrum of 2,5-TTF-py-diisopropyltetrazane (**3.17**) in $CH_3CN$.

Electrochemical studies were carried out on both the tetrazane **(3.17)** and the TTF donor **(3.10)**, at room temperature in DMF, Figure 3.8. The cyclic voltammogram for

TTF comprises of two reversible oxidation potentials. The first oxidation potential at 0.45 V corresponds to the formation of the radical cation $[TTF]^{\cdot+}$ and the second oxidation potential at 0.68 V corresponds to the formation of the dication $[TTF]^{2+}$.[82]

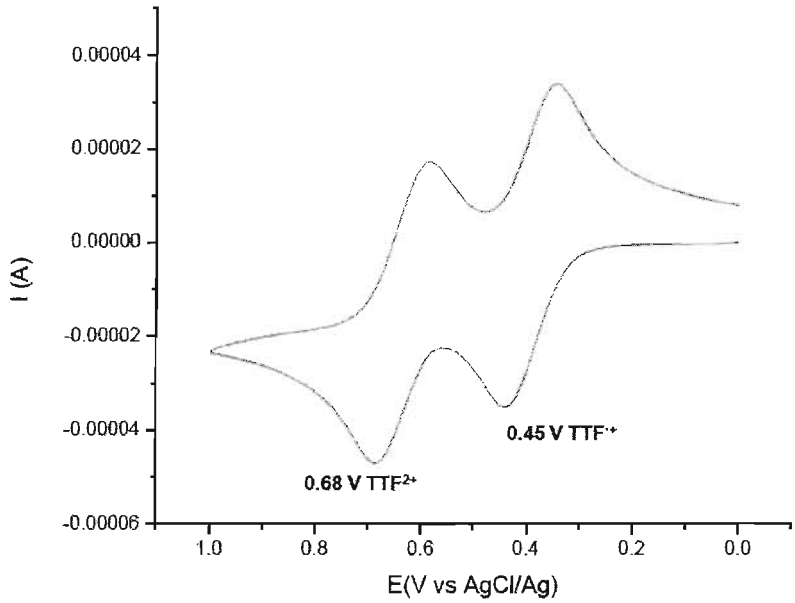


**Figure 3.8:** Cyclic voltammogram of TTF **(3.10)** in DMF at 0.1 V/s using a glassy carbon electrode as the working electrode, Ag/AgCl as a reference and tetrabutylammonium hexafluorophosphate (0.1 M) as the supporting electrolyte.

The cyclic voltammogram of 2,5-TTF-py-(diisopropyl)tetrazane **(3.17)** is similar to TTF, showing two quasi-reversible oxidation potentials at relatively low potentials, corresponding to the generation of the radical cation $[TTF]^{\cdot+}$ at 0.50 V and the dication $[TTF]^{2+}$ at 0.74 V, Figure 3.9. Both oxidation potentials are anodically shifted in comparison with neutral TTF, with the second potential being shifted to a greater extent. This is consistent with the electron-withdrawing nature of the pyridine ring which increases the oxidation potential of the TTF donor. The second oxidation potential at 0.74 V is a four electron process and also accounts for the three electron oxidation of the

tetrazane to the verdazyl radical, which is consistent with the redox potential of the pyridyl-(diisopropyl)tetrazane **(3.26)**.[91]

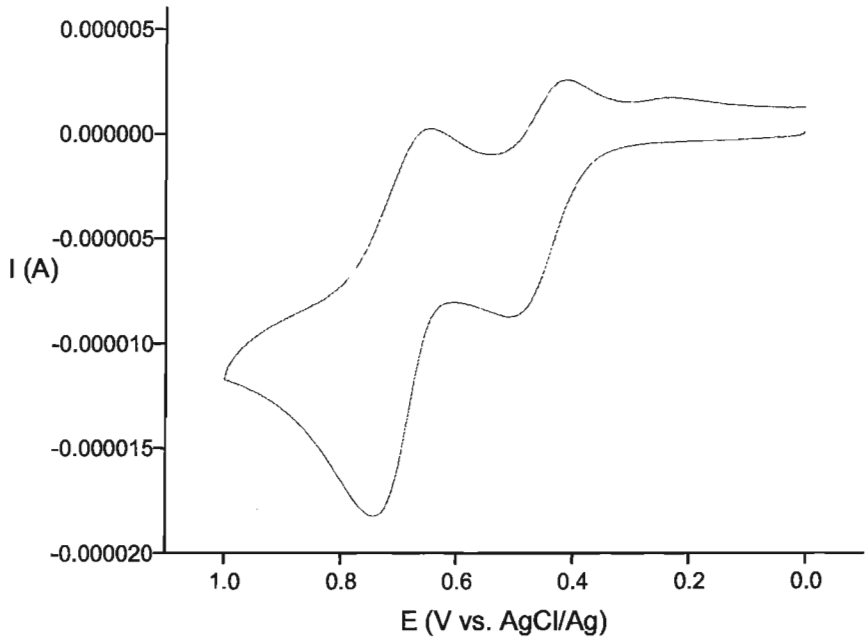


**Figure 3.9:** Cyclic voltammogram of 2,5-TTF-py-diisopropyltetrazane **(3.17)** in DMF at 0.1 V/s using a glassy carbon electrode as the working electrode, Ag/AgCl as a reference and tetrabutylammonium hexafluorophosphate (0.1 M) as the supporting electrolyte.

All four tetrazanes display very similar chemical and physical properties to the 2,5-derivative and these are summarized in Table 3.1. The molecular structures of the 2,6- and the 2,3-derivatives, **(3.18)** and **(3.20)**, have been determined by X-ray crystallography. In both cases, suitable single crystals were grown via the slow evaporation of a DCM solution of the tetrazane at room temperature. The molecular structure of the 2,6-derivative **(3.18)** is shown in Figure 3.10. The molecule crystallizes in the triclinic space group P-1, with one independent molecule in the unit cell. The TTF unit and the pyridyl ring are fairly coplanar, with a torsion angle of 178° between their best planes.

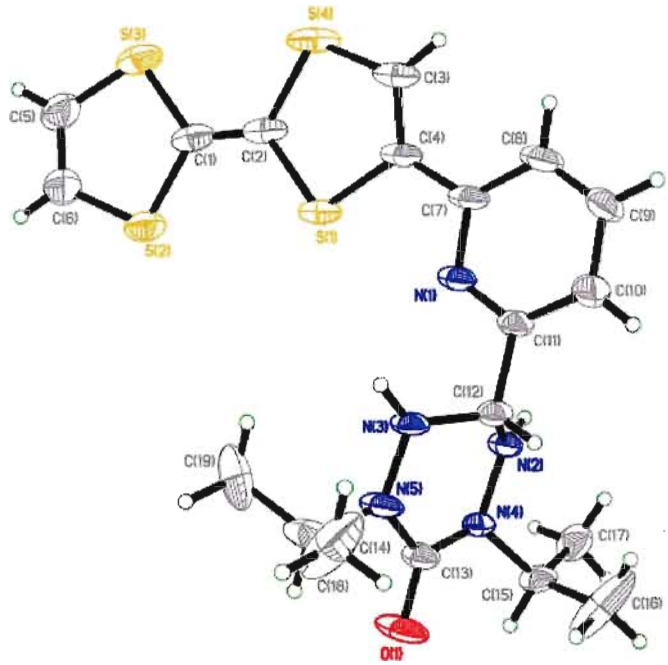


**Figure 3.10:** ORTEP[110] representation of the molecular structure of the 2,6-TTF-py-(diisopropyl) tetrazane **(3.18)** at 150 K. Thermal ellipsoids are plotted at 50% probability.

The isopropyl groups have large thermal ellipsoids indicating some disorder. The tetrazane ring adopts a chair-like, non-planar conformation and is twisted away from the best plane of the pyridine ring by an angle 76°.

The molecular structure of the 2,3-tetrazane **(3.20)** is shown in Figure 3.11. This compound crystallizes in the monoclinic space group C2/c with two independent molecules in the asymmetric unit. In contrast to the structure above, the TTF and pyridine ring in the 2,3-derivative **(3.20)** are much less co-planar. It is seems reasonable to suggest that the TTF is twisted out of the plane of the pyridine ring for steric reasons, in order to avoid the bulky diisopropyl groups on the tetrazane moiety. In this respect, the torsion angles between the TTF and the pyridine ring are 165° and 159° for molecules **A** and **B** respectively. The tetrazane is also twisted out of the plane of the pyridine ring by 74° and

72.5° for the two independent molecules. As observed in the molecular structure of the 2,6-derivative, the tetrazane rings in both molecules of **(3.20)** adopt a chair-like, non planar conformation.

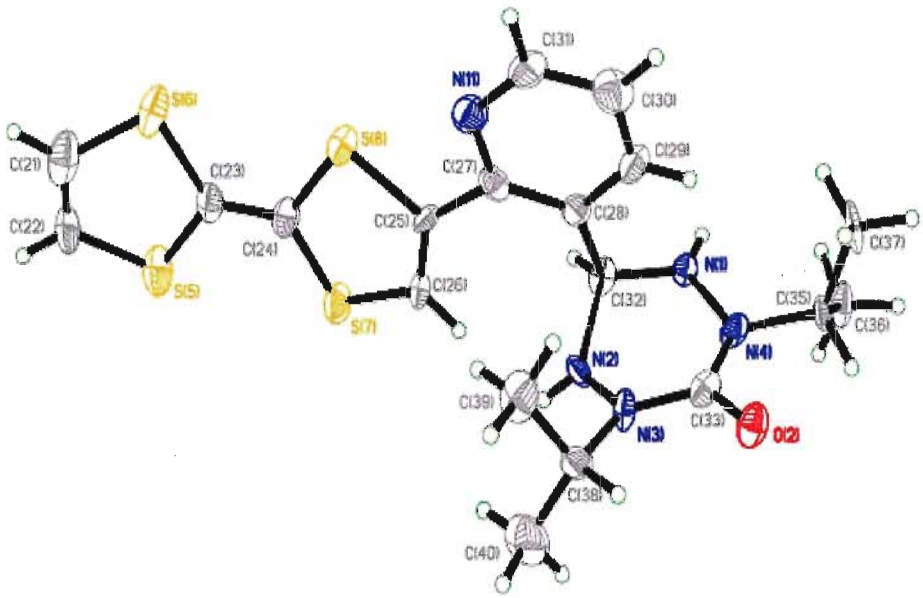


**Figure 3.11:** ORTEP[110] representation of the molecular structure of one of the two independent molecules of 2,3-TTF-py-(diisopropyl)tetrazane **(3.20)** at 150 K. Thermal ellipsoids are plotted at 50% probability.

### 3.4 Characterization of TTF-py-(diisopropyl)verdazyl radicals

All four TTF-py-(diisopropyl)verdazyl radicals **(3.5)** – **(3.8)** were prepared via the chemical oxidation of their corresponding tetrazanes as discussed earlier, Figure 3.12.

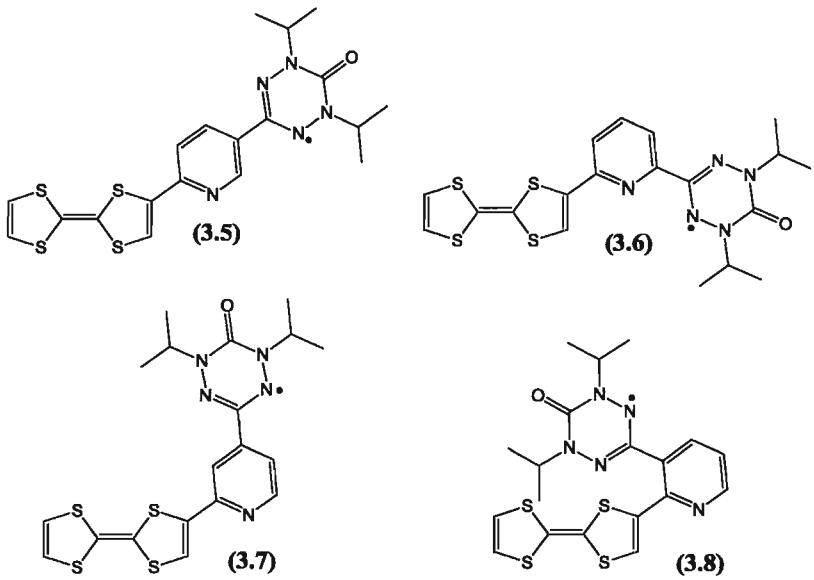


**Figure 3.12:** Molecular structures of TTF-py-verdazyl radicals **(3.5)** to **(3.8)**.

The first radical prepared and characterized was the 2,5-derivative **(3.5)**. It was isolated as a purple solid in 56% yield. The FAB mass spectrum has a parent ion at *m/z* = 462. The microanalytical data was an excellent fit for ($C_{19}H_{20}N_5OS_4$). The absence of the NH str above 3400 $cm^{-1}$ in the IR spectrum is consistent with the formation of the verdazyl radical. A C=O str is present at 1681 $cm^{-1}$ which is red shifted when compared to its tetrazane precursor **(3.17)**. The UV-Vis spectrum for compound **(3.5)** is similar to the tetrazane precursor **(3.17)**. There are two absorption maxima visible at $\lambda_{max}$ = 320 and 440 nm. As previously mentioned for the tetrazane, the band at $\lambda$ = 320 nm is assigned to the lowest $\pi$-$\pi^*$ intramolecular transitions of the conjugated $\pi$-system of the TTF.[129] The second band at the longer wavelength is now broader in comparison with its tetrazane precursor **(3.17)**. This band is assigned as $\pi$–$\pi^*$ and n–$\pi^*$ transitions involving the pyridine and verdazyl moieties and is consistent with data reported for the py-diisopropyl verdazyl radical **(3.27)**, Figure 3.13.[130]

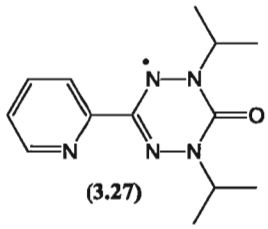


(3.27)

**Figure 3.13:** Molecular structure of 1,5-diisopropyl-3-pyridin-2-yl-6-oxoverdazyl **(3.27)**.[125]

The cyclic voltammogram of **(3.5)** shows two reversible oxidation potentials, Figure 3.14. The assignment is analogous to tetrazane **(3.17)** for the generation of the radical cation $[TTF]^{\cdot+}$ at 0.47 V and the dication $[TTF]^{2+}$ at 0.75 V.[82] The second oxidation potential is overlapped with the reversible one-electron oxidation of the verdazyl radical, the oxidation potentials for the radical **(3.5)** are in good agreement with the previously measured literature values for radical **(3.27)**.[125]

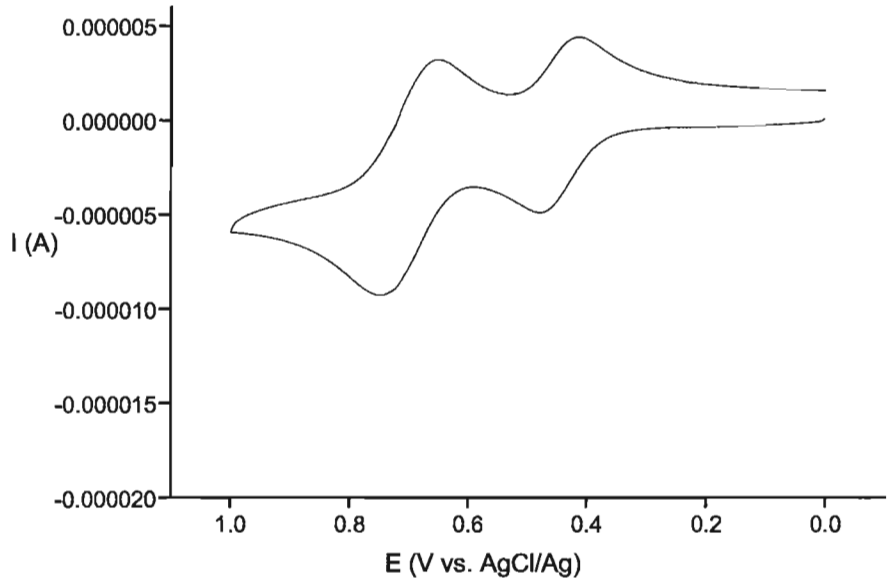


**Figure 3.14:** Cyclic voltammogram of 2,5-TTF-py-(diisopropyl)verdazyl radical **(3.5)** in DMF at 0.1 V/s using a glassy carbon electrode as the working electrode, Ag/AgCl as a reference and tetrabutylammonium hexafluorophosphate (0.1 M) as the supporting electrolyte.

The EPR spectrum of **(3.5)** is comprised of 7 lines that can be attributed to the hyperfine coupling of the radical coupled to the four verdazyl nitrogen atoms and two CH hydrogen atoms of the isopropyl group, Figure 3.15. This is consistent with the data reported by Pare *et al.* for the characterization of the pyridine-(diisopropyl)verdazyl radical **(3.27)**.[125]

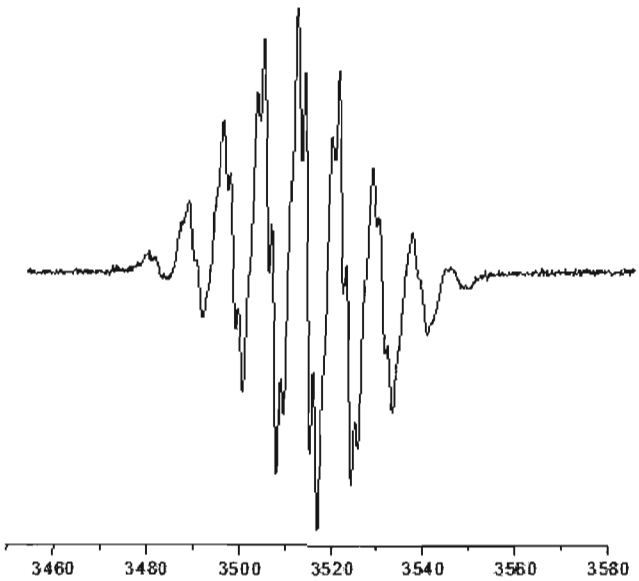


**Figure 3.15:** EPR spectrum of **(3.5)** in benzene at 298 K.

The molecular structure of the 2,5-TTF-py-verdazyl radical **(3.5)** has also been determined by X-ray crystallography at 150 K. Single crystals were grown via the slow evaporation of a DCM solution of the radical. The molecular structure of **(3.5)** is shown in Figure 3.16.

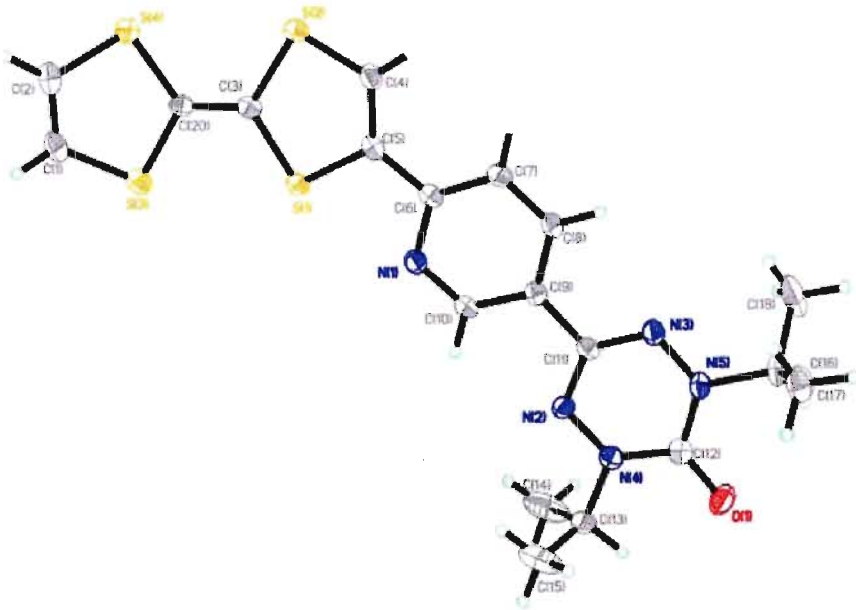

**Figure 3.16:** ORTEP[110] representation of the molecular structure of the 2,5-TTF-py-(diisopropyl)verdazyl radical **(3.5)**; thermal ellipsoids are plotted at 50%. The DCM solvent is omitted for clarity.

The molecule crystallizes in the monoclinic space group $P2_1/c$ along with one DCM solvent molecule. In contrast to the tetrazanes, the TTF and verdazyl radical moieties are almost coplanar with respect to the pyridine ring with torsion angles of 175.8 and 178°, respectively. The verdazyl radical is relatively planar with respect to the best plane of the pyridine ring, with the largest deviation being 0.116 Å for the carbon atom of the carbonyl group, C(12). The TTF molecule twists a little more out of the best plane of the pyridine ring, with the sulfur atoms deviating between 0.188 and 0.384 Å, and the central carbon atoms C(3) and C(4) deviating by 0.263 and 0.313 Å, respectively. There is also a slight bend in the TTF molecule at C(1) and C(2) which is consistent with structural data reported for other neutral TTF molecules.[131] Selected bond lengths and angles for **(3.5)** are presented in Tables 6.6 and 6.7, in the Appendix section of this thesis.

The TTF-py-(diisopropyl)verdazyl radicals pack in a head-to-tail arrangement of dimers with intermolecular S···S distances of 3.441 Å between the molecules, Figure

3.17. The shortest intermolecular S···S distances are 3.357 Å, between neighbouring dimer pairs. The DCM molecules occupy channels in the structure and are involved in H-bonding interactions, Figure 3.17. In this respect, the DCM molecules are H-bonded to the carbonyl oxygen atoms of neighboring verdazyl radicals (H···O-C = 2.322 Å and 2.327 Å). The crystal packing arrangement is also stabilized by H-bonds between the diisopropyl CH protons and the verdazyl carbonyl oxygen atoms (O···H-C = 2.38 Å and 2.43 Å). It should be noted that the verdazyl radicals do not take part in any π-π stacking interactions and neighbouring verdazyl radicals are separated by a distance of 5.605 Å. There is no evidence of any dimerization of the verdazyl radicals in the solid state.

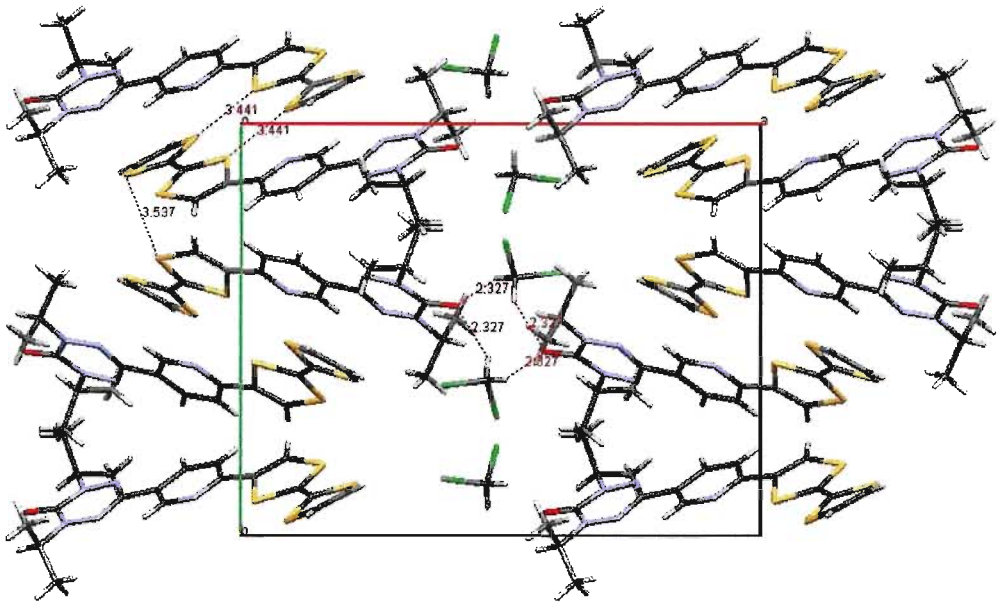


**Figure 3.17:** Packing diagram for the 2,5-verazyl radical **(3.5)**. View down the *c*-axis. S···S contacts and H-bonding interactions are shown as red dashed lines. Distances are given in Å.[111]

As previously mentioned, four TTF-py-verdazyl radicals have been prepared and characterized following the strategy presented in Scheme 3.1. The EPR spectra of all four radicals are very similar to the data presented for the 2,5-derivative. For comparison, selected data for all four TTF-py-(diisopropyl)verdazyl radicals is presented in Table 3.2.

**Table 3.2:** Selected data for TTF-py-verdazyl radicals **(3.5)** - **(3.8)**.

| Compound | FAB-MS | CHN | Appearance and % yield | UV-Vis $\lambda_{max}$ (nm) | Cyclic Voltammetry $^*E^1_{1/2/ox}$, $^*E^3_{1/2/ox}$ | | IR ($\upsilon$, $cm^{-1}$) |
|---|---|---|---|---|---|---|---|
| 2,5-**(3.5)** | $m/z$ = 462 $[M]^+$ (100%). | Found C:49.29, H: 4.35, N: 14.90%; Calcd. for ($C_{19}H_{20}N_5OS_4^{\cdot}$) C: 49.32; H: 4.36; N: 15.14%. | dark purple crystalline solid, 56% yield. | 320, 440 | 0.475, | 0.751 | 3234, 2964, 1681, 1456 |
| 2,6-**(3.6)** | $m/z$ = 462 $[M]^+$ (51%). | Found C:49.95, H: 5.37, N: 14.22%; Calcd. for ($C_{19}H_{20}N_5OS_4^{\cdot}$) C: 49.32; H: 4.36; N: 15.14%. | dark orange solid, 64% yield. | 320, 435 | 0.469, | 0.727 | 3423, 2962, 1670, 1456 |
| 2,4-**(3.7)** | $m/z$ = 462 $[M]^+$ (9.4%). | ----- | red solid, 42% yield. | 315, 440 | 0.475, | 0.760 | 3421, 2964, 1677, 1596 |
| 2,3-**(3.8)** | $m/z$ = 462 $[M]^+$ (4%). | ----- | yellow/brown solid, 40% yield. | 315, 440 | 0.469, | 0.769 | 3446, 2962, 1681, 1565 |

The molecular structure of the 2,6-verdazyl radical **(3.6)** has also been characterized by X-ray crystallography and is shown in Figure 3.18.

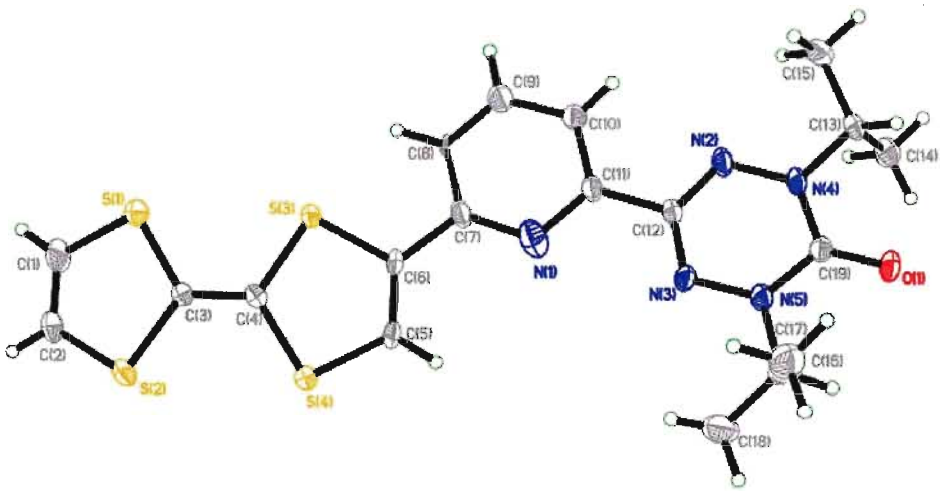


**Figure 3.18:** ORTEP[110] representation of the molecular structure of 2,6-TTF-py-(diisopropyl)verdazyl radical **(3.6)**, thermal ellipsoids are plotted at 50% probability.

The molecule crystallizes in the triclinic space group P-1. In contrast to its tetrazane counterpart **(3.18)**, the radical is more planar. The torsion angle between the verdazyl radical and the pyridine ring is 168.7°, while the torsion angle between the TTF and pyridine ring is 176.5°. The verdazyl radical is twisted with respective to the plane of the pyridine ring with a deviation of 0.231 Å at the carbonyl carbon C(12). The TTF shows less of a deviation from the plane of the pyridine ring for the 2,6-verdazyl radical **(3.6)** in comparison with the 2,5-derivative **(3.5)**. In this case the sulfur atoms deviate from 0.011 to 0.229 Å, and the central $sp^2$ carbon atoms C(3) and C(4) deviate by only 0.084 and 0.025 Å, respectively. There is however a larger deviation at carbons atoms C(1) and C(2), deviating from the plane of the pyridine ring by 0.570 and 0.457 Å, respectively. Selected bond lengths and angles for **(3.6)** are presented in Tables 6.8 and 6.9.

The crystal packing diagram for **(3.6)** is shown in Figure 3.19. The molecules pack in an offset arrangement of head-to-tail dimers with intermolecular hydrogen bonding interactions between neighboring stacks, Figure 3.19. There are no short intermolecular S···S contacts between neighbouring TTF molecules. Fairly short H-bonds are found between the $sp^2$ protons of a TTF molecule and the oxygen atom of the carbonyl group on the verdazyl radical (C=O···H = 2.35 Å), Figure 3.19.

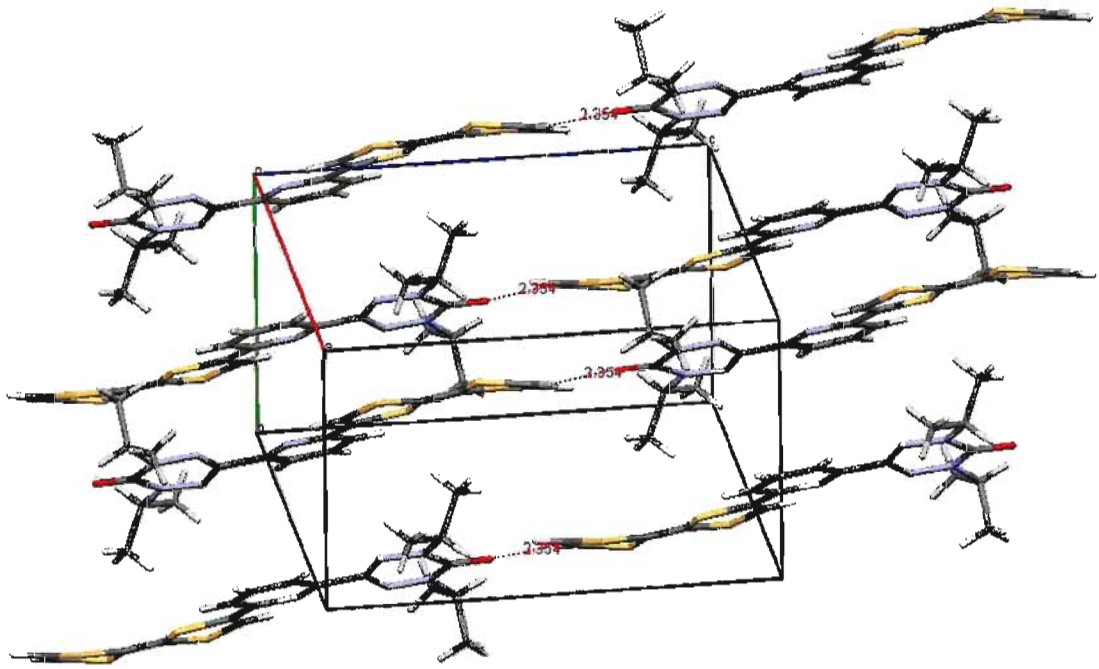

**Figure 3.19:** Packing diagram of the 2,6-TTF-py-verazyl radical **(3.6)**; view down the *a*-axis.[111]

## 3.5 Preparation and characterization of a (2:1) CT salt of the 2,5-TTF-py-(diisopropyl)verdazyl radical and TCNQ (3.28)

Since the 2,5- and 2,6- derivatives seemed easier to crystallize than the other two members of the series, attempts focused on the preparation of charge transfer salts of these two donor radicals. In this respect, the challenge was to find suitable conditions for the preparation and characterization of single crystals of a charge transfer salt, in order to

probe its structural, magnetic and electronic properties. Reaction of one equivalent of the 2,5-TTF-py-(diisopropyl) verdazyl radical donor with two equivalents of the tetracyanoquinodimethane (TCNQ) acceptor afforded dark purple single crystals of a (2:1) charge transfer (CT) complex **(3.28)** after a few days.

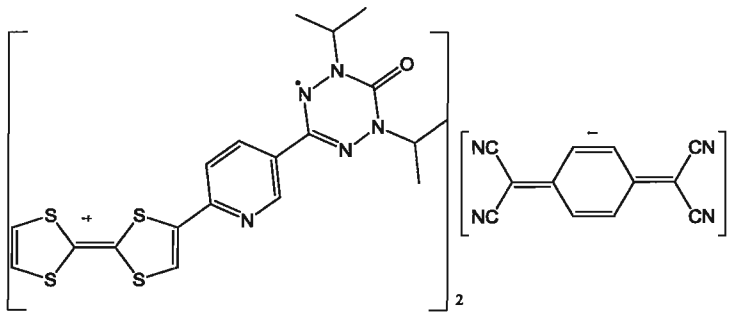

**(3.28)**

The FAB mass spectrum of this complex showed two fragment ions at *m/z* = 462 for the 2,5-TTF-py-(diisopropyl)verdazyl radical and *m/z* = 209 for the TCNQ acceptor. The IR spectrum contains a C=O str at 1678 $cm^{-1}$ consistent with the presence of the verdazyl radical. Following the methodology of Chappell *et al.*[132] the extent of the charge transfer in the complex can be estimated by examining the position of the CN str in the TCNQ molecule. In this respect, the CN str of the TCNQ is blue shifted by 12 $cm^{-1}$ when compared with the CN str for a neutral TCNQ molecule. The shift in IR frequency is due to the change in bond length and differences in the intramolecular frequencies after the formation of the TCNQ radical anion.[133] According to Chappell *et al.* this difference is consistent with 0.5 $e^-$ charge transfer from the TTF donor to the TCNQ acceptor.[132] It is important to probe the degree of charge transfer in CT salts, since partial transfer between donor and acceptor molecules is a requirement for conductivity.[134]

The UV-Vis spectrum of the CT salt is presented in Figure 3.20. The UV-Vis spectra of the CT salt comprises four bands at $\lambda_{max}$ = 416, 496, 737 and 836 nm. The

absorption at $\lambda$ = 400 nm is characteristic of the TTF radical cation.[135] The broad band at $\lambda$ = 496 nm, can be attributed to n to $\pi^*$ and $\pi$ to $\pi^*$ absorptions from the verdazyl radical and pyridine ring, overlapping with the $\pi$-$\pi^*$ transitions of the TTF radical cation.[136] Comparing the UV-Vis spectrum of the complex to the spectrum of TCNQ it is clear that the bands at $\lambda$ = 730 and 830 nm are due to electronic transitions involving the TCNQ acceptor. The increased absorptivity of these bands correspond to the ionized TCNQ acceptor, (TCNQ anion).[137] The band centered around $\lambda$ = 830 nm is assigned to the intramolecular CT band between TCNQ and the aromatic molecules.[138, 139]

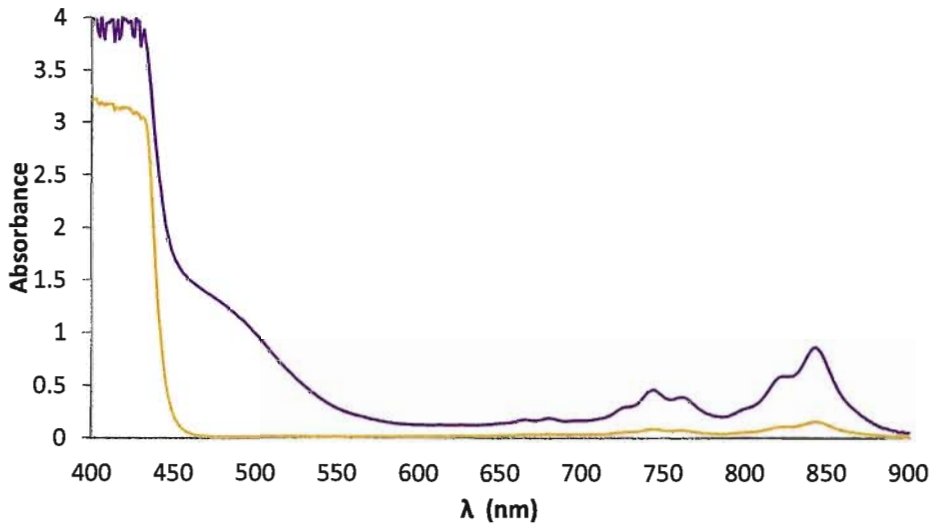


**Figure 3.20:** UV-Vis spectra of the CT salt **(3.28)** (purple) and TCNQ (yellow) in $CH_3CN$.

EPR measurements were carried out in a benzene solution of **(3.28)** at Brock University by Prof. A. van der Est. The EPR spectrum shows one broad signal, which suggests that the $TTF^{\cdot+}$ and verdazyl radical spins are most likely cancelling each other out and we are only seeing a contribution from the $TCNQ^{\cdot-}$ radical anion in the spectrum. The broad singlet in Figure 3.21 is observed in both solution and solid state EPR studies and is consistent with EPR measurements carried out on $Cu^{+}TCNQ^{-}$.[140]

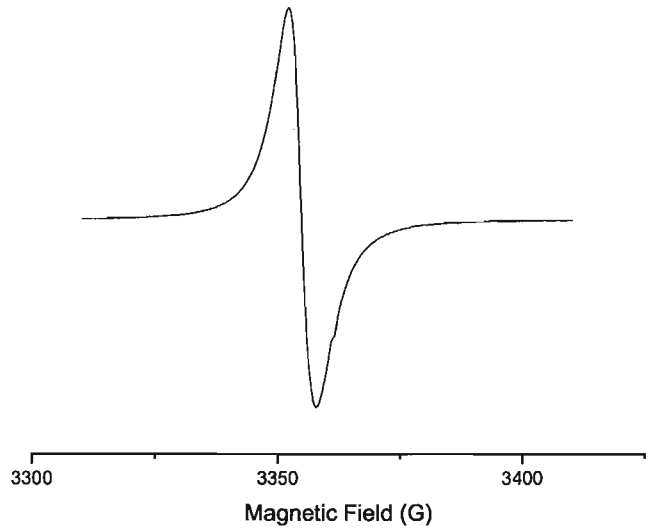


**Figure 3.21:** EPR spectrum of **(3.28)** in benzene at 298 K.

The molecular structure of the charge transfer salt **(3.28)** has been determined by X-ray crystallography. As mentioned previously, dark purple single crystals suitable for X-ray diffraction were obtained from the reaction mixture. The molecular structure of the CT salt **(3.28)** is shown in Figure 3.22. A summary of the bond lengths and angles is presented in the Appendix section, Tables 6.10 and 6.11, respectively. The molecule crystallizes in the triclinic space group P-1 with two independent TTF molecules and one independent TCNQ molecule in the unit cell. In this respect, it is clear that the complex has (2:1) stoichiometry. Although the crystal structure solved readily, refining the data was far from trivial. A detailed analysis of the geometry of the two independent donor molecules reveals that they are almost identical, just differing slightly in the degree of twisting of the verdazyl radical from the plane of the pyridine ring. This can be seen by examining the torsion angles between the verdazyl radical and the pyridine ring which are 163.4° and 157.2° for molecules **A** and **B**, respectively. Without these differences, the two molecules would be structurally equivalent, related by symmetry and the asymmetric unit would comprise of just one independent TTF donor and half of a TCNQ

molecule. Given the similarity of the structures of the two molecules, two space groups monoclinic, $P2_1/c$ and the lower symmetry, triclinic, P-1 are reasonable for this structure. Since $P2_1/c$ gives pseudo symmetry, and ignores the differences in the verdazyl-pyridyl torsion angles, the lower symmetry space group, P-1 was selected. The torsion angle between the TTF and pyridine moieties are 177.2° and 178.8° for molecules **A** and **B**, respectively. In this respect, the TTF and pyridine moieties are co planar.

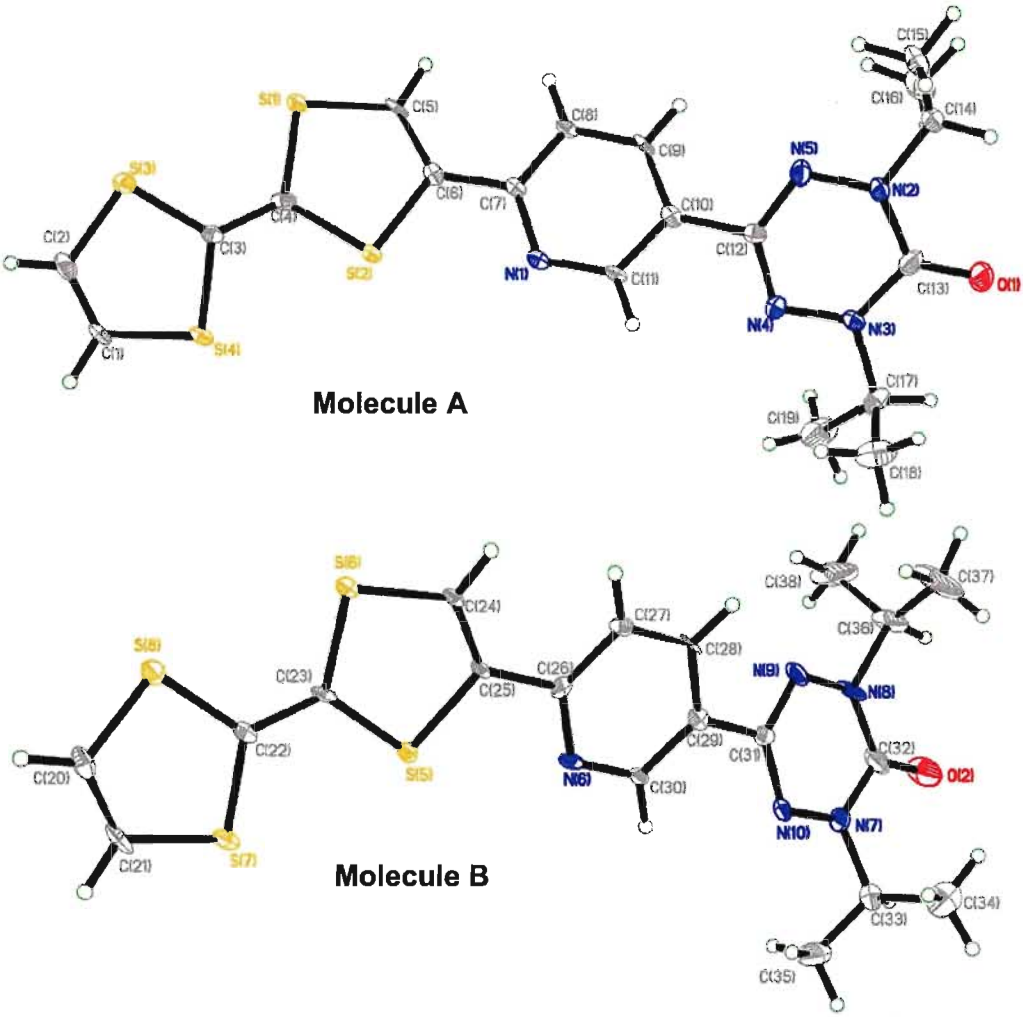


**Figure 3.22:** ORTEP[110] representation of the molecular structures of the two independent donor TTF molecules in the CT salt **(3.28)**. Thermal ellipsoids are plotted at 50%. The TCNQ is omitted for clarity.

As previously mentioned, computational studies were carried out to examine the effect torsion angles would have on the sign and magnitude of the *J* value for the diradical cation with a benzene rather than a pyridyl linker, Figure 3.23.[93] It was determined that as the TTF and verdazyl moieties twist out of the plane of the linker molecule, the *J* value decreases.[93] The *para*-substituted linker has been theoretically predicted to exhibit a ferromagnetic exchange when disregarding the effect of the torsion angles.[93] The magnitude of *J vs.* torsion angle for the *para*-substituted benzene linker is plotted in Figure 3.23. The torsion angles for donor molecule **A** in the charge transfer complex are $\theta_{SC1} = 2.8°$ and $\theta_{SC2} = 16.6°$. Extrapolating from the graphs, it is predicted that molecule **A** should have a *J* value of roughly 75 K. Molecule **B** has similar torsion angles of $\theta_{SC1} = 1.2°$ and $\theta_{SC2} = 22.8°$, since the *J* value is not significantly affected when the torsion angle is less than 45° molecule **B** is also predicted to have a positive *J* value with a magnitude of about 75 K.[93]

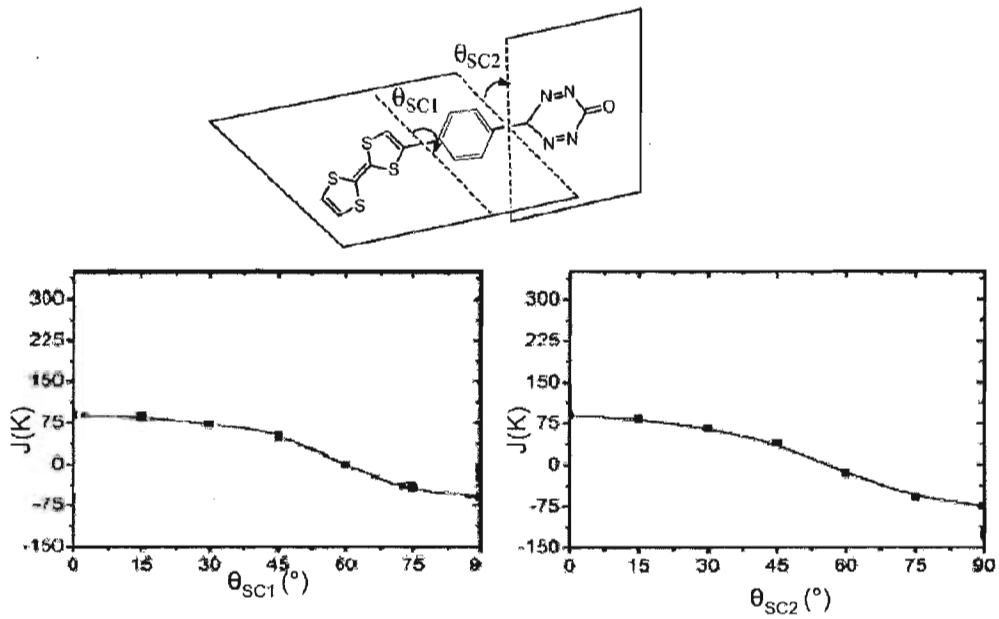


**Figure 3.23:** B3LYP/6-31G(d,p) calculated *J* values for a TTF-benzene-verdazyl diradical cation upon torsion of TTF and verdazyl groups ($\theta_{SC1}$ and $\theta_{SC2}$).[93] Adapted from Scheme 3 and Figure 2 of reference 93.

The crystal packing diagram for the CT salt **(3.28)** is shown in Figure 3.24. The molecules pack in a D-D-A-D-D-A arrangement of mixed stacks.

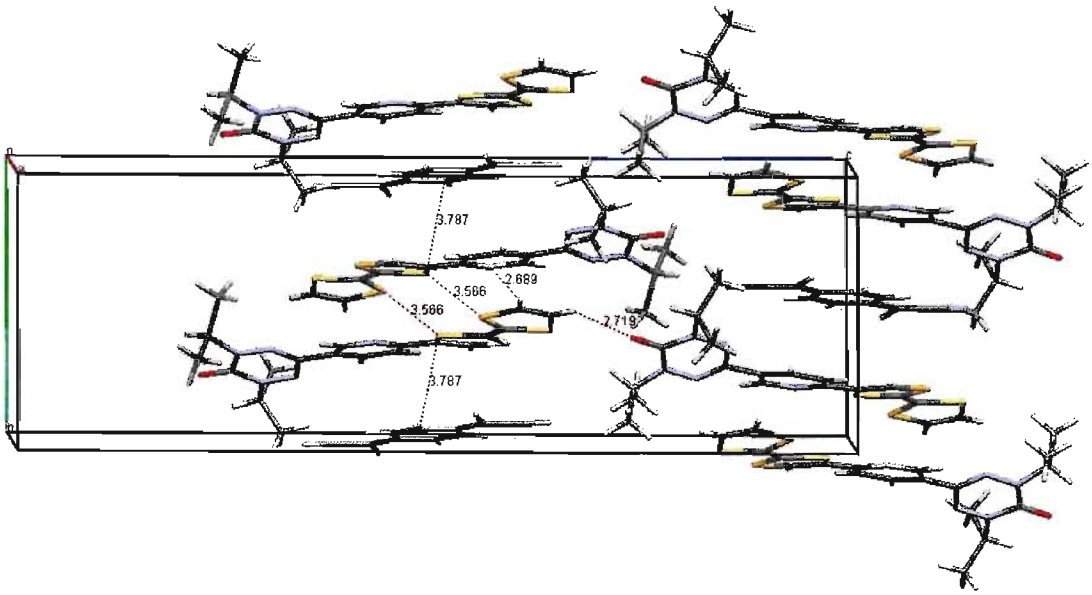


**Figure 3.24:** Packing diagram for the CT salt **(3.28)**. View down the *b*-axis. S····S and H-bonding interactions are shown as red dashed lines, distances are given in Å.[111]

π-π Interactions between TCNQ acceptor molecules and TTF donors within a stack are 3.787 Å, Figure 3.24. There are also short intermolecular S···S contacts (3.560 Å) between TTF donor molecules within a stack. Medium strength H-bonding interactions are present between the C-H protons of a TTF molecule and the nitrogen atom of a pyridine ring (N···H-C = 2.689 Å). There is also a slightly longer H-bond between the protons of a TTF molecule and the adjacent carbonyl oxygen atom of a verdazyl radical (O···H-C = 2.719 Å), Figure 3.25. This particular packing arrangement is not consistent with that of the well known TTF-TCNQ organic conductor, which assembles into segregated stacks of donor and acceptor molecules, Figure 3.25.[85]

The crystal packing diagram for the CT salt **(3.28)** is shown in Figure 3.24. The molecules pack in a D-D-A-D-D-A arrangement of mixed stacks.

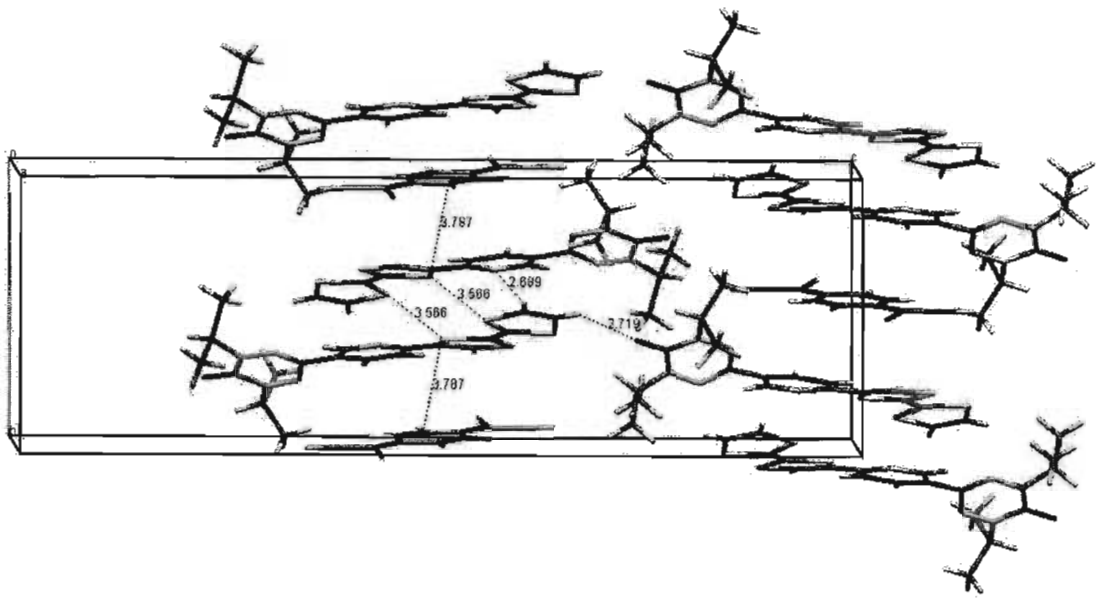


**Figure 3.24:** Packing diagram for the CT salt **(3.28)**. View down the *b*-axis. S····S and H-bonding interactions are shown as red dashed lines, distances are given in Å.[111]

π-π Interactions between TCNQ acceptor molecules and TTF donors within a stack are 3.787 Å, Figure 3.24. There are also short intermolecular S···S contacts (3.560 Å) between TTF donor molecules within a stack. Medium strength H-bonding interactions are present between the C-H protons of a TTF molecule and the nitrogen atom of a pyridine ring (N···H-C = 2.689 Å). There is also a slightly longer H-bond between the protons of a TTF molecule and the adjacent carbonyl oxygen atom of a verdazyl radical (O···H-C = 2.719 Å), Figure 3.25. This particular packing arrangement is not consistent with that of the well known TTF-TCNQ organic conductor, which assembles into segregated stacks of donor and acceptor molecules, Figure 3.25.[85]

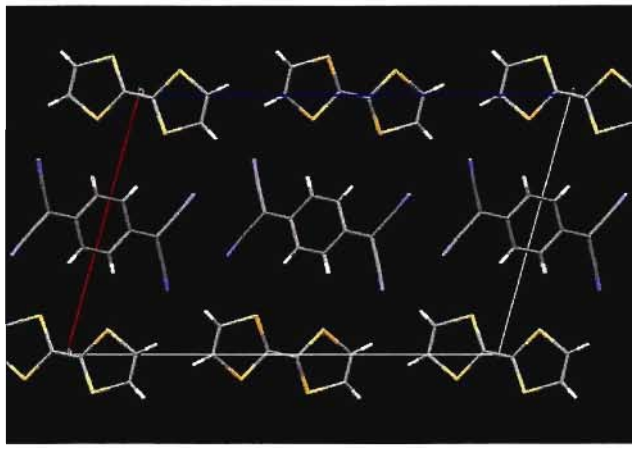

**Figure 3.25:** Packing arrangement of a TTF-TCNQ CT salt with known conductivity.[85]

The alignment of donor and acceptor molecules into segregated stacks is the optimal packing arrangement facilitating a conduction pathway for the itinerant electrons.[134] It is reported that if the donor and acceptor molecules alternately stack in a mixed fashion, then conductivity cannot be achieved since the unpaired electrons tend to localize on the acceptor molecule sandwiched between the donor molecules.[134]

Although in earlier years, the degree of charge transfer in these materials was primarily investigated by IR spectroscopy, in more recent times, the C-S bond lengths determined from the X-ray crystal structure analysis have been studied as a more accurate indication of the degree of charge transfer. In this respect, Clemente *et al.* reported that the C-S (*) bond lengths of TTF donors are more affected by the degree of charge transfer than the C-C and C=C bond lengths, Figure 3.26.[141] Clemente *et al.* found that the C-S bond length is very sensitive to the charge on the TTF molecule.[141] It was determined that upon oxidation of the TTF molecule, the C-S bond lengths decrease.[141]

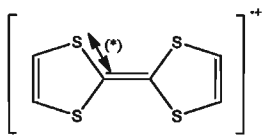


**Figure 3.26:** C-S bond length (*) used to estimate the degree of charge-transfer for a $TTF^{\bullet+}$ radical cation.

Clemente *et al.* developed a linear relationship in order to the correlate C-S bond lengths reported in literature for different $TTF^{\cdot+}$ radical cations together with their degree of charge transfer.[141] By applying Clemente's linear formula we can estimate that molecule **A** donates about 0.218 of charge to the TCNQ acceptor and molecule **B** about 0.211. Comparing this data with the 0.5 charge transfer estimated from the IR data, it seems reasonable to conclude that the amount of charge transfer in the complex is around 0.5. In this respect, each independent TTF donor donates about a quarter of an electron to the TCNQ acceptor.

Analysis of the structural data leads us to conclude that we have prepared a charge transfer salt where a quarter of an electron from each of the donor molecules is transferred to the TCNQ acceptor. Given the crystal packing, it is most likely that the CT salt will possess insulator properties, but considering the planar geometry of the molecule and the substitution pattern of the pyridyl ring, it is likely that the two radicals within the donor diradical cation will interact in a ferromagnetic manner. In order to confirm this, conductivity and magnetic susceptibility studies were carried out.

### 3.6 Magnetism and conductivity measurements of the CT salt (3.28)

Analysis of the conducting properties of the CT salt **(3.28)**, were carried out in collaboration with Dr. S. Turner at the University of Surrey. Measurements were performed on single crystals using a Keithley 2001 multimeter, with gold wires attached to the surface of the crystal by carbon conducting cement. The resistance of the (2:1) CT salt **(3.28)** was measured at 290 K and it was determined that the material exhibits insulating behavior. This is in complete agreement with the structural data since the

crystal packing arrangement does not provide a suitable conduction pathway for the itinerant electrons of the TTF radical cations.

Preliminary magnetic measurements for **(3.28)** were carried out on crushed single crystals from 5 to 300 K, by Prof. M. Lemaire on the SQUID magnetometer at Brock University, Figure 3.27.

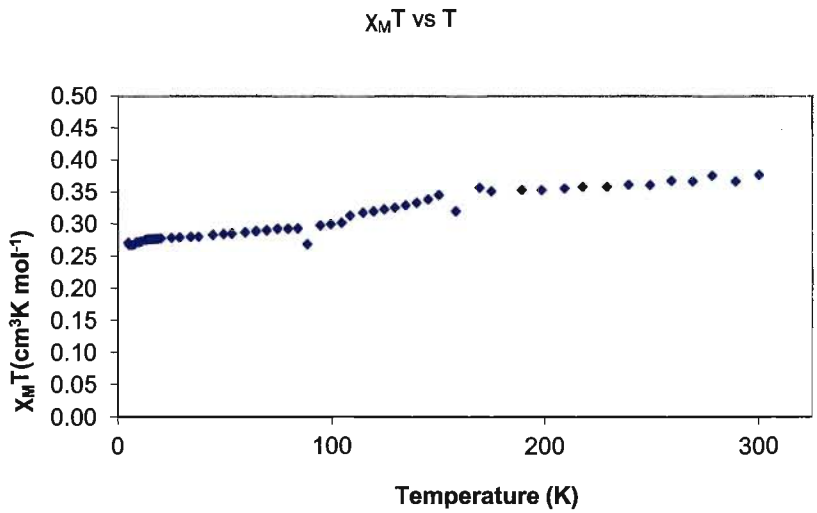


**Figure 3.27:** A plot of $\chi_M$T vs. T for the CT salt **(3.28)**.

The value of $\chi_M$T at 300 K is 0.376 cm$^3$ K mol$^{-1}$ is consistent with a single unpaired electron. As the temperature is decreased, the magnetic susceptibility decreases to reach a minimum of 0.269 cm$^3$ K mol$^{-1}$ at 5.35 K. Clearly since this material is not a conductor, all of the charged species can potentially contribute to the overall magnetism as they all individually have localized unpaired electron density. Since at 300 K, we observe the equivalent of one electron per mole in the susceptibility data, then there must be antiferromagnetic interactions that give a lower $\chi_M$T value than the maximum. This antiferromagnetism could intuitively come from intermolecular interactions between TTF-py-verdazyl moieties, or an intramolecular exchange within these molecules. The

geometry of the donor molecules together with theoretical calculations support intramolecular ferromagnetic exchange[93], so this implies that it is most likely intermolecular antiferromagnetism that is reducing the contribution. Meaning, that if there is perfect pairing, the TTF dimers will not be paramagnetic. The EPR data supports this explanation showing a signal for TCNQ only, i.e. nothing from the TTF radical cation or the verdazyl radical, although we cannot completely rule out that these are being masked by the broad TCNQ signal. From our data it also does not look like this effect completely negates all the paramagnetic contribution from the TTF-py-verdazyl. In this respect, the overall magnetism comes from the TCNQ $0.5^-$ anions (max S=1/4, i.e. half of an electron, since $TCNQ^{\cdot -}$ contributes S=1/2), with the remainder from a partial contribution from the cation "dimers", but mitigated by weak antiferromagnetic exchange between them, weak since they do not entirely cancel each other, which fits with them being not too close to each other in the X-ray crystal structure, Figure 3.28.

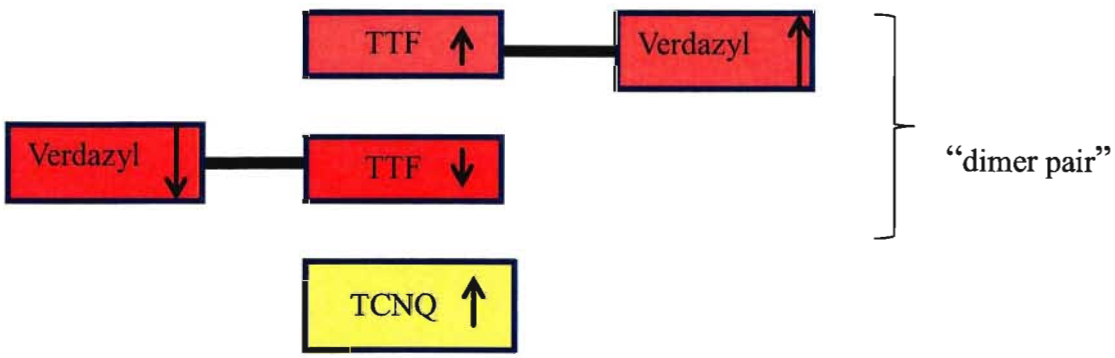


**Figure 3.28:** Cartoon representation of the magnetic interactions in the charge transfer salt **(3.28)**.

### 3.7 Preparation of a TTF-divinylene-(diisopropyl)verdazyl radical (3.9)

The next step in the project was to investigate whether or not extending the conjugation of the ethylene linker affords stronger ferromagnetic interactions between the TTF and verdazyl radicals of the molecule. A new divinylene bridged donor **(3.9)**, was

prepared following the synthetic strategy presented in Scheme 3.2. TTF **(3.10)** was reacted with the aldehyde precursor (*N*-methyl-*N*-phenylamino)-2,4-pentadienal **(3.29)** to yield TTF-divinylene-aldehyde **(3.30)** as a red solid in 57% yield.[142] Treatment of **(3.30)** with 2,4-diisopropylcarbonohydrazide *bis*-hydrochloride **(3.11)**, and sodium acetate resulted in the isolation TTF-divinylene-(diisopropyl)tetrazane **(3.31)** as a red-brown oil in 58% yield. The tetrazane **(3.31)** was then oxidized by treatment with 1,4-benzoquinone in benzene affording the desired radical as a (1:1) mixture with hydroquinone. The mixture was separated by flash chromatography immediately after oxidation, to afford the TTF-divinylene-(diisopropyl)verdazyl radical **(3.9)** as a dark purple solid in 59% yield.

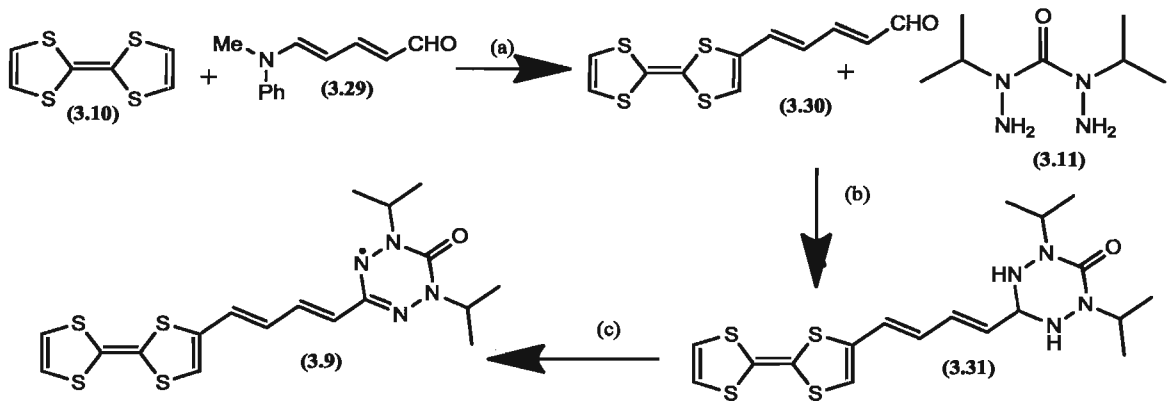


**Reagents and conditions**
(a) LDA, THF, -78°C; (b) MeOH, NaOAc, reflux overnight; (c) 1,4-benzoquinone, $C_6H_6$, 60°C, 1 h.

**Scheme 3.2:** Synthetic procedure for the preparation of the TTF-divinylene-(diisopropyl)verdazyl radical **(3.9)**.

### 3.8 Characterization of the TTF-divinylene-(diisopropyl)tetrazane (3.31)

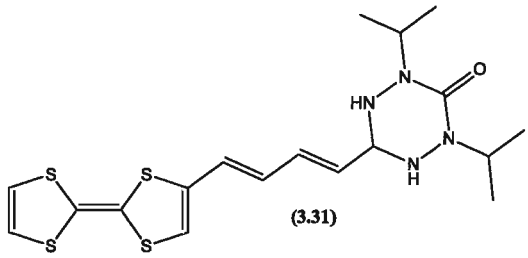


(3.31)

As mentioned for the pyridyl series, the tetrazane is the key intermediate in the preparation of the verdazyl radical since it can be prepared and stored in large quantities and is very stable to air and moisture. The tetrazane **(3.31)** has been fully characterized. The FAB mass spectrum shows a parent ion at $m/z$ = 440, consistent with its molecular structure. The IR spectrum has a C=O str at 1639 $cm^{-1}$ characteristic for the carbonyl of the tetrazane. Interestingly, no bands at 3400 $cm^{-1}$ were visible for the NH str of the tetrazane moiety. It was difficult to purify the final tetrazane **(3.31)** for accurate elemental analysis, even after several attempts by column chromatography. The 300 MHz $^1H$ NMR spectrum of the tetrazane is shown in Figure 3.29. The two singlets at 6.89 ppm and 6.75 ppm can be assigned to the TTF C-H protons at C-5, and C-1,2, respectively. The doublet at 6.66 ppm corresponds to the vinylene proton at C-8. The multiplet at 6.47 ppm is assigned to the vinylene proton at C-7. The two doublet of doublets at 6.12 ppm and 5.82 ppm are also assigned to the vinylene protons at C-9 and C-10, respectively. The doublet at 4.74 ppm and the multiplet at 4.43 ppm are assigned to the CH protons at positions C-11 and C-13, respectively. The broad peak at 3.96 ppm corresponds to the NH protons and the multiplet at 0.99 ppm is assigned to the isopropyl protons on C-14 and C-15.

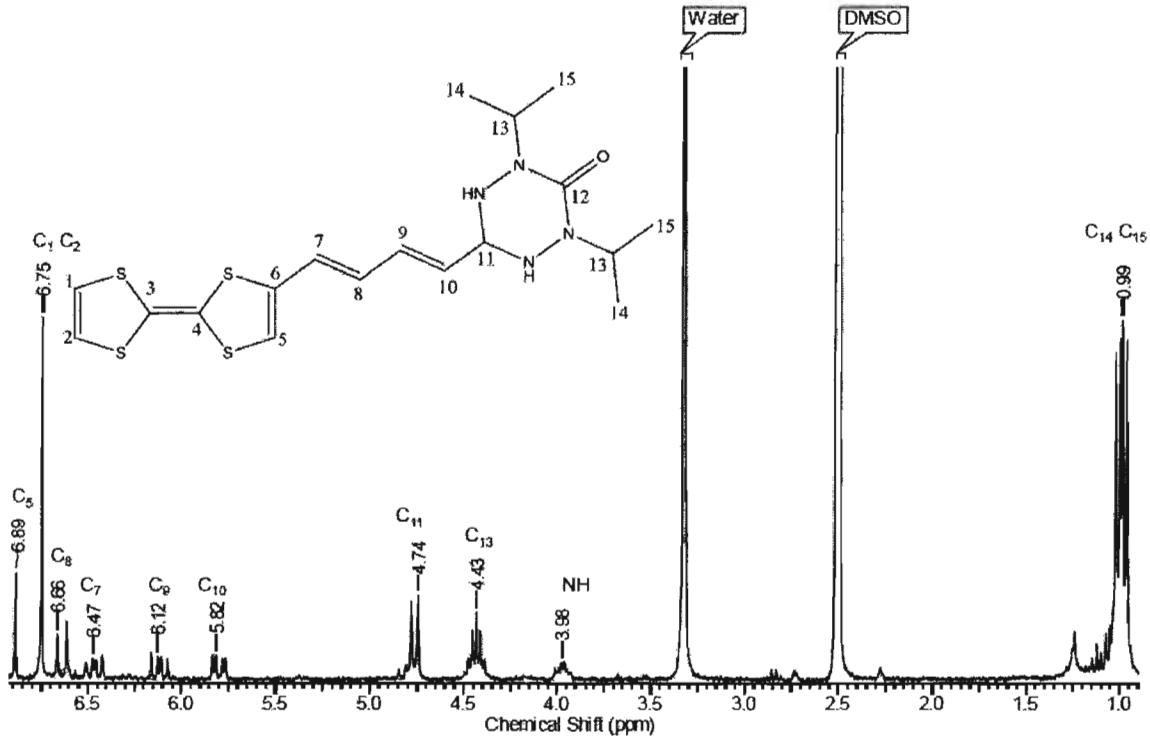


**Figure 3.29:** 300 MHz $^{1}$H NMR spectrum of TTF-divinylene-(diisopropyl)tetrazane **(3.31)** in DMSO.

The cyclic voltammogram of the tetrazane **(3.31)** shows two quasi-reversible oxidation potentials, Figure 3.30. The potentials at 0.54 V and 0.79 V are consistent with those presented for the 2,5-TTF-py-(diisopropyl)tetrazane **(3.17)**.[82] The additional irreversible wave seen at 0.74 V, partially overlapping with the second oxidation potential of the TTF moiety, corresponds to the electrochemical oxidation of the tetrazane to the verdazyl radical.[92] The oxidation potentials for the divinylene tetrazane **(3.31)** are similar to the results observed for the previously reported TTF-π-(diimethyl)tetrazane **(3.33)**.[92]

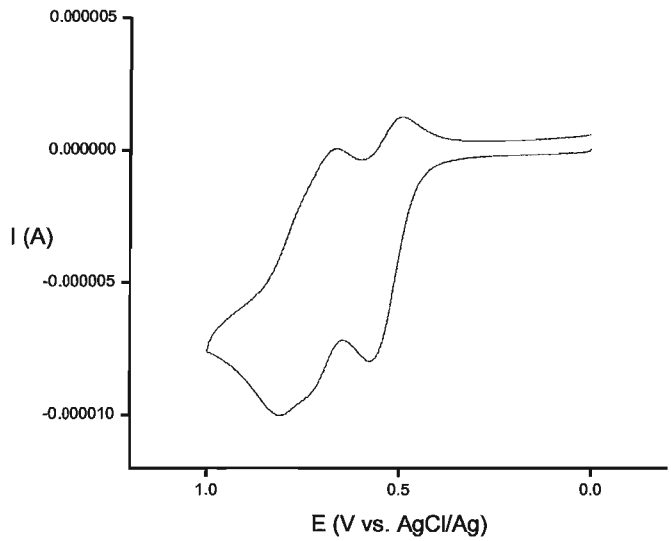


**Figure 3.30:** Cyclic voltammogram of TTF-divinylene-(diisopropyl)tetrazane **(3.31)** in DMF at 0.1 V/s using a glassy carbon electrode as the working electrode, Ag/AgCl as a reference and tetrabutylammonium hexafluorophosphate (0.1 M) as the supporting electrolyte.

The divinylene-radical **(3.9)** was characterized by IR-spectroscopy, and FAB-MS. The FAB mass spectrum shows a parent ion at *m/z* = 437 $[M]^+$, consistent with the molecular structure. The IR spectrum shows a stretch at 1664 $cm^{-1}$ characteristic for the carbonyl group of the verdazyl radical which is red shifted in comparison to its tetrazane **(3.31)**.

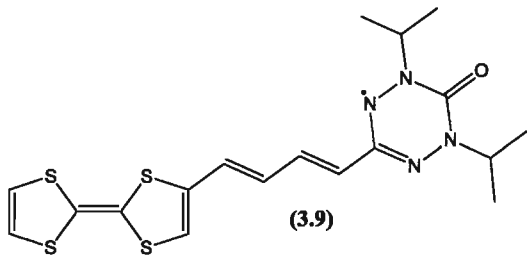


**(3.9)**

The electronic properties of the aldehyde **(3.30)**, tetrazane **(3.31)** and verdazyl radical **(3.9)** have been studied by UV-Vis spectroscopy, Figure 3.31.

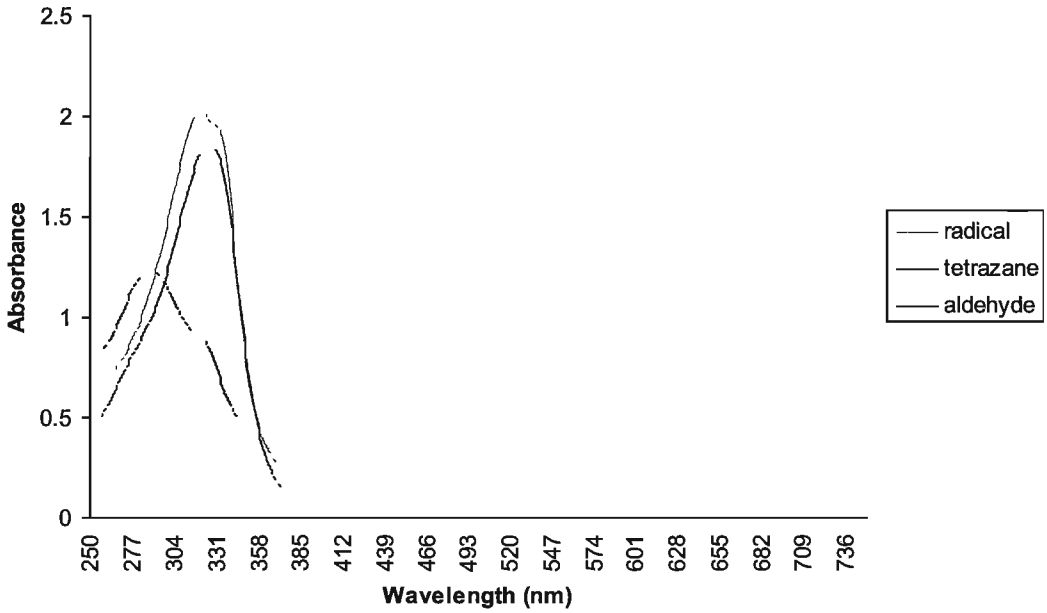


**Figure 3.31:** UV-Vis spectrum of **(3.30)**, **(3.31)** and **(3.9)** in $CH_3CN$.

Two absorption bands appear at $\lambda_{max}$ = 320 and 495 nm for the aldehyde **(3.30)**, $\lambda_{max}$ = 280 and 420 nm for the tetrazane **(3.31)** and $\lambda_{max}$ = 325 and 440 nm for the radical **(3.9)**. The UV-Vis spectrum for the tetrazane **(3.31)** appears to be blue shifted in comparison with the aldehyde **(3.30)** and the verdazyl radical **(3.9)**. The band around $\lambda$ = 280-325 nm has been previously assigned to is assigned to the lowest $\pi$-$\pi^*$ intramolecular transitions of the conjugated $\pi$-system of the TTF..[93] The molar absorptivities for the second band are 301, 426, and 528 $M^{-1}cm^{-1}$ for **(3.30)**, **(3.31)**, and **(3.9)**, respectively. The second absorption band is also shifted for the three different systems, as it does for the ethylene bridge results. This second broader band is assigned to the presence of an intramolecular charge transfer (ICT) from the TTF moiety to the acceptor group.[92] Generally, the strongest acceptor gives rise to the lowest energy ICT band, in this respect, the verdazyl radical is a slightly better electron withdrawer than the tetrazane.[92] This is contrary to the results determined for the TTF-$\pi$-verdazyl radical where the tetrazane

**(3.33)**, is a slightly better electron withdrawer when compared to verdazyl radical **(3.2)**.[92] The $\lambda_{max}$ values for the aldehyde **(3.30)** and the verdazyl radical **(3.9)** appear to be red shifted in comparison to the previously reported TTF-π-aldehyde **(3.32)**, and TTF-π-verdazyl radical **(3.2)**, Figure 3.32.[92] However, the tetrazane **(3.31)** appears to be blue shifted in comparison to the TTF-π-tetrazane **(3.33)**, Figure 3.32.[92] It can be concluded from these results that the more conjugated TTF-divinylene-(diisopropyl)verdazyl radical **(3.9)**, is a better electron withdrawer than the TTF-π-verdazyl radical **(3.2)**.

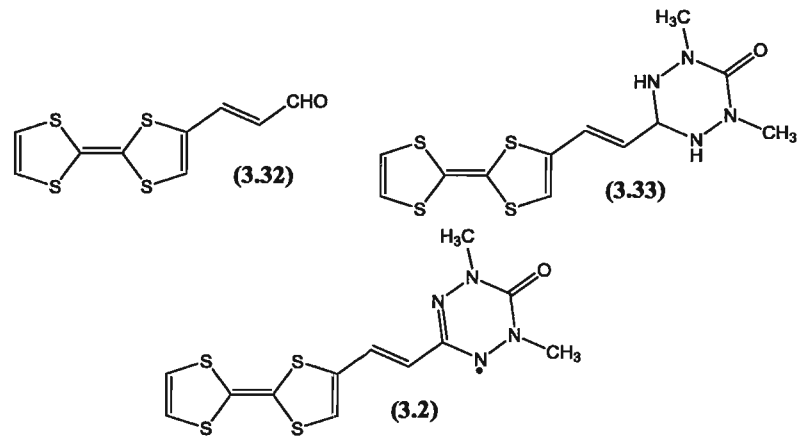


**Figure 3.32:** Molecular structures of TTF-π-aldehyde (**3.32**); TTF-π-(dimethyl)-tetrazane (**3.33**); and TTF-π-(dimethyl)verdazyl radical (**3.2**).[92]

The cyclic voltammogram of the TTF-divinylene-(diisopropyl)verdazyl radical **(3.9)** can be seen in Figure 3.33. It shows two quasi-reversible oxidation potentials at 0.57 V and 0.81 V assigned analogous to radical **(3.5)**. The additional irreversible wave at 0.75 V corresponds to the oxidation of the verdazyl radical. It is noticeable that the oxidation potential of the verdazyl radical **(3.9)**, is anodically shifted when compared to the value of >0.800 V reported for Pilkington *et al.*'s TTF-π-verdazyl radical **(3.2)**.[92] Therefore, an electron can be more easily removed from the divinylene bridged system in comparison to the π-bridged system.

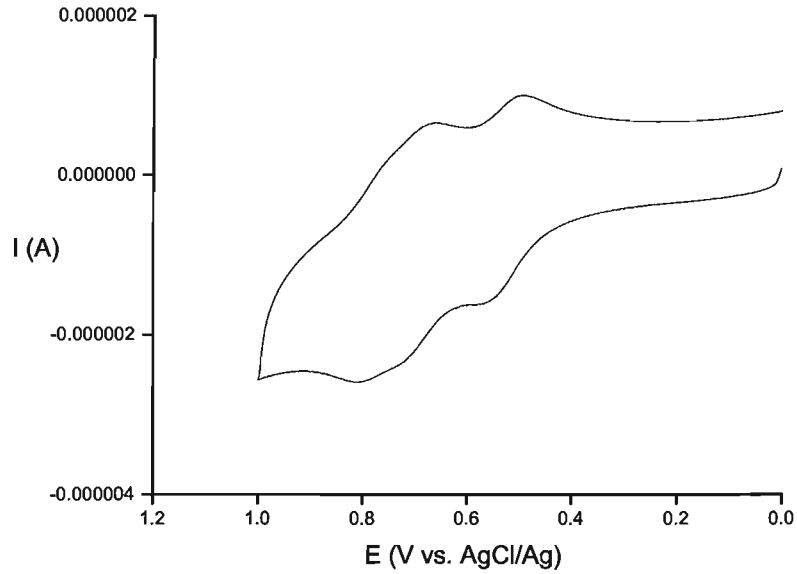


**Figure 3.33:** Cyclic voltammograms of the TTF-divinylene-(diisopropyl)verdazyl radical (**3.9**) in DMF at 0.1 V/s using a glassy carbon electrode as the working electrode, Ag/AgCl as a reference and tetrabutylammonium hexafluorophosphate (0.1 M) as the supporting electrolyte.

The divinylene-verdazyl radical **(3.9)** was characterized by EPR spectroscopy. The spectrum shows the expected hyperfine splitting pattern consistent with the formation of the verdazyl radical.[125]

### 3.9 Molecular structure of TTF-divinylene-(diisopropyl)verdazyl radical (3.9)

Single crystals of **(3.9)** suitable for X-ray crystallography were grown via the slow evaporation of a DCM solution of the radical. Dark brown needles were obtained after a few days. The molecule crystallizes in the monoclinic space group $P2_1/n$, with one independent molecule in the unit cell, Figure 3.34. As expected, the molecules are close to planar. The torsion angle between the best plane of the verdazyl radical and the divinylene chain is 165.1° and the torsion angle between the best plane of the TTF donor and the divinylene chain is 173.6°. A summary of the bond lengths and angles for **(3.9)** are presented in the Appendix, Tables 6.12 and 6.13.

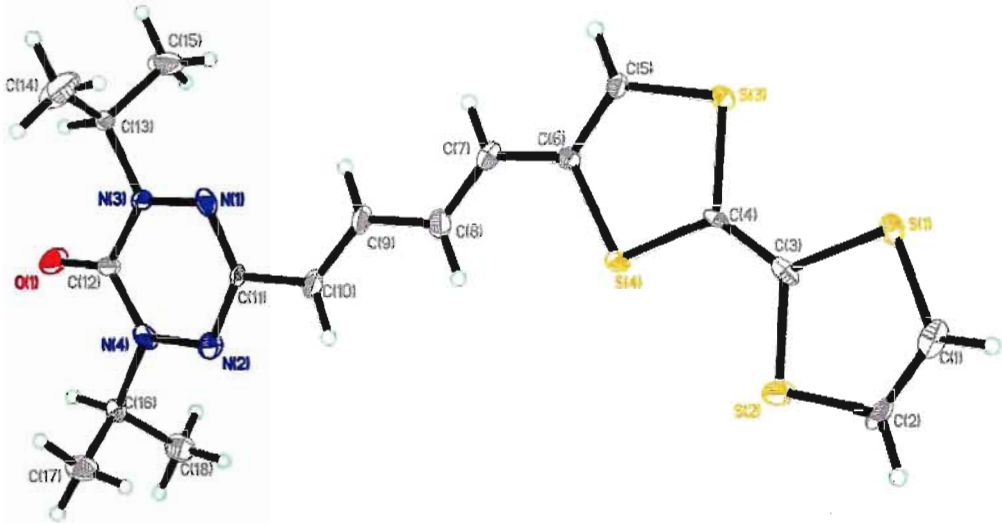


**Figure 3.34:** ORTEP[110] representation of the molecular structure of the TTF-divinylene-(diisopropyl)verdazyl radical **(3.9)**; thermal ellipsoids are plotted at 50%.

The crystal packing for **(3.9)** is shown in Figure 3.35. The radicals pack nicely in a head-to-head arrangement of "dimers" forming stacks. Close examination of the packing arrangement reveals that the distance between adjacent donor molecules is not uniform, Figure 3.35.

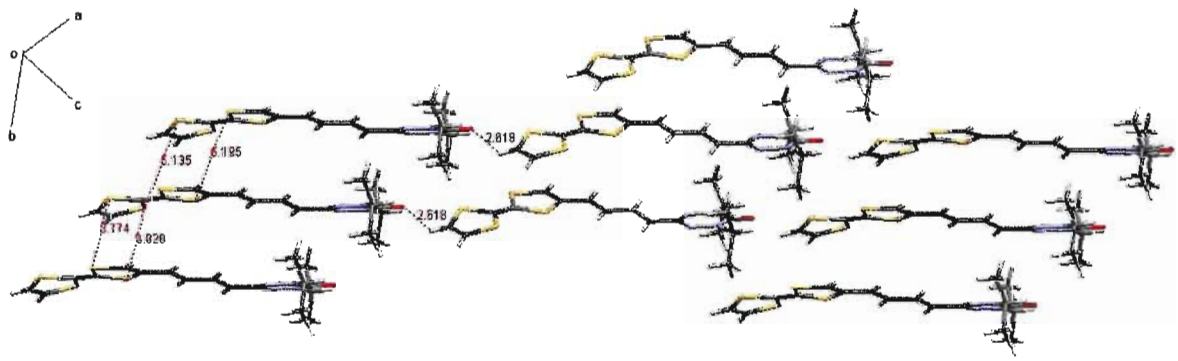


**Figure 3.35:** Packing arrangement of the TTF-divinylene-(diisopropyl)verdazyl radicals **(3.9)**. View down the a-axis. S···S contacts and H-bonding interactions are shown as red dashed lines. Distances are given in Å.[111]

The S···S distances between two "dimeric units" within a stack are 3.774 and 3.820 Å. The S···S distances between neighbouring donors of "dimeric units" are much

longer, being 5.135 and 5.195 Å. There is only one significant H-bond in the structure involving the C-H proton of a TTF molecule and the carbonyl oxygen atom from a neighbouring verdazyl radical (C=O···H = 2.618 Å), Figure 3.35.

Having the TTF molecules stack in a segregated fashion is optimal for the formation of a conduction pathway, so this is promising for the assembly of ferromagnetic conductors. The disadvantage of this system are the bulky isopropyl groups that seem to be hindering the molecules from packing more closely together and perhaps also dictating the offset packing arrangement.

When drawing a comparison between the pyridine and divinylene linked molecules in the solid state, it can be noted that the most significant difference is their packing arrangement. The pyridine radicals **(3.5)** and **(3.6)** pack in a head-to-tail fashion with dimer pairs. The divinylene radical **(3.9)** packs also as dimer pairs but in head-to-head stacks where the donor molecules are aligned. These studies demonstrate how changing the linkers has a significant influence on the structural and therefore the physical properties of these systems, since their electronic and magnetic properties are strongly influenced by the packing arrangements of the molecules in the solid state. The divinylene linker seems promising, promoting a head to head stacking arrangement of donors in the solid state. Attempts to grow single crystals of charge transfer salts of this donor radical have not been successful to-date, but efforts to study charge transfer salts of this donor radical and the preparation of radical cation salts by electrocrystallization methods are in progress.

### 3.10 Conclusion and Future Work

To conclude, four novel TTF-py-(diisopropyl)verdazyl radicals have been prepared and characterized. Within the timeframe of this MSc thesis, attention was focused on the characterization and the preparation of charge transfer salts from the 2,5-py-verdazyl **(3.5)** and the 2,6-py-verdazyl **(3.6)** radicals. The molecular structures of both radicals have been elucidated by X-ray crystallography. The growth of single crystals of a (2:1) charge transfer salt of the 2,5-TTF-(diisopropyl)verdazyl radical together with TCNQ was successful and its structure has been elucidated by X-ray crystallography. Resistivity measurements support the crystal packing arrangement in that there is no conducting pathway so the molecule is a rather good insulator. The degree of charge transfer between the donor and acceptor molecules has been probed via IR spectroscopy and by studying the C-S bond lengths of the donors determined from the crystal structure. Magnetic susceptibility and EPR data is consistent with a ferromagnetic ordering of spins within a molecule and antiferromagnetic interactions between neighboring dimer units that essentially reduce the magnetic contribution to just the electron spin on the TCNQ radical anion. To the best of my knowledge, this is the first example of a charge transfer complex assembled from a TTF-py-verdazyl radical that has been structurally, magnetically and electronically characterized.

A second class of compound for which the TTF donor and verdazyl radical are linked via a conjugated divinylene linker has been prepared and characterized. In this case the molecules are planar and stack in a favorable head-to-head arrangement. It is not clear at this time whether or not after oxidation of the TTF units, the bulky isopropyl groups will prevent the donors from packing close enough to facilitate orbital overlap and

allow for a conducting pathway. The design and characterization of suitable building blocks for ferromagnetic conductors is an extremely challenging project. Without being able to structurally characterize the molecules in the solid state it is difficult to understand how they organize. In order to design a more crystalline system, the use of bulkier groups is often necessary. On the one hand this helps from the crystal engineering perspective, however, the disadvantage is that the steric hindrance caused by bulky substituents can sometimes prevent the molecules from packing in a favourable manner.

As previously mentioned work on this project is ongoing. The Pilkington group is currently working to find suitable conditions for the preparation of charge transfer complexes and radical cation salts of all five TTF-verdazyl-(diisopropyl)radicals.

# CHAPTER 4- Experimental

## 4.1 General Information

All experiments were carried out using standard Schlenk line procedures unless otherwise stated. Dry solvents were used for all experiments performed under nitrogen. Anhydrous solvents were obtained from a Puresolve PS MD-4 solvent purification system. All reagents were commercially purchased from Sigma Aldrich or Alfa Aesar. Thin layer chromatography (TLC) was performed on Merck pre-coated silica oxide aluminum sheets that were 0.2 mm (thick) x 20 mm (wide) x 40 mm (long). Silica gel (75-250 Mesh, 60 Å) was purchased from Desican *Inc.* for column chromatography. Elemental analysis was carried out by Atlantic Microlab, *Inc.* Norcross, GA, USA.

## 4.2 Instrumentation

**Mass Spectroscopy:** Mass spectra (MS) were recorded on a Carlo Erba/ Kratos EC/ms Concept 1S double focusing mass spectrometer interfaced to a Kratos DART acquisition system and a SPARC workstation. Samples were introduced through a direct inlet system. The internal standard used was *tris*(perfluoroheptyl)-S-triazine.

**Melting Point:** All solids were determined using a Stuart Scientific SMP 10 melting point apparatus.

**UV-Vis:** Spectra were measured using a ThermoSpectronic/ Unicam UV-4 UV-Vis spectrometer equipped with a Vision data system and thermostated sampling. Unless otherwise stated UV-Vis spectra were collected at 295 K. Variable temperature UV-Vis data were collected on a Shimadzu 3600 spectrometer.

**Cyclic Voltammetry:** Measurements were performed on a BAS Epsilon potentiostat at room temperature (22 ± 2 °C) in acetonitrile containing 0.1 M of n-$Bu_4NPF_6$. Glassy carbon (diameter 3 mm) was used as the working electrode. Platinum wire and AgCl/Ag were used as counter and reference electrodes, respectively. The working electrode was polished on alumina before use. iR compensations were applied for all experiments for potential measurements.

**FT-IR:** Spectra were recorded on a ThermoMattson RS-1 spectrometer using the WinFirst data acquisition system. Samples were prepared as KBr pellets for solids and KBr plates were used for oils.

**Circular Dichroism:** Spectra were collected on a Jasco J-600 spectrometer at room temperature, using J7STDANL software.

**EPR:** Spectra were measured by Dr. Poddutoori and Sam Mula at Brock University. The spectra were recorded in solution in quartz tubes on a Bruker Elexsys E580 pulsed and CW X-band (9 GHz) spectrometers. The EPR data were modelled by Sam Mula using Easy Spin 3.1.7 simulation software.

**Conductivity:** Resistivity measurements were carried out by Dr. Scott Turner at the University of Surrey, U.K. The measurements were carried out using a Keithley 2001 multimeter with gold wires attached to the surface of the single crystal using a carbon conducting cement.

**Magnetic Susceptibility Measurements:** Magnetic measurements for the CT salt **(3.28)** were carried out by Prof. M. Lemaire at Brock University on a Quantum Design SQUID magnetometer MPMS in an applied field of 5000 G between 5 and 300 K. *DC* analyses

were performed on the polycrystalline samples, carefully weighed into gelatine capsules, which were loaded into plastic straws and attached to the sample transport rod. Magnetic data for macrocycles **(2.9)**, **(2.11)**, and **(2.12)** was collected by Dr. Cédric Desplanches and Dr. Hongfeng Wang at the CNRS in Bordeaux, France using a Quantum Design SQUID magnetometer. The magnetization was recorded from 10 to 350 K. Photomagnetic measurements on macrocycles **(2.9)** and **(2.11)** were performed by irradiating the samples with light of different wavelengths. The best photomagnetic conversion was seen after illumination of **(2.9)** with green light ($\lambda$ = 514 nm) at 10 K.

**NMR: General** - $^{1}$H and $^{13}$C-NMR spectra were recorded at 300 and 75 MHz, respectively, on a Bruker Advance AV 300 Digital NMR spectrometer in deuterated solvents in collaboration with Razvan Simunescou. Bruker TOPSPIN 2.1 PL6 software was used for data acquisition and analysis.

**Variable temperature NMR:** $^{1}$H-, $^{13}$C and 2-D-NMR spectra were recorded on a 600 MHz Bruker Advance AV 600 Digital NMR spectrometer equipped with a BBO Z-gradient ATMA probehead. Data acquisition and analysis were performed using Bruker TOPSPIN 2.1 PL6 software run on a Microsoft Windows 7 Professional platform. Variable temperature $^{1}$H-NMR spectra were recorded on paramagnetic complexes **(2.1)**, **(2.9)** and **(2.10)** with a sweep of 106.8 ppm from -40 ppm to 140 ppm. $^{13}$C-NMR spectra for the paramagnetic complexes **(2.1)**, **(2.9)** and **(2.10)** were performed with a sweep of 497.9 ppm from 0 ppm to 185 ppm. The temperature was varied from 195 to 295 K. The 1-D spectra were acquired with a sweep width of 20.5 ppm, and decoupled 1-D $^{13}$C spectra were acquired with a sweep width of 238.3 ppm. The 2-D spectra were acquired with 2048 points and 256 increments and they were processed with 1024 x 1024 points.

The number of scans acquired was 1 for COSY, 2 for HSQC and NOESY, and 4 for HMBC. NOESY spectra were acquired with 300 ms mixing time. The HC-coupling constant in the HSQC and HMBC was set to 145 Hz and the long-range coupling constant in the HMBC was set to 10 Hz.

**X-ray structure determination:** For low temperature measurements, the single crystals were suspended in paraffin oil and mounted on a nylon loop on the end of a copper pin and flash cooled on the diffractometer. X-ray data was collected on an APEX II CCD Kappa diffractometer equipped with an Oxford low temperature device. The data were processed using the Bruker SHELXTL[121] software package. The structures were solved by direct methods using the SHELXS-97 program[121]. The structures were refined using the SHELX-97 program in the Bruker SHELXTL[121] suite. Molecular structures and packing diagrams were prepared using Mercury[111] and ORTEP[110] graphics programs. The single crystal data were collected, solved and refined by Prof. M. Pilkington and Shari Venneri. We acknowledge the help of Prof. Jim Britten, at McMaster University for the refinement of the CT salt **(3.28)**.

## 4.3 Project 1

### 4.3.1 Synthesis of (5*R*,6*R*)-5,6-diphenyl-4,7-dioxa-1,9-decadiene (2.3)[108]

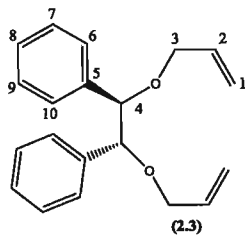

(*R,R*)-(+)-hydrobenzoin **(2.2)** (5.00 g, 23.3 mmol) was dissolved in THF (120 mL). Sodium hydride (1.80 g, 74.8 mmol) was added to the solution and the reaction mixture was stirred for 1 h at 30 °C. A solution of allyl bromide (6.94 mL, 82.1 mmol) in THF (20 mL) was then added slowly over 30 min, after which time the reaction mixture was stirred and heated to 40 °C for 2 h and then refluxed at 90° C for an additional 24 h. The progress of the reaction was monitored by TLC (DCM/MeOH (9.5:0.5)) ($R_f$ = 1). When no starting material remained, the reaction was allowed to cool to room temperature. A white precipitate was then removed by filtration and discarded and the filtrate was evaporated to dryness. The resulting yellow oil was dissolved in DCM (100 mL), washed with $H_2O$ (2 x 50 mL), brine (2 x 50 mL), and dried over $MgSO_4$. Removal of the solvent under reduced pressure afforded **(2.3)** as a pale yellow oil (4.98 g, 73% yield).

| | |
|---|---|
| FAB-MS: | *m/z* = 294 $[M]^+$ (0.60%). |
| HRMS (FAB): | Found *m/z* = 294.1625 $[M]^+$; Calcd. 294.1620 for $C_{20}H_{22}O_2$. |
| $^1$H NMR ($CDCl_3$, 300 MHz) δ (ppm): | 7.21 (s, 6H, 7, 8, 9-H), 7.10 (s, 4H, 6, 10-H), 5.91 (m, 2H, 2-H), 5.27 (d, *J* = 15.59 Hz, 2H, 1-H), 5.15 (d, *J* = 9.23 Hz, 2H, 1-H), 4.54 (s, 2H, 4-H), 4.07 (dd, *J* = 13.19 Hz, 1H, 3-H), 3.92 (dd, *J* = 13.56 Hz, 1H, 3-H). |
| $^{13}$C NMR ($CDCl_3$, 75 MHz) δ (ppm): | 138.8 (5-C), 135.1 (6-C, 10-C), 128.1 (7-C, 9-C), 127.7 (8-C), 127.4 (2-C), 116.5 (1-C), 85.1 (4-C), 70.2. (3-C). |
| IR (KBr, $cm^{-1}$): | 3084, 3063, 2861, 1646, 1453, 1080, 942, 701. |

### 4.3.2 (4*R*,5*R*)-4,5-diphenyl-3,6-dioxa-1,8-octanediol (2.4)[108]

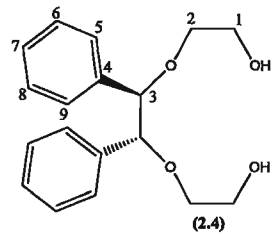


(2.4)

Compound **(2.3)** (6.48 g, 22.0 mmol) and $OsO_4$ (0.16 g, 0.648 mmol) in a (3:1) mixture of THF/$H_2O$ (80 mL) were stirred in the dark at room temperature for 4 h. $NaIO_4$ (27.54 g, 0.129 mol) was then added portionwise and the mixture was allowed to stir in the dark for an additional 20 h. TLC was used to monitor the progress of the reaction (pet. ether/ether (25:1)) ($R_f$ = 1). Upon completion, the solvent was removed and the remaining product was dissolved in a (1:1) mixture of DCM/MeOH (250 mL) and gravity filtered affording a pale brown solution. The solution was stirred vigorously in an ice bath during which time $NaBH_4$ (5.61 g, 0.148 mol) was added cautiously over a 1 h period. The reaction mixture was then stirred for an additional 19 h at room temperature. The progress of the reaction was monitored by TLC (DCM/MeOH (10:1)) ($R_f$ = 0.3). On completion, the solvent was removed, and the crude product was dissolved in $H_2O$ (500 mL) and stirred in a beaker for 1 h. The product was extracted into DCM (3 x 300 mL) and the organic phase was washed with 1 M HCl (2 x 50 mL), water (2 x 50 mL) and brine (2 x 50 mL), and then dried over $MgSO_4$. The solvent was then removed under reduced pressure to afford the crude product that was purified via column chromatography on silica gel, eluting with a (20:1) mixture of $CHCl_3$/MeOH to give **(2.4)** as a yellow oil (5.64 g, 84% yield).

FAB-MS: $m/z = 303\ [M+H]^+$ (7%)

| | |
|---|---|
| HRMS (FAB): | Found *m/z* = 303.1596 $[M]^+$; Calcd. 303.1582 for $C_{18}H_{23}O_4$. |
| $^1H$ NMR ($CDCl_3$, 300 MHz) δ (ppm): | 7.21 (s, 6H, 7-H, 8-H, 9-H), 7.08 (s, 4H, 6-H, 10-H), 4.50 (s, 2H, 4-H), 3.78 (m, 4H, 3-H), 3.71 (m, 2H, 2-H), 3.52 (m, 2H, 2-H), 3.04 (s, 2H, 1-H). |
| $^{13}C$ NMR ($CDCl_3$, 75 MHz) δ (ppm): | 138.3 (5-C), 128.2 (6-C, 10-C), 127.9 (7-C, 9-C), 127.6 (8-C), 86.9 (4-C), 71.2 (3-C), 61.8 (2-C). |
| IR (KBr, $cm^{-1}$): | 3490, 3344, 3030, 2869, 1709, 1453, 1363, 1222, 1067. |

### 4.3.3 (4*R*,5*R*)-4,5-diphenyl-3,6-dioxa-1,8-octanediphthalimide (2.5)

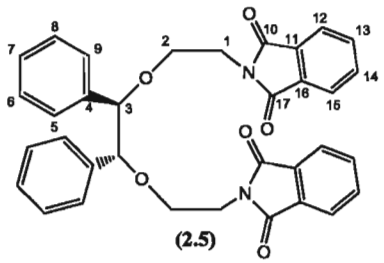


Diisopropyl azodicarboxylate (DIAD) (8.11 g, 40.1 mmol) dissolved in THF (20 mL) was added dropwise to a solution of **(2.4)** (5.50 g, 18.2 mmol), phthalimide (5.89 g, 40.1 mmol) and triphenylphosphine (10.52 g, 40.1 mmol) in THF (140 mL). The reaction mixture was stirred at room temperature for 4 days. The progress of the reaction was monitored by TLC (hexane/ethyl acetate (2:1)) ($R_f$ = 0.7). Upon completion, the solvent was removed and the crude product was purified via flash $SiO_2$ chromatography by first eluting with a (2:1) mixture of hexane/ ethyl acetate and then redissolving the product in DCM and carrying out a second column eluting with a (3:1) mixture of petroleum ether/ethyl acetate ($R_f$ = 0.42). Removal of the solvent afforded **(2.5)** as a white solid (3.77 g, 37% yield).

| | |
|---|---|
| M.p.: | 180-182° C. |
| FAB-MS: | $m/z$ = 561 $[M+H]^+$ (7 %) |
| HRMS (FAB): | Found $m/z$ = 561.1962 $[M]^+$; Calcd. 561.2026 for $C_{34}H_{29}N_2O_6$. |
| $^1$H NMR ($CDCl_3$, 300 MHz) δ (ppm): | 7.84 (s, 4H, 12-H, 15-H), 7.74 (s, 4H, 13-H, 14-H), 6.94 (m, 6H, 6-H, 7-H, 8-H), 6.83 (d, $J$ = 7.54 Hz, 4H, 5-H, 9-H), 4.41 (s, 2H, 3-H), 3.78 (dt, $J$ = 15, 4.95 Hz, 4H, 2-H), 3.61 (t, $J$ = 5.65 Hz, 4H, 1-H). |
| $^{13}$C NMR ($CDCl_3$, 75 MHz) δ (ppm): | 168.5 (10-C), 137.9 (4-C), 134.1 (Ph), 133.2 (Ph), 127.8 (Ph), 123.2 (Ph), 85.7 (3-C), 66.2 (2-C), 37.7 (1-C). |
| CHN: | Found C: 71.65, H: 5.24, N: 4.84%; Calcd. for $(C_{34}H_{28}N_2O_6)\cdot 0.5H_2O$ C: 71.69; H: 5.13; N: 4.92%. |
| IR (KBr, $cm^{-1}$): | 3032, 2887, 1774, 1720, 1396, 1105, 1026, 711. |

### 4.3.4 (4*R*,5*R*)-4,5-diphenyl-3,6-dioxa-1,8-octanediamine (2.6)[113]

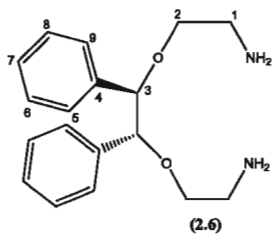


(2.6)

Hydrazine monohydrate (3.46 g, 6.90 mmol) was added to a suspension of **(2.5)** (3.87 g, 6.90 mmol) in warm ethanol (95%, 200 mL), and the reaction mixture was refluxed for 28 h. The progress of the reaction was monitored by TLC (DCM) ($R_f$ = 0.8). On completion, the mixture was cooled to room temperature and a white precipitate was removed by gravity filtration. The precipitate was washed with cold ethanol (2 x 3 mL) and cold DCM (2 x 3 mL). The filtrate was then collected and evaporated under reduced pressure. The resulting residue was dissolved in DCM (300 mL), and washed with 2N

HCl (3 x 150 mL). The aqueous phase was collected and the pH was adjusted to 10 by the addition of a 20% solution of NaOH. The mixture was then stirred for 30 minutes, and the product was extracted into DCM (3 x 60 mL), washed with $H_2O$ (2 x 50 mL), brine (2 x 50 mL), and then dried over $Na_2SO_4$. The solvent was removed to afford **(2.6)** as a pale yellow oil (1.60 g, 78 % yield).

| | |
|---|---|
| FAB-MS: | $m/z$ = 301 $[M+H]^+$ (27.1%). |
| $^1H$ NMR ($CDCl_3$, 300 MHz) δ (ppm): | 7.19 (m, 6H, 6-H, 7-H, 8-H), 7.11 (m, 4H, 5-H, 9-H), 4.44 (s, 2H, 3-H), 3.46 (dt, $J$ = 9.52, 4.85 Hz, 2H, 2-H), 3.35 (dt, $J$ = 9.52, 4.85 Hz, 2H, 2-H), 2.82, (t, $J$ = 5.23 Hz, 4H, 1-H), 2.20 (s, 4H, NH). |
| $^{13}C$ NMR ($CDCl_3$, 75 MHz) δ (ppm): | 139.0 (4-C), 127.8 (Ph), 127.5 (Ph), 86.0 (3-C), 71.9 (2-C), 41.9 (1-C). |
| CHN: | Found C: 68.39, H: 8.04, N: 8.34%; Calcd. for $(C_{18}H_{24}N_2O_2)\cdot H_2O$ C: 67.9; H: 8.23; N: 8.80%. |
| IR (KBr, $cm^{-1}$): | 3364, 3294, 3030, 2921, 2866, 1453, 1265, 1102, 701. |

### 4.3.5 Preparation of *R,R* $[Fe(N_3O_2)(CN)_2]$ (2.9)[41]

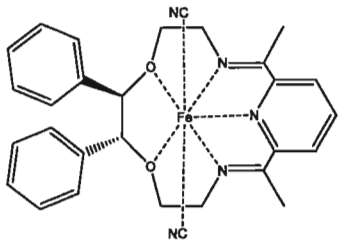

(2.9)

2,6-Diacetylpyridine (136 mg, 0.833 mmol) and $Na_2S_2O_4$ (99 mg, 0.569 mmol) in degassed $H_2O$ (8 mL) was added to a solution of $FeCl_2\cdot 4H_2O$ (166 mg, 0.833 mmol) and **(2.6)** (250 mg, 0.833 mmol) in degassed MeOH (10 mL). The reaction mixture was refluxed gently for 12 h and then filtered into a solution of NaCN (810 mg, 16.4 mmol)

and $Na_2S_2O_4$ (48 mg, 0.276 mmol) in degassed $H_2O$ (5 mL). The product was collected by filtration, washed with $H_2O$ (15 mL), a (1:1) mixture of $Et_2O$/THF (6 mL), and $Et_2O$ (5 x 5 mL). Complex **(2.9)** was isolated as a blue solid, (240 mg, 54% yield). Single crystals suitable for X-ray diffraction were grown via the vapour diffusion of diethyl ether into an acetonitrile solution of the macrocycle **(2.9)**.

| | |
|---|---|
| MS-FAB: | *m/z* = 509 [$M^+$] (100%). |
| CHN: | Found C: 60.81, H: 5.71, N: 12.24%; Calcd. for $(C_{29}H_{29}N_5O_2Fe)\cdot 2H_2O$ C: 60.95; H: 5.82; N: 12.26%. |
| IR (KBr, $cm^{-1}$): | 3420, 2096, 1634, 1454, 1082, 1059, 704. |
| UV-vis (EtOH) λ (nm): 293 K | 494 ($\varepsilon = 218\ M^{-1}cm^{-1}$), 624 ($\varepsilon = 450\ M^{-1}cm^{-1}$) |
| 77 K | 490 ($\varepsilon = 1421\ M^{-1}cm^{-1}$), 615 ($\varepsilon = 433\ M^{-1}cm^{-1}$), 711 ($\varepsilon = 136\ M^{-1}cm^{-1}$). |

### 4.3.6 Synthesis of (5*S*,6*S*)-5,6-diphenyl-4,7-dioxa-1,9-decadiene (2.3)[108]

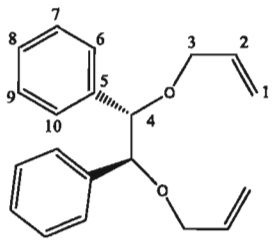

S,S (2.3)

The synthesis of ***S,S*** **(2.3)** was carried out following the same synthetic procedure described for the preparation of the *R,R* enantiomer **(2.3)**. Compound ***S,S*** **(2.3)** was isolated as a pale yellow oil (6.48 g, 95% yield).

| | |
|---|---|
| FAB-MS: | *m/z* = 294 [$M]^+$ (2.3%). |
| HRMS (FAB): | Found *m/z* = 294.1622 [$M]^+$; Calcd. 294.1620 for $C_{20}H_{22}O_2$. |

| | |
|---|---|
| $^1$H NMR ($CDCl_3$, 300 MHz) δ (ppm): | 7.21 (s, 6H, 7-H, 8-H, 9-H), 7.12 (s, 4H, 6-H, 10-H), 5.91 (m, 2H, 2-H), 5.33 (d, *J* = 14.32 Hz, 2H, 1-H), 5.21 (d, *J* = 10.55 Hz, 2H, 1-H), 4.62 (s, 2H, 4-H), 4.12 (dd, *J* = 13.19 Hz, 1H, 3-H), 3.97 (dd, *J* = 13.56 Hz, 1H, 3-H). |
| $^{13}$C NMR ($CDCl_3$, 75 MHz) δ (ppm): | 138.8 (5-C), 135.1 (6-C, 10-C), 128.0 (7-C, 9-C), 127.8 (8-C), 127.5 (2-C), 116.5 (1-C), 85.0 (4-C), 70.2. (3-C). |
| IR (KBr, $cm^{-1}$): | 3084, 3030, 2860, 1647, 1453, 1087, 924, 701. |

### 4.3.7 (4*S*,5*S*)-4,5-diphenyl-3,6-dioxa-1,8-octanediol (2.4)[108]

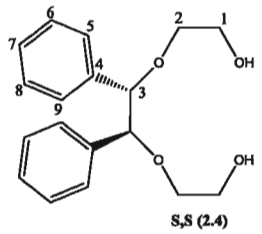

S,S (2.4)

The synthesis of ***S,S* (2.4)** was carried out following the synthetic procedure described for the preparation of the *R,R* enantiomer **(2.4)**. The diol ***S,S* (2.4)** was isolated as a yellow oil (5.42 g, 82% yield).

| | |
|---|---|
| FAB-MS: | *m/z* = 303 $[M+H]^+$ (5.2%). |
| HRMS (FAB): | Found *m/z* = 303.1537 $[M]^+$; Calcd. 303.1596 for $C_{18}H_{23}O_4$. |
| $^1$H NMR ($CDCl_3$, 300 MHz) δ (ppm): | 7.21 (s, 6H, 6-H, 7-H, 8-H), 7.06 (s, 4H, 5-H, 9-H), 4.50 (s, 2H, 3-H), 3.78 (m, 4H, 1-H), 3.66 (m, 2H, 2-H), 3.51 (m, 2H, 2-H), 3.18 (s, 2H, OH). |
| $^{13}$C NMR ($CDCl_3$, 75 MHz) δ (ppm): | 138.1 (4-C), 128.1 (5-C, 9-C), 127.9 (6, 8-C), 127.5 (7-C), 86.8 (3-C), 71.1 (2-C), 61.8 (1-C). |
| IR (KBr, $cm^{-1}$): | 3350, 3030, 2923, 2870, 1709, 1453, 1363, 1222, 1108, 1077. |

### 4.3.8 (4*S*,5*S*)-4,5-diphenyl-3,6-dioxa-1,8-octanediphthalimide (2.5)

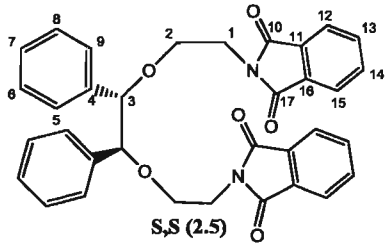


The synthesis of ***S,S* (2.5)** was carried out following the synthetic procedure described for the preparation of the *R,R* enantiomer **(2.5)**. Compound ***S,S* (2.5)** was isolated as a white solid (3.94 g, 39% yield).

| | |
|---|---|
| Mp. | 180-182 °C. |
| FAB-MS: | *m/z* = 561 $[M+H]^+$ (1.6%). |
| HRMS (FAB): | Found *m/z* = 561.2068 $[M]^+$; Calcd. 561.2026 for $C_{34}H_{29}N_2O_6$. |
| $^1$H NMR ($CDCl_3$, 300 MHz) δ (ppm): | 7.83 (s, 4H, 12-H, 15-H), 7.73 (s, 4H, 13-H, 14-H), 6.94 (m, 6H, 6-H, 7-H, 8-H), 6.82 (d, *J* = 6.78 Hz, 4H, 5-H, 9-H), 4.41 (s, 2H, 3-H), 3.79 (dt, *J* = 15, 4.95 Hz, 4H, 2-H), 3.62 (t, *J* = 5.65 Hz, 4H, 1-H). |
| $^{13}$C NMR ($CDCl_3$, 75 MHz) δ (ppm): | 168.2 (10-C), 137.8 (Ph), 133.7 (Ph), 132.1 (Ph), 127.6 (Ph), 123.2 (Ph), 85.6 (3-C), 66.0 (2-C), 37.7 (1-C). |
| CHN: | Found C: 71.84, H: 5.22, N: 4.81%; Calcd. for $(C_{34}H_{28}N_2O_6)\cdot 0.35H_2O$ C: 72.03; H: 5.10; N: 4.94%. |
| IR (KBr, $cm^{-1}$): | 3032, 2887,1774, 1720, 1397, 1106, 1026, 712. |

### 4.3.9 (4*S*,5*S*)-4,5-diphenyl-3,6-dioxa-1,8-octanediamine (2.7)[113]

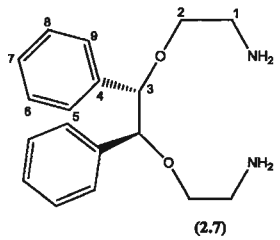


(2.7)

The synthesis of **(2.7)** was carried out following the synthetic procedure described for the preparation of the *R,R* enantiomer **(2.6)**. The diamine **(2.7)** was isolated as a pale yellow oil (1.62 g, 78% yield).

| | |
|---|---|
| FAB-MS: | $m/z$ = 301 $[M+H]^+$ (31.4%). |
| $^1$H NMR ($CDCl_3$, 300 MHz) δ (ppm): | 7.18 (m, 6H, 6-H, 7-H, 8-H), 7.11 (m, 4H, 5-H, 9-H), 4.45 (s, 2H, 3-H), 3.47 (dt, $J$ = 9.52, 4.85 Hz, 2H, 2-H), 3.32 (dt, $J$ = 9.52, 4.85 Hz 2H, 2-H), 2.80, (t, $J$ = 5.23 Hz, 4H, 1-H), 1.45 (s, 4H, NH). |
| $^{13}$C NMR ($CDCl_3$, 75 MHz) δ (ppm): | 138.8 (4-C), 128.1 (Ph), 127.5 (Ph), 86.1 (3-C), 72.0 (2-C), 42.0 (1-C). |
| CHN: | Found C: 67.28, H: 7.84, N: 8.39%; Calcd. for $(C_{18}H_{24}N_2O_2)\cdot 1H_2O$ C: 67.90; H: 8.23; N: 8.80%. |
| IR (KBr, cm$^{-1}$): | 3366, 3330, 3030, 2866, 1492, 1453, 1265, 1104, 701. |

### 4.3.10 Preparation of *S,S* $[Fe(N_3O_2)(CN)_2]\cdot 3H_2O$ (2.10)[41]

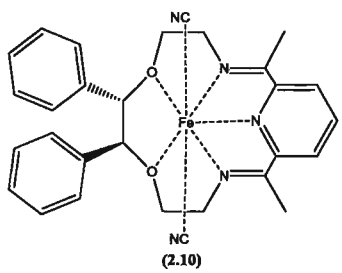


(2.10)

The synthesis of **(2.10)** was carried out following the synthetic procedure described for the preparation of the *R,R* enantiomer **(2.9)**. The macrocycle **(2.10)** was isolated as a blue solid (330 mg, 74% yield).

| | |
|---|---|
| FAB-MS: | $m/z$ = 509 $[M]^+$ (100%). |
| CHN: | Found C: 58.52, H: 5.25, N: 11.45%; Calcd. for $(C_{29}H_{29}N_5O_2Fe)\cdot 3H_2O$ C: 59.09; H: 5.98; N: 11.88%. |
| IR (KBr, $cm^{-1}$): | 3419, 2885, 2095, 1632, 1454, 1082, 1022, 703. |
| UV-vis (EtOH) λ (nm): 293 K | 486 ($\varepsilon$ = 850 $M^{-1}cm^{-1}$), 627 ($\varepsilon$ = 1499 $M^{-1}cm^{-1}$). |
| 77 K | 486 ($\varepsilon$ = 1421 $M^{-1}cm^{-1}$), 610 ($\varepsilon$ = 450 $M^{-1}cm^{-1}$), 708 ($\varepsilon$ = 136 $M^{-1}cm^{-1}$). |

### 4.3.11 Preparation of *racemic* $[Fe(N_3O_2)(CN)_2]\cdot H_2O$ (2.11)[41]

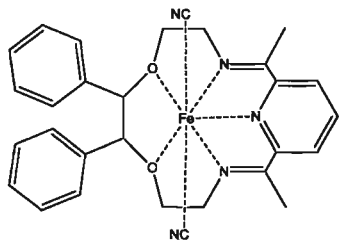

(2.11)

The *racemic* complex **(2.11)** was prepared from a (1:1) *racemic* mixture of primary diamines **(2.6)** and **(2.7)**, following the synthetic procedure described for complex **(2.9)**. The macrocycle was isolated as a blue solid (240 mg, 54% yield). Single crystals of **(2.11)** suitable for X-ray diffraction were grown via the diffusion of hexane into a DCM solution of the macrocycle.

| | |
|---|---|
| FAB-MS: | $m/z$ = 509 $[M^+]$ (100%). |
| CHN: | Found C: 63.35, H: 5.46, N: 12.41%; Calcd. for $(C_{29}H_{31}N_5O_3Fe)\cdot H_2O$ C: 62.93; H: 5.61; N: 12.66%. |

| | |
|---|---|
| IR (KBr, $cm^{-1}$): | 3421, 2903, 2093, 1629, 1454, 1316, 1132, 1081, 703. |
| UV-vis (EtOH) λ (nm): 293 K | 495 ($\varepsilon = 234\ M^{-1}cm^{-1}$), 626 ($\varepsilon = 445\ M^{-1}cm^{-1}$) |
| 77 K | 490 ($\varepsilon = 1426\ M^{-1}cm^{-1}$), 615 ($\varepsilon = 428\ M^{-1}cm^{-1}$) 710 ($\varepsilon = 148\ M^{-1}cm^{-1}$). |

### 4.3.12 Synthesis of (*meso*)-5,6-Diphenyl-4,7-dioxa-1,9-decadiene (2.3)[108]

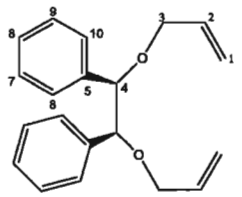

meso (2.3)

Compound ***meso*** **(2.3)** was prepared from *meso*-hydrobenzoin **(2.14)** following the procedure reported for the preparation of the *R,R* derivative **(2.3)**. Compound ***meso*** **(2.3)** was isolated as an oil, (6.14 g, 91% yield).

| | |
|---|---|
| EI-MS: | $m/z = 294\ [M]^+$ (0.3 %). |
| HRMS (FAB): | Found $m/z$ = 294.1604 $[M]^+$; Calcd. 294.1620 for $C_{20}H_{22}O_2$. |
| $^1H$ NMR ($CDCl_3$, 300 MHz) δ (ppm): | 7.39 (s, 10H, 6-H, 7-H, 8-H, 9-H, 10-H), 5.82 (s, 4H, 2-H), 5.09 (m, 4H, 1-H), 4.55 (s, 2H, 4-H), 4.12 (m, 2H, 3-H), 3.80 (m, 2H, 3-H). |
| $^{13}C$ NMR ($CDCl_3$, 75 MHz) δ (ppm): | 139.5 (5-C), 134.8 (6-C, 10-C), 128.1 (7-C, 9-C), 127.8 (8-C), 127.6 (2-C), 116.2 (1-C), 84.3 (4-C), 69.8 (3-C) |
| IR (KBr, $cm^{-1}$): | 3083, 3030, 2861, 1647, 1453, 1099, 925, 701. |

### 4.3.13 Synthesis of (*meso*)-4,5-diphenyl-3,6-dioxa-1,8-octanediol (2.4)[108]

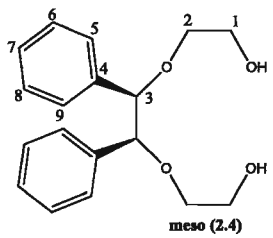


Compound ***meso*** **(2.4)** was prepared from ***meso*** **(2.3)** following the procedure reported for the *R,R* derivative **(2.4)**. The crude product was purified via column chromatography on silica gel, eluting with a (20:1) mixture of $CHCl_3$/MeOH to afford ***meso*** **(2.4)** as a yellow oil (2.51 g, 40% yield).

| | |
|---|---|
| FAB-MS: | *m/z* = 303 $[M+H]^+$ (2.9%). |
| HRMS (FAB) | Found *m/z* = 303.1554 $[M]^+$; Calcd. 303.1596 for $C_{18}H_{23}O_4$. |
| $^1H$ NMR ($CDCl_3$, 300 MHz) δ (ppm): | 7.31 (s, 10H, 5-H, 6-H, 7-H, 8-H, 9-H), 4.41 (s, 2H, 3-H), 3.58 (m, 6H, 1, 2-H), 3.26 (m, 2H, 1-H), 1.85 (s, 2H, OH). |
| $^{13}C$ NMR ($CDCl_3$, 75 MHz) δ (ppm): | 139.0 (4-C), 128.2 (5-C, 9-C), 127.6 (6-C, 8-C), 127.0 (7-C), 85.4 (3-C), 70.7 (2-C), 61.6 (1-C). |
| IR (KBr, $cm^{-1}$): | 3418, 3031, 2911, 2870, 1711, 1453, 1363, 1222, 1108, 1077, 703. |

### 4.3.14 Synthesis of *meso*-4,5-diphenyl-3,6-dioxa-1,8-octanediphthalimide (2.5)

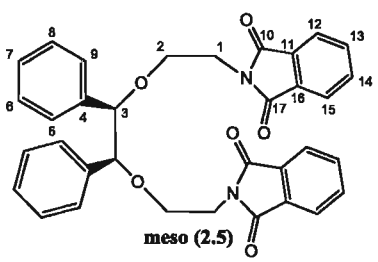

Compound ***meso* (2.5)** was prepared from the diol ***meso* (2.4)** following the procedure previously described for the *R,R* derivative **(2.5)**. The product ***meso* (2.5)** was isolated as a white solid (625 mg, 25% yield).

| | |
|---|---|
| M.p.: | 180-182° C. |
| FAB-MS: | $m/z = 561$ $[M+H]^+$ (0.8%). |
| $^1H$ NMR ($CDCl_3$, 300 MHz) δ (ppm): | 7.80 (m, 4H, 12-H, 15-H), 7.74 (m, 4H, 13-H, 14-H), 7.16 (d, $J$ = 7.91 Hz, 6H, 6-H, 7-H, 8-H), 6.95 (m, 4H, 5-H, 9-H), 4.20 (s, 2H, 3-H), 3.70 (m, 4H, 2-H), 3.60 (m, 4H, 1-H) 3.32 (m, 2H). |
| $^{13}C$ NMR ($CDCl_3$, 75 MHz) δ (ppm): | 168.0 (10-C), 139.2 (4-C), 133.7 (Ph), 132.2 (Ph), 127.6 (Ph), 123.2 (Ph), 85.2 (3-C), 65.6 (2-C), 37.6 (1-C). |
| CHN: | Found C: 71.84, H: 5.22, N: 4.81%; Calcd. for ($C_{34}H_{28}N_2O_6$) C: 72.03; H: 5.10; N: 4.94%. |
| IR (KBr, $cm^{-1}$): | 3028, 2870, 1769, 1714, 1396, 1115, 1038, 724. |

### 4.3.15 Synthesis of *meso*-4,5-diphenyl-3,6-dioxa-1,8-octanediamine (2.8)[113]

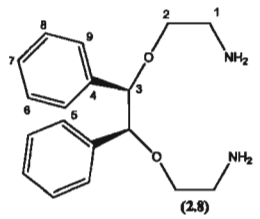

(2.8)

Compound **(2.8)** was prepared from the *bis* phthalamide ***meso* (2.5)** following the procedure described for the preparation of the *R,R* derivative **(2.6)**. The *bis* diamine **(2.8)** was isolated as an oil (249 mg, 88% yield).

| | |
|---|---|
| FAB-MS: | $m/z = 301$ $[M+H]^+$ (31.4%). |

| | |
|---|---|
| $^1$H NMR ($CDCl_3$, 300 MHz) δ (ppm): | 7.40 (m, 10H, 5-H, 6-H, 7-H, 8-H, 9-H), 4.32 (s, 2H, 3-H), 3.37 (m, 2H, 2-H), 3.08 (m, 2H, 2-H), 2.63, (s, 4H, 1-H), 1.03 (s, 4H, NH). |
| $^{13}$C NMR ($CDCl_3$, 75 MHz) δ (ppm): | 140.2 (5-C), 128.0 (Ph), 127.9 (4-C), 85.3 (3-C), 71.5 (2-C), 41.7 (1-C). |
| CHN: | Found C: 66.02, H: 7.44, N: 7.71%; Calcd. for $(C_{18}H_{24}N_2O_2)\cdot 1.5H_2O$ C: 66.03; H: 8.31; N: 8.56%. |
| IR (KBr, $cm^{-1}$): | 3358, 3283, 3030, 2921, 1602, 1493, 1453, 1106, 701. |

### 4.3.16 Preparation of *meso*-$[Fe(N_3O_2)(CN)_2]\cdot H_2O$ (2.12)[41]

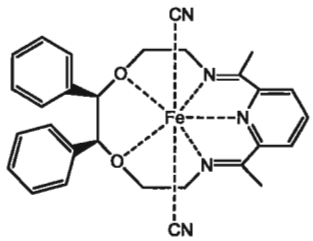


**(2.12)**

Compound **(2.12)** was prepared following the procedure described for the preparation of the *R,R* macrocycle **(2.9)**. The *meso* complex **(2.12)** was isolated as a purple solid, (240 mg, 54 % yield).

| | |
|---|---|
| FAB-MS: | $m/z$ = 509 [$M^+$] (100%). |
| CHN: | Found C: 62.74, H: 5.87, N: 11.79%; Calcd. for $(C_{29}H_{29}N_5O_2Fe)\cdot H_2O$ C: 62.94; H: 5.65; N: 12.65%. |
| IR (KBr, $cm^{-1}$): | 3536, 3436, 2877, 2094, 1636, 1453, 1313, 1230, 1077, 1024, 711. |
| UV-vis (EtOH) λ (nm): 293 K | 485 (ε = 1034 $M^{-1}cm^{-1}$), 626 (ε = 678 $M^{-1}cm^{-1}$) |
| 77 K | 485 (ε = 1320 $M^{-1}cm^{-1}$), 615 (ε = 713 $M^{-1}cm^{-1}$) |

### 4.3.17 Preparation of *R,R* $[Fe(N_3O_2)(H_2O)(ClO_4)]ClO_4 \cdot 4H_2O$ (2.15)[143]

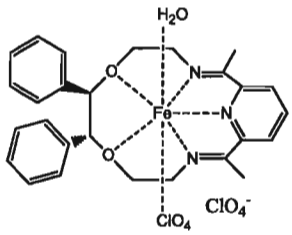


(2.15)

A solution of degassed ethanol (3 mL) containing 2,6-diacetylpyridine (160 mg, 0.967 mmol) was added to a (1:1) degassed $H_2O$/ethanol solution (6 mL), containing $FeCl_2 \cdot 4H_2O$ (190 mg, 0.967 mmol) and $Na_2S_2O_4$ (115 mg, 0.662 mmol). A solution of **(2.6)** (290 mg, 0.967 mmol) in degassed ethanol (4 mL) was then slowly added and the reaction mixture was stirred at 60 °C for 5 h. A degassed solution of $NaClO_4 \cdot H_2O$ (136 mg, 0.967 mmol) and $Na_2S_2O_4$ (58 mg, 0.330 mmol) in $H_2O$ (5 mL) was then added. The resulting mixture was stirred for 0.5 h at room temperature and then filtered to remove any insoluble material. The solvent was partially removed and the product was precipitated via the addition of cold diethyl ether. Compound **(2.15)** was isolated as a green-blue solid, (398 mg, 65% yield).

| | |
|---|---|
| MS FAB: | *m/z* = 582 $[Fe(N_3O_2)ClO_4]^+$ (87.4%). |
| CHN: | Found C: 41.12, H: 4.51, N: 5.24%; Calcd. for $(C_{27}H_{31}Cl_2N_5O_{11}Fe) \cdot 4H_2O$ C: 41.99; H: 5.09; N: 5.44%. |
| IR (KBr, $cm^{-1}$): | 3493, 2963, 2359, 1647, 1593, 1455, 1262, 1084, 1025, 1020, 940, 703, 627. |
| UV-Vis (EtOH) λ (nm): 293 K | 620 ($\varepsilon$ = 269 $M^{-1}cm^{-1}$) |

### 4.3.18 Preparation of *R,R* {[$Mn(N_3O_2)Cl_2$][$Mn(N_3O_2)Cl(MnCl_3)$]}$_2$. (2.16)[48]

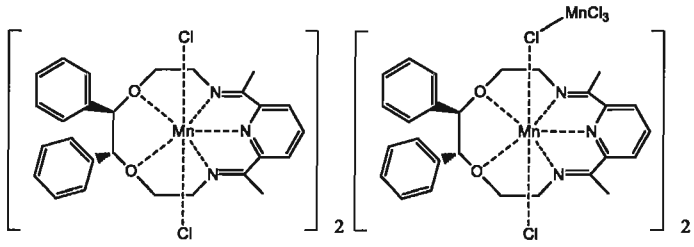


(2.16)

2,6-Diacetylpyridine (109 mg, 0.667 mmol) in ethanol (3 mL) was added to an ethanol solution (3 mL) of $MnCl_2 \cdot 4H_2O$ (132 mg, 0.667 mmol). A second solution of **(2.6)** (200 mg, 0.667 mmol) in ethanol (5 mL) was then added over 15 min with continuous stirring at 50 °C. The reaction was refluxed for 6 h, after which time the solvent was partially removed. Diethyl ether was then added to afford the product as a dark yellow solid (158 mg, 46%). Single crystals of the complex suitable for X-ray diffraction were grown via the slow evaporation of an acetonitrile solution of **(2.16)**.

FAB-MS: *m/z* = 517 [$M^+$] (100%).

IR (KBr, $cm^{-1}$): 3387, 3063, 2944, 2889, 1649, 1589, 1454, 1274, 1201, 1079, 1051, 1018, 703.

### 4.3.19 Preparation of *R,R* $[Mn(N_3O_2)(H_2O)(Cl)]ClO_4 \cdot 8H_2O$ (2.17)[143]

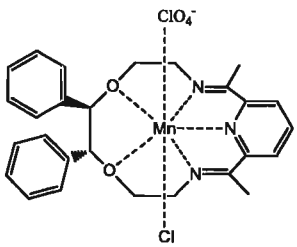


(2.17)

Compound **(2.17)** was prepared following the strategy previously described, but instead of reducing the solvent and isolating the product, NaClO4·H2O (136 mg, 0.967 mmol)

was added directly to the final solution. The mixture was stirred for 0.5 h at room temperature and then filtered to remove any insoluble material. After the solvent was partially removed, diethyl ether was added. A pale yellow precipitate was isolated by filtration, washed with diethyl ether, and dried in air. Compound **(2.17)** was obtained as a pale yellow solid, (336 mg, 64% yield).

| | |
|---|---|
| FAB-MS: | *m/z* = 535 $[Mn(N_3O_2)(Cl)(H_2O)]^+$ (100%); 581 $[Mn(N_3O_2)(ClO_4)]^+$ (9.8%); 599 $[Mn(N_3O_2)(ClO_4)\ (H_2O)]^+$ (9.4%). |
| CHN: | Found C: 39.74, H: 4.68, N: 5.35%; Calcd. for $[C_{27}H_{31}Cl_2N_5O_{11}Mn]\cdot 8H_2O$ C: 37.21; H: 5.44; N: 8.04%. |
| IR (KBr, $cm^{-1}$): | 3434, 2018, 1647, 1455, 1116, 1082, 921, 703, 628. |

## 4.4 Project 2

### 4.4.1 Synthesis of tetrathiafulvalene (3.10)[144]

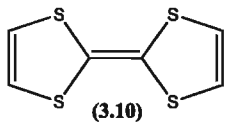

**(3.10)**

The large scale preparation of TTF was achieved following a modification of the synthetic procedure first reported by Bryce *et al.*[127] TTF **(3.10)** was afforded as orange needles, (13 g, 65%).

| | |
|---|---|
| M.p.: | 119-120°C; Lit [119-119.5 °C][144] |
| $^1H$ NMR ($CDCl_3$, 300 MHz) δ (ppm): | 6.33 (s, 4H, CH). |
| $^{13}C$ NMR ($CDCl_3$, 75 MHz) δ (ppm): | 119.1, 110.1 |

### 4.4.2 Synthesis of 2,4-diisoprpylcarbonylhydrazide *bis*-hydrochloride (3.11)[125]

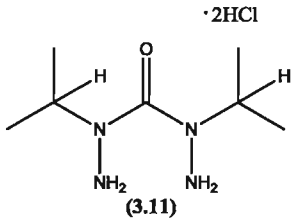

(3.11)

The 2,4-diisopropylcarbonylhydrazide *bis*-hydrochloride **(3.11)** was prepared following the literature procedure presented by Pare *et al*[125]. Compound **(3.11)** was afforded as an off-white crystalline solid (1.94 g, 98% yield).

| | |
|---|---|
| M.p.: | 179-181 °C; Lit [188-190 °C][125] |
| FAB-MS: | $m/z$ = 175 $[M]^+$ (61%). |
| $^1$H NMR ($D_2O$, 300 MHz) δ (ppm): | 4.18 (m, 4H, $NH_2$), 1.18 (d, $J$ = 6.7 Hz, 12H, isopropyl-H), 1.04 (d, $J$ = 6 Hz, 2H, CH). |

### 4.4.3 Synthesis of stannyl-tetrathiafulvalene (3.12)[144]

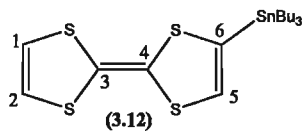

(3.12)

Lithium diisopropylamide (5.90 mL, 45.0 mmol) was added dropwise over 20 min to a solution of tetrathiafulvalene **(3.10)** (2.00 g, 9.79 mmol) in THF (200 mL) at -78 °C. Once the addition was complete, the solution was stirred for a further 2 h. Subsequently, tributyltin chloride (2.17 mL, 8.52 mmol) was added dropwise to the reaction mixture over 5 min at -78 °C and the solution was stirred for 1.5 h before it was allowed to warm to room temperature where it was stirred overnight. The progress of the reaction was monitored by TLC (DCM) ($R_f$ = 0.9). Upon completion, the solution was then poured

into water (100 mL) and the product was extracted with $CH_2Cl_2$ (3 x 75 mL). The combined organic layers were washed with water (2 x 100 mL) and dried over $MgSO_4$. Evaporation of the solvent under reduced pressure, afforded **(3.12)** as a viscous brown/orange oil, (3.89 g, 80% yield).

| | |
|---|---|
| FAB-MS: | $m/z = 175$ $[M]^+$ (84%). |
| $^1H$ NMR ($CDCl_3$, 300 MHz) δ (ppm): | 6.32 (d, $J = 6.78$ Hz, 2H, 1-H 2-H), 6.13 (s, 1H, 5-H), 1.57 (m, 6H, $SnBu_3$-H), 1.34 (m, 6H, $SnBu_3$-H), 1.11 (t, 6H, $SnBu_3$-H), 0.91 (t, 9H, $SnBu_3$-H). |

**4.4.4 General procedure (A) for the preparation of TTF-py-aldehydes (3.13) - (3.16).**

$Pd(PPh_3)_4$ (0.530 g, 0.459 mmol) was added to a solution of stannyl-TTF **(3.10)** (4.36 g, 8.77 mmol) and the appropriate 2-bromo-formyl pyridine (1.21 g, 6.48 mmol), in toluene (60 mL). The reaction mixture was heated to 120 °C for 12 h. The progress of the reaction was monitored by TLC (DCM) ($R_f$ = 0.9). On completion, the solution was poured into water (200 mL) and the product was extracted into $CH_2Cl_2$ (3 x 100 mL). The combined organic layers were then washed with water (2 x 100 mL), dried over $MgSO_4$ and filtered. Evaporation of the solvent under reduced pressure yielded the crude product that was purified by column chromatography ($SiO_2$, $CH_2Cl_2$) to afford compounds **(3.13)** to **(3.16)**.

**4.4.4.1 6-(2-(1,3-dithiol-2-ylidene)-1,3-dithiol-4-yl)pyrid-3-ylcarbaldehyde (3.13)[91]**

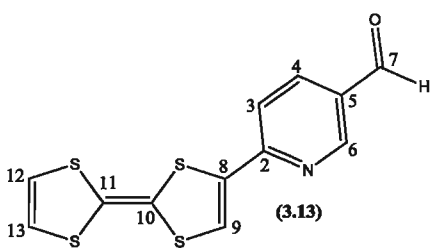

**(3.13)**

Following general procedure (A), compound (**3.13**) was obtained as a dark purple crystalline solid, (2.22 g, 82 % yield).

| | |
|---|---|
| M.p.: | 199 °C |
| EI-MS: | $m/z = 309$ $[M]^+$ (100%). |
| HRMS (FAB): | Found $m/z$ = 308.9416 $[M]^+$; Calcd. 308.9411 for $C_{12}H_7NOS_4$. |
| $^1H$ NMR ($CDCl_3$, 300 MHz) δ (ppm): | 10.07 (s, 1H, 7-H), 9.01 (s, 1H, 6-H), 8.26 (d, $J = 8.7$ Hz, 1H, 4-H), 8.06 (d, $J = 8.4$ Hz, 1H, 3-H), 7.99 (s, 1H, 9-H), 6.78 (s, 2H, 12, 13-H). |
| $^{13}C$ NMR ($CDCl_3$, 75 MHz) δ (ppm): | 192.3 (7-C), 154.3 (2-C), 152.3 (6-C), 137.43 (8-C), 136.8 (4-C), 130.1 (5-C), 124.9 (10-C, 11-C), 120.7 (12-C), 120.5 (13-C), 112.9 (3-C), 107.1 (9-C). |
| IR (KBr, $cm^{-1}$): | 3058, 2956, 2922, 2831, 1691, 1554, 1359, 1207, 823, 651. |

### 4.4.4.2 Synthesis of 6-(2-(1,3-dithiol-2-ylidene)-1,3-dithiol-4-yl)pyrid-2-ylcarbaldehyde (3.14)[91]

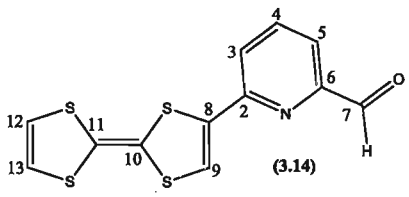

(3.14)

Following general procedure (A), compound **(3.14)** was isolated as an orange solid, (0.68 g, 97% yield).

| | |
|---|---|
| M.p.: | 144 °C |
| EI-MS: | $m/z = 309$ $[M]^+$ (100%). |

| | |
|---|---|
| HRMS (FAB): | Found *m/z* = 308.9408 $[M]^+$; Calcd. 308.9411 for $C_{12}H_7NOS_4$. |
| $^1H$ NMR ($CDCl_3$, 300 MHz) δ (ppm): | 9.97 (s, 1H, 7-H), 8.17 (d, *J* = 7.2 Hz, 1H, 5-H), 8.11 (t, *J* = 8.1 Hz, 1H, 4-H), 7.95 (s, 1H, 9-H), 7.86 (d, *J* = 3.6 Hz, 1H, 3-H), 6.80 (s, 2H, 12, 13-H). |
| $^{13}C$ NMR ($CDCl_3$, 75 MHz) δ (ppm): | 193.1 (7-C), 152.3 (2-C), 150.8 (6-C), 137.5 (8-C), 132.3 (4-C), 128.6 (5-C), 128.4 (10-C, 11-C), 123.1 (12-C), 119.8 (13-C), 119.6 (3-C), 119.3 (9-C). |
| IR (KBr, $cm^{-1}$): | 3052, 2930, 2904, 2862, 1694, 1554, 1370, 1217, 796, 638. |

### 4.4.4.3 Synthesis of 6-(2-(1,3-dithiol-2-ylidene)-1,3-dithiol-3-yl)pyrid-2-ylcarbaldehyde (3.15)[91]

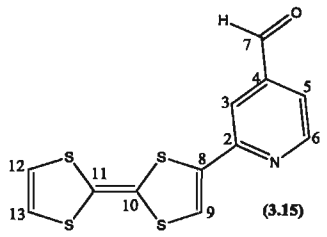

(3.15)

Following general procedure (A), compound **(3.15)** was isolated as a brown/red solid, (2.20 g, 89% yield).

| | |
|---|---|
| M.p: | 249 °C |
| EI-MS: | *m/z* = 309 $[M]^+$ (100%). |
| HRMS (FAB): | Found *m/z* = 308.9401 $[M]^+$; Calcd. 308.9411 for $C_{12}H_7NOS_4$. |
| $^1H$ NMR ($CDCl_3$, 300 MHz) δ (ppm): | 10.10 (s, 1H, 7-H), 8.80 (d, *J* = 5.4 Hz, 1H, 5-H), 8.32 (s, 1H, 3-H), 7.93 (s, 1H, 9-H), 7.72 (d, *J* = 5.4 Hz, 1H, 6-H), 6.77 (s, 2H, 12-H, 13-H). |

| | |
|---|---|
| $^{13}C$ NMR ($CDCl_3$, 75 MHz) δ (ppm): | 193.2 (7-C), 152.4 (4-C), 151.0 (2-C), 142.6 (6-C), 121.9 (8-C), 121.1 (10-C), 120.9 (11-C), 120.7 (12-C, 13-C), 118.8 (5-C), 116.2 (9-C), 113.9 (3-C). |
| IR (KBr, $cm^{-1}$): | 3036, 2962, 2925, 2850, 1679, 1557, 1425, 1381, 1260, 783, 673. |

### 4.4.4.4 Synthesis of 2-(2-(1,3-dithiol-2-ylidene)-1,3-dithiol-4-yl)pyrid-3-ylcarbaldehyde (3.16)[91]

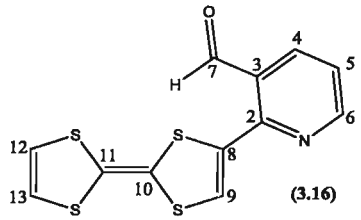

(3.16)

Following general procedure (A), compound **(3.16)** was isolated as a brown/red solid, (1.30 g, 66% yield).

| | |
|---|---|
| M.p.: | 143 °C |
| EI-MS: | $m/z$ = 309 $[M]^+$ (100%). |
| HRMS (FAB): | Found $m/z$ = 308.9410 $[M]^+$; Calcd. 308.9411 for $C_{12}H_7NOS_4$. |
| $^1H$ NMR ($CDCl_3$, 300 MHz) δ (ppm): | 10.19 (s, 1H, 7-H), 8.80 (d, $J$ = 4.5 Hz, 1H, 4-H), 8.23 (d, $J$ = 7.8 Hz, 1H, 6-H), 7.57 (t, $J$ = 5.4 Hz, 1H, 5-H), 7.43 (s, 1H, 9-H), 6.78 (s, 2H, 12-H, 13-H). |
| $^{13}C$ NMR ($CDCl_3$, 75 MHz) δ (ppm): | 190.8 (7-C), 153.7 (2-C), 152.0 (6-C), 137.4 (8-C), 134.1 (4-C), 129.7 (10-C), 127.1 (11-C), 124.1 (5-C), 121.3 (3-C), 120.1 (12-, 13-C), 112.9 (9-C). |
| IR (KBr, $cm^{-1}$): | 3060, 3043, 2830, 2805, 1706, 1553, 1367, 1168, 778, 656. |

### 4.4.5 General procedure (B) for the preparation of TTF-py-tetrazanes (3.17) – (3.20)

A solution of the appropriate TTF-py-aldehyde **(3.13)** to **(3.16)** (0.457 g, 1.48 mmol), 2,4-diisopropylcarbonylhydrazide *bis*-hydrochloride **(3.11)** (0.383 g, 1.54 mmol) and sodium acetate (0.419 g, 3.08 mmol) in MeOH (55 mL) were refluxed overnight and the resulting solid was removed by filtration. The filtrate was collected and evaporated to dryness. Purification by flash chromatography on silica gel eluting with a (1:1) mixture of DCM/EtOAc ($R_f$ = 0.8), afforded the tetrazanes **(3.17)** to **(3.20)**.

#### 4.4.5.1 Synthesis of 6-(6-(2-(1,3-Dithiol-2-ylidene)-1,3-dithiol-4-yl)-pyrid-3-yl)-2,4-diisopropyl-1,2,4,5-tetrazane 3-Oxide (3.17)[91]

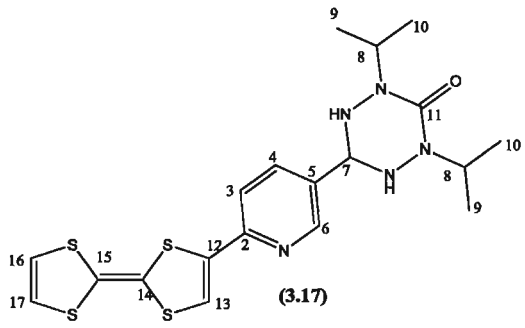

(3.17)

Following the procedure described in general method (B), compound **(3.17)** was obtained as an orange/red solid (0.38 g, 55% yield).

| | |
|---|---|
| M.p.: | 153 °C |
| FAB-MS: | $m/z$ = 465 $[M]^+$ (100%). |
| HRMS (FAB): | Found $m/z$ = 440.0811 $[M]^+$; Calcd. 440.0833 for $C_{19}H_{20}N_5OS_4$. |
| CHN: | Found C: 49.95, H: 5.37, N: 14.15%; Calcd. for ($C_{19}H_{23}N_5OS_4$) C: 49.01; H: 4.98; N: 15.04%. |
| $^1$H NMR (DMSO, 300 MHz) δ (ppm): | 8.68 (s, 1H, 6-H), 7.97 (d, $J$ = 2 Hz, 1H, 3-H), 7.89 (d, $J$ = 8.3 Hz, 1H, 4-H), 7.72 (s, |

| | |
|---|---|
| | 1H, 13-H), 6.74 (s, 2H, 16, 17-H), 5.76 (d, *J* = 11.4 Hz, 2H, NH), 5.16 (t, *J* = 10.8 Hz, 1H, 7-H), 4.48 (m, 1H, 8-H), 1.04 (d, *J* = 10.17 6H, 9-H, 10-H), 0.97 (d, *J* = 10.17 6H, 9-H, 10-H). |
| $^{13}$C NMR (DMSO, 300 MHz) δ (ppm): | 153.8 (11-C), 150.2 (2-C), 148.1 (6-C), 137.5 (12-C), 135.7 (4-C), 131.4 (14-C), 121.2 (15-C), 120.7 (3-C), 120.5 (13-C), 119.4 (16-C, 17-C), 108.1 (5-C), 70.0 (7-C), 47.1 (8-C), 20.1 (9, 10-C). |
| IR (KBr, cm$^{-1}$): | 3412, 3239, 2967, 1625, 1536. |
| UV-vis ($CH_3CN$) λ (nm): | 320 (ε = 3328 M$^{-1}$cm$^{-1}$), 430 (ε = 470 M$^{-1}$cm$^{-1}$). |

### 4.4.5.2 Synthesis of 2,4-diisoprpylcarbonylhydrazide *bis*-hydrochloride (3.18)[91]

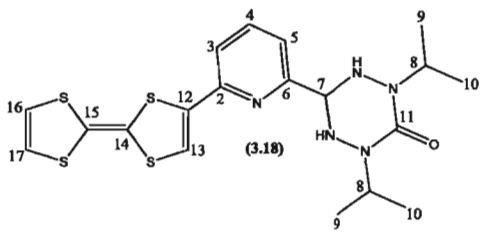


Following the procedure described in general method (B), compound **(3.18)** was isolated as an orange solid, (0.57 g, 63% yield).

| | |
|---|---|
| M.p.: | 187 °C |
| FAB-MS: | *m/z* = 465 [M]$^+$ (100%). |
| CHN: | Found C: 48.69, H: 5.76, N: 14.55%; Calcd. for ($C_{19}H_{23}N_5OS_4$) C: 49.00; H: 4.98; N: 15.04%. |
| $^1$H NMR (DMSO, 300 MHz) δ (ppm): | 7.92 (t, *J* = 7.7 Hz, 1H, 4-H ), 7.82 (d, *J* = 7.7 Hz, 1H, 5-H), 7.78 (s, 1H, 13-H), 7.54 (d, *J* = 7.5 Hz, 1H, 3-H), 6.75 (s, 2H, 16-H, 17-H), 5.14 (d, *J* = 11.4 Hz, 2H, NH), 4.50 |

| | |
|---|---|
| | (t, $J$ = 6.9 Hz, 1H, 7-H), 4.01 (m, 1H, 11-H) 1.03 (s, 12H, 9-H, 10-H). |
| $^{13}$C NMR (DMSO, 75 MHz) δ (ppm): | 154.1 (11-C), 152.9 (6-C), 149.8 (2-C), 138.2 (12-C), 136.9 (4-C), 123.9 (5-C), 122.1 (14-C), 120.8 (15-C), 119.5 (16-C, 17-C), 111.5 (13-C), 108.4 (3-C), 71.9 (7-C), 47.7(8-C), 19.2 (9, 10-C). |
| IR (KBr, cm$^{-1}$): | 3412, 2964, 1716, 1608, 1456. |
| UV-vis ($CH_3CN$) λ (nm): | 320 (ε = 1260 M$^{-1}$cm$^{-1}$) 440 (ε =. 233 M$^{-1}$cm$^{-1}$). |

### 4.4.5.3 Synthesis of 6-(6-(2-(1,3-Dithiol-2-ylidene)-1,3-dithiol-4-yl)-pyrid-3-yl)-1,5-dimethyl-6-oxoverdazyl (3.19)[91]

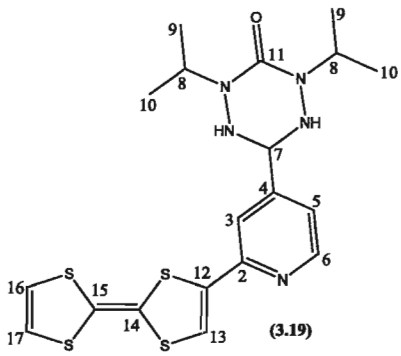


Following the procedure described in general method (B), compound **(3.19)** was isolated as an orange oil, (0.20 g, 36% yield).

| | |
|---|---|
| FAB-MS: | $m/z$ = 465 [M]$^+$ (30%). |
| $^1$H NMR (DMSO, 300 MHz) δ (ppm): | 8.55 (s, 1H, 3-H), 8.37 (d, $J$ = 4.2 Hz, 1H, 5-H), 7.79 (s, 1H, 13-H), 7.67 (d, $J$ = 5.4 Hz, 1H, 6-H), 6.74 (s, 2H, 16, 17-H), 5.20 (d, $J$ = 11. Hz, 2H, NH), 4.48 (t, $J$ = 11.1 Hz, 1H, 6-H), 4.04 (m, 1H, 14-H), 1.04 (s, 12H, 9-H, 10-H) |
| $^{13}$C NMR (DMSO, 75 MHz) δ (ppm): | 172.3 (11-C), 153.9 (2-C), 149.4 (6-C), 146.3 (4-C), 138.3 (12-C), 122.2 (14-C), 121.4 (15-C), 120.5 (13-C), 119.3 (16-, 17- |

C), 108.1 (5-C), 70.9 (7-C), 47.3 (8-C), 21.7 (9-C, 10-C).

IR (KBr, $cm^{-1}$): 3415, 3232, 2967, 1598, 1409.

UV-vis ($CH_3CN$) λ (nm): 315 (ε = 1463 $M^{-1}cm^{-1}$), 435 (ε = 233 $M^{-1}cm^{-1}$).

### 4.4.5.4 Synthesis of 6-(6-(2-(1,3-Dithiol-2-ylidene)-1,3-dithiol-4-yl)-pyrid-5-yl)-1,5-diisopropyl-1,2,4,5-tetrazane 6-Oxide (3.20)[91]

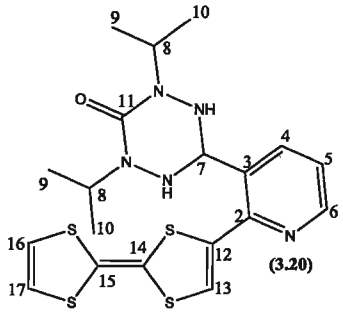


Following the procedure described in general method (B), compound **(3.20)** was isolated as an orange oil (0.31 g, 52% yield).

FAB-MS: *m/z* = 465 $[M]^+$ (30.5%).

$^1H$ NMR (DMSO, 300 MHz) δ (ppm): 8.58 (d, *J* = 3.9 Hz, 1H, 4-H), 8.11 (d, *J* = 8.7 Hz, 1H, 6-H), 7.47 (t, *J* = 4.8 Hz, 1H, 5-H), 7.33 (s, 1H, 13-H), 6.75 (s, 2H, 16, 17-H), 5.41 (d, *J* = 10.9 Hz, 2H, NH), 4.57 (t, *J* = 9.6 Hz, 1H, 7-H), 4.48 (m, 1H, 8-H), 1.02 (s, 12H, 9-H, 10-H).

$^{13}C$ NMR (DMSO, 75 MHz) δ (ppm): 154.5 (11-C), 149.3 (2-C), 136.3 (6-C), 135.2 (12-C), 130.8 (4-C), 123.6 (14-C), 121.9 (15-C), 121.1 (13-C), 120.2 (16, 17-C), 111.9 (3-C), 107.6 (5-C), 68.9 (7-C), 47.1 (8-C), 23.7 (9, 10-C).

IR (KBr, $cm^{-1}$): 3436, 3251, 1585, 1425.

UV-vis ($CH_3CN$) λ (nm): 310 (ε = 2994 $M^{-1}cm^{-1}$), 415 (ε = 502 $M^{-1}cm^{-1}$).

### 4.4.6 General procedure (C) for the preparation of TTF-py-verdazyl radicals (3.5) to (3.8)

1,4-Benzoquinone (38 mg, 0.351 mmol) was added in one portion to a solution of the appropriate TTF-py-tetrazane **(3.21)** to **(3.24)** (100 mg, 0.215 mmol) in benzene (10 mL). The reaction was refluxed for 3 h at 60 °C after which time a solid precipitated from a the solution. The precipitate was removed and discarded and the filtrate was evaporated to dryness to give a crude product that was purified via column chromatography ($SiO_2$, $CH_2Cl_2$) ($R_f = 0.7$), to afford the TTF-py-verdazyl radicals **(3.3)** to **(3.6).**

#### 4.4.6.1 Synthesis of 6-(6-(2-(1,3-Dithiol-2-ylidene)-1,3-dithiol-4-yl)-pyrid-3-yl)-1,5-diisopropyl-6-oxoverdazyl (3.5)[91]

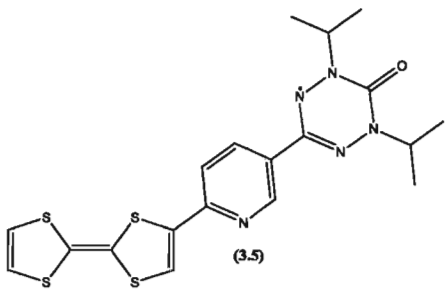


Following the strategy presented in general procedure (C), compound **(3.5)** was isolated as a dark purple crystalline solid (56 mg, 56% yield). Single crystals suitable for X-ray crystallography were grown from the slow evaporation of a DCM solution of radical **(3.5)**.

| | |
|---|---|
| M.p.: | 123 °C |
| FAB-MS: | $m/z = 462$ $[M]^+$ (100%). |
| CHN: | Found C:49.29, H: 4.35, N: 14.90%; Calcd. for ($C_{19}H_{20}N_5OS_4^{\cdot}$) C: 49.32; H: 4.36; N: 15.14%. |
| IR (KBr, $cm^{-1}$): | 3234, 2964, 1681, 1456. |

| | |
|---|---|
| UV-vis ($CH_3CN$) λ (nm): | 310 ($\varepsilon = 3875\ M^{-1}cm^{-1}$), 440 ($\varepsilon = 245\ M^{-1}cm^{-1}$). |

### 4.4.6.2 Synthesis of 6-(6-(2-(1,3-Dithiol-2-ylidene)-1,3-dithiol-4-yl)-pyrid-2-yl)-1,5-diisopropyl-6-oxoverdazyl (3.6)[91]

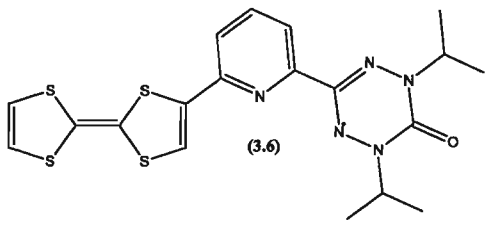

(3.6)

Following the strategy presented in general procedure (C), compound **(3.6)** was isolated as a dark orange solid, (64 mg, 64% yield). Single crystals suitable for X-ray crystallography were grown via the slow evaporation of a DCM solution of radical **(3.6)**.

| | |
|---|---|
| FAB-MS: | $m/z = 462\ [M]^+$ (51%). |
| CHN: | Found C: 49.95, H: 5.37, N: 14.22%; Calcd. for ($C_{19}H_{20}N_5OS_4^{\cdot}$) C: 49.32; H: 4.36; N: 15.14%. |
| IR (KBr, $cm^{-1}$): | 3423, 2962, 1670, 1456. |
| UV-vis ($CH_3CN$) λ (nm): | 320 ($\varepsilon = 3682\ M^{-1}cm^{-1}$), 435 ($\varepsilon = 246\ M^{-1}cm^{-1}$). |

### 4.4.6.3 Synthesis of 6-(6-(2-(1,3-Dithiol-2-ylidene)-1,3-dithiol-4-yl)-pyrid-5-yl)-1,5-dimethyl-6-oxoverdazyl (3.7)[91]

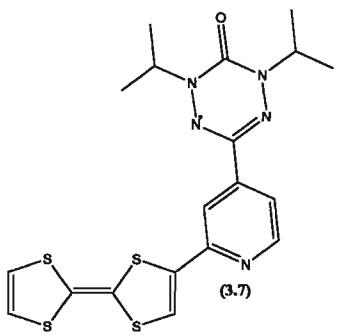

(3.7)

Following the strategy presented in general procedure (C), compound **(3.7)** was isolated as a red solid (42 mg, 42% yield).

| | |
|---|---|
| M.p.: | 151 °C |
| FAB-MS: | $m/z = 462$ $[M]^+$ (9.4%). |
| HRMS (FAB): | Found $m/z$ = 462.0533 $[M]^+$; Calcd. 462.0551 for $C_{19}H_{20}N_5OS_4$. |
| IR (KBr, $cm^{-1}$): | 3421, 2964, 1677, 1596. |
| UV-vis ($CH_3CN$) λ (nm): | 315 (ε = 5174 $M^{-1}cm^{-1}$), 440 (ε = 548 $M^{-1}cm^{-1}$). |

### 4.4.6.4 Synthesis of 6-(6-(2-(1,3-Dithiol-2-ylidene)-1,3-dithiol-4-yl)-pyrid-5-yl)-1,5-diisopropyl-6-oxoverdazyl (3.8)[91]

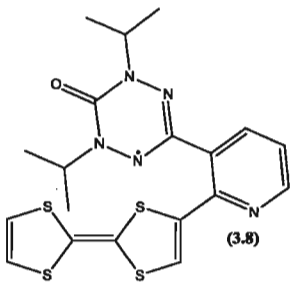

(3.8)

Following the strategy presented in general procedure (C), compound **(3.8)** was isolated as a yellow/brown solid, (40 mg, 40% yield).

| | |
|---|---|
| M.p.: | 151°C |
| FAB-MS: | $m/z = 462$ $[M]^+$ (4%). |
| HRMS (FAB): | Found $m/z$ = 462.0501 $[M]^+$; Calcd. 462.0551 for $C_{19}H_{20}N_5OS_4$. |
| IR (KBr, $cm^{-1}$): | 3446, 2962, 1681, 1565. |
| UV-vis ($CH_3CN$) λ (nm): | 315 (ε = 6032 $M^{-1}cm^{-1}$), 440 (ε = 457 $M^{-1}cm^{-1}$). |

### 4.4.7 Synthesis of a (2:1) TTF-py-verdazyl/TCNQ charge transfer salt (3.28)

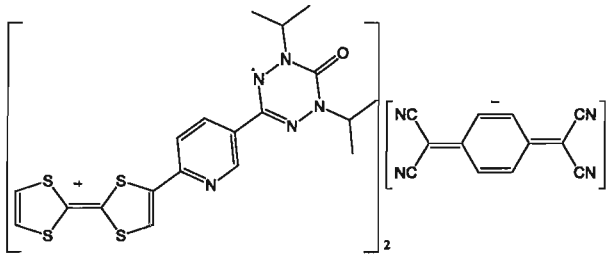

(3.28)

The 2,5-TTF-py-verdazyl radical **(3.5)** (3 mg, 0.00649 mmol) and 7,7,8,8-tetracyanoquinodimethane (TCNQ) (25 mg, 0.122 mmol) were dissolved in DCM (10 mL) and the resulting solution was heated to 60 °C for about a minute. The mixture was then allowed to slowly evaporate at room temperature affording purple crystals of the (2:1) charge transfer salt **(3.28)** (32 mg, 80% yield).

| | |
|---|---|
| M.p.: | 275 °C |
| FAB-MS: | *m/z* = 462 $[M]^{+}$ (45.6%), 205 $[M]^{-}$ (2.9%). |
| HRMS (FAB): | Found *m/z* = 462.0539 $[M]^{+}$; Calcd. 462.0551 for $C_{19}H_{20}N_5OS_4$. |
| IR (KBr, $cm^{-1}$): | 3428, 3053, 2210, 1676, 1457, 1348. |
| UV-vis ($CH_3CN$) λ (nm): | 331 (ε = 10397 $M^{-1}cm^{-1}$), 416 (ε = 7494 $M^{-1}cm^{-1}$), 493 (ε = 2593 $M^{-1}cm^{-1}$), 737 (ε = 661 $M^{-1}cm^{-1}$), 836 (ε = 1353$M^{-1}cm^{-1}$). |

### 4.4.8 Synthesis of 5-(*N*-methyl-*N*-phenylamino)-2,4-pentadienal (3.29)[146]

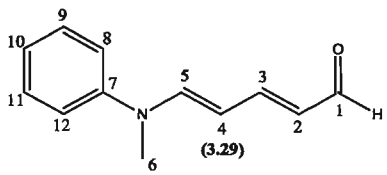

(3.29)

To a solution of methyl-(5-[*N*-methyl-*N*-phenylamino]-2,4-pentadienylidene)-phenylammonium chloride (0.25 g, 0.80 mmol) in MeOH (20 mL) at room temperature was added dropwise a solution of sodium bicarbonate (0.75 g, 8.92 mmol) in water (10 mL). The reaction mixture was refluxed for 15 min, and then allowed to stand for 24 h at room temperature, resulting in the formation of an orange precipitate. The solid was collected and recrystallized from MeOH/$Et_2O$ to afford **(3.29)** as a brown/yellow powder (0.13 g, 86% yield).

| | |
|---|---|
| M.p.: | 69-71 °C |
| FAB-MS: | $m/z$ = 187 $[M]^+$ (26.3%). |
| $^1$H NMR (DMSO, 300 MHz) δ (ppm): | 9.31 (d, $J$ = 8.3 Hz, 1H,1-H), 7.50 (s, 1H, 3-H), 7.39 (d, $J$ = 12.8 Hz, 1H, 10-H), 7.46 (d, $J$ = 3 Hz, 1H, 8-H), 7.39 (t, $J$ = 7.5 Hz, 1H, 9-H) 7.29 (d, $J$ = 4 Hz, 2H, 7-H,11-H), 7.14 (t, $J$ = 7.2 Hz, 1H, 5-H), 5.90 (d, $J$ = 6 Hz, 1H, 2-H), 5.79 (d, $J$ = 11.7 Hz, 1H, 4-H), 3.19 (s, 3H, 6-H). |

### 4.4.9 Synthesis of 5-(tetrathiafulvalenyl)penta-2,4-dien-1-al (3.30)[142]

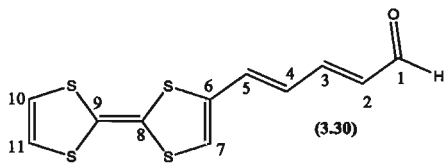

(3.30)

Under a nitrogen atmosphere, at -78 °C, a 1.5 M lithium diisopropylamide solution in THF (3.87 mL, 5.79 mmol) was added to a solution of tetrathiafulvalene **(3.10)** (1.09 g, 5.33 mmol) in THF (60 mL). Compound **(3.29)** was then added and the reaction mixture was allowed to slowly warm to room temperature overnight. On completion, the reaction mixture was poured into a 2 M aqueous solution of hydrochloric acid. The organic layer was extracted into DCM and dried over $Na_2SO_4$. The solvent was removed under

reduced pressure to afford the crude product that was purified by flash chromatography eluting with a (1:1) mixture of hexane and DCM on a silica gel ($R_f$ = 1). Compound **(3.30)** was obtained as a red solid, (0.83 g, 57% yield).

| | |
|---|---|
| M.p.: | 141-143 °C |
| EI-MS: | *m/z* = 284 $[M]^+$ (77%). |
| HRMS (FAB): | Found *m/z* = 283.9458 $[M]^+$; Calcd. 283.9458 for $C_{11}H_8OS_4$. |
| $^1H$ NMR ($CDCl_3$, 300 MHz) δ (ppm): | 9.62 (d, *J* = 7.9 Hz, 1H, 1-H), 7.17 (m, 1H, 2-H), 6.79 (m, 2H, 10-H, 11-H), 6.62 (s, 1H, 7-H), 6.36 (s, 2H, 5-H, 4-H), 6.26 (m, 2H, 3-H). |
| $^{13}C$ NMR ($CDCl_3$, 75 MHz) δ (ppm): | 193.2 (1-C), 150.5 (3-C), 135.3 (6-C), 132.3 (2-C), 131.9 (4-C), 128.7 (8-C, 9-C), 125.2 (10-C, 11-C), 119.1 (5-C), 114.6 (7-C). |
| IR (KBr, $cm^{-1}$): | 3415, 1836, 1689, 1594, 1518, 1129, 987, 822, 656. |

### 4.4.10 Synthesis of 5-(tetrathiafulvalenyl)penta-2,4-dien-1-2,4-diisopropyl-1,2,4,5-tetrazane-3-Oxide (3.31)

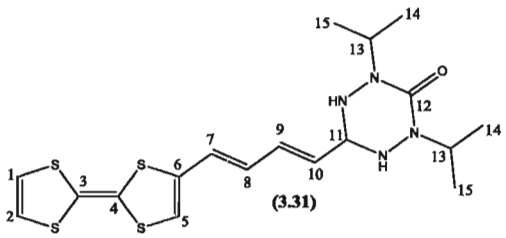

**(3.31)**

A solution containing **(3.30)** (0.09 g, 0.329 mmol), 2,4-diisopropylcarbonylhydrazide *bis*-hydrochloride **(3.11)** (0.10 g, 0.395 mmol) and sodium acetate (0.11 g, 0.790 mmol) in MeOH (30 mL) was refluxed overnight after which time a brown solid precipitated from a dark orange-red solution. The precipitate was removed by filtration and discarded. The

filtrate was collected and evaporated to dryness under reduced pressure. The crude product was purified by flash chromatography ($SiO_2$, $CH_2Cl_2$) ($R_f = 0.6$), to afford **(3.31)** as a red/brown oil (0.10 g, 58% yield).

| | |
|---|---|
| FAB-MS: | *m/z* = 440 $[M]^+$ (70.4%). |
| HRMS (FAB): | Found *m/z* = 440.0811 $[M]^+$; Calcd. 440.0833 for $C_{18}H_{24}N_4O_1S_4$. |
| $^1H$ NMR (DMSO, 300 MHz) δ (ppm): | 6.89 (s, 1H, 5-H), 6.75 (s, 2H, 1, 2-H), 6.61 (d, *J* = 12 Hz, 1H, 7-H), 6.51 (m, 1H, 8-H), 6.16 (dd, *J* = 10.5, 1H, 9-H), 5.83 (dd, *J* = 5.65 Hz , 1H, 10-H), 4.78 (d, *J* = 10.2 Hz, 1H, 11-H), 4.44 (m, 2H, 13-H), 3.96 (s, 2H, NH), 0.99 (m, 12H, 14-H, 15-H). |
| $^{13}C$ NMR ($CDCl_3$, 300 MHz) δ (ppm): | 153.7 (12-C), 134.9 (6-C), 132.9 (8-C), 131.2 (3, 4-C), 130.2 (9-C), 125.5 (10-C), 121.4 (7-C), 120.5 (1-C 2-C), 112.9 (5-C), 69.7 (11-C), 46.9 (13-C), 19.9 (14-C), 19.3 (15-C). |
| IR (KBr, $cm^{-1}$): | 2973, 2926, 2892, 1639, 1454, 1089, 1051, 881, 627. |
| UV-vis ($CH_3CN$) λ (nm): | 280 (ε = 1876 $M^{-1}cm^{-1}$), 420 (ε = 426 $M^{-1}cm^{-1}$). |

### 4.4.11 Synthesis of 5-(Tetrathiafulvalenyl)penta-2,4-dien-1-1,5-diisopropyl-6-oxoverdazyl (3.9)

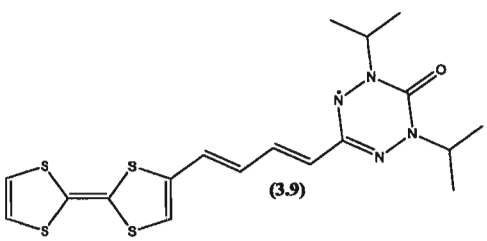

(3.9)

1,4-Benzoquinone (47 mg 0.435 mmol) was added in one portion to a solution of **(3.31)** (100 mg, 0.227 mmol) in benzene (10 mL). The reaction mixture was stirred for 3 h at 60 °C after which time a brown solid precipitated from a dark red solution. The precipitate was removed by filtration and discarded. The filtrate was collected and evaporated under reduced pressure. The crude product was purified via flash chromatography ($SiO_2$, $CH_2Cl_2$) ($R_f$ = 0.8), to afford the radical **(3.9)** as a dark purple solid (52 mg, 59% yield).

| | |
|---|---|
| M.p.: | 128-130 °C. |
| FAB-MS: | *m/z* = 437 $[M]^+$ (5.7%) |
| HRMS (FAB): | Found *m/z* = 437.0581 $[M]^+$; Calcd. 437.0598 for $C_{18}H_{24}N_4OS_4$. |
| IR (KBr, $cm^{-1}$): | 2963, 2925, 2360, 1664, 1261, 1098, 1019, 801. |
| UV-vis ($CH_3CN$) λ (nm): | 325 (ε = 3075 $M^{-1}cm^{-1}$), 440 (ε = 528 $M^{-1}cm^{-1}$). |

## CHAPTER 5- References


1. N. Avarvari and J. D. Wallis, *J. Mater. Chem.*, 2009, 19, 4061-4076.
2. J. V. Yakhmi, *B Mater. Sci.*, 2009, 32, 217-225.
3. C. D. Graham, and B.D. Cullity, *Introduction to Magnetic Materials 2nd Edition*, Wiley, New Jersey, 2009.
4. J. S. Miller and A. J. Epstein, *Mrs. Bull.*, 2000, 25, 21-28.
5. J. M. D. Coey, *Magnetism and Magnetic Materials*, Cambridge University Press, New York, 2010.
6. J. S. Miller and A. J. Epstein, *Ange. Chem. Int. Ed. in English*, 1994, 33, 385-415.
7. T. Pradeep, *Advances in Physical Chemistry*, Allied Publisher Limited, New Dehli, 1999.
8. S. Hatscher, H. Schilder, H. Lueken and W. Urland, *Pure Appl. Chem.*, 2005, 77, 497-511.
9. S. Saini, R. B. Frankel, D. D. Stark and J. T. Ferrucci, *Am. J. Roentgenol*, 1988, 150, 735-743.
10. D. O'Hare, D. Bruce, and R. Walton, *Molecular Materials*, Wiley, West Sussex, 2010.
11. N. A. Spaldin, *Magnetic Materials Fundamentals and Applications*, Cambridge, Santa Barbara, 2003.
12. J. S. Miller, J. C. Calabrese, A. J. Epstein, R. W. Bigelow, J. H. Zhang and W. M. Reiff, *J. Chem. Soc. Chem. Comm.*, 1986, 1026-1028.
13. Y. Pei, M. Verdaguer, O. Kahn, J. Sletten and J. P. Renard, *J. Am. Chem. Soc.*, 1986, 108, 7428-7430.
14. D. Luneau, *Curr. Opin. Solid St. Mat.*, 2001, 5, 123-129.
15. T. Lis, *Acta Crystallogr. B*, 1980, 36, 2042-2046.
16. D. Gatteschi, L. Pardi, A. L. Barra, A. Muller and J. Doring, *Nature*, 1991, 354, 463-465.
17. G. Christou, D. Gatteschi, D. N. Hendrickson and R. Sessoli, *Mrs. Bull.*, 2000, 25, 66-71.
18. R. Sessoli, D. Gatteschi, A. Caneschi and M. A. Novak, *Nature*, 1993, 365, 141-143.

19. H. Miyasaka, K. Nakata, L. Lecren, C. Coulon, Y. Nakazawa, T. Fujisaki, K. Sugiura, M. Yamashita and R. Clerac, *J. Am. Chem. Soc.*, 2006, 128, 3770-3783.
20. S. Brooker and J. A. Kitchen, *Dalton Trans.*, 2009, 7331-7340.
21. A. Caneschi, D. Gatteschi, N. Lalioti, C. Sangregorio, R. Sessoli, G. Venturi, A. Vindigni, A. Rettori, M. G. Pini and M. A. Novak, *Angew. Chem. Int. Ed.*, 2001, 40, 1760-1763.
22. A. Ludi, *Chimia*, 1972, 26, 647-647.
23. J. S. Miller and M. Drillon, *Magnetism: Molecules to Materials V*, Wiley-VHC, Weinheim, 2005.
24. W. P. Fehlhammer and M. Fritz, *Chem. Rev.*, 1993, 93, 1243-1280.
25. S. Ferlay, T. Mallah, R. Ouahes, P. Veillet and M. Verdaguer, *Nature*, 1995, 378, 701-703.
26. O. Sato, T. Iyoda, A. Fujishima and K. Hashimoto, *Science*, 1996, 272, 704-705.
27. J. D. Cafun, G. Champion, M. A. Arrio, C. C. D. Moulin and A. Bleuzen, *J. Am. Chem. Soc.*, 2010, 132, 11552-11559.
28. A. Bleuzen, C. Lomenech, V. Escax, F. Villain, F. Varret, C. C. D. Moulin and M. Verdaguer, *J. Am. Chem. Soc.*, 2000, 122, 6648-6652.
29. J. M. Lehn, *Supramolecular Chemistry*, VCH, Weinheim, 1995.
30. J. A. Real, A. B. Gaspar, V. Niel and M. C. Munoz, *Coordin. Chem. Rev.*, 2003, 236, 121-141.
31. P. Gutlich and H. A. Goodwin, *Top. Curr. Chem.*, 2004, 233, 1-47.
32. E. M. Kober, M. H. Chisholm, D. J. Ironmonger, and P. Thorton, *Polyhedron*, 1985, 4, 1869.
33. P. Gamez, J. S. Costa, M. Quesada and G. Aromi, *Dalton Trans.*, 2009, 7845-7853.
34. P. E. Figgins and D. H. Busch, *J. Am. Chem. Soc.*, 1960, 82, 820-824.
35. E. Konig and K. Madeja, *Chem. Commun.*, 1966, 61.
36. J. Jung, H. Spiering, Z. Yu and P. Gutlich, *Hyperfine Interact.*, 1995, 95, 107-128.
37. S. Decurtins, P. Gutlich, C. P. Kohler, H. Spiering and A. Hauser, *Chem. Phys. Lett.*, 1984, 105, 1-4.
38. A. Hauser, *Chem. Phys. Lett.*, 1986, 124, 543-548.

39. P. Gutlich, Y. Garcia and H. A. Goodwin, *Chem. Soc. Rev.*, 2000, 29, 419-427.
40. J. P. Launay and O. Kahn, *Chemtronics*, 1988, 3.
41. M. G. B. Drew, A. H. B. Othman, S. G. Mcfall, P. D. A. Mcilroy and S. M. Nelson, *J. Chem. Soc. Dalton*, 1977, 1173-1180.
42. E. Konig, G. Ritter, J. Dengler and S. M. Nelson, *Inorg. Chem.*, 1987, 26, 3582-3588.
43. S. Hayami, Z. Gu, Y. Einaga, Y. Kobayasi, Y. Ishikawa, Y. Yamada, A. Fujishima and O. Sato, *Inorg. Chem.*, 2001, 40, 3240-3242.
44. A. G. Sharpe and C.E. Housecroft, *Inorganic Chemistry 3rd Edition*, Pearson Prentice Hall, Essex, 2008.
45. H. W. Liu, A. Fujishima and O. Sato, *Appl. Phys. Lett.*, 2004, 85, 2295-2297.
46. P. Guionneau, F. Le Gac, A. Kaiba, J. S. Costa, D. Chasseau and J. F. Letard, *Chem. Commun.*, 2007, 3723-3725.
47. J. Wang, B. Slater, A. Alberola, H. Stoeckli-Evans, F. S. Razavi and M. Pilkington, *Inorg. Chem.*, 2007, 46, 4763-4765.
48. F. Bonadio, M. C. Senna, J. Ensling, A. Sieber, A. Neels, H. Stoeckli-Evans and S. Decurtins, *Inorg. Chem.*, 2005, 44, 969-978.
49. S. Hayami, G. Juhasz, Y. Maeda, T. Yokoyama and O. Sato, *Inorg. Chem.*, 2005, 44, 7289-7291.
50. C. Paraschiv, M. Andruh, Y. Journaux, Z. Zak, N. Kyritsakas and L. Ricard, *J. Mater. Chem.*, 2006, 16, 2660-2668.
51. Y. Z. Zhang and O. Sato, *Inorg. Chem.*, 2010, 49, 1271-1273.
52. B. W. Wang, Y.Z. Zhang, O. Sato, and S. Gao, *Chem. Commun.*, 2010, 46.
53. R. G. Hicks, *Org. Biomol. Chem.*, 2007, 5.
54. R. G. Hicks, *Org. Biomol. Chem.*, 2006, 5, 1321-1338.
55. M. Gomberg, *J. Am. Chem. Soc.*, 1900, 22, 757-771.
56. M. J. Plater, S. Kemp and E. Lattmann, *J. Chem. Soc. Perk. Trans.*, 2000, 971-979.
57. D. Maspoch, J. Gomez-Segura, N. Domingo, D. Ruiz-Molina, K. Wurst, C. Rovira, J. Tejada and J. Veciana, *Inorg. Chem.*, 2005, 44, 6936-6938.

58. F. Dietz, N. Tyutyulkov and M. Baumgarten, *J. Phys. Chem. B*, 1998, 102, 3912-3916.

59. W. C. Danen and D. D. Newkirk, *J. Am. Chem. Soc.*, 1976, 98, 516-520.

60. T. M. Barclay, A. W. Cordes, N. A. George, R. C. Haddon, M. E. Itkis, M. S. Mashuta, R. T. Oakley, G. W. Patenaude, R. W. Reed, J. F. Richardson and H. Zhang, *J. Am. Chem. Soc.*, 1998, 120, 352-360.

61. G. Wolmershauser and R. Johann, *Angew. Chem. Int. Ed*, 1989, 28, 920-921.

62. W. Fujita and K. Awaga, *Science*, 1999, 286, 261-262.

63. J. L. Brusso, O. P. Clements, R. C. Haddon, M. E. Itkis, A. A. Leitch, R. T. Oakley, R. W. Reed and J. F. Richardson, *J. Am. Chem. Soc.*, 2004, 126, 14692-14693.

64. J. L. Brusso, O. P. Clements, R. C. Haddon, M. E. Itkis, A. A. Leitch, R. T. Oakley, R. W. Reed and J. F. Richardson, *J. Am. Chem. Soc.*, 2004, 126, 8256-8265.

65. A. J. Banister, N. Bricklebank, I. Lavender, J. M. Rawson, C. I. Gregory, B. K. Tanner, W. Clegg, M. R. J. Elsegood and F. Palacio, *Angew. Chem. Int. Ed.*, 1996, 35, 2533-2535.

66. T. M. Barclay, L. Beer, A. W. Cordes, R. T. Oakley, K. E. Preuss, R. W. Reed and N. J. Taylor, *Inorg. Chem.*, 2001, 40, 2709-2714.

67. M. Tamura, Y. Nakazawa, D. Shiomi, K. Nozawa, Y. Hosokoshi, M. Ishikawa, M. Takahashi and M. Kinoshita, *Chem. Phys. Lett.*, 1991, 186, 401-404.

68. B. D. Koivisto and R. G. Hicks, *Coord. Chem. Rev.*, 2005, 249, 2612-2630.

69. R. Kuhn and H. Trischmann, *Angew. Chem. Int. Ed.*, 1963, 75, 294-297.

70. F. A. Neugebauer, H. Fischer and R. Siegel, *Chem. Ber.*, 1988, 121, 815-822.

71. V. Chemistruck, D. Chambers and D. J. R. Brook, *J. Org. Chem.*, 2009, 74, 1850-1857.

72. F. A. Neugebauer, R. Kuhn, and H. Trischmann, *Monatsh. Chem.*, 1966, 97, 525.

73. R. Bernhardt, F.A. Neugebauer, and H. Fischer, *Chem. Berl. Recl.*, 1977, 110, 2254.

74. J. Yamauchi, N. Azuma, K. Mukai, H. Ohyanish, and Y. Deguchi, *Bull. Chem. Soc. Jpn.*, 1973, 46, 2728-2734.

75. G. Srdanov, P.M. Allemand, and F. Wudl, *J. Am. Chem. Soc.*, 1990, 112, 9391.

76. B. Kanellakopulos, R.K. Kremer, P. Bele, H. Brunner, and F.A. Neugebauer, *Chem. Phys. Lett.*, 1994, 230, 255-259.

77. M. T. Lemaire, R. G. Hicks, L. Ohrstrom, J. F. Richardson, L. K. Thompson, and Z. Q. Xu, *J. Am. Chem. Soc.*, 2001, 7154-7159.

78. V. Lynch, D.J.R. Brook, B. Conklin, and M.A. Fox, *J. Am. Chem. Soc.*, 1997, 119, 5155.

79. M. T. Lemaire, R. G. Hicks, L. K. Thompson, and T. M. Barclay, *J. Am. Chem. Soc.*, 2000, 122, 8077-8078.

80. M. Clemente-Leon, E. Coronado, J. R. Galán-Mascarós, C. Giménez-Saiz, C. J. Gómez-García and E. Martínez-Ferrero, *J. Chem. Soc. Dalton Trans.*, 2000, 3989-3998.

81. E. Coronado and J. R. Galan-Mascaros, *J Mater Chem*, 2005, 15, 66-74.

82. F. Wudl, G. M. Smith and E. J. Hufnagel, *J. of the Chem. Soc. D-Chem. Commun.*, 1970, 1453-1454.

83. D. Canevet, M. Salle, G. X. Zhang, D. Q. Zhang and D. B. Zhu, *Chem. Commun.*, 2009, 2245-2269.

84. J. R. Galan-Mascaros, E. Coronado, C.J. Gomez-Garcõa, and V. Laukhin *Nature*, 2000, 405, 447-449.

85. R. H. Blessing and P. Coppens, *Solid State Commun.*, 1974, 15, 215-221.

86. K. Yamaguchi, H. Namimoto, T. Fueno, T. Nogami and Y. Shirota, *Chem. Phys. Lett.*, 1990, 166, 408-414.

87. A. Alberola and M. Pilkington, *Curr. Org. Synth.*, 2009, 6, 66-78.

88. R. Kumai, M. M. Matsushita, A. Izuoka and T. Sugawara, *J. Am. Chem. Soc.*, 1994, 116, 4523-4524.

89. J. Nakazaki, M. M. Matsushita, A. Izuoka and T. Sugawara, *Tetrahedron Lett.*, 1999, 40, 5027-5030.

90. H. Komatsu, M. M. Matsushita, S. Yamamura, Y. Sugawara, K. Suzuki and T. Sugawara, *J. Am. Chem. Soc.*, 2010, 132, 4528-4529.

91. M. Chahma, X. S. Wang, A. van der Est and M. Pilkington, *J. Org. Chem.*, 2006, 71, 2750-2755.

92. M. Chahma, K. Macnamara, A. Van der Est, A. Alberola, V. Polo and M. Pilkington, *New. J. Chem.*, 2007, 31, 1973-1978.

93. V. Polo, A. Alberola, J. Andres, J. Anthony and M. Pilkington, *Phys. Chem. Chem. Phys.*, 2008, 10, 857-864.

94. J. Crassous, *Chem. Soc. Rev.*, 2009, 38, 830-845.

95. J. Veciana, *Angew. Chem. Int. Ed.*, 2002, 41, 586-589.

96. T. Ruchon, M. Vallet, J. Thépot, A. Le Floch, and R. W. Boyd , *Physique*, 2000, 5, 273-277.

97. G. L. J. A. Rikken and E. Raupach, *Nature*, 1997, 390, 493-494.

98. L. D. Barron, *Nat. Mater.*, 2008, 7, 691-692.

99. N. A. Spaldin and M. Fiebig, *Science*, 2005, 309, 391-392.

100. C. Train, M. Gruselle, K. Boubekeur, P. Gredin, and N. Ovanesyan, *Coord. Chem. Rev.*, 2006, 250, 2491-2500.

101. C. Train, R. Gheorghe, V. Krstic, L. M. Chamoreau, N. S. Ovanesyan, G. L. J. A. Rikken, M. Gruselle and M. Verdaguer, *Nat. Mater.*, 2008, 7, 729-734.

102. D. Whang, J. S. Seo, H. Lee, S. Jun, J. Oh,Y. J. Jeon and K. Kim, *Nature*, 2000, 404, 982-986.

103. S. Iijima T. Sato, M. Kojima, and N. Matsumoto, *Chem. Lett.*, 2009, 38, 178-179.

104. Y. Ikuta, Y.Sunatsuki, N. Matsumoto,H. Ohta, M. Kojima, S. Iijima,S. Hayami, Y.Maeda, S. Kaizaki, F. Dahan, and J.P. Tuchagues, *Angew. Chem. Int. Ed.*, 2003, 42, 1614-1618.

105. S. Iijima, T. Sato, M. Kojima, and N. Matsumoto, *Chem. Lett.*, 2009, 38, 178-179.

106. Y. Ikuta, Y. Sunatsuki, N. Matsumoto, H. Ohta, M. Kojima, S. Iijima, S. Hayami, Y.Maeda, S. Kaizaki, F. Dahan, and J.P. Tuchagues, *Angew. Chem. Int. Ed.*, 2003, 42, 1614-1618.

107. T. F. Tomotaka Hashibe, Daisuke Furusho, Naohide Matsumoto, and Yukinari Sunatsuki, *Inorg. Chim. Acta*, 2011, 375, 338-342.

108. J. Crosby, J. F. Stoddart, X. Q. Sun and M. R. W. Venner, *Synth.-Stutt.*, 1993, 141-145.

109. S. M. Nelson, P. D. A. Mcllroy, C. S. Stevenson, E. Konig, G. Ritter and J. Waigel, *J. Chem. Soc. Dalton*, 1986, 991-995.

110. L. J. Farrugia, *J. Appl. Crys.*, 1997, 30, 565.

111. I. J. Bruno, C. F. Macrae, J. A. Chisholm, P. R. Edgington, P. McCabe, E. Pidcock, L. Rodriguez-Monge, R. Taylor, J. van de Streek and P. A. Wood, *J. of Appl. Cryst.*, 2008, 466-470.

112. I. C. João Costa Pessoa, Gisela Gonçalves and Isabel Tomaz, *The Journal of the Argentine Chemical Society*, 2009, 97, 151-165.

113. Q. Wang, and M. Pilkington, unpublished results, 2011.

114. S. Alvarez, P. Alemany and D. Avnir, *Chem. Soc. Rev.*, 2005, 34, 313-326.

115. E. Konig, *Coordin. Chem. Rev.*, 1968, 3, 471.

116. L. Latos-Grazynski and A. Berlicka, *Inorg. Chem.*, 2009, 48, 7922-7930.

117. G. E. Ball, D. G. Lonnon, I. Taylor, D. C. Craig, and S. B. Colbran, *Inorg. Chem.*, 2009, 48, 4863-4872.

118. H. G. Jang, L. J. Ming, and L. Que, *Inorg. Chem.*, 1992, 31, 359-364.

119. M. G. Enrique Colacio, Helen Stoeckli-Evans, Francesc Lloret, and C. P. Jose Maria Moreno, *Inorg. Chem.*, 2001, 40, 4876-4883.

120. H. J. Emeleus, *Advances in inorganic chemistry and radiochemistry*, Academic Press Inc., Orlando, 1984.

121. G. M. Sheldrick, *Act. Cryst. Sec. A*, 2008, 64, 112-122.

122. R. P. Schuman, *The Radiochemistry of Manganese,* National Technical Information Services, Oak Ridge, 1971.

123. K. Nakamoto, *Infrared and Raman Spectra of Inorganic and Coordination Compounds Part B*, John Wiley and Sons Inc., Hoboken, 2009.

124. H. B. Burgi, and J. Dunitz, *Structure and Correlation*, VCH, Weinhiem, 1994.

125. E. C. Pare, D. J. R. Brook, A. Brieger, M. Badik and M. Schinke, *Org. Biomol. Chem.*, 2005, 3, 4258-4261.

126. R. G. Hicks, M. T. Lemaire, L. K. Thompson and T. M. Barclay, *J. Am. Chem. Soc.*, 2000, 122, 8077-8078.

127. A. J. Moore and M. R. Bryce, *Synthesis*, 1997, 4, 407-409.

128. S. G. Bougessa, A. K.; Golhen, S.; Ouahab, L.; Fabre, J. M. Gruselle, C. Train, K. Boubekeur, P. Gredin, and N. Ovanesyan, *Tetrahedron Lett*, 2003, 44, 9275-9278.

129. Y. Song, A. S. Dhindsa, J. P. Badyal, M. R. Bryce, Y. M. Lvovm, C. Petty, and J. Yarwood, *Chem. Matter.*, 1992, 4, 724-728.

130. S. Fornell, D. J. R. Brook, J. E. Stevens, B. Noll, T. H. Koch, and W. Eisfeld, *Inorg. Chem.*, 2000, 39, 562-567.

131. P. M. Viruela, R. Viruela, R. Pou-Amerigo, and E. Orti, *Synthetic Metals*, 1999, 103, 1991-1992.

132. J. S. Chappell, A. N. Bloch, W. A. Bryden, M. Maxfield, T. O. Poehler and D. O. Cowan, *J. Am. Chem. Soc.*, 1981, 103, 2442-2443.

133. R. B. Alberto Girlando, and Cesare Pecile, *Chem. Phys. Lett.*, 1974, 25, 409-412.

134. T. P. Radhakrishnan, *Resonance*, 1998, 2, 6-23.

135. C. K. F. Shen, H. M. Duong, G. Sonmez and F. Wudl, *J. Am. Chem. Soc.*, 2003, 125, 16206-16207.

136. K. Tanaka, T. Matsumoto, F. Ishiguro and Y. Chujo, *J. Mater. Chem.*, 2011, 21, 9603-9607.

137. R. Yuge, A. Miyazaki, T. Enoki, K. Tamada, F. Nakamura and M. Hara, *J Phys. Chem. B*, 2002, 106, 6894-6901.

138. R. M. Satoru Shimomura, Takashi Tsujino, Takashi Kawamura and Susumu Kitagawa, *J. Am. Chem. Soc.*, 2006, 128, 16416-16417.

139. B. Scott, F. B. Kaufman, and J.B. Torrance, *Solid State Commun.*, 1975, 17, 1369-1373.

140. R. C. Thompson, Y. Hoyano and C. F. Schwerdtfeger, *Solid State Commun.*, 1977, 23, 633-635.

141. D. A. Clemente and A. Marzotto, *J. Org. Chem.*, 1996, 6, 941-946.

142. B. Insuasty, C. Atienza, C. Seoane, N. Martin, J. Garin, J. Orduna, R. Alcala and B. Villacampa, *J. Org. Chem.*, 2004, 69, 6986-6995.

143. B. W. Wang, D. Zhang, Y. Chem, L. Zhang, L. Tian, J.H. Ni, and J. Jiang, *Dalton Trans.*, 2009, 9418-9425.

144. J. Moore, *J. Org. Chem.*, 1996, 407.

145. C. Gallina, R. Calabretta, and C. Giodano, *Synthesis*, 1991, 7, 536-539.

146. O. J. Garın, J. Ruperez, R. Alcala, B. Villacampa, C. Sanchez, N. Martın, J.L. Segura, and M. Gonzalez, *Tetrahedron Lett.*, 1998, 39, 3577-3580.

# CHAPTER 6- Appendix

## 6.1 NMR characterization

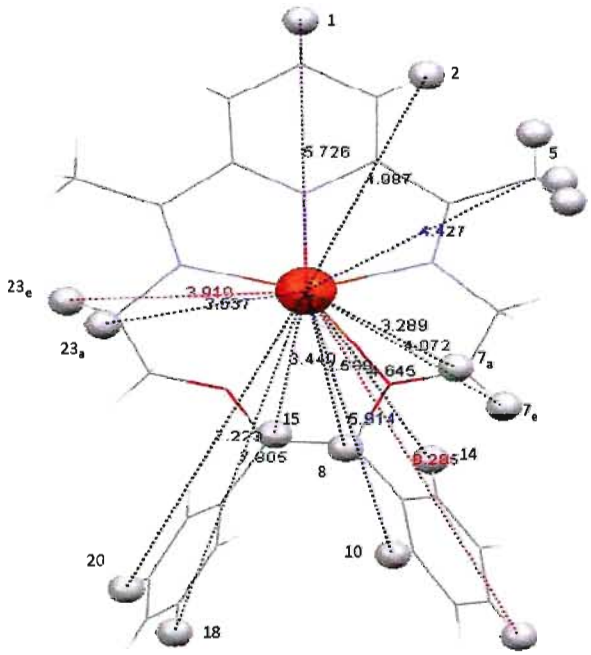


**Figure 6.1:** Mercury[111] representation of the 7-coordinate high spin *R,R* $[Fe(N_3O_2)(CN)_2]$ macrocycle **(2.9)**. Dashed lines represent intramolecular distances from the protons to the Fe(II) centre. Distances are given in Å. The subscripts *e* and *a* refer to equatorial and axial protons, respectively.

**Table 6.1:** Assignment of the $^{13}C$ NMR spectrum for *S,S* $[Fe(N_3O_2)(CN)_2]$ **(2.10)** in $CD_2Cl_2$ at 295 K.

| Assignment | Chemical shift δ (ppm) | Average Fe(II) bond distance (Å) | Line width (Hz) | HSQC $^1H$ shift |
|---|---|---|---|---|
| C-25,4 | 784.9 | 2.9 | 390 | --- |
| C-3,26 | 491.2 | 2.8 | 430 | --- |
| C-1 | 248.4 | 4.7 | 76 | --- |
| C-10,14,17,21 | 155.8 | 5.6 | 288 | --- |
| C-12,19 | 132.8 | 7.5 | 56 | 4.65 |
| C-8,15 | 127.7 | 4.8 | 200 | --- |
| C-11,13,18,20 | 124.6 | 6.9 | 140 | 5.37 |
| C-2,27 | 32.0 | 4.2 | 160 | --- |
| C-5,24 | -3.4 | 4.5 | 129 | --- |

| | | | | |
|---|---|---|---|---|
| C-9,16 | -61.9 | 3.4 | 140 | --- |
| C-7,22 | -85.2 | 3.2 | 170 | --- |
| C-6,23 | -156.2 | 3 | 320 | --- |
| CN | -484 | 2 | 555 | --- |

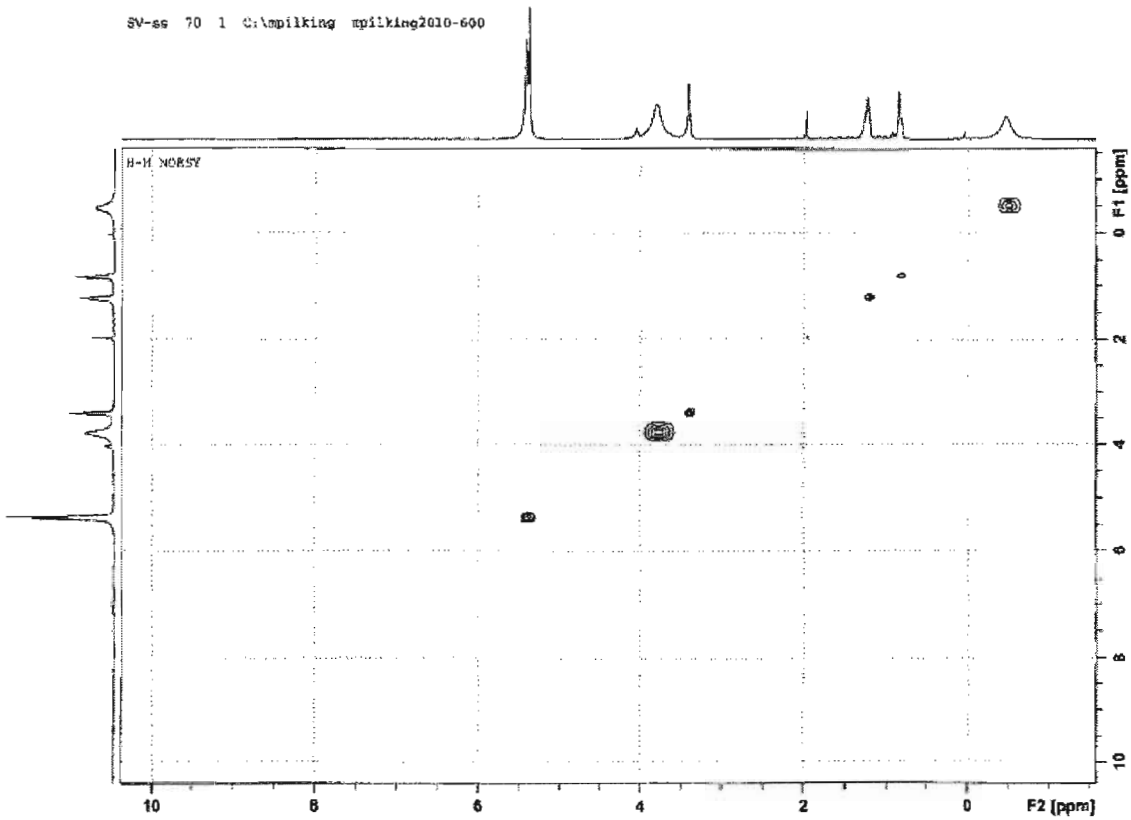


**Figure 6.2:** 600 MHz $^1$H-$^1$H NOESY NMR spectrum of *S,S* $[Fe(N_3O_2)(CN)_2]$ macrocycle **(2.10)** in $CD_2Cl_2$ at 295 K.

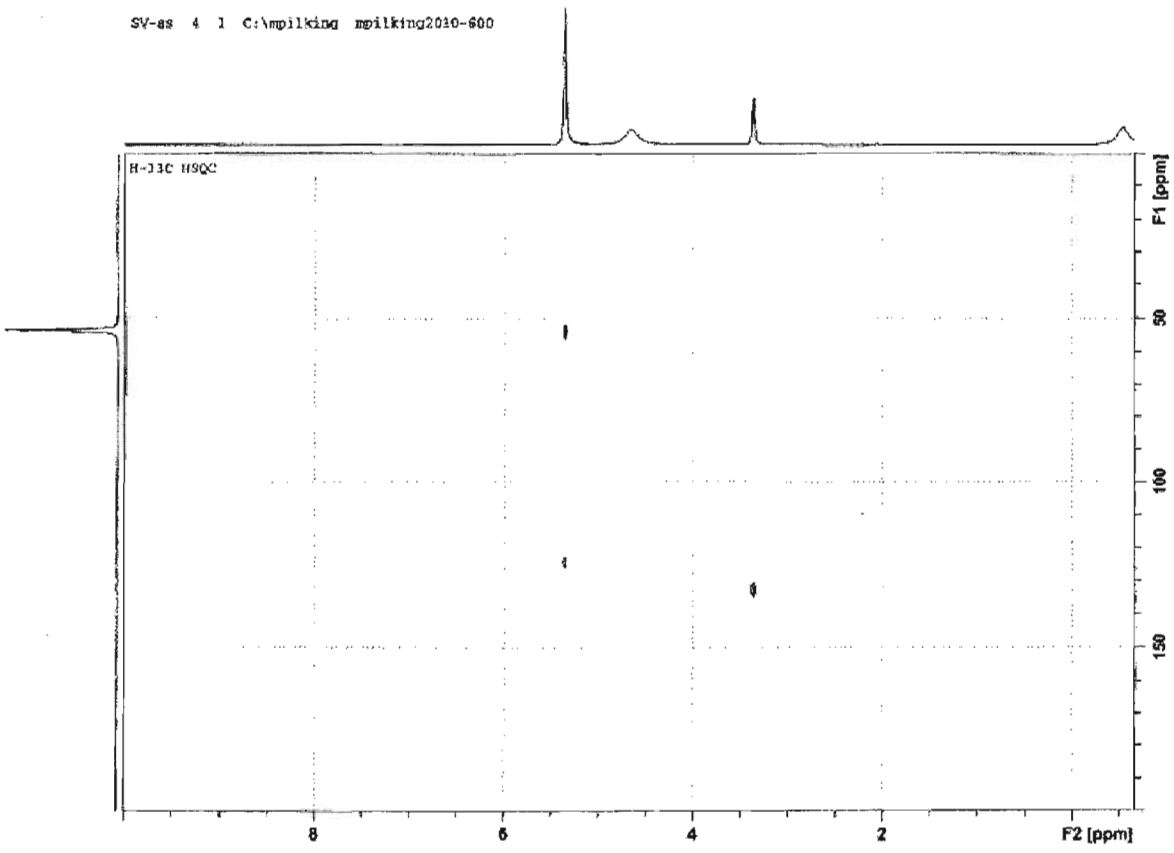


**Figure 6.3:** 600 MHz $^{1}H$-$^{13}C$ HSQC NMR spectrum of *S,S* $[Fe(N_3O_2)(CN)_2]$ macrocycle **(2.10)** in $CD_2Cl_2$ at 295 K.

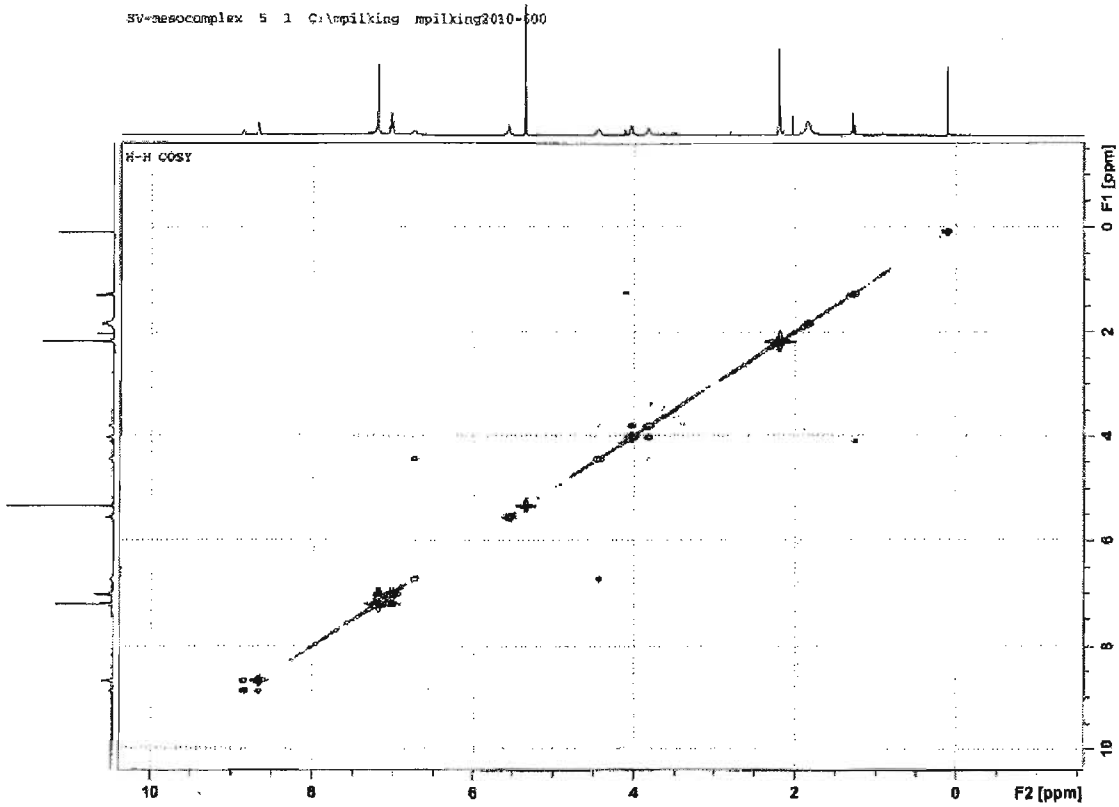


**Figure 6.4:** 600 MHz $^1$H-$^1$H COSY NMR spectrum of *meso* $[Fe(N_3O_2)(CN)_2]$ macrocycle **(2.12)** in $CD_2Cl_2$ at 295 K.

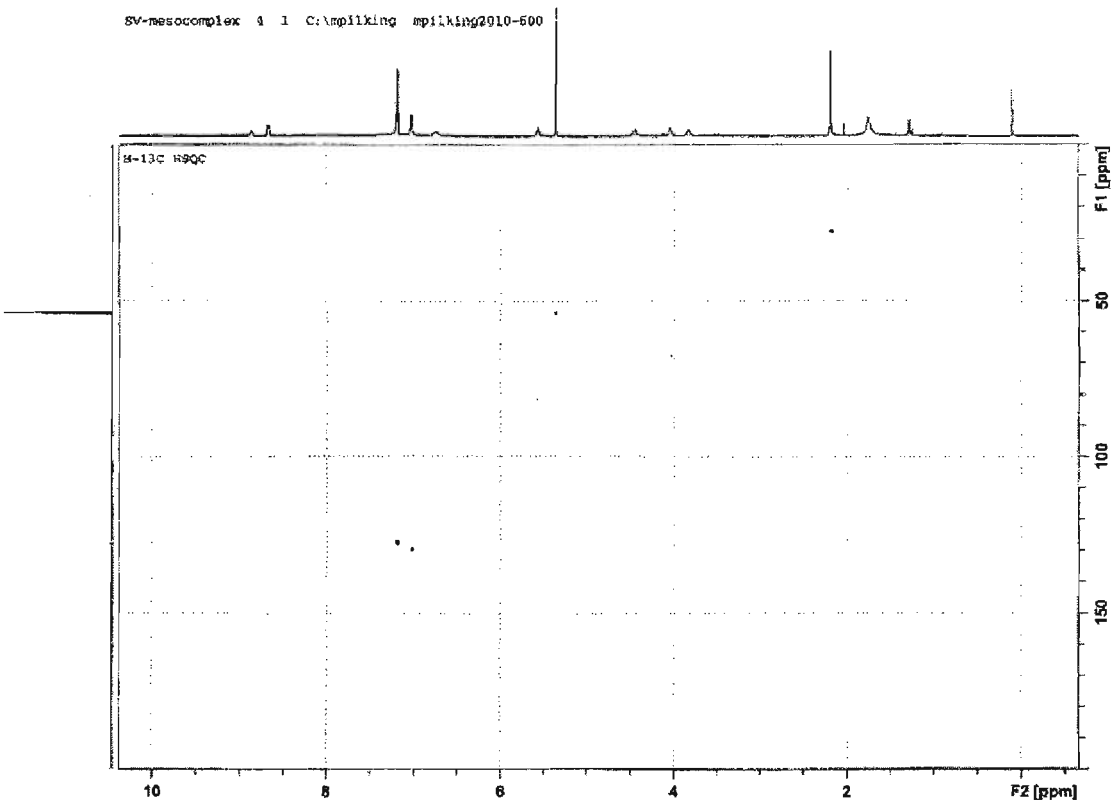


**Figure 6.5:** 600 MHz $^{1}H$-$^{13}C$ HSQC NMR spectrum of *meso* $[Fe(N_3O_2)(CN)_2]$ macrocycle **(2.12)** in $CD_2Cl_2$ at 295 K.

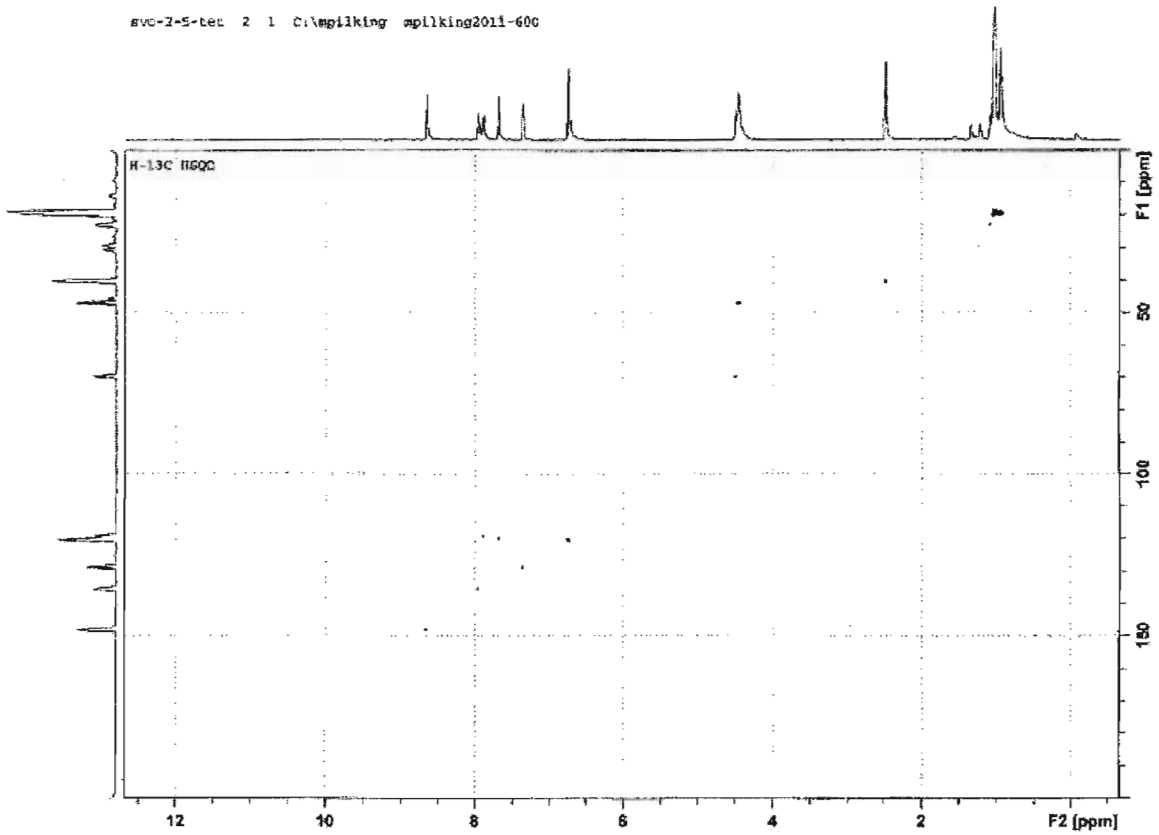


**Figure 6.6:** 600 MHz $^{1}H$-$^{13}C$ HSQC NMR spectrum of 2,5-tetrazane **(3.17)** in $CD_2Cl_2$ at 295 K.

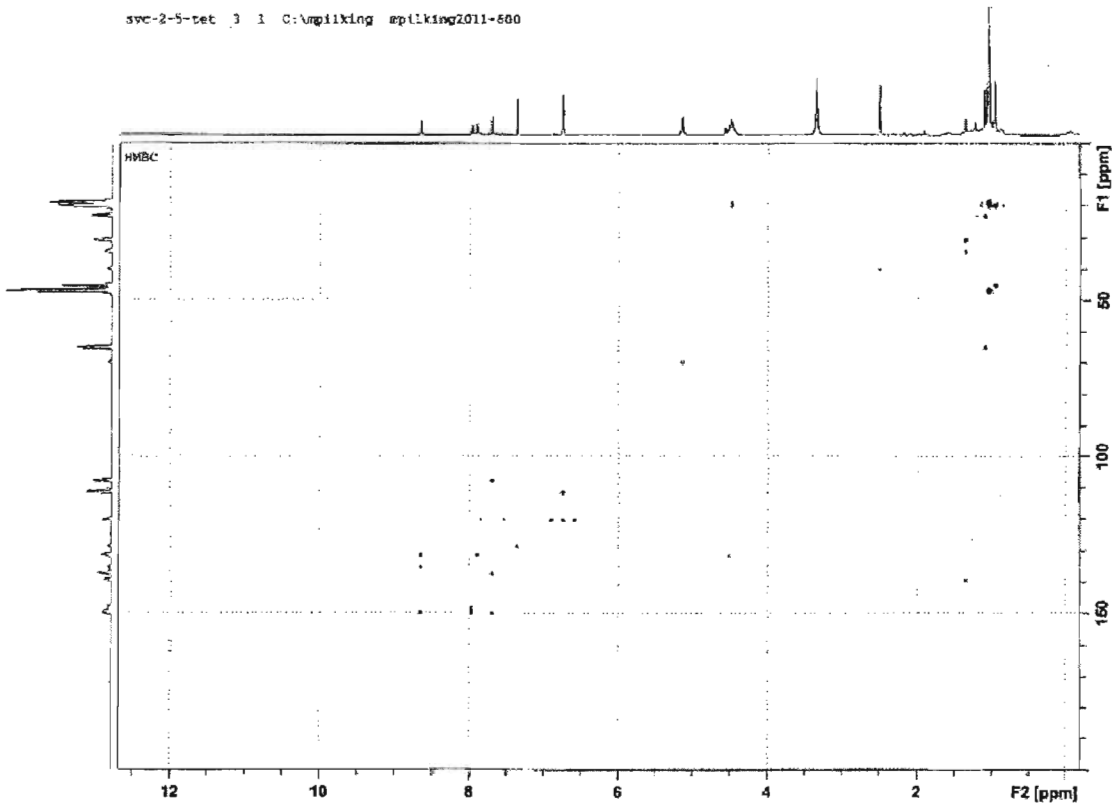


**Figure 6.7:** 600 MHz $^{1}H$-$^{13}C$ HMBC NMR spectrum of 2,5-tetrazane **(3.17)** in $CD_2Cl_2$ at 295 K.

## 6.2 Powder diffraction pattern

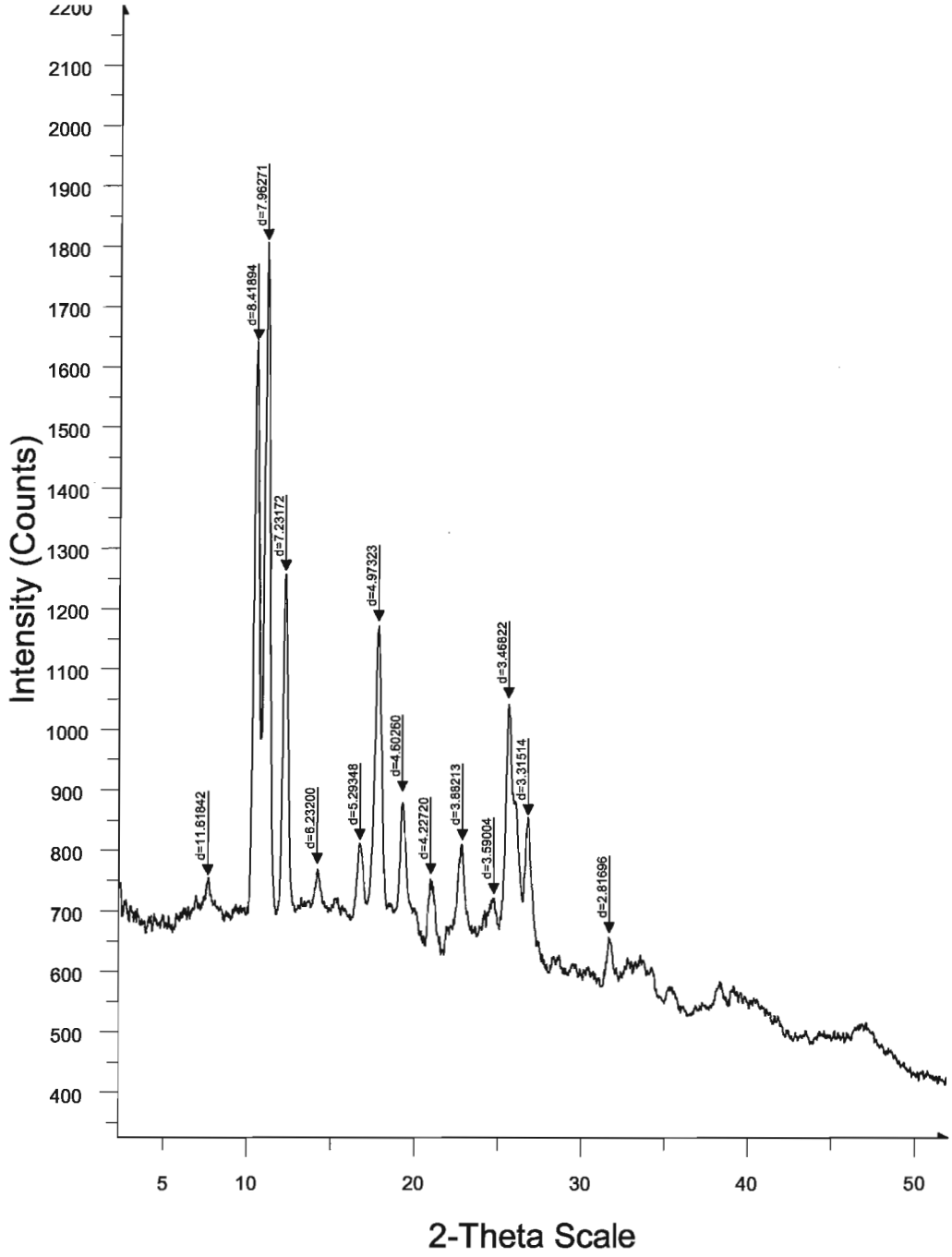


**Figure 6.8:** Powder pattern for *meso* complex **(2.12)**.

## 6.3 Crystallographic tables

**Table 6.2:** Crystal data and structure refinement parameters for compounds **(2.9)** and **(2.16)**.

| | **(2.9) 100 K** | **(2.9) 250 K** | **(2.16)** |
|---|---|---|---|
| Empirical formula | $C_{66}H_{74}Fe_2N_{12}O_5$ | $C_{66}H_{74}Fe_2N_{12}O_5$ | $C_{54}H_{58}C_{17}Mn_3N_6O_4$ |
| Formula weight | 1227.07 | 1227.07 | 1268.03 |
| Temperature | 100(2) K | 250(2) K | 100(2) K |
| Wavelength | 0.71073 A | 0.71073 A | 0.71073 Å |
| Crystal system, space group | Monoclinic, $P2_1$ | Monoclinic, $P2_1$ | Monoclinic $P2_1$ |
| Unit cell dimensions | a = 14.1310(16) Å α = 90°<br>b = 10.5819(10) Å β = 99.233(4)°<br>c = 20.876(2) Å γ = 90° | a = 14.3466(19) Å α = 90°<br>b = 10.7143(12) Å β = 100.195(4)°<br>c = 21.144(3) Å γ = 90° | a = 18.4095(11) Å α= 90°<br>b = 15.8305(10) Å β = 113.018(2)°<br>c = 23.5246(18) Å γ = 90°. |
| Volume | 3081.2(6) $A^3$ | 3198.8(7) $A^3$ | 6310.0(7) $Å^3$ |
| Z, Calculated density | 2, 1.323 $Mg/m^3$ | 2, 1.274 $Mg/m^3$ | 4, 1.335 $Mg/m^3$ |
| Absorption coefficient | 0.531 $mm^{-1}$ | 0.512 $mm^{-1}$ | 0.933 $mm^{-1}$ |
| F(000) | 1292 | 1292 | 2600 |
| Crystal size | 0.33 x 0.065 x 0.02 mm | 0.44 x 0.09 x 0.07 $mm^3$ | 0.36 x 0.34 x 0.27 $mm^3$ |
| Theta range for data collection | 0.99 to 28.26° | 1.88 to 26.45° | 1.59 to 25.00°. |
| Limiting indices | -16<=h<=18, -13<=k<=13,<br>-24<=l<=27 | -17<=h<=17, -13<=k<=13,<br>-26<=l<=26 | -21<=h<=21, -18<=k<=17,<br>-27<=l<=27 |
| Reflections collected / unique | 23943 / 13021 [R(int) = 0.0564] | 37579 / 12591 [R(int) = 0.0572] | 89379/ 21371 [R(int) = 0.0438] |
| Completeness to theta | 28.26 94.2 % | 26.45 98.7 % | 99.90% |
| Absorption correction | Semi-empirical from equivalents | Semi-empirical from equivalents | Semi-empirical from equivalents |
| Max. and min. transmission | 0.7457 and 0.6361 | 0.7454 and 0.6514 | 0.234 and 0.768 |
| Refinement method | Full-matrix least-squares on $F^2$ | Full-matrix least-squares on $F^2$ | Full-matrix least-squares on F2 |
| Data / restraints / parameters | 13021 / 6 / 774 | 12591 / 15 / 773 | 21371 / 37 / 1329 |
| Goodness-of-fit on $F^2$ | 1.044 | 1.102 | 0.776 |
| Final R indices [I>2 σ(I)] | R1 = 0.0783, wR2 = 0.1718 | R1 = 0.0775, wR2 = 0.1588 | R1 = 0.0718, wR2 = 0.1859 |
| R indices (all data) | R1 = 0.1480, wR2 = 0.2170 | R1 = 0.1138, wR2 = 0.1790 | R1 = 0.0764, wR2 = 0.1900 |
| Absolute structure parameter | 0.08(3) | 0.16(2) | 0.15(2) |
| Largest diff. peak and hole | 1.457 and -0.839 $e.A^{-3}$ | 0.986 and -0.507 $e.A^{-3}$ | 1.066 and -1.466 $e.Å^{-3}$ |

**Table 6.3:** Crystal data and structure refinement parameters for compound **(2.11)**.

| | **(2.11) 100 K** | **(2.11) 200 K** |
|---|---|---|
| Empirical formula | $C_{32}H_{35}C_{16}FeN_5O_2$ | $C_{32}H_{35}C_{16}FeN_5O_2$ |
| Formula weight | 790.2 | 790.2 |
| Temperature | 100(2) K | 200(2) K |
| Wavelength | 0.71073 A | 0.71073 A |
| Crystal system, space group | Monoclinic, P2(1)/c | Monoclinic, P2(1)/c |
| Unit cell dimensions | a = 11.0023(8) Å α = 90°<br>b = 42.915(3) Å β = 111.81°<br>c = 8.1767(6) Å γ = 90° | a = 11.1259(11) Å α = 90°<br>b = 43.231(4) Å β = 111.391(2)°<br>c = 8.2764(7) Å γ = 90° |
| Volume | 3584.3(5) $Å^3$ | 3706.6(6) $Å^3$ |
| Z, Calculated density | 4, 1.464 $Mg/m^3$ | 4, 1.416 $Mg/m^3$ |
| Absorption coefficient | 0.905 $mm^{-1}$ | 0.875 $mm^{-1}$ |
| F(000) | 1624 | 1624 |
| Crystal size | 0.38 x 0.1 x 0.03 mm | 0.38 x 0.1 x 0.03 mm |
| Theta range for data collection | 1.90 to 24.49° | 1.88 to 24.00° |
| Limiting indices | -12<=h<=11, -50<=k<=43, -7<=l<=9 | -11<=h<=12, -49<= k<=49, -9<=l<=9 |
| Reflections collected / unique | 14507 / 4168 [R(int) = 0.0801] | 19899 / 5817 [R(int) = 0.0895] |
| Completeness to theta | 24.49 69.8% | 24.00 99.7% |
| Absorption correction | Semi-empirical from equivalents | Semi-empirical from equivalents |
| Max. and min. transmission | 0.7457 and 0.5862 | 0.7454 and 0.5375 |
| Refinement method | Full-matrix least-squares on $F^2$ | Full-matrix least-squares on $F^2$ |
| Data / restraints / parameters | 4168 / 92 / 415 | 5817 / 68 / 401 |
| Goodness-of-fit on $F^2$ | 1.165 | 1.184 |
| Final R indices [I>2 σ(I)] | R1 = 0.1045, wR2 = 0.2261 | R1 = 0.1072, wR2 = 0.2369 |
| R indices (all data) | R1 = 0.1550, wR2 = 0.2631 | R1 = 0.1589, wR2 = 0.2696 |
| Largest diff. peak and hole | 0.632 and -0.566 $e.Å^{-3}$ | 0.743 and -0.614 $e.A^{-3}$ |

**Table 6.4:** Crystal data and structure refinement parameters for compounds **(3.5)** and **(3.6)**.

| | **(3.5)** | **(3.6)** |
|---|---|---|
| Empirical formula | $C_{20}H_{22}C_{l2}N_5OS_4$ | $C_{19}H_{20}N_5OS_4$ |
| Formula weight | 547.57 | 462.64 |
| Temperature | 150(2) K | 150(2) K |
| Wavelength | 0.71073 Å | 0.71073 Å |
| Crystal system | Monoclinic | Triclinic |
| Space group | P 21/c | P-1 |
| Unit cell dimensions | a = 19.204(2) Å α = 90°<br>b = 14.9860(17) Å β = 98.439(4)°<br>c = 8.7313(9) Å γ = 90° | a = 8.7282(4) Å, α = 89.159(3)°.<br>b = 8.7336(5) Å, β = 85.176(3)°<br>c = 14.5253(7) Å, γ = 71.793(3)°. |
| Volume | 2485.6(5) $Å^3$ | 1048.00(9) $Å^3$ |
| Z | 4 | 2 |
| Density (calculated) | 1.463 $Mg/m^3$ | 1.466 $Mg/m^3$ |
| Absorption coefficient | 0.621 $mm^{-1}$ | 0.475 $mm^{-1}$ |
| F(000) | 1132 | 482 |
| Crystal size | 0.233 x 0.120 x 0.100 $mm^3$ | 0.25 x 0.12 x 0.03 $mm^3$ |
| Theta range for data collection | 1.73 to 31.00° | 2.46 to 33.17°. |
| Index ranges | -27<=h<=27, -21<=k<=21, -12<=l<=12 | -13<=h<=13, -13<=k<=12, -22<=l<=22 |
| Reflections collected | 49431 | 39339 |
| Independent reflections | 7737 [R(int) = 0.0678] | 7765 [R(int) = 0.0717] |
| Completeness to theta = 31.00° | 97.60% | 96.90% |
| Absorption correction | Semi-empirical from equivalents | Semi-empirical from equivalents |
| Max. and min. transmission | 0.7461 and 0.6515 | 0.9859 and 0.8905 |
| Refinement method | Full-matrix least-squares on $F^2$ | Full-matrix least-squares on $F^2$ |
| Data / restraints / parameters | 7737 / 0 / 293 | 7765/ 0 /226 |
| Goodness-of-fit on F2 | 1.067 | 1.018 |
| Final R indices [I>2sigma(I)] | R1 = 0.0689, wR2 = 0.1793 | R1 = 0.0524, wR2 = 0.1257 |
| R indices (all data) | R1 = 0.1000, wR2 = 0.1988 | R1 = 0.1207, wR2 = 0.1592 |
| Largest diff. peak and hole | 0.821 and -0.836 $e.Å^{-3}$ | 0.952 and -0.966 $e.Å^{-3}$ |

**Table 6.5:** Crystal data and structure refinement parameters for compounds **(3.28)** and **(3.9)**.

| | **(3.28)** | **(3.9)** |
|---|---|---|
| Empirical formula | $C_{18}H_{21}N_4OS_4$ | $C_{50}H_{44}N_{14}O_2S_8$ |
| Formula weight | 437.63 | 1129.47 |
| Temperature | 150(2) K | 200(2) K |
| Wavelength | 0.71073 Å | 0.71073 Å |
| Crystal system | Monoclinic | Triclinic |
| Space group | P 21/n | P -1 |
| Unit cell dimensions | a = 5.0799(6) Å α = 90°<br>b = 15.262(2) Å β = 92.029(4)°<br>c = 26.690(3) Å γ = 90° | a = 8.5821(8) Å α = 89.762(5)°<br>b = 10.1665(9) Å β = 89.439(4)°<br>c = 31.440(3) Å γ = 78.963(4)° |
| Volume | 2067.9(4) $Å^3$ | 2692.3(4) $Å^3$ |
| Z | 4 | 2 |
| Density (calculated) | 1.406 $Mg/m^3$ | 1.393 $Mg/m^3$ |
| Absorption coefficient | 0.476 $mm^{-1}$ | 0.386 $mm^{-1}$ |
| F(000) | 916 | 1172 |
| Crystal size | 0.270 x 0.020 x 0.020 $mm^3$ | 0.23 x 0.12 x 0.10 $mm^3$ |
| Theta range for data collection | 2.03 to 22.50° | 1.94 to 25.00° |
| Index ranges | -5<=h<=4, -16<=k<=16, -28<=l<=28 | -10<=h<=8, -12<=k<=12, -37<=l<=37 |
| Reflections collected | 18391 | 45462 |
| Independent reflections | 2713 [R(int) = 0.0974] | 9339 [R(int) = 0.0564] |
| Completeness to theta = 31.00° | 99.70% | 98.50% |
| Absorption correction | Semi-empirical from equivalents | Semi-empirical from equivalents |
| Max. and min. transmission | 0.7454 and 0.6367 | 0.7457 and 0.6295 |
| Refinement method | Full-matrix least-squares on $F^2$ | Full-matrix least-squares on $F^2$ |
| Data / restraints / parameters | 2713 / 0 / 248 | 9339 / 0 / 671 |
| Goodness-of-fit on F2 | 1.208 | 1.242 |
| Final R indices [I>2sigma(I)] | R1 = 0.0811, wR2 = 0.1297 | R1 = 0.1295, wR2 = 0.2953 |
| R indices (all data) | R1 = 0.1117, wR2 = 0.1414 | R1 = 0.1389, wR2 = 0.2996 |
| Largest diff. peak and hole | 0.403 and -0.406 $e.Å^{-3}$ | 1.266 and -0.756 $e.Å^{-3}$ |

**Table 6.6:** Bond lengths (Å) for the 2,5-TTF-py-(diisopropyl)verdazyl radical **(3.5)**.

| **Atoms** | **Bond length (Å)** | **Atoms** | **Bond Length (Å)** |
|---|---|---|---|
| S1-C5 | 1.762(3) | C13-C15 | 1.496(4) |
| S1-C3 | 1.750(3) | C13-C14 | 1.499(4) |
| S2-C3 | 1.760(3) | C16-C18 | 1.510(4) |
| S2-C4 | 1.736(3) | C16-C17 | 1.507(4) |
| S3-C20 | 1.759(3) | S3-C1 | 1.732(3) |

| | | | |
|---|---|---|---|
| S4-C20 | 1.758(3) | S4-C2 | 1.750(3) |
| O1-C12 | 1.224(3) | N1-C10 | 1.325(3) |
| N1-C6 | 1.346(3) | N2-N4 | 1.359(3) |
| N2-C11 | 1.338(3) | N3-N5 | 1.362(3) |
| N3-C11 | 1.322(3) | N4-C13 | 1.478(3) |
| N4-C12 | 1.374(3) | N5-C12 | 1.377(3) |
| N5-C16 | 1.483(3) | C1-C2 | 1.318(4) |
| C3-C20 | 1.344(4) | C4-C5 | 1.338(4) |
| C5-C6 | 1.456(4) | C6-C7 | 1.395(4) |
| C7-C8 | 1.373(4) | C8-C9 | 1.386(4) |

**Table 6.7:** Bond angles (°) for the 2,5-TTF-py-(diisopropyl)verdazyl radical **(3.5)**.

| **Atoms** | **Angle (°)** | **Atoms** | **Angle (°)** |
|---|---|---|---|
| C3-S1-C5 | 94.81(13) | C8-C9-C11 | 123.0(2) |
| C3-S2-C4 | 94.25(12) | C10-C9-C11 | 120.3(2) |
| C1-S3-C20 | 94.68(13) | N1-C10-C9 | 125.0(2) |
| C2-S4-C20 | 93.85(14) | N2-C11-N3 | 126.9(2) |
| C6-N1-C10 | 117.5(2) | N2-C11-C9 | 115.6(2) |
| N4-N2-C11 | 115.15(19) | N3-C11-C9 | 117.4(2) |
| N5-N3-C11 | 114.9(2) | O1-C12-N4 | 123.1(2) |
| N2-N4-C12 | 124.2(2) | O1-C12-N5 | 122.9(2) |
| N2-N4-C13 | 115.03(18) | N4-C12-N5 | 114.0(2) |
| C12-N4-C13 | 120.7(2) | N4-C13-C14 | 110.4(2) |
| N3-N5-C12 | 124.44(19) | N4-C13-C15 | 109.8(2) |
| N3-N5-C16 | 115.9(2) | C14-C13-C15 | 112.7(2) |
| C12-N5-C16 | 119.3(2) | N5-C16-C17 | 110.4(2) |
| S3-C1-C2 | 117.5(2) | N5-C16-C18 | 110.3(2) |
| S4-C2-C1 | 118.1(2) | C17-C16-C18 | 111.5(2) |
| S1-C3-S2 | 115.02(15) | S3-C20-S4 | 113.63(14) |

| | | | |
|---|---|---|---|
| S1-C3-C20 | 122.3(2) | S3-C20-C3 | 121.2(2) |
| S2-C3-C20 | 122.7(2) | S4-C20-C3 | 125.2(2) |
| S2-C4-C5 | 118.9(2) | S1-C5-C4 | 116.3(2) |
| S1-C5-C6 | 114.94(19) | C4-C5-C6 | 128.6(2) |
| N1-C6-C5 | 113.9(2) | N1-C6-C7 | 121.9(2) |
| C5-C6-C7 | 124.1(2) | C6-C7-C8 | 119.1(2) |
| C7-C8-C9 | 119.9(2) | C8-C9-C10 | 116.7(2) |

**Table 6.8:** Bond lengths (Å) for 2,6-TTF-py-(diisopropyl)verdazyl radical (**3.6**).

| **Atoms** | **Bond length (Å)** | **Atoms** | **Bond length (Å)** |
|---|---|---|---|
| S1-C1 | 1.726(5) | C10-C11 | 1.380(6) |
| S1-C3 | 1.751(4) | C11-C12 | 1.488(5) |
| S2-C2 | 1.733(5) | C13-C14 | 1.514(6) |
| S2-C3 | 1.759(4) | C13-C15 | 1.529(6) |
| S3-C4 | 1.758(4) | C16-C17 | 1.527(7) |
| S3-C6 | 1.760(5) | C16-C18 | 1.502(6) |
| S4-C4 | 1.762(4) | S4-C5 | 1.733(4) |
| O1-C19 | 1.217(5) | N1-C7 | 1.391(6) |
| N1-C11 | 1.395(5) | N2-N4 | 1.364(4) |
| N2-C12 | 1.331(5) | N3-N5 | 1.366(4) |
| N3-C12 | 1.320(5) | N4-C13 | 1.484(5) |
| N4-C19 | 1.382(5) | N5-C16 | 1.483(6) |
| N5-C19 | 1.379(5) | C1-C2 | 1.327(6) |
| C3-C4 | 1.346(6) | C5-C6 | 1.327(6) |
| C6-C7 | 1.478(6) | C7-C8 | 1.343(6) |
| C8-C9 | 1.325(6) | C9-C10 | 1.397(6) |

**Table 6.9:** Bond angles (°) for 2,6-TTF-py-(diisopropyl)verdazyl radical **(3.6)**.

| Atoms | Angle (°) | Atoms | Angles (°) |
|---|---|---|---|
| C1-S1-C3 | 94.1(2) | C7-C8-C9 | 117.8(3) |
| C2-S2-C3 | 94.4(2) | C8-C9-C10 | 122.9(4) |
| C4-S3-C6 | 94.49(19) | C9-C10-C11 | 119.1(4) |
| C4-S4-C5 | 94.5(2) | N1-C11-C10 | 118.7(4) |
| C7-N1-C11 | 118.0(4) | N1-C11-C12 | 120.4(4) |
| N4-N2-C12 | 114.5(3) | C10-C11-C12 | 120.9(4) |
| N5-N3-C12 | 114.7(3) | N2-C12-N3 | 128.0(3) |
| N2-N4-C13 | 117.0(3) | N2-C12-C11 | 115.1(3) |
| N2-N4-C19 | 124.2(3) | N3-C12-C11 | 116.9(3) |
| C13-N4-C19 | 118.8(3) | N4-C13-C14 | 110.2(3) |
| N3-N5-C16 | 116.1(3) | N4-C13-C15 | 110.4(3) |
| N3-N5-C19 | 124.2(3) | C14-C13-C15 | 111.0(4) |
| C16-N5-C19 | 118.9(3) | N5-C16-C17 | 108.6(3) |
| S1-C1-C2 | 118.8(3) | N5-C16-C18 | 110.2(4) |
| S2-C2-C1 | 117.0(3) | C17-C16-C18 | 112.2(4) |
| S1-C3-S2 | 114.2(2) | O1-C19-N4 | 122.9(4) |
| S1-C3-C4 | 122.2(3) | O1-C19-N5 | 122.9(4) |
| S2-C3-C4 | 123.6(3) | N4-C19-N5 | 114.3(4) |
| S3-C4-S4 | 114.8(2) | S3-C4-C3 | 121.1(3) |
| S4-C4-C3 | 124.2(3) | S4-C5-C6 | 118.9(3) |
| S3-C6-C5 | 117.1(3) | S3-C6-C7 | 114.2(3) |
| C5-C6-C7 | 128.8(4) | N1-C7-C6 | 122.8(4) |
| N1-C7-C8 | 123.6(4) | C6-C7-C8 | 113.7(4) |

**Table 6.10:** Bond lengths (Å) for CT salt **(3.28)**.

| Atoms | Bond length (Å) | Atoms | Bond length (Å) |
|---|---|---|---|
| S3-C4 | 1.76(1) | C6-C7 | 1.46(2) |
| S3-C6 | 1.77(1) | C7-C8 | 1.39(2) |
| S1-C1 | 1.74(1) | C8-C9 | 1.37(2) |
| S1-C3 | 1.74(1) | C10-C11 | 1.38(2) |
| S4-C4 | 1.75(1) | C11-C10 | 1.39(2) |
| S4-C5 | 1.72(1) | C11-C12 | 1.47(2) |
| S2-C2 | 1.76(1) | C14-C16 | 1.38(3) |
| S2-C3 | 1.75(1) | C14-C15 | 1.34(4) |
| O1-C13 | 1.22(2) | N7-C20 | 1.14(2) |
| N3-N5 | 1.36(2) | N6-C21 | 1.13(2) |
| N3-C12 | 1.33(2) | C21-C23 | 1.38(2) |
| N1-C7 | 1.33(2) | C21-C22 | 1.42(2) |
| N1-C10 | 1.33(2) | C21-C20 | 1.45(2) |
| N2-N4 | 1.36(1) | C23-C25 | 1.44(2) |
| N2-C12 | 1.33(2) | C23-C24 | 1.44(2) |
| N4-C13 | 1.39(2) | C25-C24 | 1.34(2) |
| N4-C14 | 1.49(2) | C27-C26 | 1.34(2) |
| N5-C17 | 1.49(2) | N8-C30 | 1.14(2) |
| N5-C13 | 1.35(2) | N9-C31 | 1.13(2) |
| C17-C19 | 1.41(4) | C29-C28 | 1.38(2) |
| C17-C18 | 1.66(4) | C29-C30 | 1.42(2) |
| C2-C1 | 1.32(2) | C29-C31 | 1.45(2) |
| C3-C4 | 1.37(2) | C28-C26 | 1.44(2) |
| C5-C6 | 1.33(2) | C28-C27 | 1.44(2) |

**Table 6.11:** Bond angles (°) for CT salt **(3.28)**.

| Atoms | Angles (°) | Atoms | Angles (°) |
|---|---|---|---|
| C4-S3-C6 | 94.1(6) | S4-C4-C3 | 123.6(9) |
| C1-S1-C3 | 94.1(6) | S4-C5-C6 | 120.5(9) |
| C4-S4-C5 | 93.9(6) | S3-C6-C5 | 115.8(9) |
| C2-S2-C3 | 93.8(6) | S3-C6-C7 | 116.0(8) |
| N5-N3-C12 | 113(1) | C5-C6-C7 | 128(1) |
| C7-N1-C10 | 118(1) | N1-C7-C6 | 116(1) |
| N4-N2-C12 | 116(1) | N1-C7-C8 | 124(1) |

| | | | |
|---|---|---|---|
| N2-N4-C13 | 123(1) | C6-C7-C8 | 120(1) |
| N2-N4-C14 | 116(1) | C7-C8-C9 | 117(1) |
| C13-N4-C14 | 120(1) | C8-C9-C11 | 121(1) |
| N3-N5-C17 | 112(1) | C9-C11-C10 | 118(1) |
| N3-N5-C13 | 126(1) | C9-C11-C12 | 122(1) |
| C17-N5-C13 | 121(1) | C10-C11-C12 | 120(1) |
| N5-C17-C19 | 114(2) | N1-C10-C11 | 122(1) |
| N5-C17-C18 | 106(2) | N3-C12-N2 | 128(1) |
| C19-C17-C18 | 111(2) | N3-C12-C11 | 114(1) |
| S2-C2-C1 | 117(1) | N2-C12-C11 | 118(1) |
| S1-C1-C2 | 119(1) | O1-C13-N4 | 121(2) |
| S1-C3-S2 | 116.0(7) | O1-C13-N5 | 124(2) |
| S1-C3-C4 | 122(1) | N4-C13-N5 | 114(1) |
| S2-C3-C4 | 121.4(9) | N4-C14-C16 | 110(2) |
| S3-C4-S4 | 115.6(7) | N4-C14-C15 | 108(2) |
| S3-C4-C3 | 120.8(9) | C16-C14-C15 | 114(3) |

**Table 6.12:** Bond lengths (Å) for verdazyl radical (**3.9**).

| **Atoms** | **Bond length (Å)** | **Atoms** | **Bond length (Å)** |
|---|---|---|---|
| S1-C5 | 1.742(6) | C12-O1 | 1.207(9) |
| S1-C4 | 1.772(6) | N2-C16 | 1.492(8) |
| S2-C6 | 1.751(6) | C3-C4 | 1.326(8) |
| S2-C4 | 1.756(6) | C5-C6 | 1.338(8) |
| S3-C3 | 1.773(6) | C15-C13 | 1.49(1) |
| S3-C2 | 1.740(7) | C15-C14 | 1.51(1) |
| S4-C3 | 1.764(6) | C9-C10 | 1.324(9) |
| S4-C1 | 1.747(6) | C9-C8 | 1.442(9) |
| N4-N1 | 1.356(7) | C6-C7 | 1.441(8) |
| N4-C11 | 1.330(9) | C10-C11 | 1.467(8) |
| N1-C12 | 1.392(8) | C1-C2 | 1.33(1) |
| N1-C15 | 1.476(8) | C7-C8 | 1.342(9) |
| N3-N2 | 1.366(8) | C17-C16 | 1.52(1) |
| N3-C11 | 1.329(8) | C18-C16 | 1.51(1) |
| C12-N2 | 1.379(9) | | |

**Table 6.13:** Bond angles (°) for verdazyl radical **(3.9)**.

| Atoms | Angles (°) | Atoms | Angles (°) |
|---|---|---|---|
| C5-S1-C4 | 94.4(3) | N1-C15-C14 | 110.0(6) |
| C6-S2-C4 | 95.8(3) | C13-C15-C14 | 112.9(6) |
| C3-S3-C2 | 94.5(3) | C10-C9-C8 | 125.3(6) |
| C3-S4-C1 | 94.8(3) | S2-C6-C5 | 116.2(5) |
| N1-N4-C11 | 115.0(5) | S2-C6-C7 | 118.9(5) |
| N4-N1-C12 | 124.5(5) | C5-C6-C7 | 124.9(6) |
| N4-N1-C15 | 115.7(5) | C9-C10-C11 | 124.6(6) |
| C12-N1-C15 | 119.7(5) | S4-C1-C2 | 117.4(5) |
| N2-N3-C11 | 114.6(5) | C6-C7-C8 | 125.8(6) |
| N1-C12-N2 | 113.5(6) | C9-C8-C7 | 124.5(6) |
| N1-C12-O1 | 122.9(6) | N4-C11-N3 | 127.5(6) |
| N2-C12-O1 | 123.6(6) | N4-C11-C10 | 117.1(6) |
| N3-N2-C12 | 124.8(6) | N3-C11-C10 | 115.4(5) |
| N3-N2-C16 | 115.2(5) | S1-C4-S2 | 114.3(3) |
| C12-N2-C16 | 119.9(5) | S1-C4-C3 | 123.0(5) |
| S3-C3-S4 | 113.7(3) | S2-C4-C3 | 122.6(5) |
| S3-C3-C4 | 123.4(5) | S3-C2-C1 | 118.2(5) |
| S4-C3-C4 | 123.0(5) | N2-C16-C17 | 110.0(5) |
| S1-C5-C6 | 119.3(5) | N2-C16-C18 | 109.3(5) |
| N1-C15-C13 | 110.2(6) | C17-C16-C18 | 112.4(6) |